

NUREG/CR-3784  
SAND84-0689  
R3  
Printed August 1984

# Light Water Reactor Safety Research Program Semiannual Report, April 1983 - September 1983

Marshall Berman

Prepared by  
Sandia National Laboratories  
Albuquerque, New Mexico 87185 and Livermore, California 94550  
for the United States Department of Energy  
under Contract DE-AC04-76DP00789

B412190369 B41031  
PDR NUREG  
CR-3784 R PDR

Prepared for  
**U. S. NUCLEAR REGULATORY COMMISSION**

#### **NOTICE**

This report was prepared as an account of work sponsored by an agency of the United States Government. Neither the United States Government nor any agency thereof, or any of their employees, makes any warranty, expressed or implied, or assumes any legal liability or responsibility for any third party's use, or the results of such use, of any information, apparatus product or process disclosed in this report, or represents that its use by such third party would not infringe privately owned rights.

Available from  
GPO Sales Program  
Division of Technical Information and Document Control  
U.S. Nuclear Regulatory Commission  
Washington, D.C. 20555

and

National Technical Information Service  
Springfield, Virginia 22161

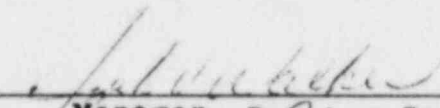
NUREG/CR-3784  
SAND84-0689  
R3

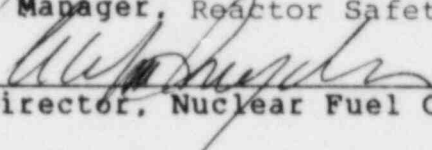
LIGHT WATER REACTOR SAFETY RESEARCH PROGRAM  
SEMIANNUAL REPORT, APRIL 1983 - SEPTEMBER 1983

Marshall Berman

August 1984

Approved:

  
\_\_\_\_\_  
Manager, Reactor Safety Research

  
\_\_\_\_\_  
Director, Nuclear Fuel Cycle Programs

Sandia National Laboratories  
Albuquerque, NM 87185  
Operated by  
Sandia Corporation \*  
for the  
U.S. Department of Energy

Prepared for  
Office of Nuclear Regulatory Research  
U.S. Nuclear Regulatory Commission  
Washington, D.C. 20555  
Under Memorandum of Understanding DOE 40-550-75  
NRC FIN Nos. A-1019, A-1030, A-1246,  
A-1255, A-1301, A-1336

## ABSTRACT

This report describes the investigations and analyses conducted at Sandia National Laboratories, Albuquerque, in support of the Light Water Reactor Safety Research Program from April 1983 through September 1983. The Molten Fuel/Concrete Interactions (MFCI) Study investigates the mechanism of concrete erosion by molten core materials, the nature and rate of generation of evolved gases, and the effects of fission-product release. The Core Melt/Coolant Interactions (CMCI) Study investigates the characteristics of explosive and nonexplosive interactions between molten core materials and concrete, and the probabilities and consequences of such interactions. In the Hydrogen Program, the HECTR code for modelling hydrogen deflagration is being developed, experiments (including those in the FITS facility) are being conducted, and the Grand Gulf Hydrogen Igniter System II is being reviewed. All activities are continuing.

## CONTENTS

	<u>Page</u>
1. MOLTEN-FUEL/CONCRETE INTERACTIONS STUDY	1-1
2. CORE-MELT/COOLANT INTERACTIONS	2-1
2.1 Summary	2-1
2.1.1 Intermediate-Scale Experiments	2-1
2.1.2 Modeling and Analysis	2-10
2.2 Intermediate-Scale Experiments	2-12
2.2.1 EXO-FITS Coarse Mixing Experiment Series (CM)	2-12
2.2.1.1 Experimental Apparatus and Methods	2-12
2.2.1.2 Initial Conditions and Independent Parameters	2-15
2.2.1.3 CM Experiments	2-17
2.2.1.3.1 Experiment CM-1	2-17
2.2.1.3.2 Experiment CM-2	2-17
2.2.1.3.3 Experiment CM-3	2-18
2.2.1.3.4 Experiment CM-4	2-19
2.2.1.3.5 Experiment CM-5	2-23
2.2.1.3.6 Experiment CM-6	2-27
2.2.1.3.7 Experiment CM-7	2-30
2.2.1.3.8 Experiment CM-8	2-32
2.2.1.3.9 Experiment CM-9	2-34
2.2.1.3.10 Experiment CM-10	2-38
2.2.1.3.11 Experiment CM-11	2-45
2.2.1.3.12 Experiment CM-12	2-45
2.2.1.4 Discussion of CM Experiments	2-47
2.3 Modeling and Analysis of Fuel/Coolant Interactions	2-52
2.3.1 Fuel/Coolant Mixing	2-52
2.3.1.1 Limits to Fuel/Coolant Mixing	2-53
2.3.1.2 FITS Analysis	2-59
2.3.2 Triggering	2-63
2.3.2.1 Dynamics of Vapor-Film Growth	2-63
2.3.2.2 Conceptual Picture of Explosion Trig- gering and Molten-Fuel Fragmentation	2-75
2.3.3 Explosion Phase -- A Parametric Model	2-76

## CONTENTS (Cont.)

	<u>Page</u>
2.3.3.1 Description of the Parametric Model	2-79
2.3.3.2 Numerical Solution and Representative Results	2-84
2.3.3.3 Design of Sensitivity Study	2-85
2.3.4 Reactor Application: "Steam Spike" Phenomena	2-85
2.3.5 A Critique of the Paper "Interpretation of Large-Scale Vapor Explosion Experiments with Application to LWR Accidents"	2-95
2.4 References for Section 2	2-101
3. HYDROGEN PROGRAM	3-1
3.1 Analysis and Code Development	3-1
3.1.1 HECTR Analysis and Code Development	3-1
3.1.1.1 Ice-Condenser Containment Analysis	3-1
3.1.1.1.1 Results	3-5
3.1.1.1.2 Effectiveness of Igniter System	3-5
3.1.1.1.3 Unresolved Issues	3-7
3.1.1.2 Transport Analysis	3-7
3.1.1.3 NTS Calculations	3-10
3.1.1.4 BWR Mark III Models	3-10
3.1.1.5 Heat Transfer Upgrades	3-14
3.1.1.6 Additional Upgrades and Preparation for Code Release	3-14
3.1.2 Vortex Dynamics Modeling of Flame Acceleration	3-14
3.1.3 Comparison of CONCHAS-SPRAY and Vortex Dynamics Flame Acceleration Calculations	3-18
3.1.4 One-Dimensional Flame Propagation Code ODFLAME	3-25
3.1.5 CSQ Detonation Calculations	3-28
3.2 Experimental Facilities, Tests, and Plans	3-34
3.2.1 FITS Facility	3-34
3.2.2 Review of HCOG and NTS Hydrogen Combustion Experiments	3-37
3.2.3 Velocity Measurements in a Hydrogen Combustion Tank	3-37

## CONTENTS (Cont.)

	<u>Page</u>
3.2.4 Combustible Gas in Containment Program	3-38
3.2.5 Effects of Aerosols on Hydrogen:Air Combustion	3-39
3.2.6 Effects of Hydrogen:Air Combustion on Aerosols	3-43
3.2.7 Water Drop Diagnostics	3-43
3.2.8 Tests of Monodisperse Water Drop Generator	3-44
3.2.9 Operability of Tayco Igniters in a Water Spray Environment	3-47
3.2.10 Modification of Plant Atmospheres	3-50
3.2.11 FLAME Facility	3-53
3.2.12 Heated Detonation Tube	3-54
3.2.13 McGill Work	3-57
3.2.13.1 Hydrogen:Air Deflagration Studies	3-57
3.2.13.1.1 Flame Acceleration in Multiple Chambers	3-57
3.2.13.1.2 High Speed Turbulent Deflagrations and Transition to Detonation	3-60
3.2.13.1.3 Influence of CO <sub>2</sub> on Hydrogen:Air Deflagration	3-62
3.2.13.1.4 The Interaction of a Vortex Ring with a Spherical Flame	3-67
3.2.13.2 Influence of Obstacles on Detonation Propagation	3-69
3.2.13.3 Transmission of Detonations into Unconfined Environments through Multiple Openings	3-75
3.2.13.3.1 Transmission of Detonations through Diverging Channels	3-78
3.2.13.3.2 The Chapman-Jouquet Surface Location as an Alternative Measure of the Detonation Cell Size	3-79
3.2.13.3.3 Influence of the Ignition Source Characteristics on the Direct Initiation of Gaseous Detonations	3-81
3.2.13.3.3.1 Electrical Spark Initiation	3-81
3.2.13.3.3.2 Direct Initiation of Spherical Detonations by Cold Turbulent Jet Mixing	3-82

CONTENTS (Cont.)

	<u>Page</u>
3.2.13.3.3.2.1 Transient Jet Studies	3-82
3.2.13.3.3.2.2 Shockless Initiation Studies	3-83
3.2.13.3.3.3 Effects of Additives on Detonation Propagation	3-89
3.2.14 Steam:Hydrogen Flame Jet	3-95
3.2.15 BWR Mark III and HCOG Activities	3-95
3.2.16 FITS Test Analysis	3-97
3.2.17 EPRI NTS Experiments	3-102
3.3 References for Section 3	3-112



## LIST OF ILLUSTRATIONS

<u>Figure</u>		<u>Page</u>
2.1	Schematic Diagram of EXO-FITS Experimental Apparatus	2-14
2.2	Example of Typical Experiment Sequencing (CM-5)	2-16
2.3	Orientation of Lines along Which Melt Front Has Been Plotted	2-20
2.4	Melt Position as Function of Time (CM-3)	2-21
2.5	Melt-Front Velocity as Function of Time (CM-3)	2-22
2.6	Eruption Pressure for CM-4	2-24
2.7	Photograph of FCI just before Initiation of Second Eruption (CM-5)	2-25
2.8	Photograph of Results of Second Surface Eruption (CM-5)	2-26
2.9	Eruption Pressure for CM-5	2-27
2.10	Photograph of Base Contact Mixing and Central Void (CM-5)	2-28
2.11	Eruption Pressure for CM-6, Showing Two Peaks	2-30
2.12	Eruption Pressure for CM-6, Showing First Peak	2-31
2.13	Photograph of CM-9, just before Melt-Water Contact	2-35
2.14	Photograph of Melt-Water Contact, CM-9	2-36
2.15	Photograph of FCI after Initiation of Surface Event, CM-9	2-37
2.16	Photograph of FCI at Time of Main Event, CM-9	2-39
2.17	Photograph of FCI about 15 ms after Main Event, CM-9	2-40
2.18	Explosion Pressure for CM-9	2-41
2.19	Photograph Showing Void Fraction at Melt Entry, CM-10	2-43

## ILLUSTRATIONS (Cont.)

<u>Figure</u>		<u>Page</u>
2.20	Photograph of In-Flight Single Particle Interaction, CM-10	2-44
2.21	Photograph of Peak of Surface Eruption, CM-11	2-46
2.22	Time Histories and Event Types for CM and FITS B Experiment Series	2-51
2.23	Dimensionless Height (Mixture Height/Fuel Diameter) Correlated as Function of Derived Dimensionless Time, $T^+$	2-54
2.24	Dimensionless Mixture Volume (Mixture Volume/Fuel Volume) Correlated as Function of Dimensionless Time, $T^+$	2-55
2.25	Dimensionless Coolant Displacement (Coolant Volume Displaced/Fuel Volume) Correlated as Function of Dimensionless Time, $T^+$	2-56
2.26	Limits to Mixing as Function of Water Depth, Fuel Temperature, and Final Particle Size	2-57
2.27	Explosion Conversion Ratio ( $KE/E_f$ ) and Fuel-Debris Diameter as Functions of Coolant-to-Fuel Mass Ratio	2-61
2.28	Explosion Conversion Ratio ( $KE/E_f$ ) and Fuel-Debris Diameter as Functions of Mixture-to-Fuel Volume Ratio	2-62
2.29	Quasi-Steady Pressure Rise as Function of Coolant-to-Fuel Mass Ratio	2-64
2.30	Schematic of Dynamic Film Model	2-65
2.31	Effect of Molten-Fuel Diameter on Vapor Film Pressure	2-67
2.32	Effect of Initial Film Thickness on Heat-Transfer Rate	2-68
2.33	Effect of Initial Film Thickness on Vapor-Film Pressure	2-69
2.34	Effect of Molten-Fuel Temperature on Vapor-Film Pressure	2-70

ILLUSTRATIONS (Cont.)

<u>Figure</u>		<u>Page</u>
2.35	Effect of Initial Ambient Pressure on Vapor-Film Pressure	2-71
2.36	Effect of Coolant Temperature on Evaporation Rate	2-72
2.37	Effect of Coolant Temperature on Vapor-Film Pressure	2-73
2.38	Effect of Constant Subcooling on Vapor-Film Pressure	2-74
2.39	Radius History of Coolant Droplet in Fuel	2-77
2.40	Pressure History of Vapor Film in Fuel	2-77
2.41	Temperature History of Coolant Droplet in Fuel	2-78
2.42	Fuel Fragmentation Mechanism	2-79
2.43	One-Dimensional System Geometry	2-80
2.44	Pressure History in Explosion Zone	2-86
2.45	Kinetic Energy of Explosion Mixture	2-86
2.46	Conversion Ratio of Fuel Internal Energy	2-87
3.1	HECTR Ice-Condenser Containment Model	3-2
3.2	Five-Volume Compartmentalization of Grand Gulf	3-9
3.3	Temperature Ratios during Burn for Test P-1	3-11
3.4	Maximum Temperature Ratios for Test P-1	3-12
3.5	Flame Acceleration through a Four-Chamber Configuration	3-16
3.6	Geometry of Channel and Resulting Flame Configurations	3-17
3.7	Simulation of a Portion of the Hydrogen Flame Propagation	3-20
3.8	Vortex Dynamics Simulation of the Configuration of Figure 3.7	3-21

ILLUSTRATIONS (Cont.)

<u>Figure</u>		<u>Page</u>
3.9	Comparison of CONCHAS-SPRAY, Vortex Dynamics, and Simple Models for the Calculation of Figure 3.7	3-22
3.10	Flame Velocities vs Volume Fraction of Water	3-26
3.11	CSQ Model for GESSAR II and Ignition Locations	3-29
3.12	CSQ Pressure at Center of Dome (Central Ignition)	3-31
3.13	CSQ Pressure at Center of Dome (Wetwell Ignition)	3-31
3.14	CSQ Specific Impulse at Center of Dome (Central Ignition)	3-32
3.15	CSQ Specific Impulse at Center of Dome (Wetwell Ignition)	3-32
3.16	CSQ Pressure in Wetwell	3-33
3.17	Hydrogen:Air:Steam Flammability Limits	3-35
3.18	Comparison of Pressure Records (P2A) Made during hydrogen combustion with (14-45-1; B11H12) and without (14-43-1; B9H12) Fe <sub>2</sub> O <sub>3</sub> Aerosol, Lower and Upper Traces, Respectively	3-40
3.19	Comparison Between Thermocouple Records (TC241) Made during Hydrogen Combustion with (14-45-1; B11H12) and without (14-43-1; B9H12) Fe <sub>2</sub> O <sub>3</sub> Aerosol, Lower and Upper Traces, Respectively	3-41
3.20	Maximum Recorded Temperatures vs Weight of Powder Discharged in VGES Tank Experiments; Thermocouple TCO	3-42
3.21	Images of Spray Drops Recorded 1.2 m Below a Spraco 1126-1314 Solid Cone Nozzle	3-45
3.22	Sketch of a Cross Section of Spinning Disk-Type Generator of Monodisperse Water Drops	3-46

ILLUSTRATIONS (Cont.)

<u>Figure</u>		<u>Page</u>
3.23	Histogram Generated by the Quantimet for Optional Image Analyzer for Water Drop Images Produced in a Tinted Polyvinyl Alcohol-Coated Microscope Slide by a Monodisperse Water Drop Generator	3-48
3.24	Experimental Arrangement of the VGES Facility Used to Study the Operability of a Tayco Igniter in a Water Spray Environment	3-49
3.25	Tayco Helical Igniter Installed in Box with Spray Shield	3-51
3.26	Records of Thermocouple Spot-Welded to Tayco Igniter Exposed to Prototypical Water Spray with and without Spray Shield during Hydrogen Combustion Experiments in the VGES Facility	3-52
3.27	Flame Test 1, June 28, 1983	3-55
3.28	Schlieren Movies for Flame Propagation in Multiple Chambers	3-58
3.29	Flame Speed Profile for Flame Propagation in Multiple Chambers	3-59
3.30	Steady State Flame Speeds for Hydrogen:Air Mixtures	3-61
3.31	Overpressure at Steady State Flame Speeds for Hydrogen:Air Mixtures	3-63
3.32	Normal Burning Velocity for Hydrogen:Air:CO <sub>2</sub> Mixtures	3-65
3.33	Steady State Flame Speeds for Hydrogen:Air:CO <sub>2</sub> Mixtures	3-66
3.34	Apparatus	3-68
3.35	Interaction of a Vortex Ring with a Spherical Flame (Acceleration)	3-70
3.36	Interaction of a Vortex Ring with a Spherical Flame (Quenching)	3-70

ILLUSTRATIONS (Cont.)

<u>Figure</u>		<u>Page</u>
3.37	Pressure-Time Records	3-71
3.38	Reinitiation Distance vs Hole Diameter	3-73
3.39	Reinitiation Distance vs Wire Spacing	3-74
3.40	Experimental Apparatus	3-76
3.41	Variations of Critical Hole Diameter with Hole Spacing for Two-Hole Plate	3-77
3.42	Variations of the Critical Number of Detonation Cells Across the Channel Width with Divergence Angles	3-80
3.43	Influence of Vessel Length on Jet Penetration	3-84
3.44	Influence of Obstacles on Jet Penetration	3-85
3.45	Schematic of Apparatus for Shockless Initiation Studies	3-86
3.46	Typical Pressure and Luminosity Records	3-88
3.47	Variations of Detonation Cell Size with Initial Pressure for $2H_2 + O_2$ Undiluted and Diluted with Argon	3-90
3.48	Variations of Detonation Cell Size with Initial Pressure for $2H_2 + O_2$ Undiluted and Diluted with Helium	3-91
3.49	Variations of Detonation Cell Size with Initial Pressure for $2H_2 + O_2$ Undiluted and Diluted with $CO_2$	3-92
3.50	Increase in Cell Size of the Undiluted Mixture and Decrease in Initial Pressure Upon Addition of 5% $CH_3Cl$ or $CH_3Br$ to $2H_2 + O_2$ Mixtures	3-94
3.51	Comparison of Heat Transfer Coefficients Deduced for Cold and Hot Wall, 10% Hydrogen FITS Tests H10C and H10H	3-99
3.52	Components of the Wall Heat Flux in the Cold Wall Test H10C	3-100

ILLUSTRATIONS (Cont.)

<u>Figure</u>		<u>Page</u>
3.53	Computed Steam Fraction as a Function of Time in the Cold Wall FITS Test H10C	3-101
3.54	Pressure and Calorimeter Temperatures from July 28 Test	3-104
3.55	Pressure and Calorimeter Temperatures from August 4 Test	3-105
3.56	Pressure and Calorimeter Temperatures from August 9 Test	3-106
3.57	Pressure and Calorimeter Temperatures from August 10 Test	3-107
3.58	Pressure and Calorimeter Temperatures from August 12 Test	3-108
3.59	Total Heat Flux from the Gardon Gauge Calo- rimeter H106	3-110
3.60	Total Heat Flux from the Gardon Gauge Calo- rimeter H106	3-111

## LIST OF TABLES

<u>Table</u>	<u>Page</u>
2.1 Initial Parameters for Coarse Mixing Test Series	2-2
2.2 Event Classification and Characteristics for Coarse Mixing Test Series	2-3
2.3 Results and Comments for Coarse Mixing Test Series	2-4
2.4 Initial Parameters for Oxide-Melt Test Series	2-6
2.5 Event Classification and Characteristics for Oxide-Melt Test Series	2-7
2.6 Initial Parameters for Alternate Contact Mode Test Series	2-9
2.7 Results for Alternate Contact Mode Test Series	2-9
2.8 Initial Parameters for Rigid Container Test Series	2-10
2.9 Event Classification and Characteristics for Rigid Chamber Test Series	2-11
2.10 Ranges of Input Variables	2-87
2.11 Matrix of Input Data for Parametric FCI Model Using Randomized Plackett-Burman Screening Design	2-88
2.12 Lowest Possible Steam Spike	2-91
2.13 Best Estimate Steam Spike	2-92
2.14 Highest Possible Steam Spike	2-93
2.15 Fuel/Coolant Pairs Considered	2-97
3.1 Case Descriptions	3-3
3.2 HECTR Results	3-6
3.3 Volume Fraction of Water Required to Extinguish Various Hydrogen:Air Droplet Configurations	3-27
3.4 Thermodynamic States for Hydrogen:Dry Air Mixture	3-30



LIST OF TABLES

<u>Table</u>		<u>Page</u>
3.5	GESSAR II CSQ Calculations	3-33
3.6	Effects of Partial Depletion of Oxygen on Pressure and Temperature Rises	3-53
3.7	Initial Conditions and Burn Parameters	3-103

1. MOLTEN-FUEL/CONCRETE INTERACTIONS STUDY  
(R. K. Cole, Jr., D. P. Kelly, M. A. Ellis)

The Molten-Fuel/Concrete Interactions (MFCI) study currently consists of analytical investigations of the chemical and physical phenomena associated with interactions between molten-core materials and concrete. Such interactions are possible during hypothetical fuel-melt accidents in light-water reactors (LWRs). Our main purpose is to identify and understand the dominant phenomena in order to evaluate the following:

- (1) The generation rate and nature of evolved gases.
- (2) The effects of gas generation on fission-product release.
- (3) The mechanism, rate, and directional nature of concrete erosion by the melt.

The program is directed toward the development of the CORCON computer code, a state-of-the-art computer model of molten-core material/concrete interactions capable of providing quantitative estimates of reactor fuel-melt accident situations. We are now nearing completion of a MOD2 version of CORCON, with greater applicability than the released MOD1. The major extensions will be the inclusion of a crust-formation/freezing model and a model for (nonexplosive) interactions with coolant in the reactor cavity. In addition, other model improvements will be made based on the results of our assessment of the MOD1 code.

During this reporting period we were directed to proceed with development of a model for a stable overlying coolant layer, although vapor explosions have been observed experimentally in this geometry by both SNL and BNL. This has proved to be relatively straightforward because much of the structure and logic for the coolant layer are already included (but bypassed) in the code. At the end of September, the model was functioning in CORCON, although some problems remained to be solved for the timestep in which the coolant is depleted. Addition of coolant has surprisingly little effect on pool behavior in the few calculations performed so far, with the melt surface remaining extremely hot and heat transfer dominated by radiation. Because the surface radiated to, either the coolant or the above-pool surroundings, is much cooler than the surface of the melt, its temperature (and even its identity) make little difference to the heat flux. We intend, however, to include a full boiling curve in the final model.

We further determined that chemical reactions should be included between the flowing gas film and the melt (in current versions of the code, only gas bubbles are permitted to

react). Because this will use the existing chemical equilibrium package, no problems are anticipated.

Consideration was given to including a transient concrete-response model to replace the quasi-steady ablation model in CORCON. This would include the effects of water migration. However, the detailed two-dimensional concrete recession calculation in CORCON would make application of such a model extremely expensive both in computing time and storage. A decision was deferred, pending the outcome of scoping calculations with SLAM (the Sandia Limestone Ablation Model) to determine the importance of transient effects.

We have continued our normal debugging activities during the reporting period, finding and correcting a number of minor errors and improving the reliability of several iterative calculations. We were aided indirectly in this by Dave Bradley of Organization 6425, who used the latest standardized version of CORCON (denoted as Version 1.02.00) in a number of source-term calculations. (This version was used to avoid problems with the viscosity modeling, which exist in CORCON-MOD1). He promptly uncovered several bugs in the code that had escaped previous testing. This process, allowing people outside the immediate group to exercise the code, is valuable to us. It will be repeated before any release of CORCON-MOD2.

Other changes to the code during the period included conversion to full ANSI 77 standard FORTRAN (we believe that no nonstandard code remains). This should enhance portability of the code.

Work continued on completing the coding and documentation for the release of the CORCON-MOD2 code. Further reporting of the progress of this work will be published in the Sandia Advanced Reactor Safety Research Quarterly Progress reports.

## 2. CORE-MELT/COOLANT INTERACTIONS (M. Berman, M. L. Corradini, M. S. Krein, N. A. Evans)

The objective of the Core-Melt/Coolant Interactions (CMCI) program is to develop an understanding of molten-fuel/coolant interactions (FCIs) sufficient to resolve the following important reactor safety questions:

- (1) What are the probabilities and consequences of direct or indirect failure of the primary system or containment due to in- or ex-vessel steam explosions?
- (2) What are the rates and total magnitudes of steam and hydrogen that can be generated during FCIs?
- (3) What are the characteristics of the debris produced by FCIs, and how do the resulting particles influence debris-bed coolability?
- (4) How do FCIs influence the progression of the accident and the nature of the source term?
- (5) How do FCIs affect the probability of accident termination by the addition of water to the melt?

### 2.1 Summary

#### 2.1.1 Intermediate-Scale Experiments

Twenty experiments were conducted in the EXO-FITS facility during this period. Twelve tests were conducted in the Coarse Mixing (CM) series, four in the Oxide-Melt (OM) series, two in the Alternate Contact Mode (ACM), and two in the Rigid Confinement (RC) series. As is common with EXO-FITS tests, these experiments were primarily scoping in nature, intended to provide guidance for future in-vessel (FITS) experiments.

The CM tests were attempts to suppress steam explosions by using low-subcooled water (i.e., water near its saturation temperature); the major objective of these tests was to make quantitative (photographic) observations of the coarse mixing (or premixing) process, as the melt falls through the water. Our goal was to provide coarse mixing data to assist in distinguishing between the different existing models of this process. Additional camera coverage was provided to look up at the melt as it fell through the water. Tables 2.1 through 2.3 list the initial conditions and major observations for the twelve CM tests. Ordinary steam explosions occurred in four of the tests (CM-7, -8, -9, -12); two of those tests involved nearly saturated water (CM-8, -9). The latest delay to an explosion ever observed for these studies occurred for the cold-water test CM-7 (500 ms after melt entry into the

Table 2.1

## Initial Parameters for Coarse Mixing Test Series

Test Name	Melt Mass Delivered (kg)	Water Mass (kg)	Mass Ratio ( $M_c/M_f$ )	Water Temperature (K)	Water Subcooling (K)	Water Side Dimension (m)	Water Depth (m)	Melt Drop Height (m)	Melt Entry Velocity (m/s)	Melt Hold Time (s)	Lid in/out
CM-1	18.5	109.7	5.9	358	9	0.305	1.220	0.305	2.44 <sup>a</sup>	1.00	Out
CM-2	18.0	109.3	6.1	363	4	0.305	1.220	0.305	2.44 <sup>a</sup>	4.00	Out
CM-3	18.0	437.0	24.3	364	3	0.610	1.220	0.483	3.11	0.68	Out
CM-4	18.9	218.5	11.6	364	3	0.610	0.610	1.120	4.60	0.68	Out
CM-5	7.6	218.7	28.7	363	4	0.610	0.610	1.120	4.78	0.75	Out
CM-6	4.0	218.5	54.6	364	3	0.610	0.610	1.220	4.99	0.81	Out
CM-7	18.5	169.6	9.2	294	73	0.610	0.457	1.120	4.77	0.65	Out
CM-8	18.6	218.4	11.7	365	2	0.610	0.610	0.444	3.08	0.66	In
CM-9	18.6	218.6	11.8	364	3	0.610	0.610	0.444	3.06	0.66	In
CM-10	18.4	109.3	5.9	366	1	0.610	0.305	1.143	4.60	7.00	Out
CM-11	18.7	218.6	11.7	366	1	0.610	0.610	1.120	4.68	5.00	Out
CM-12	18.5	112.9	6.1	298	69	0.610	0.305	1.820	5.89	1.50	In

<sup>a</sup>Entry was calculated by  $[2 \times g \times h]^{(1/2)}$

Table 2.2

Event Classification and Characteristics  
for Coarse Mixing Test Series

Test Name	Event Type	Event Time after Melt Entry (ms)	Eruption Duration (ms)	Propagation Velocity (m/s)	Avg/Peak Particle Velocity (m/s)	Percent of Water Depth at Event
CM-1	ER <sup>a</sup>	30				
CM-2	ER	73				
CM-3	ER <sup>b</sup>	43	41		47/88	7.5
CM-3	TR <sup>b</sup>	56				
CM-4	ER	18	62			12.2
CM-4	TR	59, 68, 75, 89				
CM-4	BC <sup>c</sup>	197				100.0
CM-5	ER	27	119		33/43	13.0
CM-5	BC	252				100.0
CM-6	ER	22	163		20/26	11.0
CM-6	TR	66, 88, 108 132, 159				
CM-6	BC	194				100.0
CM-6	TR	203				
CM-7	ER	43			62/73	49.0
CM-7	SE <sup>d</sup>	69		301	197/--	71.8
CM-7	BC	113				100.0
CM-7	SE	503				100.0
CM-8	ER	37	179			11.8
CM-8	ER	117			41/96	24.6
CM-8	TR	195, 202				
CM-8	SE	216				67.2
CM-9	ER	65	40			21.3
CM-9	SE	105			105/350	38.9
CM-10	ER	43	69		18/24	
CM-10	SE	112			37/78	100.0
CM-10	SE	311				
CM-11	ER	52	88		32/--	25.9
CM-11	BC	160				100.0
CM-12	ER	37				15.8
CM-12	SE	69			103/110	65.6
CM-12	BC	111				100.0
CM-12	SE	125				100.0

<sup>a</sup>Eruption<sup>c</sup>Melt contact with bottom<sup>b</sup>Nonpropagating trigger<sup>d</sup>Steam explosion

Table 2.3

## Results and Comments for Coarse Mixing Test Series

Test Name	Residual Mass in Chamber (kg)	Melt Width at Entry (m)	Comments on Test
CM-1	N.O. <sup>a</sup>	N.O.	Lid skimmed water surface. High-speed cameras didn't work. Possible weak surface explosion can be seen from low-speed camera.
CM-2	3.80	N.O.	Lid skimmed water surface. Lid stuck in crucible for 1.5 to 2.0 s, making hold time 3.5 to 4.0 s. No high-speed films. Water chamber remained intact.
CM-3	4.28	0.33	One nonpropagating trigger occurred at 56 ms after melt entry. Top 1/3 of water chamber fractured.
CM-4	3.50	0.53	Strong 25 to 30 mph crosswind at test time. Stripped some melt from the falling melt mass. Water chamber destroyed by nonpropagating triggers.
CM-5	3.40	0.28	Eruption velocity seemed to increase approximately 42 ms after eruption began. No triggers observed. A large amount of fine dust-size debris remained in chamber.
CM-6	1.94	0.18	Eruption appeared to be composed of multiple events. Water chamber remained undamaged.
CM-7	N.O.	N.O.	Melt shape was not uniform, with thin arm preceding main melt mass by 13 cm. Second explosion deformed water chamber support stand.
CM-8	N.O.	0.23	Lid entered water perpendicularly. Lid quickly separated from melt and slid off to side. Main center eruption was preceded by steaming. Weak explosion.
CM-9	N.O.	0.26	Lid entered water parallel to surface. Weak explosion.
CM-10	N.O.	0.19	Severe crucible melt leak prior to release at 5-s hold time. Fragments of lid entered with rest of melt. Water was boiling froth at melt entry.
CM-11	5.80	0.20	No triggers observed. The chamber remained intact.
CM-12	N.O.	0.20	Large water swell due to eruption. Weak first explosion ruptured chamber. Strong second explosion did some mechanical damage to stand and test tower. Second explosion began on bottom.

<sup>a</sup>Not obtained

water); at the time of the explosion, it appeared from the films that almost all the water had dispersed, i.e., this late explosion occurred in a very water-lean environment.

In all twelve tests, violent eruptions occurred at or slightly below the surface of the water; these eruptions occurred approximately 20 to 80 ms after initial melt-water contact, with an average delay of about 40 ms. These eruptions were not explosions, since they lasted for extended periods of time (longer than 50 ms); water-phase pressures rose slowly and did not exceed a few tens of bars. The surface events were violent enough to prevent subsequent melt from entering the water. The presence of the bottom lid of the melt crucible (falling through the water ahead of the melt) seemed to delay the surface interaction. Longer melt hold times (time from end of thermite burn to release of melt from the crucible) also seemed to correlate with greater delays in melt expulsion. The occurrence of the surface eruption did not depend on water subcooling.

In many of the tests, approximately 4 kg of melt proceeded downward and was not involved in the surface eruptions; in most cases, those few kilograms of melt were recovered in a lump at the bottom of the chamber or in the form of agglomerated particles about a centimeter or more in diameter. These surface eruptions have not been observed on previous FITS and EXO-FITS tests. They may be a new form of FCI, or they may have resulted from changes in the experimental techniques or in the melt materials. As a result, an extensive investigation of the properties of the thermite melts is underway.

The objective of the OM series was to improve our understanding of FCIs with oxidic melts. Furthermore, rapid metal-water oxidation has been postulated as a possible explanation for the violent surface eruptions that occurred in the CM series. An oxidic melt would remove metal oxidation from consideration. In fact, no surface eruptions were observed for the (thermitically generated) iron-oxide melt. Three tests were conducted in cold water, and one in nearly saturated water, using an iron-oxide melt. (See Tables 2.4 and 2.5.) About 10 kg of the oxide melt was delivered to the water chamber. Steam explosions occurred in all tests; triggers occurred near the surface of the water and near the base of the water chamber. The hot water test OM-4 yielded two explosions; the second occurred very late, 360 ms after melt entry. This oxidic melt-hot water test closely resembled the previous iron/alumina-cold water test, CM-7.

Steam explosions have been observed experimentally in the alternate contact mode, i.e., melt poured onto water.[1,2] They have also been observed in industrial accidents.[3] Arguments have been presented that claim that energetic steam explosions are only possible when the melt has been poured into water and has produced a coarse mixture of particles a



Table 2.4

## Initial Parameters for Oxide-Melt Test Series

Parameters	Test Name			
	OM-1	OM-2	OM-3	OM-4
Melt Mass Delivered (kg)	N.O. <sup>a</sup>	9	10	9
Water Mass (kg)	66.1	100.9	131.7	218.6
Mass Ratio ( $M_c/M_f$ )	N.O.	11.2	13.2	24.3
Water Temperature (K)	298	298	298	363
Water Subcooling (K)	69	69	69	4
Water Side Dimension (m)	0.43	0.53	0.61	0.61
Water Depth (m)	0.36	0.36	0.36	0.61
Melt Drop Height (m)	0.635	0.635	0.635	0.787
Melt Entry Velocity (m/s)	3.53 <sup>b</sup>	3.83	3.34	3.56
Melt Hold Time (s)	3.8	3.8	3.8	5.0
Lid In/Out	Out	Out	In	Out
Melt Width at Entry (m)	N.O.	0.24	0.34	0.25

<sup>a</sup>Not obtained

<sup>b</sup>Entry was calculated by  $[2 \times g \times h]^{(1/2)}$

Table 2.5

## Event Classification and Characteristics for Oxide-Melt Test Series

Test Name	Event Type	Event Time after Melt Entry (ms)	Avg/Peak Particle Velocity (m/s)	Percent of Water Depth at Event	Comments on Test
OM-1	SE <sup>a</sup>	N.O. <sup>b</sup>	N.O.	N.O.	Some melt ejected through crucible vent holes, fell into chamber, and exploded. Chamber destroyed. Rest of melt released at 3.8 s and fell into empty chamber base.
OM-2	SE	47	193/272	29.2	Poor film visibility due to smoke from thermite burn. Chamber destroyed by surface explosion. Possibility of incomplete thermite reaction.
OM-3	SE	141	785/---	N.O.	Substantial melt leak from bottom of crucible prior to melt release. Poor film visibility. Only one high-speed camera and no low-speed camera.
OM-4	SE	19	332/427	N.O.	Chamber destroyed by surface explosion. Explosions at 198 and 247 ms were local explosions near west wall and did not propagate to entire melt.
OM-4	SE	198	N.O.	N.O.	
OM-4	SE	247	N.O.	N.O.	
OM-4	SE	360	132/184	100.0	

<sup>a</sup>Steam explosion<sup>b</sup>Not obtained

centimeter or less in diameter.[4] Two scoping tests were conducted to investigate the explosibility of iron/alumina-water systems in the alternate contact mode. (See Tables 2.6 and 2.7.) About 10 kg of iron/alumina melt was prepared in a crucible. Water was injected onto the melt 1 s after the thermite burn was completed. The water poured gently onto the melt for about 3 s; water and melt appeared to spontaneously mix during this time, as evidenced by surface agitation observed on the film. After 3 s, when about 0.5 liters of water had been delivered, a violent explosion occurred. In the second test, ACM-2, water injection was delayed 4.5 s after the burn was completed; no explosion occurred. From photographic observations, it appears likely that a solid crust had formed in the second test, prior to water entry. These tests indicated that explosions in this reflow mode are possible. The energetics are unknown and will certainly depend strongly on the depth of the melt.

The final two tests were conducted using a 60-cm-diameter, thick-walled steel pipe (2.5 cm) for the water container, rather than a Lucite box. (See Tables 2.8 and 2.9.) The objective was to estimate the effects of a rigid container on explosion conversion ratio. Both tests used molten-iron/alumina and cold water. In the first test, the melt hold time was 4 s. A violent surface eruption occurred, as in the CM series of tests, but there was no steam explosion. In RC-2, the melt hold time was 1.5 s after the thermite burn. A surface eruption occurred, followed by a very strong explosion. The EXO-FITS concrete pad and superstructure were destroyed. Peak particle velocities of 1000 m/s were observed. Fluorescent light fixtures in a neighboring building were shattered; this had never occurred for previous EXO-FITS tests. These observations indicate that the conversion ratio for this experiment may be substantially higher than for previous tests with the Lucite chamber. Current estimates of conversion ratio are highly uncertain, in large part due to the uncertainty in the amount of melt participating in the explosion. We estimated a middle value for conversion ratio of 3.4%, with an uncertainty of a factor of 4 up or down (from 0.8% to 14%). Subjectively, we feel that the conversion ratio was closer to the higher part of the uncertainty range. A possible explanation for this increase concerns the propagation and expansion phases of a steam explosion. In an unconfined geometry, the initiation of the expansion phase marks the end of any significant melt-water contact by driving the melt-water system apart. In contrast, the expansion phase of a confined steam explosion may serve to enhance liquid-liquid contact by driving the liquids together as they approach the walls; hence, more fragmentation and vaporization can take place before the liquids finally escape from the interaction region.

A detailed discussion of the CM series of tests is presented in Section 2.2. The other EXO-FITS tests, summarized above,

Table 2.6

## Initial Parameters for Alternate Contact Mode Test Series

Parameters	Test Name	
	ACM-1	ACM-2
Melt Mass (kg)	10.0	18.5
Water Mass (kg)	0.6	3.8
Water Temperature (K)	298	298
Water Subcooling (K)	69	69
Ambient Pressure (MPa)	0.083	0.083
Water Hold Time (s)	1.0	4.5

Table 2.7

## Results for Alternate Contact Mode Test Series

Test Name	Event Type	Time after Melt Entry (s)	Comments on Test
ACM-1	Explosion	3	Delay between end of thermite burn and water-melt contact was 1 s. Explosion occurred at 3 s after water-melt contact. Several minor eruptions before explosion.
ACM-2	No explosion		Delay between end of thermite burn and water-melt contact was 4.5 s. No explosion observed. Apparent crusting of melt prior to melt-water contact.

Table 2.8

## Initial Parameters for Rigid Container Test Series

Parameters	Test Name	
	RC-1	RC-2
Fuel Mass Delivered (kg)	19.0	18.5
Water Mass (kg)	111.7	111.6
Mass Ratio ( $M_C/M_f$ )	5.9	6.0
Water Temperature (K)	298	303
Water Subcooling (K)	69	64
Water Diameter (m)	0.559	0.559
Water Depth (m)	0.46	0.46
Drop Height (m)	1.78	1.78
Melt Entry Velocity (m/s)	5.77	5.85
Melt Hold Time (s)	4.0	1.5
Lid In/Out	In	In

will be analyzed in more detail in the next semiannual report (October 1983 - March 1984).

### 2.1.2 Modeling and Analysis

Several current models for predicting fuel/coolant mixing limits have been examined. Two of the models (by M. L. Corradini and T. Theofanous), give approximately the same results for the amount of fuel that could mix in the lower plenum of the pressure vessel. The Henry-Fauske model, however, yields mixing limits more than an order of magnitude smaller than these other models. The Henry-Fauske model has been reexamined in terms of a water fluidization limit; this modified model tends to give results that also agree with the other two models.

Table 2.9

## Event Classification and Characteristics for Rigid Chamber Test Series

Test Name	Event Type	Event Time after Melt Entry (ms)	Eruption Duration (ms)	Avg/Peak Particle Velocity (m/s)	Comments on Test
RC-1	ER <sup>a</sup>	86	232	N.O. <sup>b</sup>	Rigid vessel was 94 cm long, 55.9-cm-I.D. pipe with 2.5-cm-thick walls and a plexi-glass bottom. Entry velocity and time estimated using pipe inlet velocity and gravity.
RC-2	ER	56		N.O.	Same vessel as RC 1. Explosion lifted vessel 2 m off ground. Destroyed EXO-FITS test stand and concrete pad. Substantial ground and air shock felt.
RC-2	SE <sup>c</sup>	180		853/1122	

<sup>a</sup>Eruption<sup>b</sup>Not obtained<sup>c</sup>Steam explosion

Analysis of the FITS data continued. Trends in explosion conversion ratio and fuel debris have been plotted against fuel/coolant mass ratio. The dependence of the FITS tank gas-phase pressure on fuel/coolant mass ratios has also been examined. These data can assist in modeling steam-spike phenomena in reactor containments.

Work continued on modeling the collapse of the vapor film around a fuel droplet. A model has been developed that predicts that the vapor film thickness oscillates as the drop falls through the water, as was observed in Nelson's single-droplet experiments. The amplitudes and frequencies of these oscillations (in film thickness and vapor pressure) depend strongly on the various initial conditions: initial drop size, initial film thickness, ambient pressure, drop temperature, coolant temperature, etc.

A parametric model for the explosion phase of the FCI has been developed using empirical data from the FITS experiments. Our objective in developing this model is to assess the relative importance of the various initial conditions to the explosion conversion ratio, the rate of steam generation, and the pressurization history. This model will ultimately be used to develop a one-dimensional propagation model that will aid us in determining the proper input conditions for more complex two-dimensional explosion calculations.

Our FCI work was also applied to the so-called "steam spike" problem. We estimated the pressure rise that would occur in a large, dry PWR containment due to fuel/coolant mixing, energetic FCIs, gas discharge and entrainment, and molten-core/concrete interactions.

Finally, we reviewed a paper presented by H. K. Fauske and R. E. Henry at the ANS/CNS International Meeting on LWR Severe Accident Evaluation in Cambridge, MA, August 28, 1983. The major point of the paper was that the fuel/coolant simulant pairs used in intermediate-scale tests (i.e., molten-iron/alumina and "corium A+R") are very different from actual coriums that might occur during accidents, especially with respect to the potential for energetic explosions. We disagree with those conclusions, and we discuss the reasons for our disagreement.

## 2.2 Intermediate-Scale Experiments (M. S. Krein, M. Berman, N. A. Evans)

### 2.2.1 EXO-FITS Coarse Mixing Experiment Series (CM)

#### 2.2.1.1 Experimental Apparatus and Methods

A schematic diagram of the EXO-FITS experimental apparatus is shown in Figure 2.1. The experimental setup consisted of a support tower and base pad, melt preparation and delivery

system, water chamber, and a data acquisition and experiment control system. The purpose of the support tower is to provide an adjustable-height attachment point for the melt preparation and delivery system. The height from the crucible bottom lid to the concrete base pad is approximately 2 m. The actual melt-drop height was a function of the water depth and was adjusted by positioning the water chamber on a steel stand of appropriate height.

The melt that was used for the CM-series of experiments consisted of an iron and aluminum-oxide mixture derived from an exothermic chemical reaction involving iron oxide ( $\text{Fe}_2\text{O}_3$ ) and metallic aluminum. The melt was prepared in a graphite crucible positioned above the water chamber. The melt was delivered to the water chamber using a mechanism that removed the entire bottom lid of the crucible. The crucible lid was allowed to fall and impact the water surface along with the melt for several of the experiments. Most of the experiments of this series, however, were performed with the crucible bottom lid removed from the falling melt mass prior to water contact.

The Lucite chambers were constructed in a square pattern of the desired side dimension and depth similar to the water chamber shown in Figure 2.1. The water chambers were supported only around the base perimeter--the bottom and sides of the chambers were not supported by a rigid connection to the concrete base pad or support tower. Some bracing of the sidewalls was necessary to reduce the deformation of the Lucite in response to the water pressure and elevated water temperature. The side wall bracing did not, however, change the nonrigid nature of the FCI confinement of these experiments.

Two main types of data were collected for this series of experiments: high- and low-speed film data and water-phase pressure data. The CM series of experiments utilized three high-speed cameras and one low-speed camera. The high-speed film data were collected at framing rates between 7000 and 9000 frames per second (fps). The low-speed framing rates depended on several factors but were either 200 or 400 fps. The high-speed cameras were positioned such that their lines-of-sight intersected two vertical planes at right angles to each other, as shown in Figure 2.1. The low-speed camera was located with its line-of-sight intersecting the corner of the water chamber to provide an overall view of the entire fuel/coolant interaction. All cameras were adjusted to provide the best view of the mixing phase of the FCI.



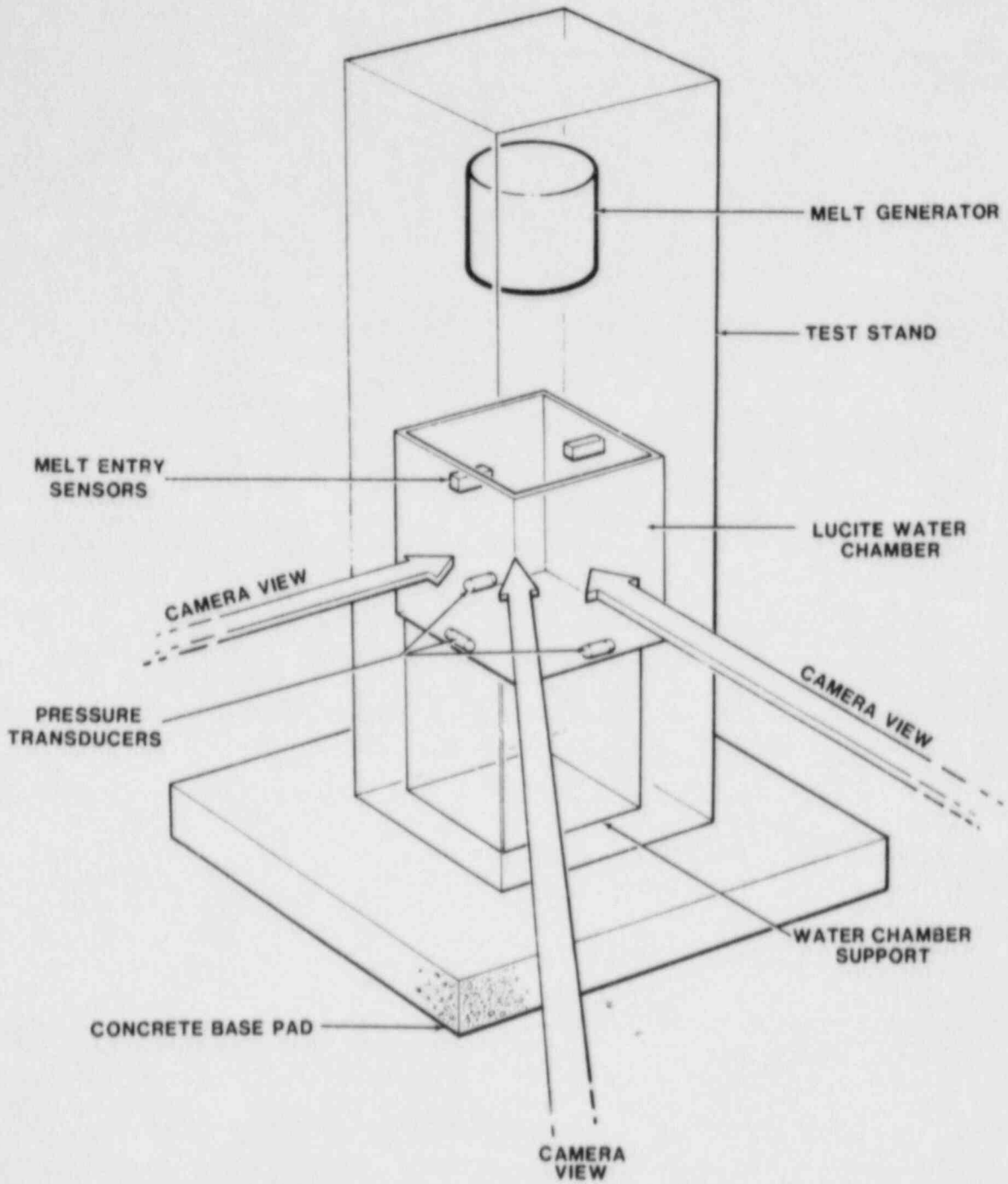


Figure 2.1. Schematic Diagram of EXO-FITS Experimental Apparatus

The water-phase pressure records were obtained from transducers mounted in the sides of the Lucite water chamber. These transducers were of various types and sensitivities and were mounted at various water depths for any given experiment. Signals that were generated by the transducers in response to some pressure phenomena were conditioned and recorded, along with a timing and system-synchronizing signal, on a multitrack instrumentation tape recorder. Known voltage levels based on transducer calibration were recorded on the tape for each specific transducer channel prior to the experiment.

Once initiated, the experiment sequence was monitored and controlled automatically. The exothermic reaction in the crucible was initiated electrically near the top surface of the thermite. The melt was held in the crucible for a predetermined time after the thermite reaction front reached the bottom of the crucible. The time at which the reaction front contacted the crucible bottom lid was determined by special transducers mounted in the crucible wall. Melt-water contact was marked on the control channels of the tape recorder by a signal generated by a melt detector located at the water surface. If an external trigger was employed, it was initiated at a predetermined time after melt-water contact was determined.

Because the high-speed camera could provide only a second or two of film time, careful attention was paid to the sequencing of the entire experiment. As an example, the sequencing of experiment CM-5 is shown in Figure 2.2. Although some experiments deviated slightly, the general apparatus and methods just described applied to all of the coarse mixing experiments.

#### 2.2.1.2 Initial Conditions and Independent Parameters

The independent variables and their values for each of the CM-series experiments have been given in Table 2.1. The independent variables included melt mass, water depth, water-chamber side dimension, water-to-melt mass ratio, water subcooling, melt entry velocity, melt hold time, and whether or not the crucible bottom lid was allowed to remain with the melt as it impacted the water surface. Several other variables were held fixed: ambient pressure, melt temperature, and melt flow rate. Melt composition also was fixed, a two-component mixture of metallic iron and aluminum oxide.

The extreme ranges of the independent variables can be seen in Table 2.1: The melt mass ranged from nearly 19 kg to 4.0 kg. The water depth ranged from 1.22 m to 0.30 m, while the side dimension of the water chamber ranged from 0.61 m to 0.30 m. The ratio of the mass of coolant to the mass of fuel (melt), which depends on the water-chamber side dimension and water depth, ranged from 54.6 to 5.93, and the actual water

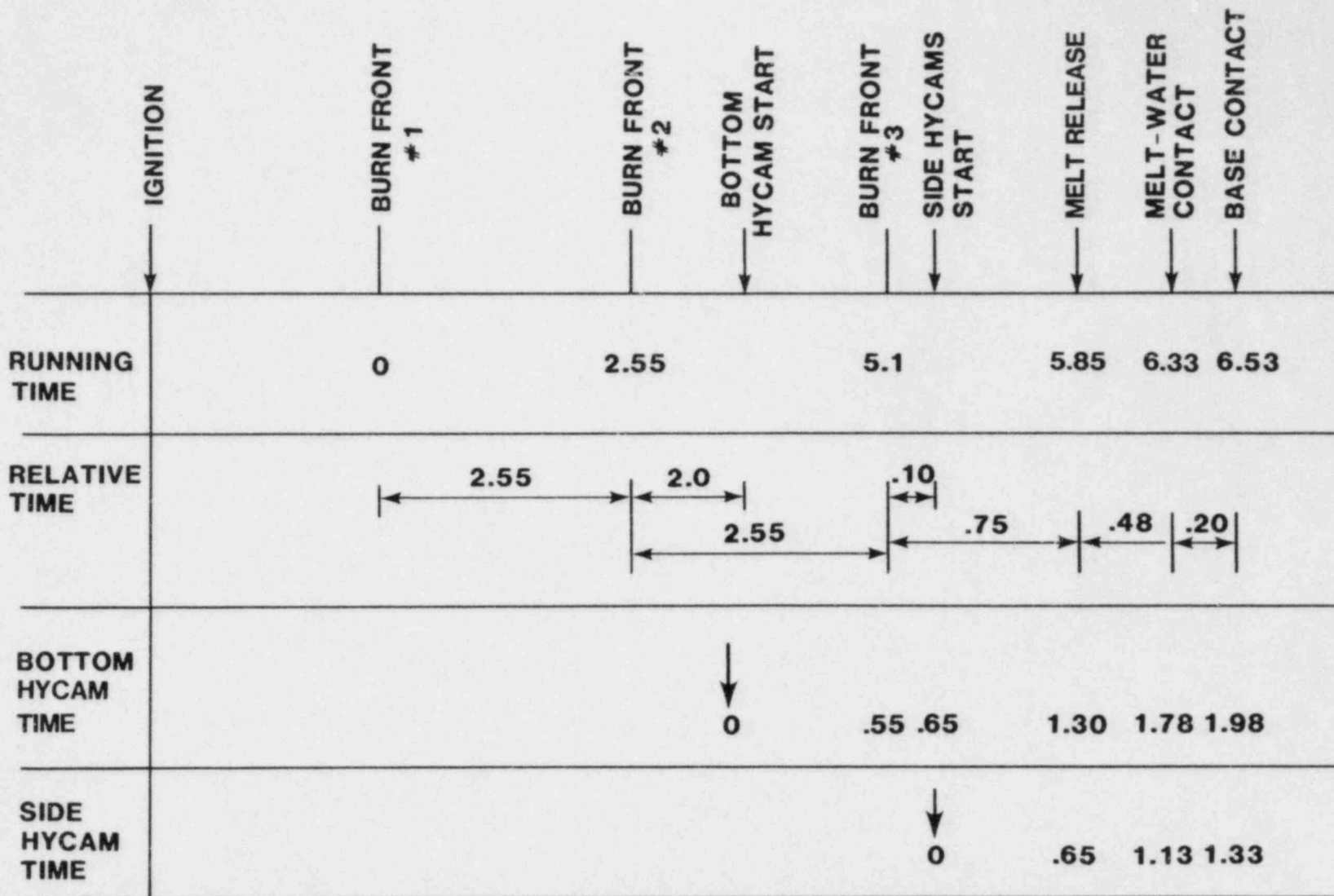


Figure 2.2. Example of Typical Experiment Sequencing (CM-5)

mass ranged from 437 kg to 109.3 kg. Most of the CM-series experiments were performed in low-subcooled water, although two experiments were performed in highly subcooled water. The melt velocity at water contact, which was governed by the drop height, ranged from a high of 5.89 m/s to a low of 2.44 m/s. Melt hold time ranged from 7.0 s to 0.650 s.

### 2.2.1.3 CM Experiments

#### 2.2.1.3.1 Experiment CM-1

Table 2.1 indicates that the thermite reaction of experiment CM-1 produced 18.5 kg of melt delivered to a 30.48-cm-square water chamber. Water depth was 1.22 m, and the water was heated to a temperature that resulted in a subcooling of about 9 K. The crucible bottom lid was removed. Only the low-speed camera worked for this experiment. The low-speed film record showed a coherent and compact melt geometry at the time of water contact.

A surface-triggered eruption of about 42-ms duration occurred approximately 30 ms after melt-water contact. The melt had penetrated the water surface to a depth of about 5.0 cm at the time of the event. The result of the surface eruption was to eject all of the incoming melt and a large portion of the melt that had previously penetrated the water surface. The eruption appeared fairly violent in that the ejected melt was highly fragmented as it fell to the ground. Also, the ejected melt mass appeared to expand spherically as it left the top of the water chamber; this may have implied a centrally located region of high pressure in the melt-water mixture. Damage to the Lucite water chamber was light and consisted of a 30-cm-tall piece of one wall fracturing and separating from the remainder of the chamber. No melt fragments were found in the water chamber even though only a small portion of the water was lost as a result of the surface-triggered event.

No measurable pressures were recorded by the pressure transducers; the transducers were designed to indicate pressures on the order of 700 bars and may not have been capable of resolving the low pressures that occurred in this experiment from the random noise in the system. Because of the limited time-resolution capability of the low-speed camera, no other data were obtained for this experiment.

#### 2.2.1.3.2 Experiment CM-2

Experiment CM-2 was a repeat of the previous experiment for the purpose of obtaining the high-speed camera data that were lost during CM-1. However, because of a crucible-lid release malfunction, which resulted in melt delivery about 1.9 s later than anticipated, the high-speed camera data were lost for

this experiment also. The low-speed camera functioned as planned and revealed a melt geometry and apparent brightness similar to those observed for the previous experiment. A surface-triggered event also occurred for this experiment. The event began at about 73 ms after melt-water contact and continued for about 333 ms. The pressure produced during the interaction, though not great enough even to fracture the Lucite water chamber, was sufficiently high to fragment the melt and eject some particles as much as 40 m from the water chamber. The surface-triggered event began after the melt had penetrated about 11 cm. The films showed an upward ejection of melt from the surface of the water. Unlike CM-1, 3.8 kg of melt was recovered in the bottom of the intact water chamber. Only about half of the original mass of water was left in the chamber after the experiment was over. The films showed that the leading 3.8 kg of melt fell through the water essentially unaffected by the ejection process that occurred above it. The recovered debris consisted predominantly of loosely agglomerated spherical masses with a diameter on the order of 1 cm.

No usable records were obtained from the pressure transducers that were installed in the walls of the water chamber.

#### 2.2.1.3.3 Experiment CM-3

Experiment CM-3 produced about 18.0 kg of melt that was delivered to a 61.0-cm-square by 122.0-cm-deep water pool. Subcooling was about 3 K, and the crucible lid was removed prior to water contact. All of the high-speed cameras functioned properly.

The film data showed a good melt release and geometry at water contact. Some melt was, however, seen to follow the crucible bottom lid as it was retracted. An eruption of unquenched melt began at 43 ms after melt-water contact. This surface eruption continued for about 41 ms and produced finely fragmented melt particles that fell to the ground within a 15-m radius of the water chamber. The top 1/3 of the Lucite water chamber was fractured into three large pieces at about 80 ms after melt-water contact. The chamber appeared to fracture at about the peak of the surface eruption.

The bottom-view high-speed camera recorded slightly different event times; the surface eruption began at about 23 ms, and a nonpropagating trigger was seen to occur at about 53 ms after melt-water contact.

Figure 2.3 shows five lines along which the melt front position as a function of time has been determined. The lines were drawn arbitrarily at 0°, at 30° and 60° to the right, and at 30° and 60° to the left of a vertical line, as shown

on the figure. The position of the melt front as a function of time (melt-water contact was  $t = 0$ ) along each of the five lines shown on Figure 2.3 has been plotted on Figure 2.4. The maximum melt-front penetration at the time of surface-event initiation occurred along a line drawn  $60^\circ$  to the left of zero. The vertical component of melt penetration at the time of the initiation of the surface eruption was about 9 cm. Melt penetration at the termination of the surface eruption was 19 cm. The slopes of the lines between the points shown in Figure 2.4 are plotted in Figure 2.5. The effect of the surface eruption on the velocity of the melt is apparent from the results shown in Figure 2.5; an approximate 5-fold increase in melt-front velocity resulted along a line  $60^\circ$  from the vertical on the left side as a result of the surface eruption. The value of the initial melt-entry velocity is shown by the horizontal dashed line.

The bottom-view high-speed camera has provided a unique view of the interaction in terms of the behavior of the entire leading surface of the melt as it advanced downward through the water chamber. Any triggers or disturbances that occur on or near the bottom surface of the melt would be clearly detectable from this viewpoint. It is important to note, based on the bottom-view camera, that the eruption of unquenched melt does not appear to have its origin on the leading melt surface, but rather somewhere else in the melt-water mixture.

The four pressure transducers installed for this experiment did not record a pressure of any significance that could be reconciled with the high-speed camera data. Also, 4.28 kg of agglomerated melt particles, most of which were spherical and 1 to 2 cm in diameter, were recovered in the water chamber.

#### 2.2.1.3.4 Experiment CM-4

This experiment delivered 18.9 kg of melt to a water volume that was 61 cm square and 61 cm deep. The water temperature was about 364 K and therefore resulted in a subcooling of about 3 K. The values of the other initial conditions are shown in Table 2.1. All cameras and other equipment functioned as planned.

The high-speed camera records showed some stripping of the melt from its surface due to the strong winds at experiment time. Also, the crucible lid did not retract quite as neatly as in the other experiments. As a result, the melt at water contact was not as compact as in previous experiments.

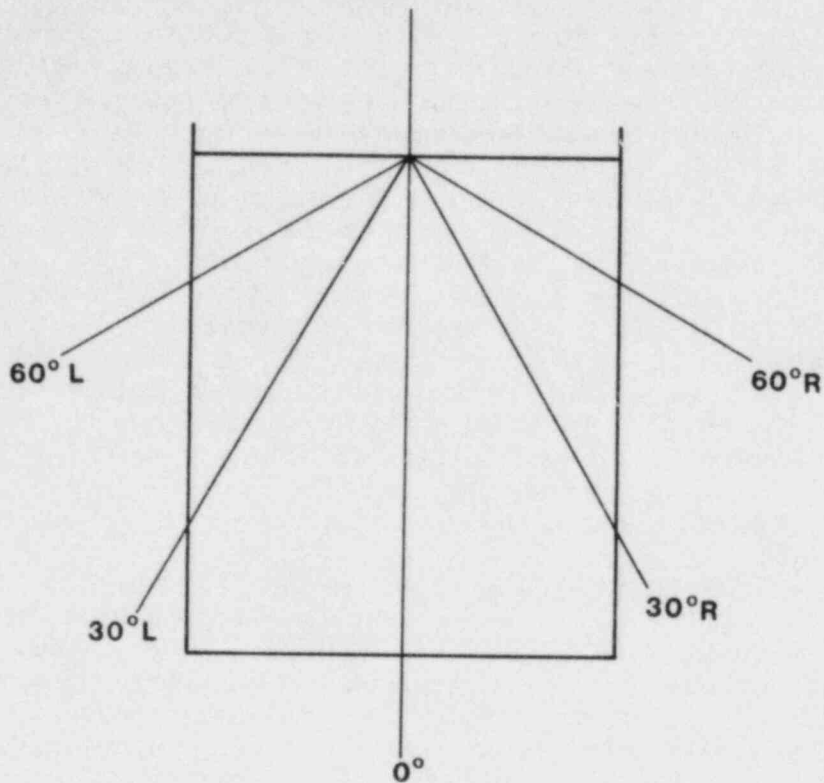


Figure 2.3. Orientation of Lines along Which Melt Front Has Been Plotted

A surface eruption began at about 18 ms after melt-water contact. Melt penetration at the time of the initiation of the eruption was about 7.5 cm. The melt appeared to be actively driven out of the interaction zone for about 62 ms, after which the upward inertia of the melt-water mixture continued to carry a great deal of melt out of the water chamber. At least four nonpropagating triggers were observed to occur at 59, 68, 75, and 89 ms after melt-water contact. These triggers fractured the water chamber in a number of locations. The leading edge of the melt appeared at times to be ill-defined and became fuzzy and even luminous--especially after the surface eruption had ended and the triggers were occurring. Bottom contact occurred at about 197 ms after melt entry.

Observation of the entire leading melt surface from the bottom-view high-speed camera showed no disturbances that correlated with the surface eruption or triggers that occurred during this experiment; the sources of these disturbances lay behind the melt front.

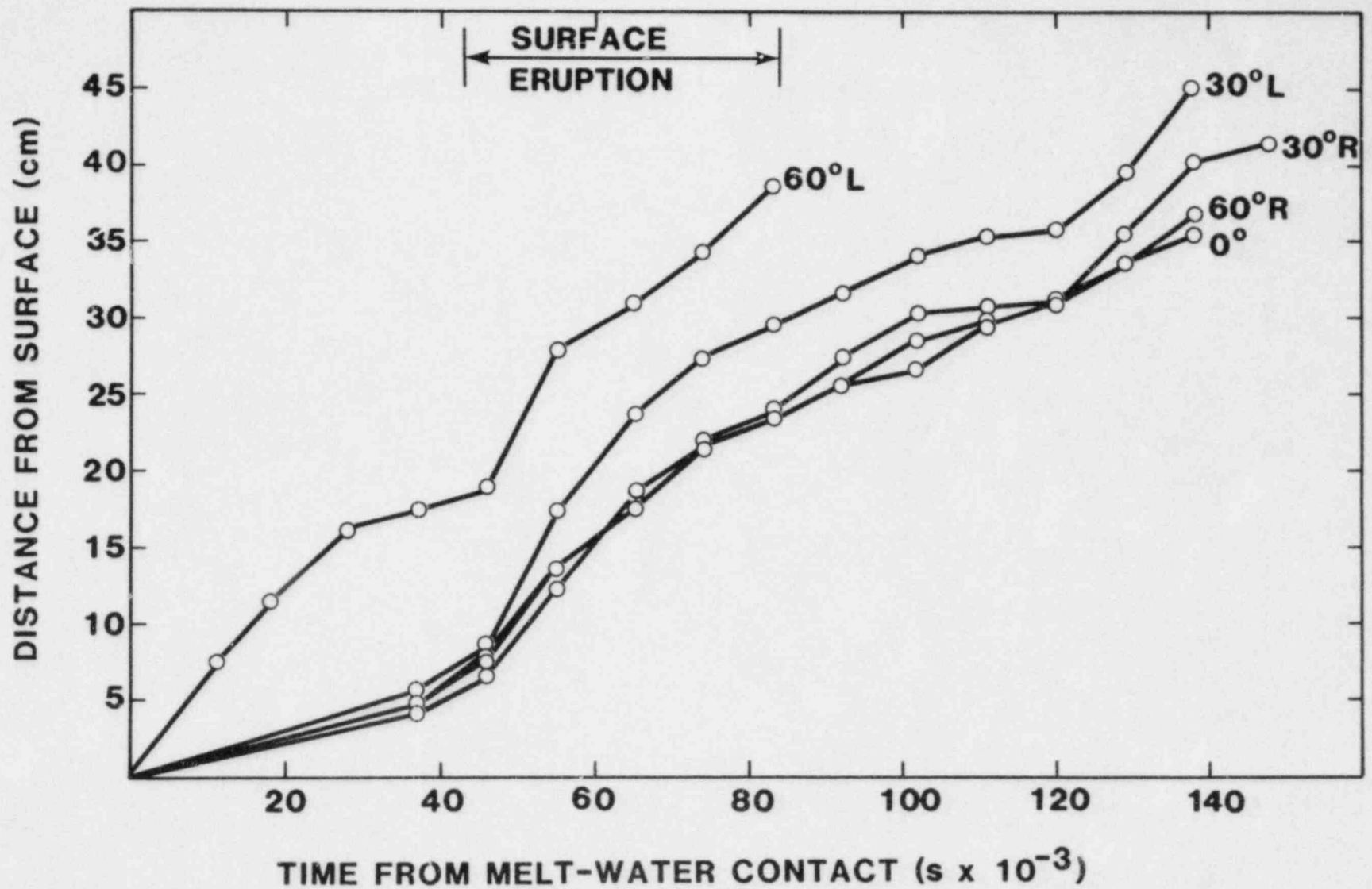


Figure 2.4. Melt Position as Function of Time (CM-3)



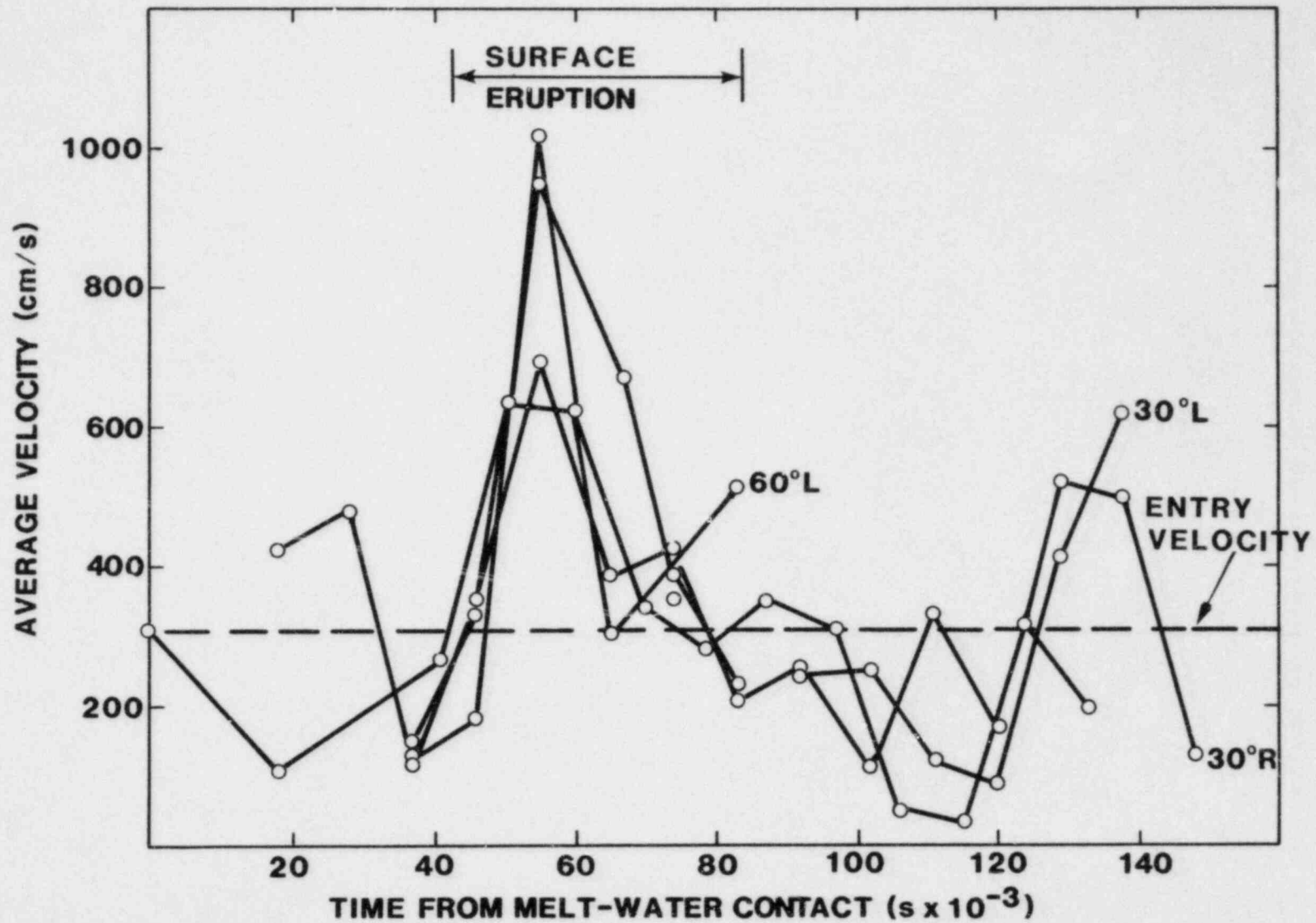


Figure 2.5. Melt-Front Velocity as Function of Time (CM-3)

The pressure history of the surface eruption was recorded by a transducer located about 10 cm above the water chamber base on the chamber side wall; these pressure data are shown on Figure 2.6. The pressure record shows an initiation at approximately 10 ms after melt entry with a long rise time of about 93 ms, and a peak pressure of about 7.2 bars. The pressure drops off quickly following the peak. The pressure pulse was reconciled with the high-speed films in terms of the time to initiation but did not correspond to the observed duration of the eruption. The reason for the discrepancy in event duration may be explained by the great uncertainty in determining when the surface eruption ceased to drive material upwards.

Even though the water chamber walls were broken into several large pieces and separated from the base, 3.5 kg of melt was recovered on the base. Water a few centimeters deep also remained on the base. The melt debris was a single molten slug, not a loosely agglomerated collection of particles like that recovered from experiment CM-3.

#### 2.2.1.3.5 Experiment CM-5

One of the purposes of this experiment was to determine what effect, if any, the melt mass had on the timing and progression of the surface eruptions seen in the four previous experiments. Consequently 8.5 kg of melt was prepared, and about 7.63 kg was delivered to the water chamber. The water volume was 61 cm square and 61 cm deep. Subcooling was about 4 K. The crucible bottom lid was retracted prior to water contact.

Very distinct and well-defined eruptions occurred for the experiment. The first eruption began 27 ms after melt-water contact and continued to about 69 ms, at which time a second eruption began and continued to approximately 146 ms after melt entry. The total duration of the event was about 119 ms. The second event appeared to be more vigorous than the first. No other triggers or disturbances were detected after the surface eruptions ended. Melt penetration at the time of the event initiation was about 8 cm. The overall view afforded by the low-speed camera, although limited in its time-resolution capacity (about 5 ms per frame), provided the following information: The two distinct surface eruptions were each preceded by an upward ejection of hot gases and melt material through the crucible vent holes. This ejection of material was probably in response to a pressure pulse or shock front that traveled through the air and was able to move some very fine material in the crucible before any other motion of the main melt mass could be detected. This ejection of material through the crucible vent holes was seen to precede the expansion of the melt mass by 1 or possibly 2

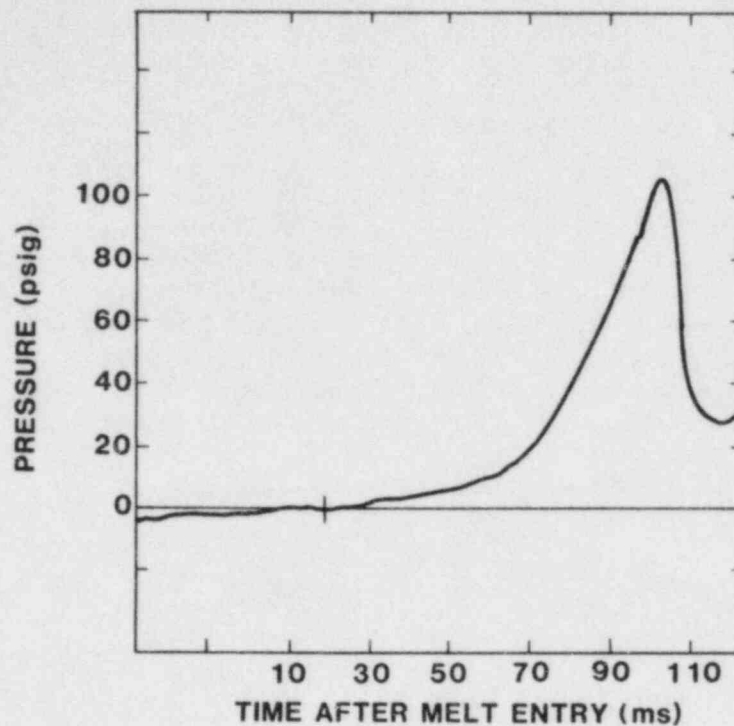


Figure 2.6. Eruption Pressure for CM-4. Peak pressure ~7.2 bar, rise time ~93 ms

frames (10 ms). Figure 2.7 shows the interaction just prior to the initiation of the second eruption. Note the presence of a small-diameter directional jet structure that has impinged on the underside of the steel plate well ahead of the expansion front of the main melt mass. Though not shown in Figure 2.7, another similar jet appeared immediately before the main mass of debris impacted the steel plate. The jet structure in Figure 2.7 appeared to consist of either very fine melt particles that were ejected at a much higher velocity than the particles of the main melt mass or very hot gases possibly undergoing combustion. Figure 2.8 shows the results of the second surface eruption. The fragmentation of the ejected melt shown in Figure 2.8 was typical of the degree of melt fragmentation seen for nearly all of the interactions of the CM series.

The water chamber was not fractured during the interaction, and about 3.4 kg of tightly agglomerated melt was recovered on the base of the chamber. Also, the water that remained in the chamber contained a large quantity of very fine material that remained suspended for several minutes. The suspended material gave the water a black appearance.

The pressure history of the surface eruption of this experiment is shown in Figure 2.9. The pressure record has been reconciled with the high-speed camera data with a reasonable



Figure 2.7. Photograph of FCI just before Initiation of Second Eruption (CM-5)

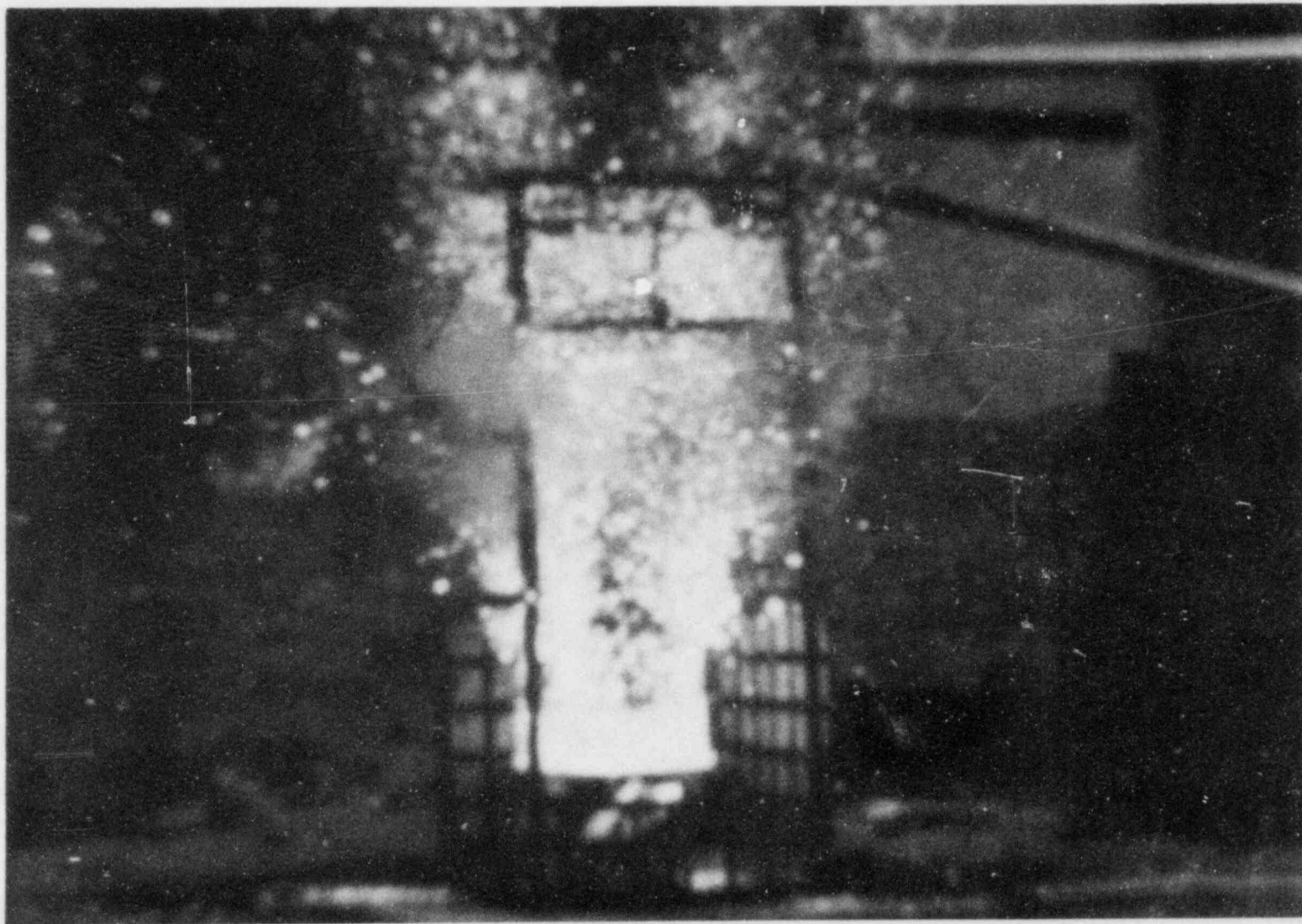


Figure 2.8. Photograph of Results of Second Surface Eruption (CM-5)

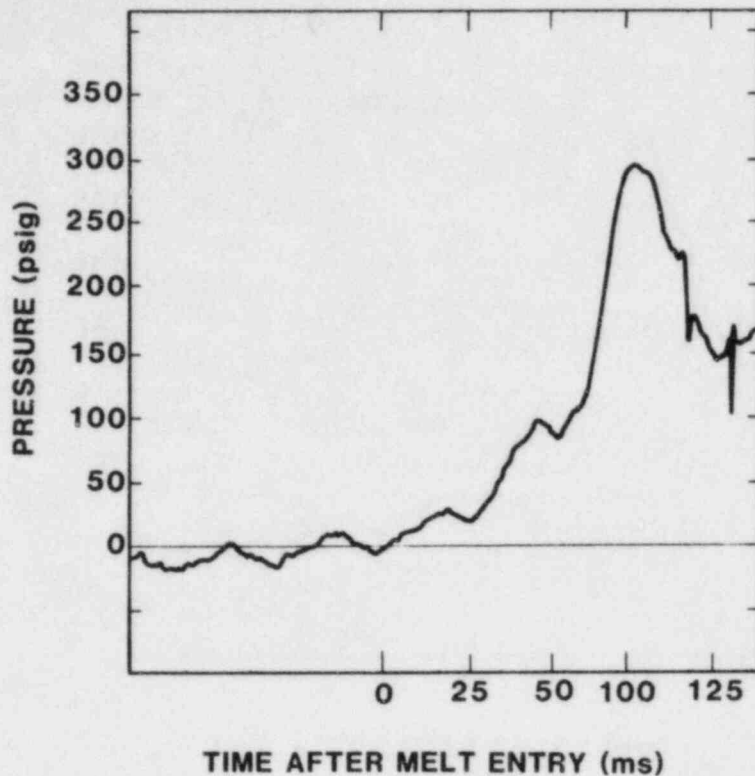


Figure 2.9. Eruption Pressure for CM-5

degree of agreement. The two surface events are shown clearly in the figure: The first event began at about 24 ms after melt entry and peaked at about 48 ms. The second event peaked at about 105 ms after melt-water contact. The maximum pressure recorded for the second event was about 21 bars, with a rise time of about 79 ms. As stated before, the discrepancy between film data and transducer data in event duration and times-to-event-peaks is due to the uncertainty encountered in the determination of these values from the high-speed film. Similar event-initiation times are a more reliable indicator of the level of agreement between the two sources of data.

Figure 2.10 shows the melt-water mixture at the time when the melt began to contact the chamber base. The melt was completely dispersed throughout the water volume. Note the "apparent" presence of a centrally located void (dark region) which was well formed at this late time in the interaction.

#### 2.2.1.3.6 Experiment CM-6

Inasmuch as the reduced melt mass of the previous experiment had no obvious effect on the nature of the interaction, an even smaller melt mass was prepared for this experiment: 4.5 kg of thermite was loaded into the crucible. About 4 kg of melt was delivered to the water chamber. The water volume was 61 cm square and 61 cm deep. The drop height was

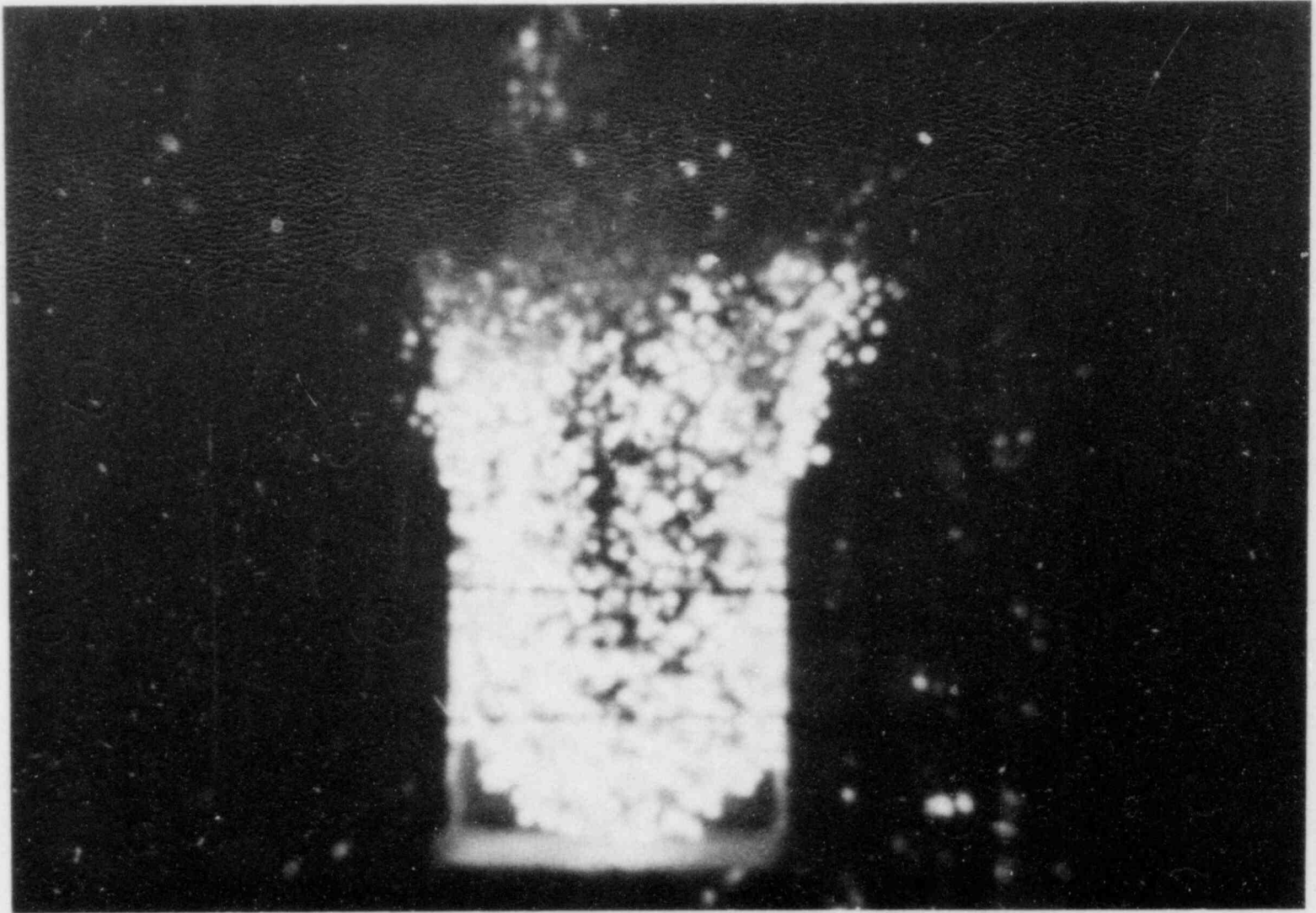


Figure 2.10. Photograph of Base Contact Mixing and Central Void (CM-5)

increased slightly from that of the previous experiment. The water was 3 K subcooled at the time of melt entry.

The low-speed camera showed a very coherent melt entry followed by an immediate surface eruption. The surface eruption appeared much less vigorous but lasted longer than those observed previously. The side-view high-speed films showed a relatively mild surface eruption that began about 22 ms after melt-water contact. The melt had penetrated the water surface to a depth of about 7 cm at the time of the interaction. The surface eruption appeared to continue to about 185 ms after melt entry; total duration of the event was 163 ms.

Besides the surface eruption, the only other event that was detected by the side-view high-speed cameras was a trigger that was either nonpropagating or only partially propagating. This trigger occurred at 159 ms after melt entry and resulted in a substantial increase in the local velocity of a small portion of the leading surface of the melt front. The trigger was observed to propagate across the surface of the melt-water mixture boundary for a short distance before it disappeared.

A careful examination of the bottom-view high-speed camera film revealed a total of seven separate and distinct events; this series of events began with the initiation of the surface eruption at about 22 ms and continued with events at 66, 88, 108, 132, 159, and 203 ms after melt entry. All of these events were seen to propagate briefly across the surface of the melt-water mixture, then dissipate before escalation to a steam explosion could occur. The most violent of these disturbances occurred at 159 ms and was the same one recorded by the side-view high-speed cameras. The melt contacted the water-chamber base 225 ms after it had contacted the water surface. The long-duration surface eruption of this experiment may have consisted of a series of separate events that occurred one after another.

The water chamber was not damaged during the interaction. After the experiment 1.94 kg of agglomerated debris, with particle sizes on the order of a centimeter in diameter, was recovered in the water chamber.

A great deal of difficulty was encountered in the interpretation of the pressure-transducer records for this experiment. Two pressure rises were recorded on the same transducer. The first pressure rise began at about 15 to 20 ms after melt entry and reached a peak at about 49 ms. A second pressure rise occurred at about 160 ms. The second rise did not, however, return to a zero level until approximately 700 ms after entry. Figure 2.11 shows this pressure record. The first rise corresponded with the film timing. The second rise in pressure also corresponded to the film observation in terms of the time of event initiation. The duration of the second



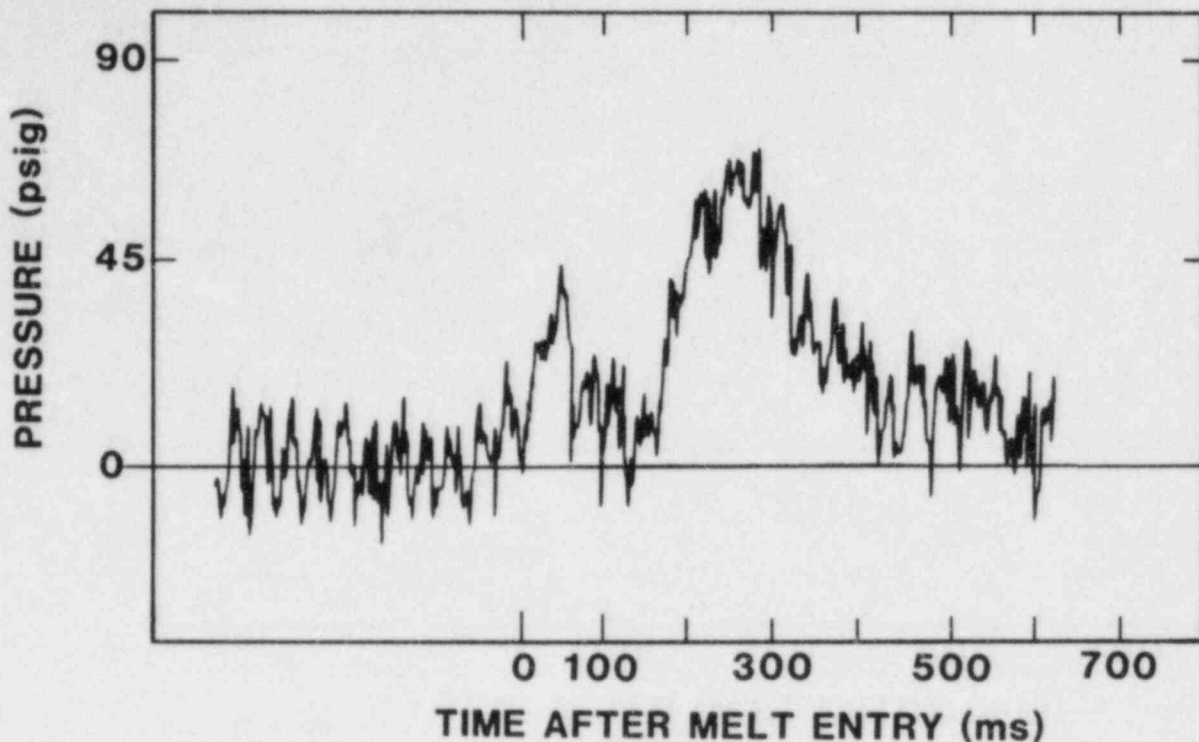


Figure 2.11. Eruption Pressure for CM-6, Showing Two Peaks

event, however, cannot be justified with the film record. The extreme radiative environment under which these measurements were taken was probably responsible for the incorrect duration of the second pressure rise. The peak pressure for the first event was, from Figure 2.11, about 3.1 bars. Figure 2.12 shows the first event separated from the second event.

#### 2.2.1.3.7 Experiment CM-7

The vigorous eruption of unquenched melt from the surface of the water had not been observed for experiments prior to the CM series. Also, prior to the CM series only a few successful experiments had been performed using low-subcooled water. Because of the very limited experience with low-subcooled water, it was not known whether the surface eruption phenomenon was a function of the hot water or some other parameter. For this reason experiment CM-7 was performed with highly subcooled water. If no surface eruption were observed, then we might conclude that the surface eruption was a function of low water subcooling. If, however, the surface eruption persisted in the highly subcooled water, then some other parameter was responsible and had obviously changed from previous experiments, possibly one of the parameters over which little or no control could be exercised such as the nature of

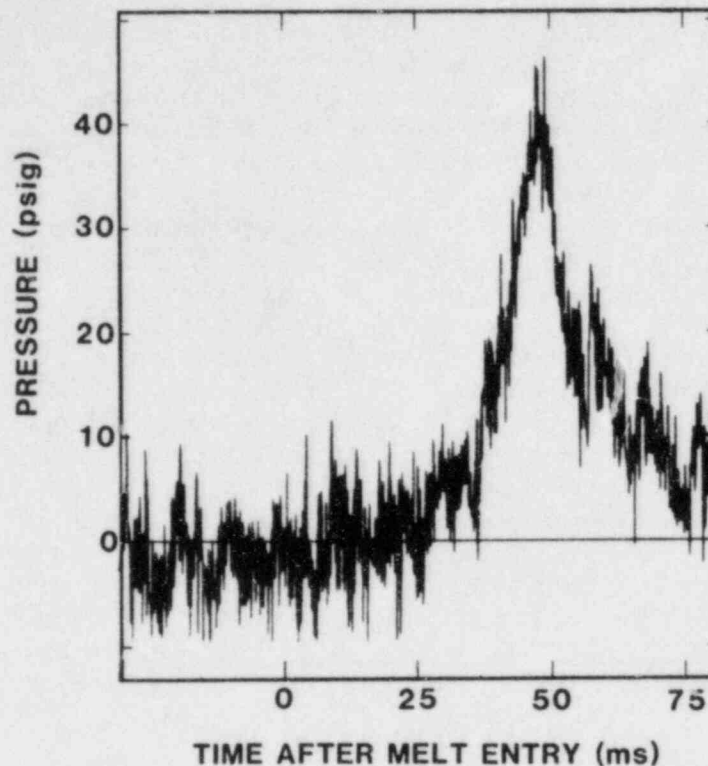


Figure 2.12. Eruption Pressure for CM-6, Showing First Peak

the melt (temperature, consistency, degree of prefragmentation, etc.). The primary purpose therefore of this experiment was to observe the dependence of the surface eruption on water subcooling.

Experiment CM-7 was performed in water at 294 K with a chamber side dimension of 61.0 cm and a water depth of 46.0 cm. Approximately 18.5 kg of melt was delivered from a height of 1.1 m to the water surface. Other initial conditions are given in Table 2.1.

The low-speed camera record showed a melt that was somewhat dispersed and not very uniform in shape at the time of water contact. Some of the problems with the melt geometry were the result of a poor crucible bottom lid release. A large portion of the melt mass was, however, delivered successfully to the water surface. An eruption of unquenched melt occurred almost immediately after the melt entered the water. The surface eruption was followed by a powerful surface-triggered explosion that was, in turn, followed by a violent bottom-triggered steam explosion that was similar to events observed for past experiments in the FITS B and MD experiment series.

The high-speed film record showed the following: Initiation of the surface eruption occurred at about 43 ms after melt-water contact at a melt penetration depth of 22 cm. The surface eruption fragmented and ejected some portion of the incoming melt in a fashion similar to the previous CM experiments. What appeared to be a small, yet energetic, surface-triggered explosion occurred at about 69 ms after melt entry--about 26 ms after the surface eruption. The surface explosion fractured all four sides of the water chamber and separated them from one another and the base plate. The melt that remained in the unconfined water mass continued to fall towards the chamber base. The melt front had a wide and nearly flat shape as it contacted the chamber base. Base contact occurred 108 ms after melt entry. The large quantity of unquenched melt and liquid water that resulted from the two surface events prevented further camera observation of the melt as it settled on the bottom. A violent steam explosion occurred 503 ms after melt-water contact, 395 ms after the melt contacted the chamber base. The steam explosion bent several members of the heavy steel water-chamber support stand. The entire EXO-FITS support tower was twisted as it rose against the guy cables that anchored it to the ground.

The four chamber side walls were found intact, one of them more than 30 m from the experiment site. The four side walls were apparently blown clear of the experiment by the surface explosion prior to the bottom explosion and were not subjected to the high-pressure, short-rise-time loading of the bottom-triggered steam explosion. The water-chamber base plate was, however, exposed to the main explosion and was fragmented into pieces no larger than about 1 to 1.5 cm maximum dimension.

The pressure transducers did not record either of the two surface events and were destroyed well before the main steam explosion occurred. The primary problem with the pressure transducers appeared to lie in their erratic response to the extreme radiative environment associated with the melt. The erratic deflection on the pressure records masked the real response to the two surface events.

#### 2.2.1.3.8 Experiment CM-8

The purpose of this experiment was to determine what effect, if any, the crucible bottom lid had on the fuel/coolant interaction. The crucible lid was not removed from the melt as in the previous CM experiments and impacted the water surface along with the melt. It was apparent from the last experiment (CM-7) that the surface-eruption phenomenon did not depend on water subcooling. The only other controllable parameter that had a different value from experiments performed in the FITS B and MD series was the crucible bottom lid. The previous experiments, particularly those of the FITS B series, always allowed the crucible bottom lid to fall

with the melt. Since all of the CM-series experiments thus far had retracted the bottom lid before water contact occurred, it was possible that the surface eruption could be a function of the presence or absence of the crucible bottom lid at water contact.

Experiment CM-8 was performed in low-subcooled water. The side dimension of the water chamber was held at 61.0 cm, and the water depth was maintained at 61.0 cm, identical to the previous experiment. The melt-drop height was lowered for this experiment to about 44 cm.

The results of the experiment were as follows: The crucible bottom lid pivoted on one of the release clamps as it began to fall from the crucible. As a result, the lid contacted the water surface in a vertical position and was displaced to one side of the melt mass. Both the lid and the melt entered the water at the same time. A very mild surface eruption occurred at about 37 ms after water contact. A much more vigorous surface eruption began at about 117 ms and at a penetration depth of about 15 cm. This vigorous surface eruption was followed by two nonpropagating triggers at 195 and 202 ms after water contact. The two triggers fractured the water-chamber side walls into several large pieces. A final event occurred at 216 ms after melt entry; the event consisted of an immediate and total darkening of the entire melt mass. The darkened melt appeared totally quenched and all camera data were lost at that point due to the lack of any luminosity of the melt-water mixture. Melt penetration depth at the time of the final event was about 41 cm. The elapsed time between the initiation of the event and the complete darkening of the melt-water mixture was about 8 ms. Though relatively mild, the final event was explosive in nature and fragmented the Lucite water chamber, including the base plate, into pieces on the order of 15 cm maximum dimension. Although some fracturing of the Lucite-chamber side walls had occurred during previous hot-water CM experiments, never had the water-chamber base been fractured.

The major difference between the results of this experiment and the results of all other low-subcooled CM experiments was found in the occurrence of a mild yet clearly explosive final event. Other aspects of a comparison between CM-8 and the previous hot-water CM experiments were similar in terms of an immediate surface eruption followed by several nonpropagating triggers. (Melt penetration at the time of the vigorous eruption was deeper for this experiment than for other comparable experiments.) It was noted earlier that the crucible bottom lid entered the water with its diametral axis vertical. The entire lid was displaced well to the side of the incoming melt mass. At no time during the mixing of melt and water was the bottom lid in contact with or in proximity to the melt-water mixture region. Whether the lid was responsible for the substantial deviation from the normal

progression of events for a low-subcooled interaction would be difficult to determine from the results of this experiment--primarily because the lid was not obviously involved in the interaction.

#### 2.2.1.3.9 Experiment CM-9

Experiment CM-9 was also performed with the crucible bottom lid not retracted in order to determine any effects the lid might have played in the surface-eruption phenomenon that was observed in the previous CM experiments. The crucible lid-release mechanism was modified, however, to ensure that the release clamps did not interfere with the lid drop as they had in experiment CM-8. Other than the release-clamp modification, nothing else was changed from experiment CM-8.

Because of the modification to the lid-release mechanism, the lid fell ahead of the melt mass and impacted the water surface "face on." Once in the water, the lid continued to fall straight down while it maintained a nearly parallel orientation with the water surface. Melt was observed to pour over the edges of lid as mixing with the water progressed. Figure 2.13 is a single frame from the low-speed camera and shows the melt mass just prior to water contact. The crucible lid was not visible at the time the frame was taken. Note the continuous column of melt that extended from the water surface to the mouth of the crucible, a length of about 44 cm. Based on a melt specific volume of  $250 \text{ cm}^3/\text{kg}$ , an 18.6-kg mass would have a volume of about  $4650 \text{ cm}^3$ . The apparent diameter of the melt column was about 27 cm, which would permit the entire 18.6 kg to be found in a column that was only about 8-cm tall. The apparent volume of the thermite column from the film data may suggest that the melt had entered the water with a large degree of prefragmentation that resulted in a high void fraction. Melt-water contact is shown in Figure 2.14. This figure was taken from a single frame of a high-speed camera. The crucible lid, though not yet visible, was parallel with the water surface at the time the frame was taken.

A very mild surface-triggered event occurred at a melt penetration depth of about 13 cm, 65 ms after melt-water contact. This event produced mostly steam with little or no eruption of melt particles; melt was always fragmented and ejected from the water surface for all other CM-series experiments. Figure 2.15 shows the interaction at a time after the initiation of the surface event. The crucible bottom lid is shown as a dark shape on the leading edge of the melt. The steam that resulted from the surface eruption is shown clearly between the water surface and the bottom of the crucible.

A relatively vigorous event occurred at 105 ms after water contact. The event was similar to that of experiment CM-8 and featured a very quick darkening of the melt mass. This

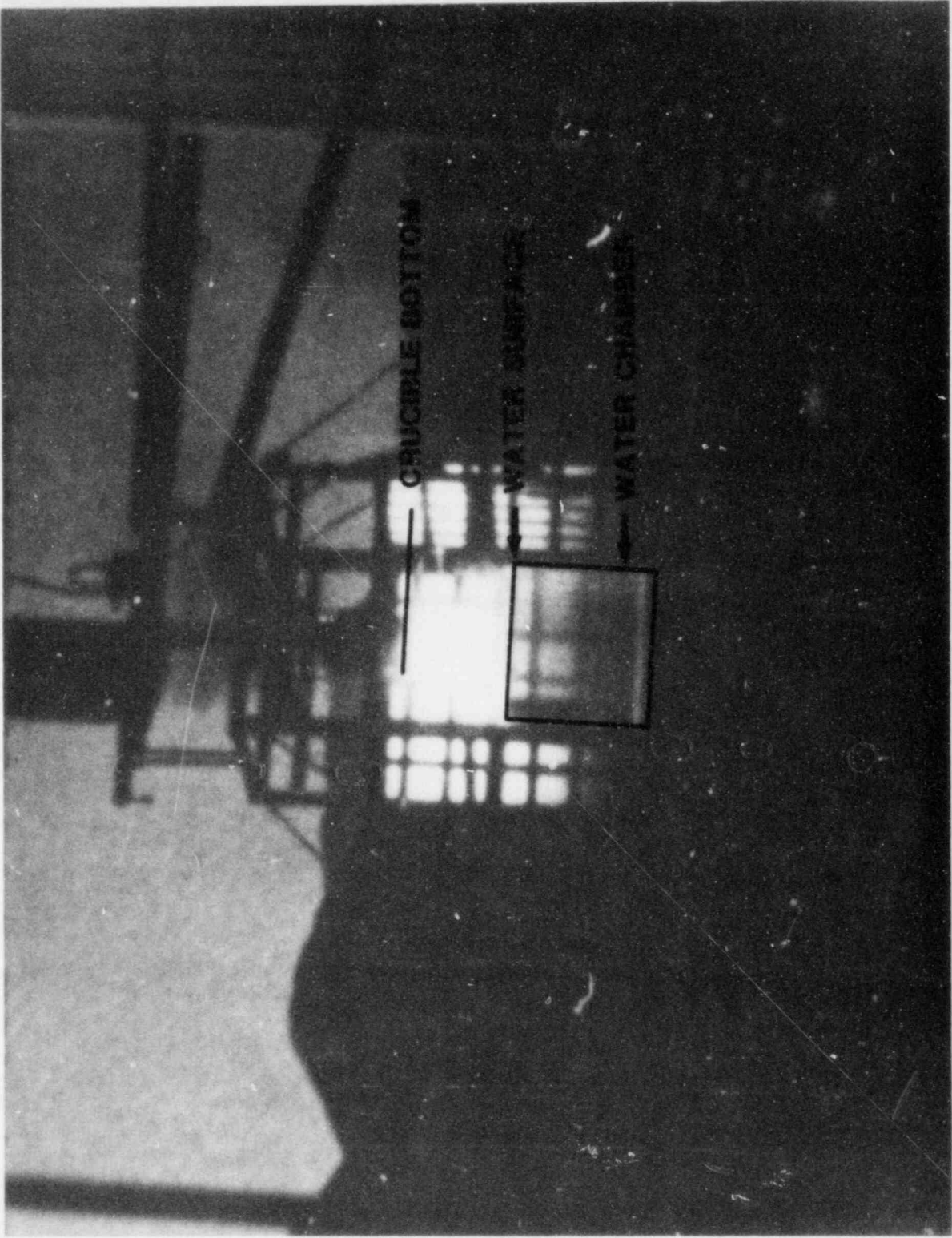


Figure 2.13. Photograph of CM-9, just before Melt-Water Contact

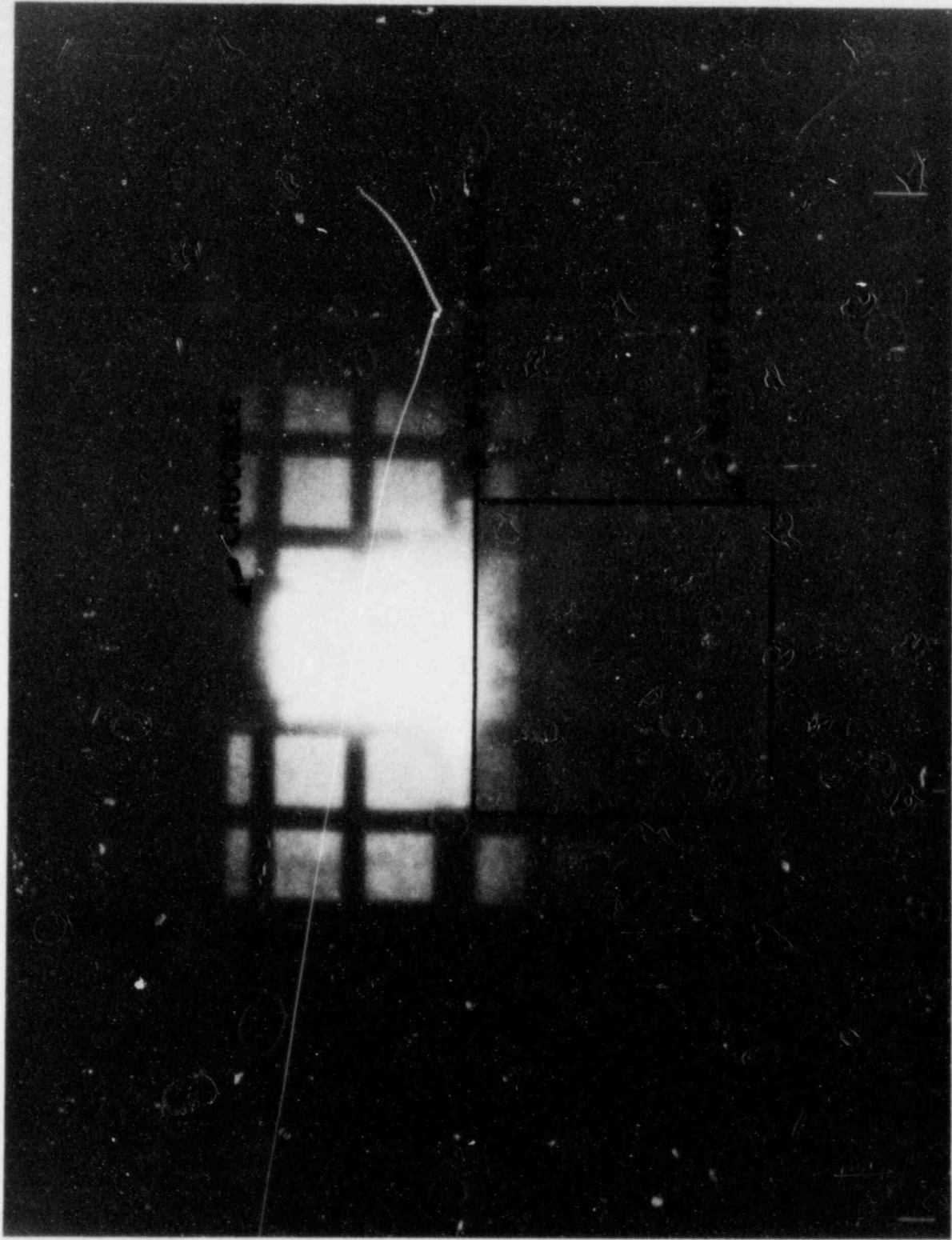


Figure 2.14. Photograph of Melt-Water Contact, CM-9

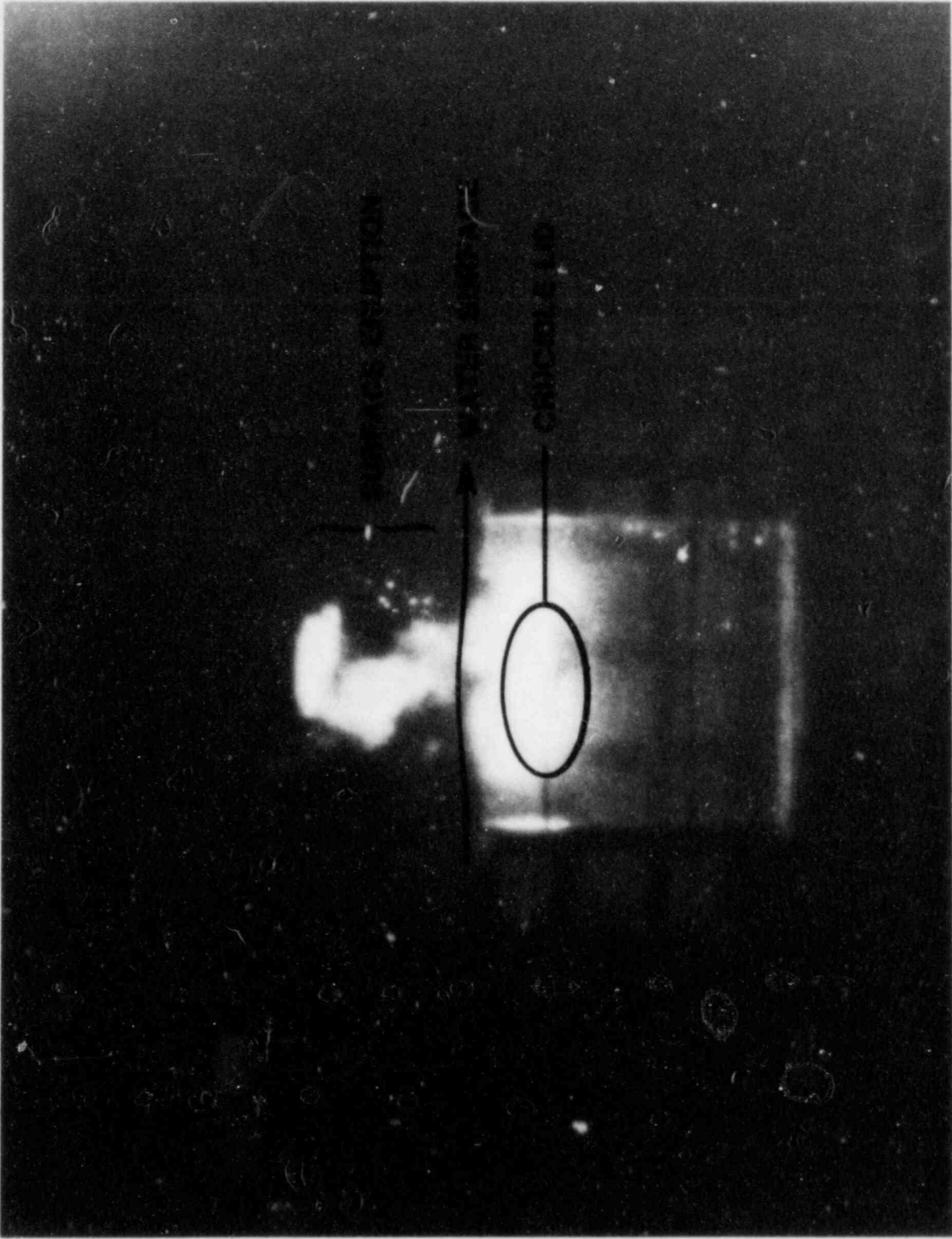


Figure 2.15. Photograph of FCI after Initiation of Surface Event, CM-9



experiment however, unlike CM-8, did not experience a total darkening of the mass, but rather a partial darkening followed by a general brightening of the entire mass. The duration of the darkening-brightening process was less than 10 ms. Figure 2.16 shows the interaction at the time of the main event. The general darkening of a portion of the melt, particularly in the upper right region of the melt-water mixture, is evident if a comparison is made between this figure and Figure 2.15. Once the event was over, the melt mass appeared to resume its original brightness. Figure 2.17 shows the interaction about 15 ms after event trigger. The bottom-view high-speed camera showed two clear disturbances that briefly traveled across the surface of the melt-water region just prior to the event. Both disturbances originated in the same general location.

The result of the main event was to eject material upwards and fracture the water chamber; several large holes were blown in the corners of the water chamber. A hole about half the size of the water-chamber base was made in the base. The water-chamber walls, however, aside from the holes in the corners, were left intact and were found standing and attached to the base after experiment.

Finally, a small but energetic steam explosion occurred ex-vessel in the free-flowing stream of melt and water that had poured out of the large hole in the water-chamber base. The explosion occurred 557 ms after water contact as the stream impacted the bottom-view mirror; the mirror was located directly below the water chamber. The explosion shattered the mirror and destroyed the light steel frame that supported it.

Although some difficulty was encountered in the justification of the pressure records, the pressure pulse produced by the main event has been shown on Figure 2.18. The record indicated a pulse with a fast rise time of about 600  $\mu$ s to a maximum pressure of about 94 bars and a total duration of less than 6 ms.

#### 2.2.1.3.10 Experiment CM-10

This experiment was performed to evaluate the effect of the parameter "hold time" on the results of a fuel/coolant interaction, with a specific goal of testing its effect on the surface-eruption phenomenon. The hold-time parameter is the length of time, after the burn, that the melt is held in the crucible before the bottom lid is removed and the melt is delivered to the water surface. More specifically, it is the preset time between thermite burn completion and melt release. The major experimental series of the past, such as the FITS B and MD series, maintained the value of the hold-time parameter at 1.5 s. The procedure for the CM series of experiments was to adjust the hold time so that the melt was delivered as soon

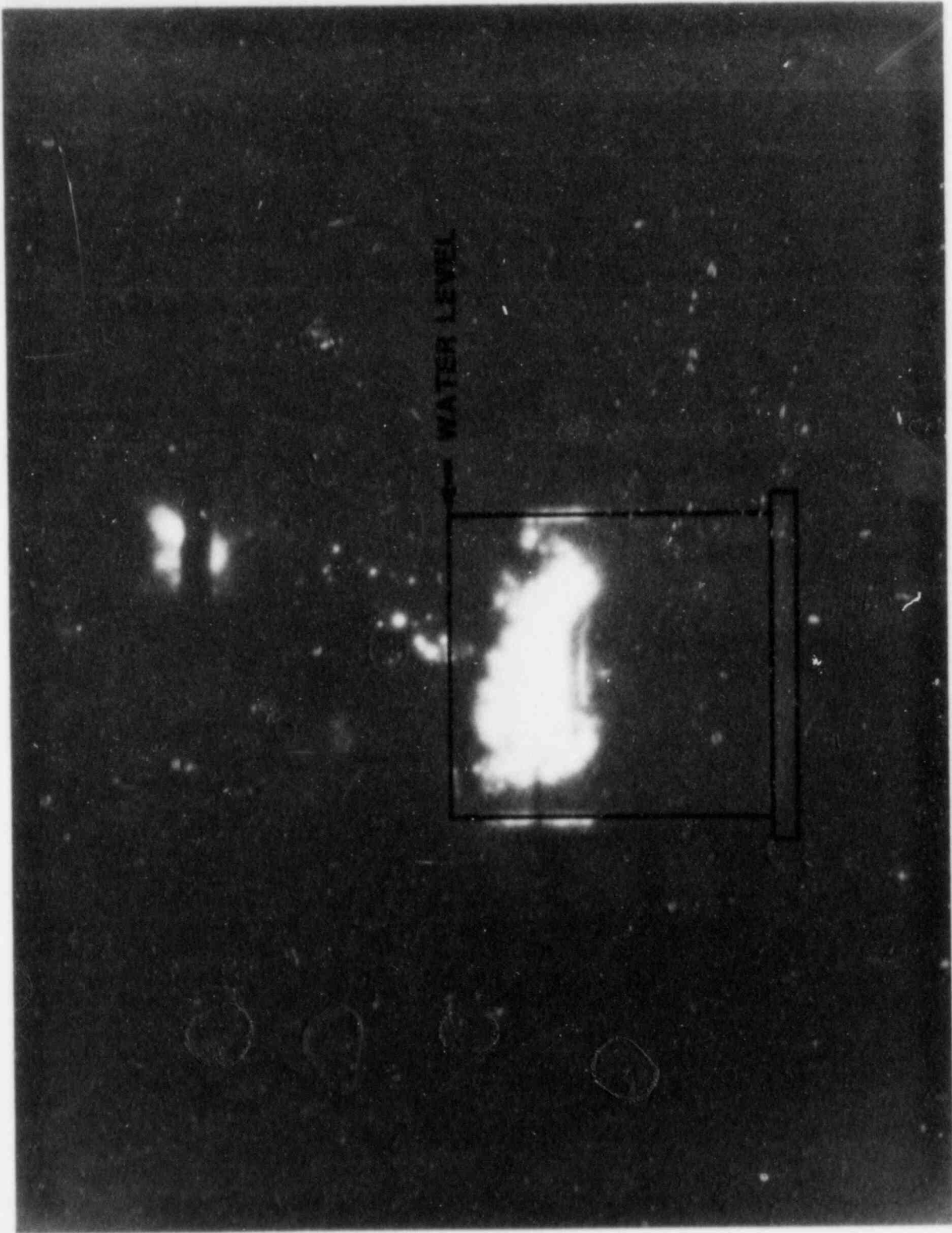


Figure 2.16. Photograph of FCI at Time of Main Event, CM-9

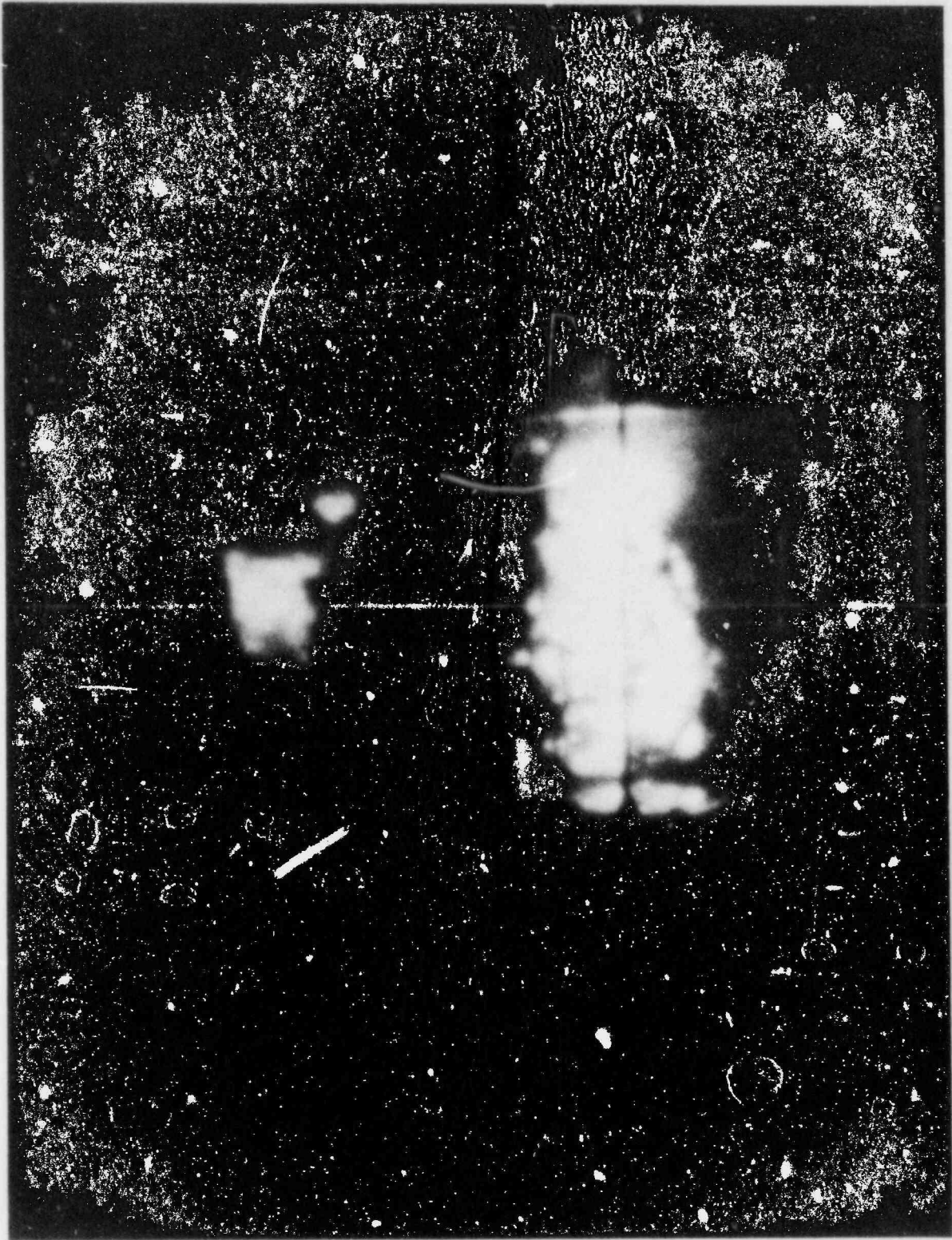


Figure 2.17. Photograph of FCI about 15 ms after Main Event, CM-9

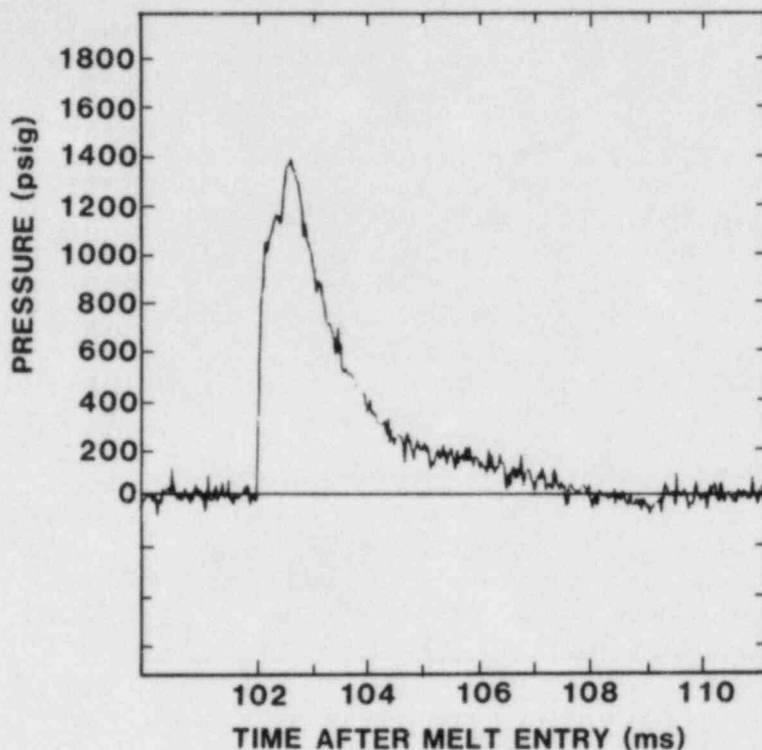


Figure 2.18. Explosion Pressure for CM-9

as the burn front contacted the crucible bottom lid. The average value of the hold time for the CM series was about 600 ms. The melt therefore was held about 2.5 times longer during the previous FITS B and MD experiments. Since surface eruptions were not observed during those experiments, the value of the hold-time parameter may have been responsible for their appearance during the CM series of experiments. The value of the hold-time parameter can affect several of the physical, chemical, and thermal properties of the melt.

Experiment CM-10 was performed in low-subcooled water with the hold time preset so that the melt was not released until 7 s after the burn front had contacted the crucible bottom lid. Table 2.1 shows the values of the other variables for this experiment. Although the experiment was successful, a problem was encountered in the attempt to hold the melt in the crucible for 7 s.

The high-speed film data showed the following results: A leak developed in the bottom-lid seal after the melt had been held for about 5 s. All of the melt that leaked from the crucible fell into the water. As a result, the water, originally only a few degrees from saturation, was boiling vigorously when the main melt was released. So vigorous was the boiling that the apparent water surface had risen as much as 30% of the original water depth at the time the main melt mass contacted the water (about 23% void fraction). It was

not possible to determine how much melt leaked from the crucible prior to the main melt release.

The high void fraction of the water, coupled with the boiling of the surface, made determination of the exact time of melt-water contact difficult. A mild surface eruption began roughly at 43 ms after melt-water contact. The surface eruption was not as violent as some of the previous eruptions. The major portion of the melt was not ejected and continued to fall through the water-steam mixture until bottom contact occurred. The initial surface eruption was followed by a very fast, but only mildly energetic, event at 112 ms after melt-water contact. The event appeared similar to the primary event of CM-9. A partially propagating trigger occurred just prior to the event. The trigger appeared to initiate near the base in the southeast corner of the water chamber and propagate upwards through the corner portion of the melt only for a distance of about 20 cm. The trigger then either dissipated or became ill-defined to the point of disappearance. The propagation velocity was less than 100 m/s. The water chamber was fractured into numerous large pieces as a result of the event. The apparent water level at the time of the event was nearly twice that of the original water level (about 50% void fraction).

Finally, an ex-chamber explosion occurred very late in the interaction, 311 ms after melt-water contact. Although it was difficult to determine the location of the explosion, it may have occurred on the concrete base pad beneath the water chamber. The explosion was small but energetic and appeared similar to previous explosions in terms of duration and the resulting expansion velocity.

The pressure records were lost as a result of the extreme thermal noise encountered during this experiment. Figure 2.19 has been included to show the high void fraction and the resultant water-level increase just prior to melt-water contact.

Another phenomenon, which has been observed previously, was particularly clear in this experiment. It is called an "air-burst," or the explosion of a single melt particle as it is impacted by water ejected during the interaction in the water chamber. These interactions occur as the melt particle is in free flight away from the water chamber. This in-flight interaction results in fine fragmentation of the single melt particle. Figure 2.20 shows two particles at the time of this in-flight interaction. Events such as this may affect some aspects of the overall fuel/coolant interaction question such as noncondensable-gas generation, direct heating, and source-term uncertainties.



Figure 2.19. Photograph Showing Void Fraction at Melt Entry, CM-10

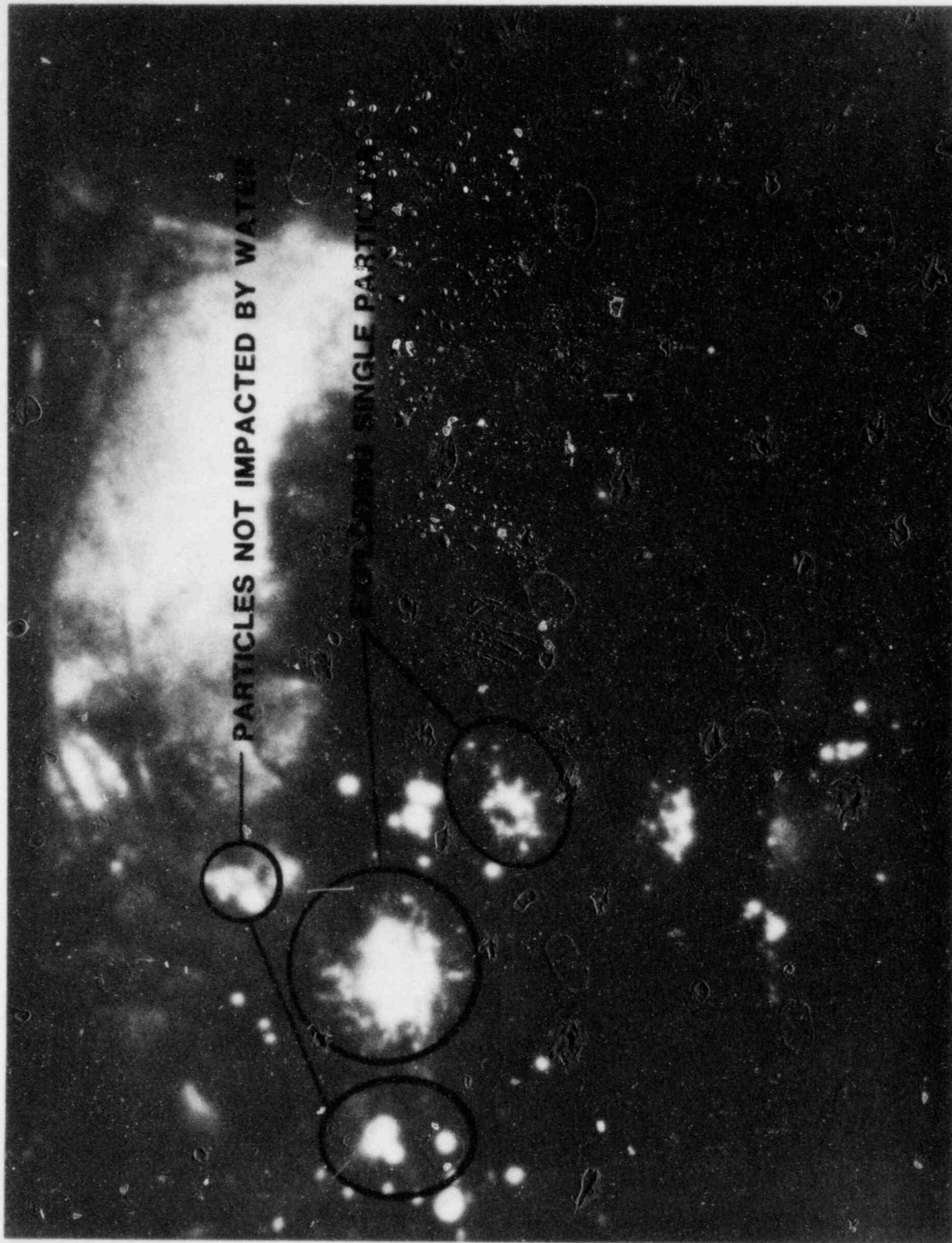


Figure 2.20. Photograph of In-Flight Single Particle Interaction, CM-10

#### 2.2.1.3.11 Experiment CM-11

The crucible bottom lid was modified for this experiment to accommodate a large value for the hold-time parameter without the development of a leak such as developed during the melt hold interval of experiment CM-10. The hold time was also reduced to 5.0 s for this experiment, as opposed to the 7.0-s hold time of the previous experiment.

The experiment was performed in water close to the saturation temperature. A mass of 18.7 kg of the melt was delivered to a water chamber that was 61.0 cm on a side. The water depth was 61.0 cm. The modifications that had been made to the bottom lid were successful, and no melt escaped from the bottom of the crucible during the 5-s hold interval. Some quantity of melt was, however, ejected from the crucible vent holes at the time the burn front contacted the bottom lid. (A disturbance in the melt is not uncommon when the burn front contacts a boundary such as the bottom lid. The disturbance during this experiment was much more intense than in previous experiments. It was not possible to determine how much melt was ejected from the vent holes.)

The melt mass was slightly deformed at water entry as a result of the lid-retraction process. The water surface was quiescent at melt entry. A single vigorous surface eruption began at 52 ms after melt-water contact. The melt had penetrated to a depth of about 16 cm at the time of the surface eruption. The surface eruption produced typical results--the ejection and fragmentation of unquenched melt. The resulting fragmentation of melt is shown in Figure 2.21. No other events or disturbances were observed. The water chamber was left undamaged, and a tightly agglomerated single slug of debris was recovered from the chamber base. The mass of the slug was 5.8 kg.

#### 2.2.1.3.12 Experiment CM-12

The final experiment of the CM-experiment series was performed as an exact repeat, insofar as the controllable parameters were concerned, of a previous experiment, FITS 2B. The primary goal of CM-12 was to close out the CM series with an experiment that could be compared with a standard experiment of the past. The FITS 2B experiment resulted in a single surface-triggered steam explosion that occurred about 84 ms after melt-water contact. The initial conditions for experiment CM-12 are shown in Table 2.1, and included water at high subcooling, 1.5-s hold time, and the crucible bottom lid not retracted.

The melt entered the water in a very compact and uniform geometry. The bottom lid impacted the water surface just ahead of the melt mass and was nearly parallel with the surface. A mild surface eruption occurred about 37 ms after





Figure 2.21. Photograph of Peak of Surface Eruption, CM-11

melt entry. The initial eruption was followed by a second eruption that was much more energetic. The second surface eruption was directional and produced a column of ejected material that had a width less than that of the water chamber. That event occurred at 69 ms after melt entry and lasted for about 13 ms. The water chamber was not fractured by this event. A bottom-triggered steam explosion occurred 125 ms after melt entry. A disturbance was observed just prior to the expansion phase. The disturbance traveled through the melt-water mixture at a speed of about 600 m/s. It was not clear whether the disturbance was the result of a propagating trigger or the effects of the expansion phase of the interaction. The melt was dispersed throughout the water chamber at the time of the explosion. The explosion was exceptionally intense and resulted in damage to the heavy water-chamber support stand. Several large pieces of plywood used as stadia markers were thrown various distances from the experiment site; the largest of these missiles, a 122-cm x 183-cm piece, was thrown about 53 m from the experiment site. Also, no remains of the water chamber were located. No pressure transducers had been installed in the water chamber for this experiment. Until the extreme problem with the thermal load on the gauges could be assessed, there was little justification for the continued waste of expensive pressure transducers. Furthermore, all supplies of transducers had been exhausted at the experiment site and new shipments had not yet arrived.

#### 2.2.1.4 Discussion of CM Experiments

The Coarse Mixing series of fuel/coolant interaction experiments displayed three distinct types of events: the steam explosion, the nonpropagating disturbance (trigger), and the surface eruption. Two of the event types, the steam explosion and the nonpropagating trigger, have been seen in previous experiment series. The violent eruption of unquenched melt from the surface of the water represents an event that was not observed for the highly subcooled experiments of the past. Some mild surface eruptions were noted, however, during the very few low-subcooled experiments that were performed prior to those of the CM series, although none of those experiments exhibited the same vigorous eruptions as were noted for the CM-series experiments. Weak steam explosions, such as occurred for the experiments CM-8, CM-9, and the surface event of CM-12, have also not been clearly observed before, although the term "partial interaction" was used by Mitchell. The strong steam explosions and nonpropagating triggers that occurred for several of the CM-series experiments were similar to those that occurred during previous experiments.

The surface-eruption phenomenon appears to be a rapid generation of steam and noncondensable gases. The steam-generation rate is not fast enough to result in a steam explosion but is

fast enough to produce a high degree of unquenched melt fragmentation. The event appears to be very localized with respect to the water surface, and (at times) directional. This localized and directional nature of the surface eruption was seen for nearly all of the CM-series experiments, most notably experiments CM-12, CM-4, and CM-5. The eruption of CM-12, for example, produced a narrow column of ejected material that appeared to originate from the center of the water chamber. The width of the ejected column was much less than that of the water chamber. Experiments CM-4 and CM-5 also showed narrow columns of material that were in some cases inclined as much as  $60^\circ$  with respect to the vertical axis. The localized nature of the eruption is apparent from a study of the high-speed film records. The effects of the eruption were generally not seen in any melt that was more than a few centimeters below the original water surface. In some instances pronounced increases in the velocity of the melt front were noted in response to an eruption, but there were no other disturbances in the subsurface melt-water mixture. The pressure required to drive the eruption process appeared to be generated in a region that did not extend more than a centimeter or two below the water surface. The bottom-view high-speed camera, which afforded a unique view of the entire surface of the falling melt front, many times did not even record the initiation of the surface event. (Nonpropagating triggers that occurred on or near the surface of the advancing melt front were clearly visible on the bottom-view film records.)

The sizes of the particles that were ejected from the surface ranged from large pieces with an apparent diameter in excess of several centimeters to particles too small to be individually resolved on the film records. Figures 2.7 and 2.8, referred to previously, demonstrate the degree of fragmentation that is produced during the surface eruption. If, for example, the eruption that is shown impinging on the plate of Figure 2.7 is made up of melt particles, they are so small that they appear as a coherent, luminous column. The particle sizes of Figure 2.8 are much larger by comparison. Because of the extreme brightness of the melt particles, it is not possible to obtain an accurate measurement of the particle sizes--only a comparison of apparent sizes.

The surface eruptions may prove important in terms of the direct-heating mode of indirect containment failure. Pressurization of the containment atmosphere through the cooling and oxidation of the ejected melt particles may be substantially affected by the character of the expelled melt mass.

The characteristics of the pressure pulses that were produced at the surface of the water proved very difficult to measure. The response of the transducer diaphragm to the radiative environment, coupled with the low level of the eruption pressures in general, were important difficulties encountered.

The few pressure records that were obtained showed some degree of variability in the peak pressure, rise time, and decay time of the eruptions. For the pressure records that have been presented, the peak eruption pressure ranged from a low of about 3 bars to a high of about 21 bars. The rise times for the surface expulsions are generally very long in comparison to other events during the fuel/coolant interaction. The rise times for the eruptions of CM-4 and CM-5 were about 100 ms each. Once the pressure peaked, the eruption dropped quickly in comparison to the slow rise time.

One explanation for why the pressures of the surface eruption are low and the durations of the events are long may be found in the location of the events. The region where the pressure is generated appears to be essentially at the water surface where there is little or no structural or inertial confinement. With a lack of any substantial confinement, the pressure can be relieved nearly as fast as it is generated. Also, the rate at which steam can be generated in any given region of the interaction may be a function of the local pressure in that region. If this were the case, then the event would tend to be long-lasting and low in pressure--never able to escalate into a full steam explosion. If, on the other hand, the event were to occur below the water surface where a sufficient degree of inertial and structural resistance to the expansion of the pressurized region could be applied, the event may have the capability to escalate into a steam explosion.

The weak steam explosions have rise times that are much shorter than the rise times for the eruptions; the peak pressures, however, can be much higher. Weak explosions can exhibit rise times similar to the stronger steam explosions, but the peak pressures are usually much lower.

Weak explosions were noted for three of the CM experiments. The high-speed film records show that these events were similar to one another in terms of rise time and total duration for all three cases. Only for experiment CM-9 was a pressure record obtained. The pressure record, which was presented previously in Figure 2.18, showed a fast rise time of about 600  $\mu$ s and a total duration of about 5 or 6 ms. Many steam explosions exhibit rise times of several hundred  $\mu$ s and total duration of a few ms. The major difference between the weak events of experiments CM-8, CM-9, and CM-12 and a full steam-explosion event, such as that recorded during the FITS 4B experiment, was in the peak pressure. The FITS 4B experiment produced a peak pressure of about 600 bars with a rise time of a few hundred  $\mu$ s. Total duration of the FITS 4B event was about 1 ms. A pressure pulse obtained during the MD-19 experiment had a rise time of about 400  $\mu$ s and a total duration of about 3.5 ms. The peak pressure was less than 200 bars.

The events noted for experiments CM-8, CM-9, and CM-12 were capable of shattering the Lucite water chamber into pieces of a size similar to those produced during the explosive events of FITS 4B and MD-19. The reason for the low peak pressure recorded for CM-9 is not clear at this time. It may be a result of the low subcooling, the low subcooling combined with a melt-mass threshold effect, a malfunctioning gage, or some other effect. It is important to note that 10 kg of purely oxidic melt exploded as violently in low-subcooled water as it did in highly subcooled water.

A summary of the event types and time histories for each of the CM-series experiment is shown in the top half of Figure 2.22. A similar summary of the FITS B results has been included for comparison purposes, in the bottom half of the figure. In general, the low-subcooled CM experiments were dominated by a surface interaction that began anywhere from 20 to 80 ms after melt-water contact. Sometimes nonpropagating triggers followed the surface eruption. Of all the low-subcooled experiments in the CM series, only experiments CM-8, CM-9, and CM-10 progressed from the surface eruption to a steam explosion. Both experiments CM-9 and CM-10 also resulted in energetic steam explosion that occurred ex-vessel. The two highly subcooled experiments, CM-7 and CM-12, began with a surface eruption followed by a surface-triggered event. The surface-triggered event of CM-7 was clearly explosive (short rise time); the surface-triggered explosion of CM-12 was not quite as clearly defined. Both experiments were terminated by energetic steam explosions. It can be shown (Figure 2.22) that the FITS B experiments were not nearly as complex or diverse in their results. None of the low-subcooled experiments exhibited a significant surface eruption; they all resulted in either one or two steam explosions. The only successful low-subcooled experiment, FITS 6B, was similar in character to the CM series of experiments, a very mild surface eruption followed by several nonpropagating triggers. It appears that during the FITS B series of experiments, the surface eruption may have been a function of the low-subcooled water. The occurrence of the surface eruption in the CM series of experiments appears, however, to be independent of the water subcooling.

Finally, some effects of the hold time, melt mass, and crucible bottom lid were observed. For example, it is clear that the crucible bottom lid tended to delay the initiation of a surface event. The lid may not, however, have been responsible for the weak explosion that occurred for CM-9 since a similar weak explosion occurred for CM-8, where the lid was not involved in the interaction (even though it was not retracted). The value of the hold time also affected the time to initiation of the surface eruption. The smallest melt mass exhibited one of the longer duration surface eruptions and also produced the greatest number of nonpropagating triggers.

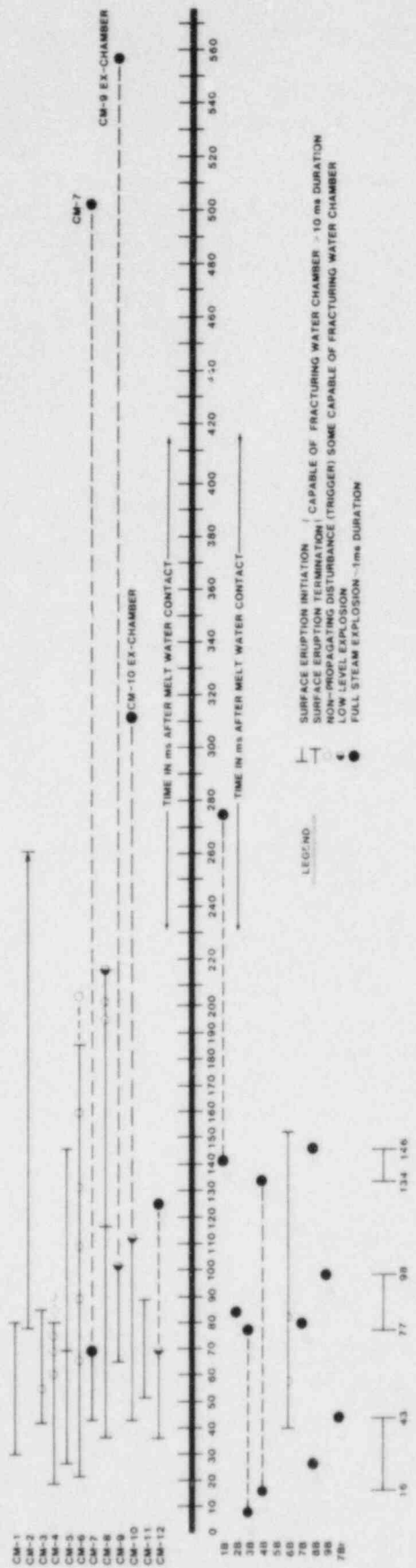


Figure 2.22. Time Histories and Event Types for CM and FITS B Experiment Series

## 2.3 Modeling and Analysis of Fuel/Coolant Interactions

Given the absence of adequate cooling water to the core of an LWR, the fission-product decay heat would eventually cause the reactor fuel and cladding to melt. This could lead to slumping of the molten-core materials into the lower plenum of the reactor vessel, possibly followed by failure of the vessel wall and pouring of the molten materials into the reactor cavity. Past analyses have indicated that residual water is likely to be present both in the lower plenum and in the reactor cavity.[5,6] Therefore, when the molten-core materials enter either region, there is a strong possibility of molten-core melt contacting water coolant. The physical process by which the molten core (fuel) contacts and mixes with the water (coolant) is important for four reasons;

- (1) Because of its potential for rapid steam generation from a fuel/coolant interaction either energetic (steam explosion) or nonenergetic (steam spike)
- (2) Because it is a source of combustible hydrogen from the oxidation of the metallic components of the molten core (e.g., iron, chromium, zirconium)
- (3) Because it will affect the size of the fuel debris, its dispersal in the reactor system of containment, and its ultimate coolability
- (4) Because of its potential for mechanical damage to the vessel and possibly containment following a steam explosion

This report focuses on recent work in the modeling of fuel/coolant interactions. In particular this semiannual report discusses results of FITS data analysis relative to fuel/coolant mixing, modeling of Nelson's single-droplet experiments, a parametric model of the FITS experiments, reactor application of WISCI (the MI-module of MEDICI) calculations, and a critique of a recent paper by H. K. Fauske and R. E. Henry.

### 2.3.1 Fuel/Coolant Mixing

Past research into fuel/coolant mixing has been directed at predicting the physical limits for which mixing could or could not occur.[7,8] Recent analysis of FITS experiments have considered this mixing to be composed of three simultaneous processes--heat transfer between fuel and coolant, mass transfer (i.e., hydrogen production by metal oxidation during mixing), and hydrodynamic breakup of the fuel due to relative velocities.[9,10] Initially, we have neglected the first two effects and considered hydrodynamic mixing alone. Based

on the concept that in the FITS experiments the fuel falls into the coolant pool and mixes with the coolant due to hydrodynamic instabilities (Kelvin-Helmholtz and Rayleigh-Taylor), we have attempted to empirically correlate the integral mixing process. One can choose to nondimensionalize the dependent variables (mixture depth- $H_m$ , mixture volume- $V_m$ , displaced coolant volume- $V_D$ ) by the fuel initial volume and diameter and correlate them based on a derived dimensionless time. Current results suggest that this approach can be used successfully to correlate mixing data from various experiments (Figures 2.23 to 2.25), and derive the integral average fuel, steam, and coolant volume fractions as a function of time.

#### 2.3.1.1 Limits to Fuel/Coolant Mixing

Limits to fuel/coolant mixing can indeed exist, e.g., steam generation could cause the fuel and coolant liquids to be carried away from the mixing region with the steam flow. One would expect this mixing process to be self-limiting, i.e., given sufficient time, the fuel would mix to an average size no smaller than that which would cause the liquids to be fluidized and swept away. This concept is similar to past models on fluidization.[11,12] Based on this concept, we have developed a simple limit-to-mixing criterion that seems to show reasonable agreement with FITS data.[10]

One could generalize this concept of a limit-to-mixing for fuel and coolant masses. The characteristic diameter of the fuel mass in the water pool is bounded by its initial diameter,  $D_{f0}$  (assuming a single spherical mass), when it enters, and its diameter at the fluidization limit,  $D_{FR}$ , when it has fallen through a sufficient depth of water after some time. The diameter of the fuel at a time between these two bounds could be approximated by a simple transient model as used in hydrodynamic droplet breakup (e.g.,  $D_f = D_{f0} (\exp(-T^+))$ ). The important variable is not time but the product of the fuel velocity and time, i.e., the depth through which the fuel has traveled. One can combine this concept with the limit-to-mixing to predict the maximum mass of fuel that could mix for a given water depth ( $v_{ft}$ ), and the final diameter of the fuel (Figure 2.26). In this figure, the fuel diameter after mixing is given for a specific depth,  $H_C = v_{ft}$ , and the initial fuel diameter,  $D_{f0}$ . We also plot the fuel fluidization limit,  $D_{FR}$ , for different fuel temperatures assuming black body radiation. All the fuel diameters after mixing to the left of the fluidization limit for a given fuel temperature can mix, while those mixing diameters to the right of the limit for a given  $H_C$  and  $D_{f0}$  will begin to fluidize. Notice that as  $H_C$  increases, the minimum diameter for mixing (given by the intersection of a fuel-mixing diameter curve and the fluidization limit for a given fuel temperature) increases significantly.



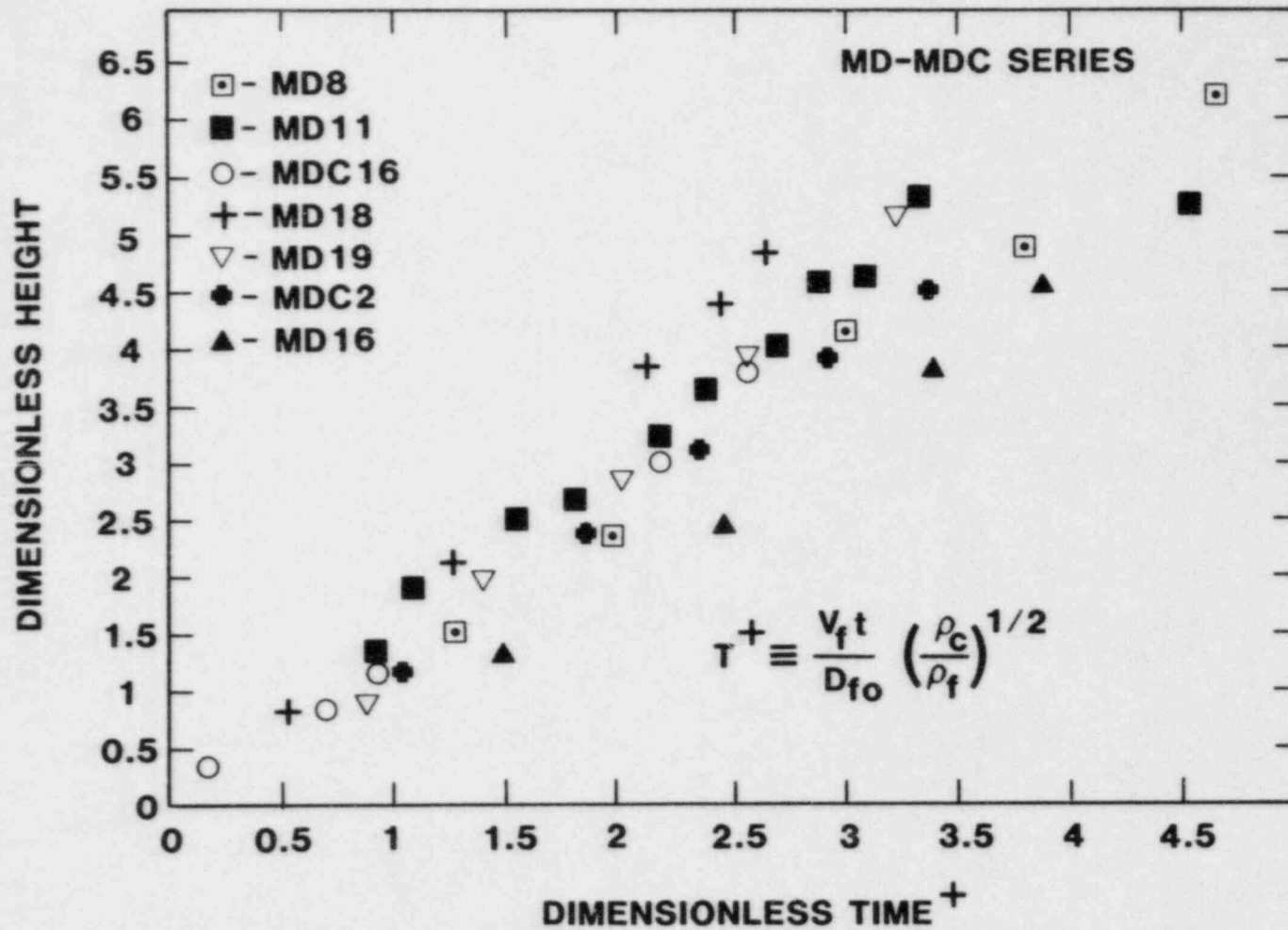


Figure 2.23. Dimensionless Height (Mixture Height/Fuel Diameter) Correlated as Function of Derived Dimensionless Time,  $T^+$

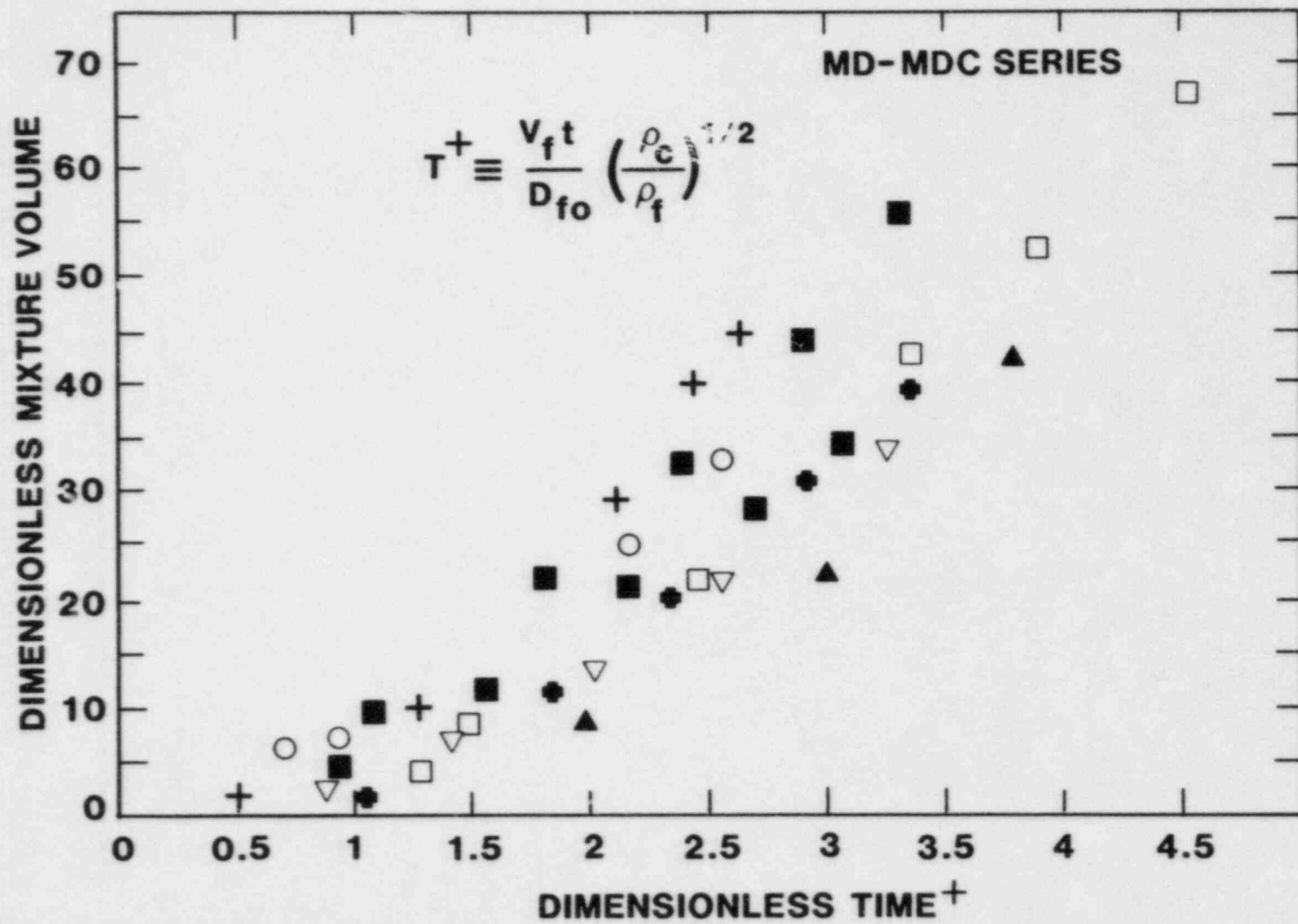


Figure 2.24. Dimensionless Mixture Volume (Mixture Volume/Fuel Volume) Correlated as Function of Dimensionless Time,  $T^+$

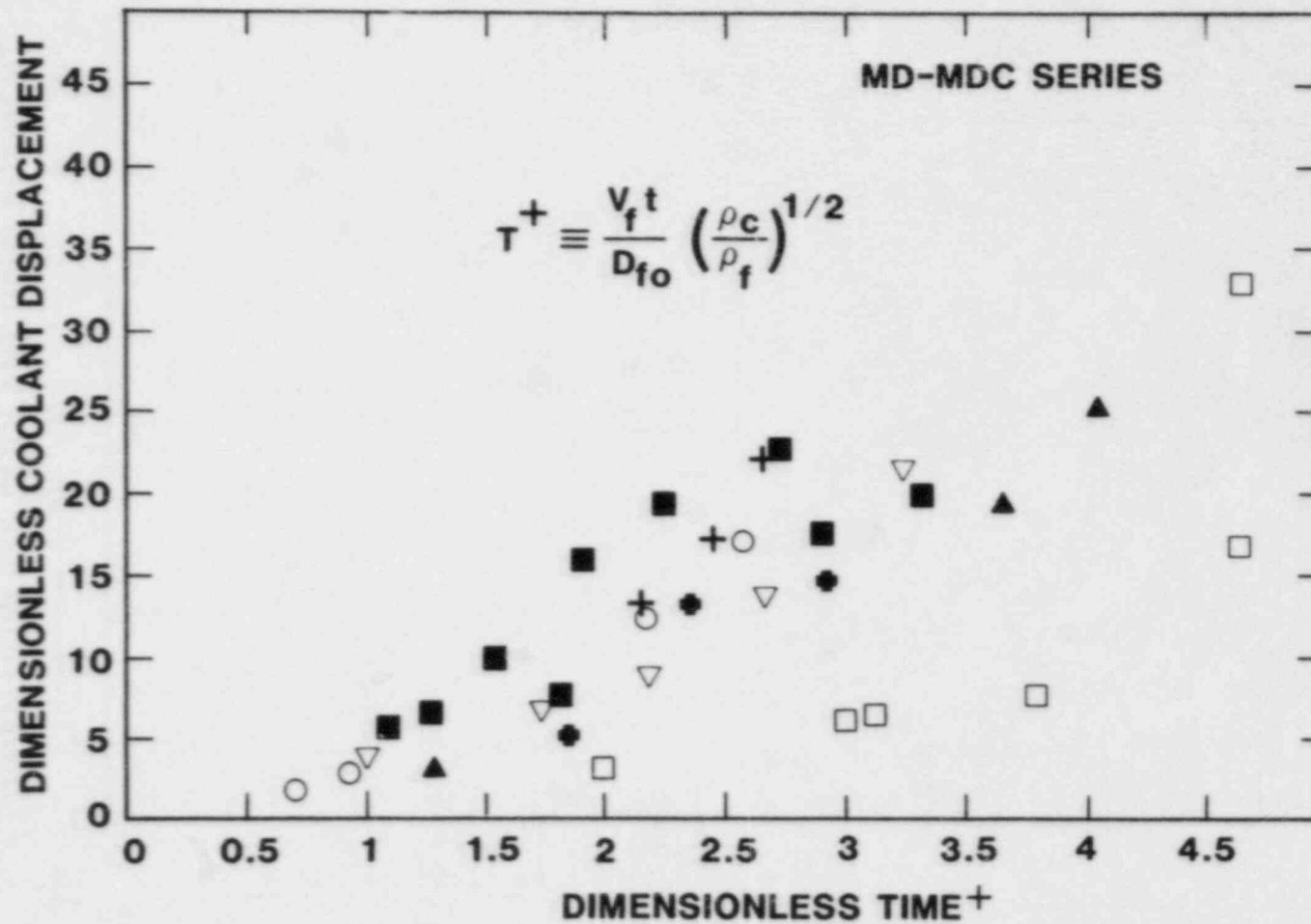


Figure 2.25. Dimensionless Coolant Displacement (Coolant Volume Displaced/Fuel Volume) Correlated as Function of Dimensionless Time,  $T^+$

## FUEL-COOLANT MIXING

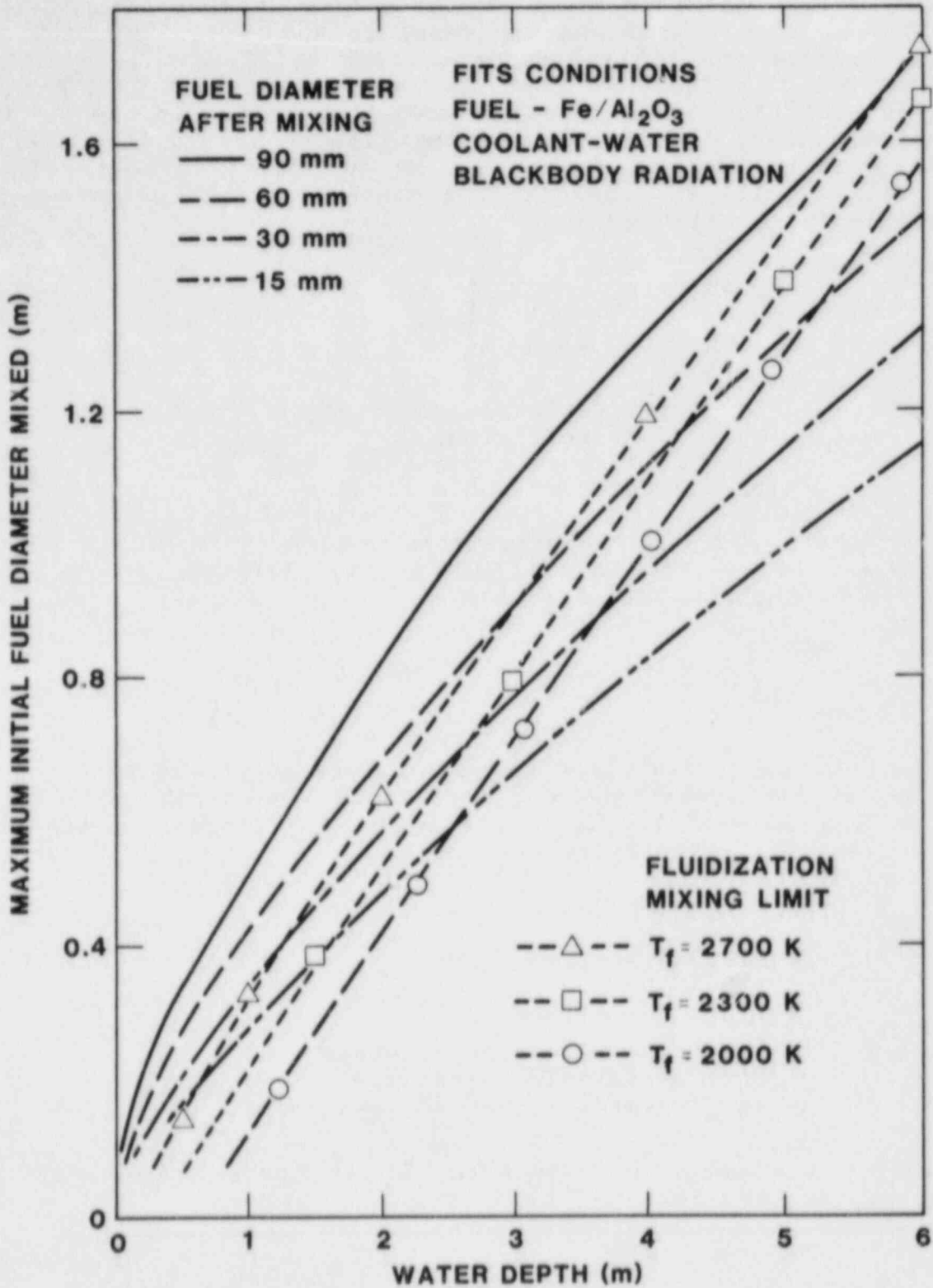


Figure 2.26. Limits to Mixing as Function of Water Depth, Fuel Temperature, and Final Particle Size

Consider the conceptual picture advanced by Henry where the fuel/coolant mixture occupies the entire chamber volume (both cross-sectional area and the depth to the base). We now want to estimate the minimum diameter of fuel given a total fuel mass (or conversely maximum fuel mass given some fuel-mixing diameter) that could co-exist with the coolant in the mixture volume before fluidization of the liquids begins (i.e., water fluidization due to steam outflow and water inflow). The local velocity for fluidization of the coolant is given by a simple force balance,

$$v_{FL} = \left[ \frac{4}{3} \frac{gD_c}{C_D} \left( \frac{\rho_c - \rho_v}{\rho_v} \right) \right]^{1/2} \quad (2.1)$$

where  $g$  = gravitational acceleration  
 $C_D$  = drag coefficient  
 $\rho_c$  = density of coolant liquid  
 $\rho_v$  = density of coolant vapor

The term  $D_c$  is the characteristic length scale of the coolant and is related to the fuel-mixing diameter,  $D_f$ , by the ratio of their volume fractions,

$$D_c = D_f \left( \frac{\alpha_c}{\alpha_f} \right)^{1/3} \quad (2.2)$$

Now this local fluidization velocity is generated by the outflow of the steam from the fuel/coolant mixture; therefore, the outflow velocity will be a maximum at the top of the mixture where all the steam must exit,

$$v_{FL} = \frac{\dot{m}_v}{\rho_v A_{CHAM} \alpha_v} \quad (2.3)$$

where  $\dot{m}_v$  = mass flow rate of steam  
 $\alpha_v$  = steam volume fraction  
 $A_{CHAM}$  = chamber cross-sectional area

Now if the water is saturated,  $\dot{m}_v$  is found by a simple energy balance to be

$$\dot{m}_v = \frac{Q_f}{i_{fg}} \quad (2.4)$$

where

$$Q_f = A_f q_f'' \quad (2.5)$$

$$A_f = 6m_f / \rho_f D_f \quad (2.6)$$

$$q_f'' = (h_{rad}) + (h_{film})(T_f - T_{sat_c}) \quad (2.7)$$

and

- $i_{fg}$  = latent heat of vaporization
- $m_f$  = fuel mass
- $\rho_f$  = fuel density
- $h_{rad}$  = radiative heat-transfer coefficient
- $h_{film}$  = film-boiling heat-transfer coefficient
- $T_f$  = fuel temperature
- $T_{sat_c}$  = coolant temperature

One can combine equations 2.1 through 2.7 and solve for the minimum fuel-mixing diameter given a fuel mass, or the maximum fuel mass given some mixing diameter. The results are

$$D_{f_{min}} = \left( \frac{6m_f}{\rho_f A_{CHAM}} \right)^{2/3} \left( \frac{q_f''}{\rho_v \alpha_v i_{fg} g^{1/2}} \right)^{2/3} \left( \frac{\alpha_f}{\alpha_c} \right)^{1/9} \left( \frac{\rho_v}{\rho_c - \rho_v} \right)^{1/3} \left( \frac{3}{4} C_D \right)^{1/3} \quad (2.8)$$

$$m_{f_{max}} = (g D_f)^{1/2} \left( \frac{\rho_v \alpha_v i_{fg}}{q_f''} \right) \left( \frac{\rho_f D_f A_{CHAM}}{6} \right) \left( \frac{\rho_c - \rho_v}{\rho_v} \right)^{1/2} \left( \frac{\alpha_c}{\alpha_f} \right)^{1/6} \left( \frac{4}{3 C_D} \right)^{1/2} \quad (2.9)$$

Using this simple model based on Henry's own criteria, one can estimate the maximum fuel that can mix. For the conditions previously stated, one finds for a saturated water depth of 3 m and ambient pressure in a PWR vessel approximately 3000 kg of fuel can mix to a size of 20 mm. This is in good agreement with the other mixing limits discussed.

### 2.3.1.2 FITS Analysis

The mixing that occurs before the explosion is triggered should have an effect on the subsequent explosion. If ample time is given for the fuel to break up into smaller diameter droplets and disperse in the liquid coolant pool, more of the fuel mass will be able to fragment rapidly during the explosion into fine debris; this, in turn, will probably increase

the explosion conversion ratio (ratio of the measured kinetic energy to the initial fuel thermal energy). This is empirically demonstrated for the FITS experiments if one plots the explosion conversion ratio,  $\eta_{KE}$ , and the fuel-debris diameter as a function of the initial coolant-to-fuel mass ratio (Figure 2.27). In these experiments, the fuel is dropped into the water as a coherent mass and triggers after mixing in the available water mass. Notice that the conversion ratio rises to almost a constant value (1% to 2%) after the fuel-to-coolant mass ratio increases above 3 to 1. In contrast, the average fuel-debris diameter continues to decrease in magnitude until the mass ratio becomes very large (20 to 1).

The same effect can be better observed if one plots the debris diameter and the conversion ratio as a function of the ratio of the fuel/coolant mixture volumes at the time of the explosion to the original fuel volume,  $V_m/V_f$ . The reasoning here is that as the mixture-to-fuel volume ratio increases, the fuel has more time to disperse in the coolant, break up into smaller sizes, and produce a more efficient explosion. Figure 2.28 indicates even more clearly the strong correlation of the explosion fuel-debris size to initial mixing behavior. Again, note how the conversion ratio quickly rises to nearly constant values.

It is interesting to note that even when the fuel debris seems relatively coarse (~1 mm as in the FITS B series), the conversion ratio is still large, 1% to 2%. This suggests that the percentage of fuel "participating" in the explosion cannot be arbitrarily taken to be small (e.g., based on a thermal equilibration time during the explosion one might estimate a diameter of 200  $\mu$ m). Rather, even the "coarse" fuel debris probably participates in the explosion to the extent that it can transfer the thermal energy of its outer surface quickly and therefore can affect the explosion conversion ratio. These data suggest one must be careful when trying to distinguish between what fuel "mixed" with water and what fuel "participated" in the explosion. This is further illustrated if one computes the "Sauter-mean" diameter for the debris. This diameter is a more accurate average value to characterize the surface-area-to-volume ratio of debris size distribution.[11]

In all the FITS experiments where any FCIs occurred, the quasi-steady pressurization of the FITS chamber atmosphere occurred in just a few seconds after fuel-melt entry. This suggests that the FCI quickly quenched the fuel in the surrounding water. This quasi-steady pressure then decreased at later times because of condensation on the cold FITS chamber steel walls. In contrast to this, when the fuel simply fell through the water without any FCI and reagglomerated on the chamber base as a coherent mass (FITS G experiments), the quasi-steady peak pressure rise took tens of seconds. This

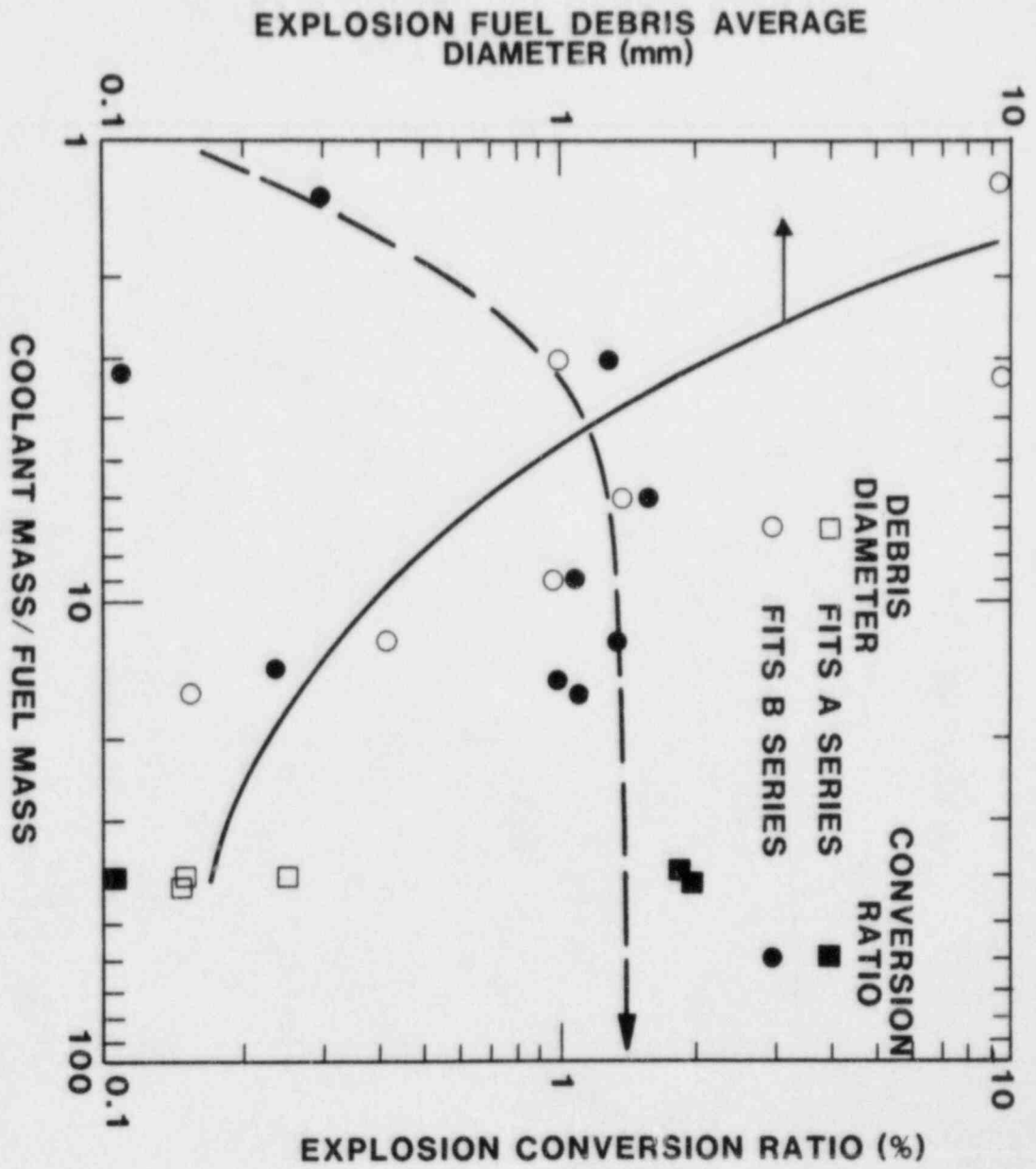


Figure 2.27. Explosion Conversion Ratio ( $KE/E_f$ ) and Fuel-Debris Diameter as Functions of Coolant-to-Fuel Mass Ratio



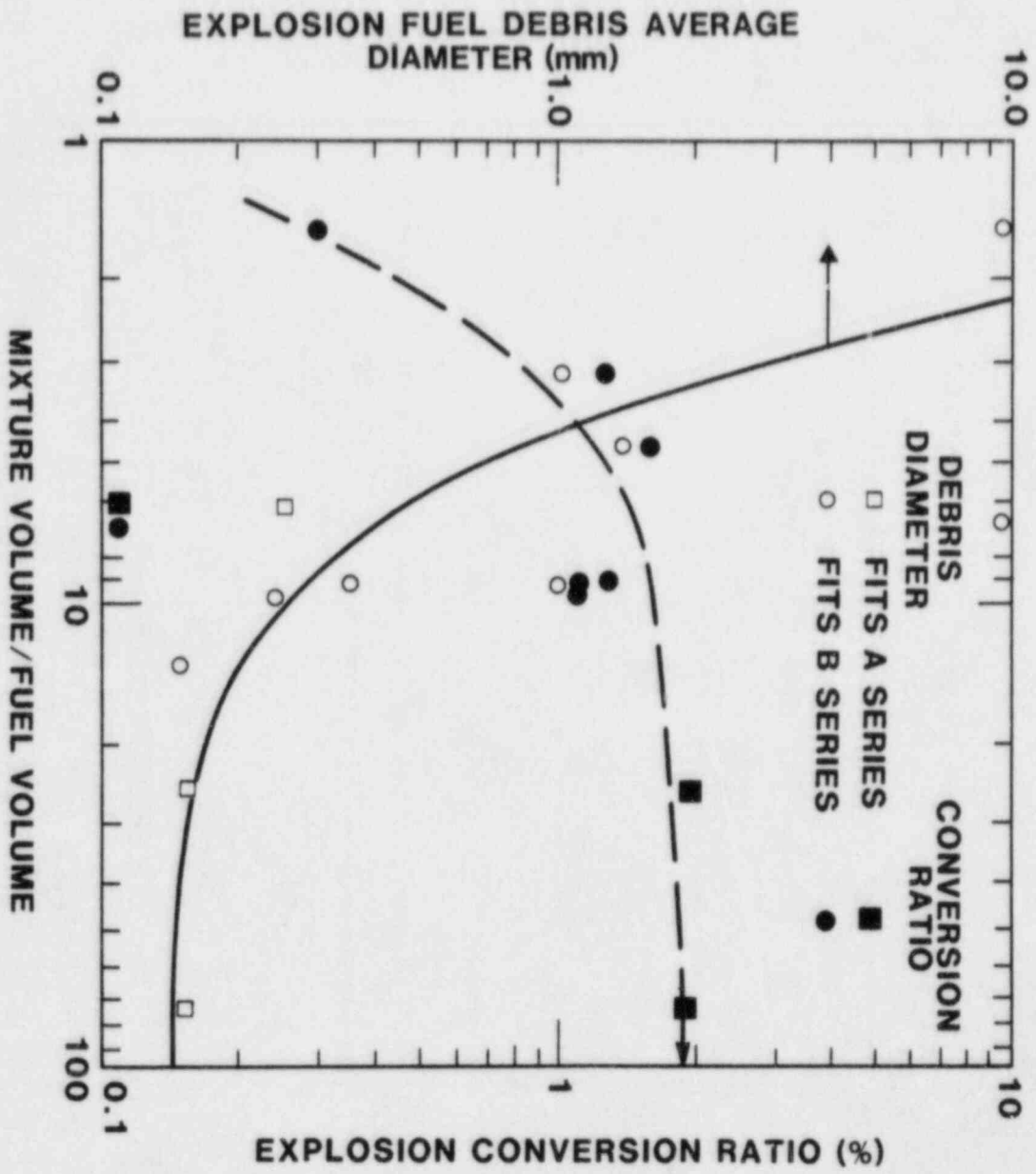


Figure 2.28. Explosion Conversion Ratio (KE/E<sub>f</sub>) and Fuel-Debris Diameter as Functions of Mixture-to-Fuel Volume Ratio

indicates the fuel quench occurred over much longer times in a stratified geometry (water above fuel), allowing more time for condensation losses to a cold wall to affect the peak pressure. Figure 2.29 illustrates the quasi-steady pressure rise in the FITS chamber plotted as a function of the mass ratio of coolant to fuel (the reference pressure is one atmosphere). One notes that the FITS pressure data decrease as the mass ratio increases. One can explain this behavior by looking at upper and lower bounds on the pressure in the FITS chamber that would be calculated by considering the FCI. The upper limit on the figure for saturated and subcooled water is arrived at by looking for the maximum amount of coolant that could be vaporized by the fuel quench without heat loss to surrounding subcooled water and cold walls. For a given fuel mass (~5 kg for FITS A, ~20 kg for FITS B&G), this limit is independent of the mass ratio. The lower limit line is arrived at by calculating the amount of coolant that could be vaporized after all the available coolant is heated up to the saturation temperature at the chamber pressure. Notice that because most of these FITS experiments are highly subcooled ( $\Delta T_{\text{sub}} \sim 75^\circ\text{C}$ ), no vaporization or pressure rise would occur for a mass ratio greater than about 8.5. This calculated curve follows the water-lean data fairly well, while at higher mass ratios, the measured pressure rise is nonzero compared to the predicted value. Finally, we correct the lower limit line for the effect of condensation on the FITS chamber cold walls by using the Uchida and Tagami condensation correlations to give a range of values.

We conclude that, as the fuel quenches, it participates with the cold water in the vicinity of the interaction. For reactor-scale conditions, the overall mass ratio is near one, and the water can be saturated; therefore, it does appear that the FCI can have a large effect on the integral steam generation rate and "steam spike" phenomena.

## 2.3.2 Triggering

### 2.3.2.1 Dynamics of Vapor-Film Growth

The purpose of this study is to investigate the effect of initial conditions and modeling assumptions on the dynamics of a coolant-vapor film surrounding a molten-fuel drop. Once this study is complete, we plan to use this model to conduct film-collapse calculations for Nelson's test conditions. We also can use this model for investigating the effect of film collapse for a collection of fuel droplets in coolant.

In formulating the model for film boiling around a fuel droplet, the following assumptions were made

- (1) The fuel/coolant system is spherically symmetric with the fuel droplet surrounded by a vapor film in a large volume of coolant (Figure 2.30).

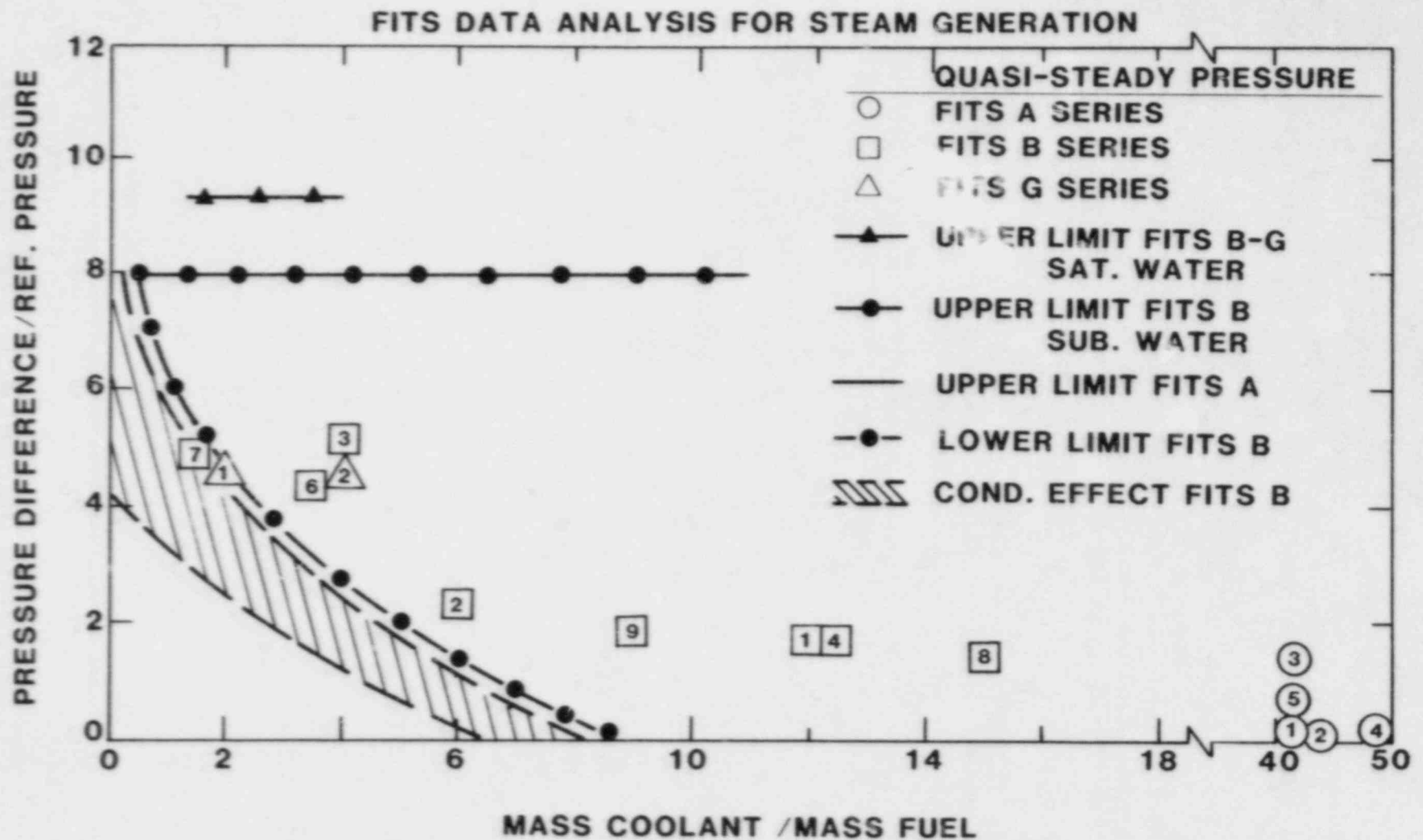


Figure 2.29. Quasi-Steady Pressure Rise as Function of Coolant-to-Fuel Mass Ratio

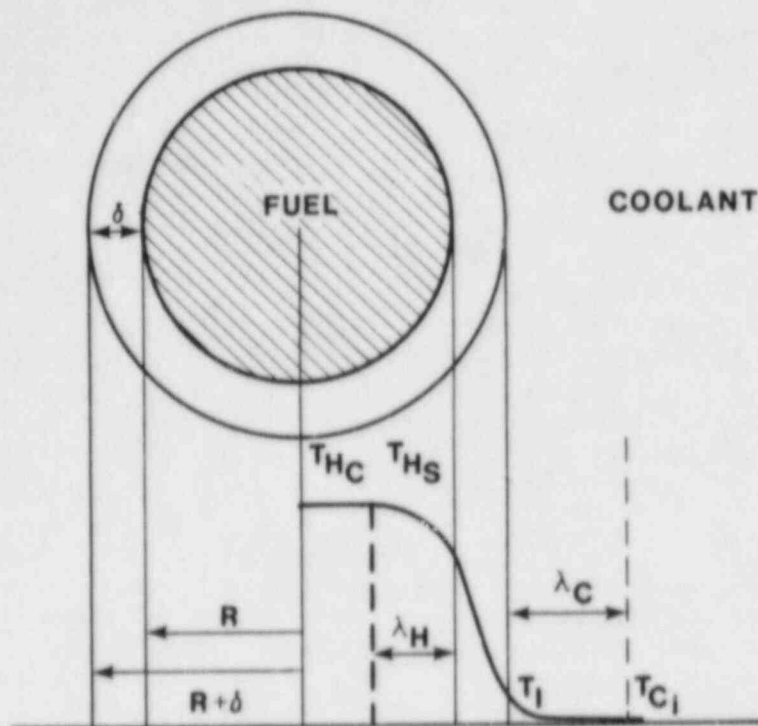


Figure 2.30. Schematic of Dynamic Film Model

- (2) All the vapor generated is retained in the film during film growth.
- (3) Initially a small gaseous film exists at the surface of the fuel.
- (4) The pressure in the film is spatially uniform.
- (5) The coolant liquid and the vapor are in thermodynamic equilibrium at the film/liquid interface.
- (6) Energy is transferred across the film by conduction and radiation.
- (7) The coolant vapor in the film is treated as a perfect gas.
- (8) The liquid coolant is considered to be incompressible.
- (9) The physical properties are considered to be constant with temperature.

These assumptions were used previously by Corradini and Kazimi in their studies of vapor-film growth.[13,14] Assumptions 7 through 9 have been investigated by including a detailed equation of state for water and fuel. The results were not significantly different from what is presented here.

The fuel/coolant system was modeled as three control volumes conserving mass and energy. This resulted in a number of simultaneous first-order differential equations. These equations were numerically solved using a one-step Runge-Kutta integration. The advantage of this method was that an estimate of the truncation error was made that allowed for an automatic step-size adjustment.

The model has been applied to a molten-fuel drop immersed in a water pool. The values of the initial conditions are those used in the base-line experiments of Nelson at Sandia.[15] In all cases of interest, the fuel drop is surrounded by a vapor film that oscillates as it grows. The oscillatory growth depends on the initial conditions during the interaction. The effects of these initial conditions are discussed below.

Effect of the Molten-Fuel Radius: The results shown in Figure 2.31 indicate that, with an increase of the initial sphere radius, the vapor-pressure oscillation has a larger amplitude with a decreased frequency. This result is directly related to the spherical-momentum equation in which the acceleration is inversely proportional to the fuel radius (i.e., changes in the inertia).

Effect on Initial Film Thickness: The initial film thickness has a significant effect on the pressure oscillations. A larger initial film thickness was found to diminish the pressure oscillation. This effect is due to the lower initial heat-transfer rate across the film that results in a reduced initial pressure pulse, as shown in Figures 2.32 and 2.33.

Effect on Molten-Fuel Temperature: The effect of a higher fuel temperature was found to be qualitatively similar to that of a larger fuel radius, i.e., a larger amplitude but a decreased frequency of the film-pressure oscillation, primarily due to the higher coolant evaporation rate, as shown in Figure 2.34.

Effect of Ambient Pressure: Figure 2.35 shows that a higher ambient pressure results in a larger and more oscillatory pressure behavior after a delay time. This result is due to the increased stiffness of the vapor film caused by the higher gas density, and ambient pressure.

Effect of Coolant Temperature: The first pressure pulse is higher for smaller subcooling because of the larger coolant vaporization rate. But the amplitude of the oscillating pressure is quickly damped out for decreased water subcooling (Figures 2.36 and 2.37).

Combined Effect of Temperature and Pressure of Coolant: Figure 2.38 shows the pressure-time history of the film for a constant water subcooling of 70 K. Even though the ambient

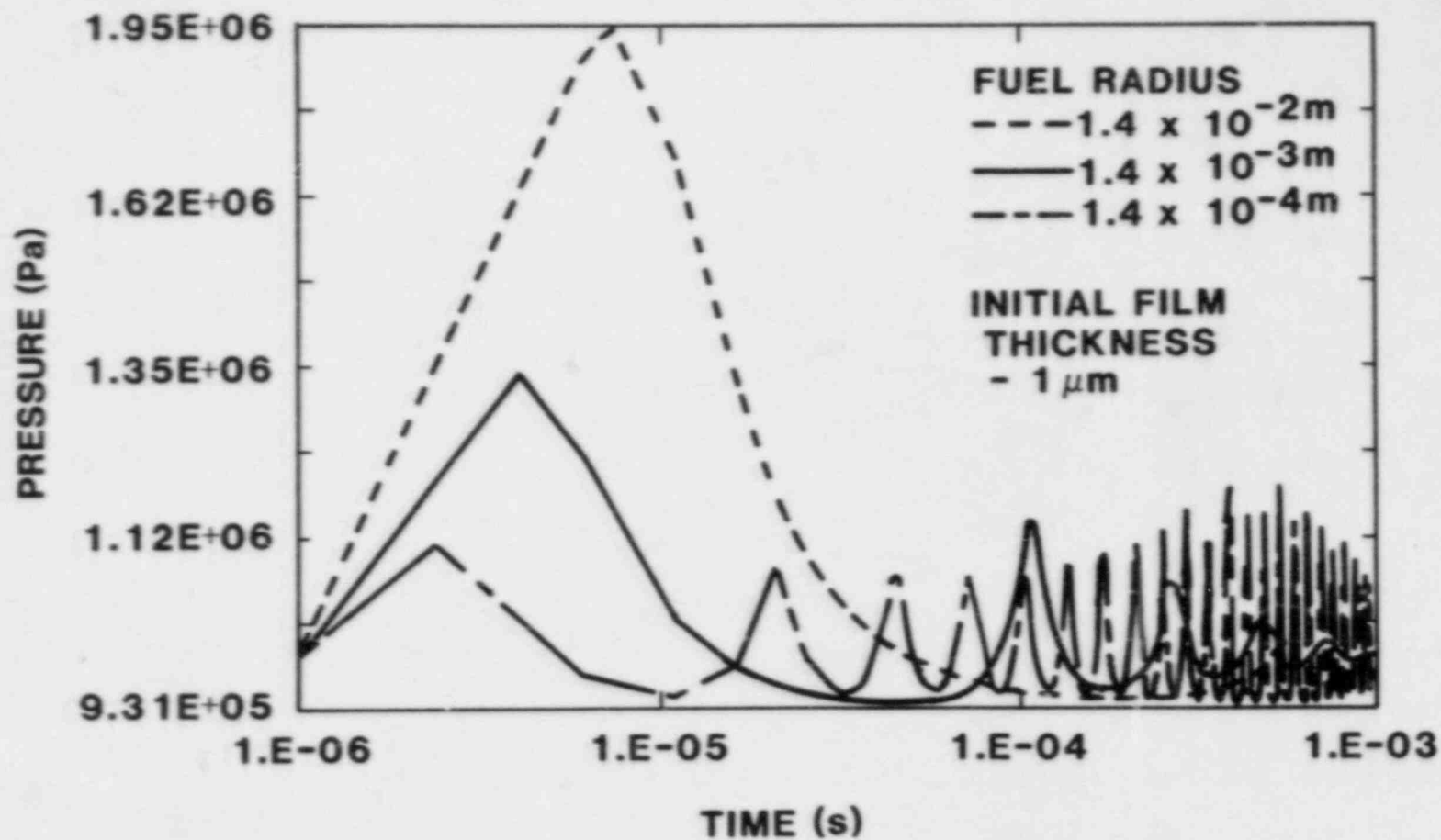


Figure 2.31. Effect of Molten-Fuel Diameter on Vapor Film Pressure.

Nominal initial conditions are from Nelson's test data:  
 Iron-oxide fuel, fuel temp. = 2233 K, water temp. 300 K, fuel  
 radius = 1.4 mm, ambient pressure = 0.1 MPa.

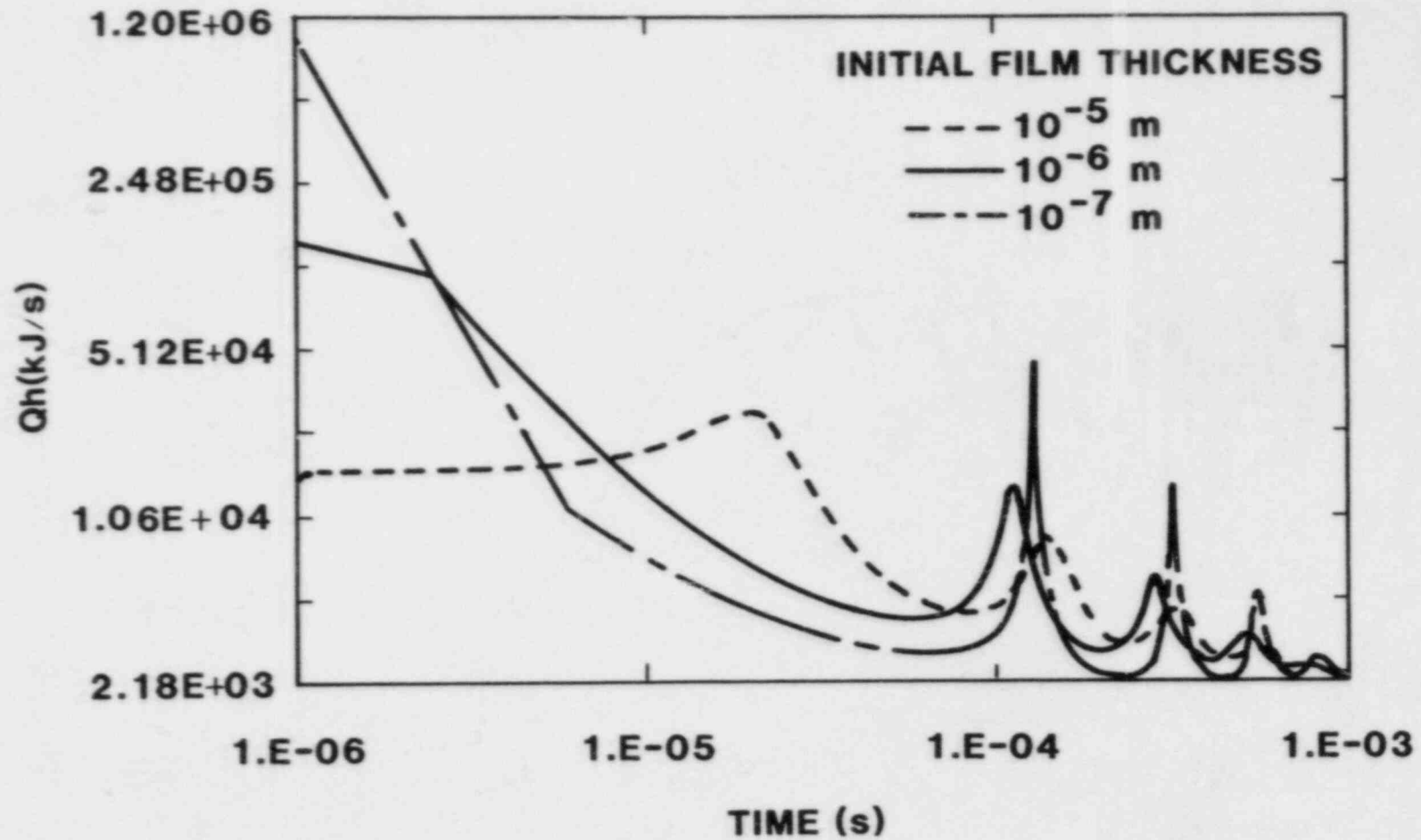


Figure 2.32. Effect of Initial Film Thickness on Heat-Transfer Rate

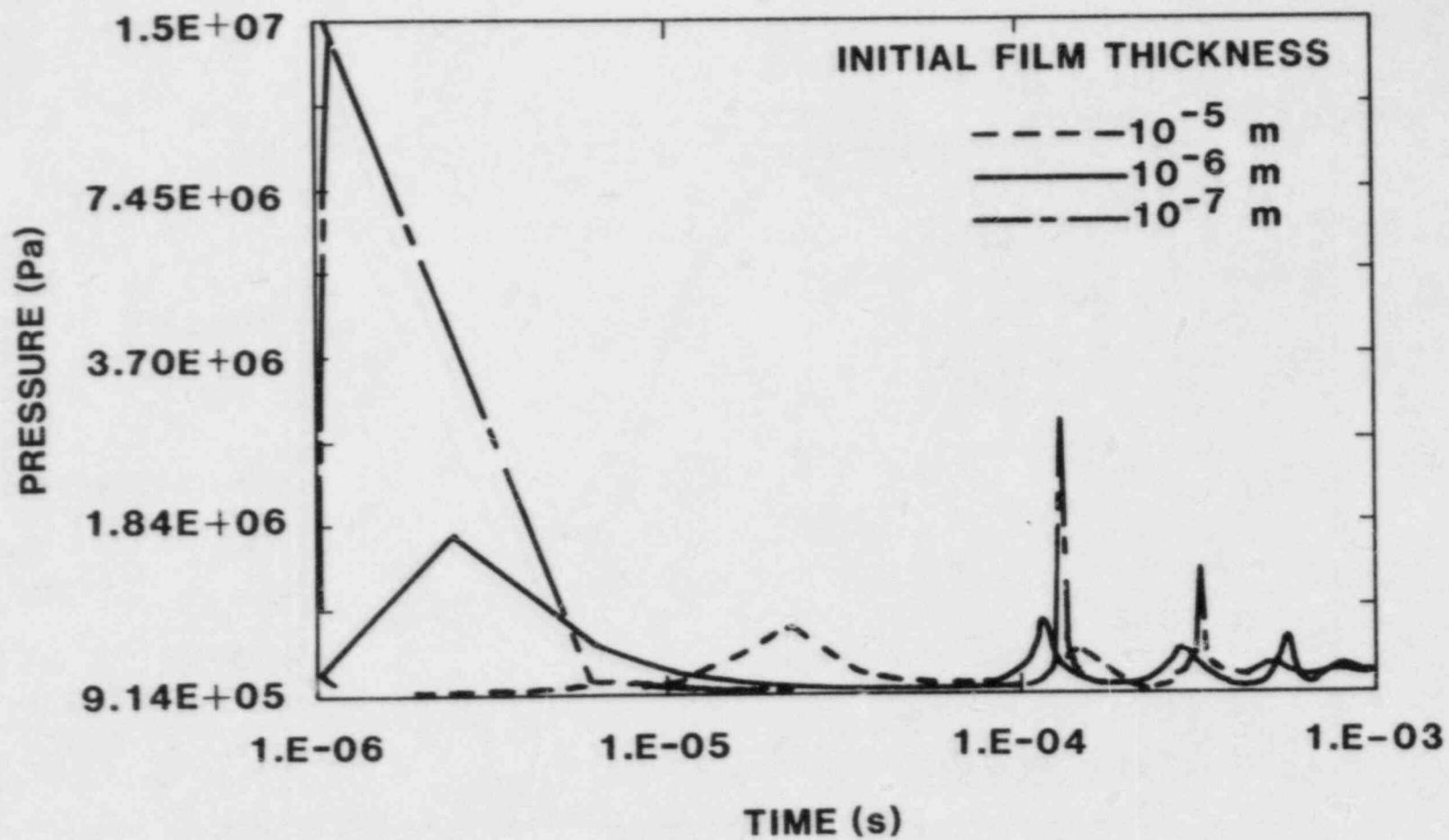


Figure 2.33. Effect of Initial Film Thickness on Vapor-Film Pressure



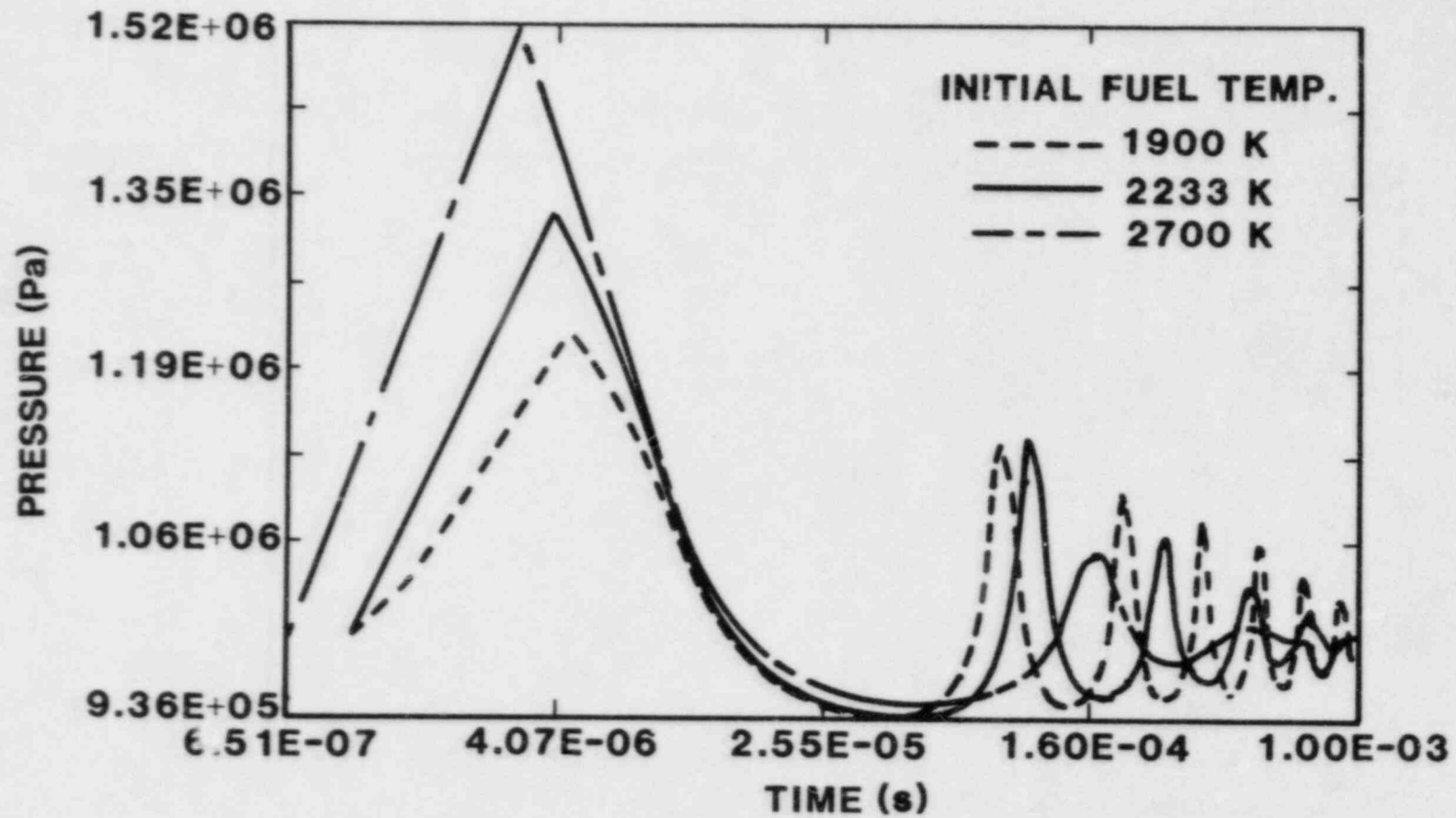


Figure 2.34. Effect of Molten-Fuel Temperature on Vapor-Film Pressure

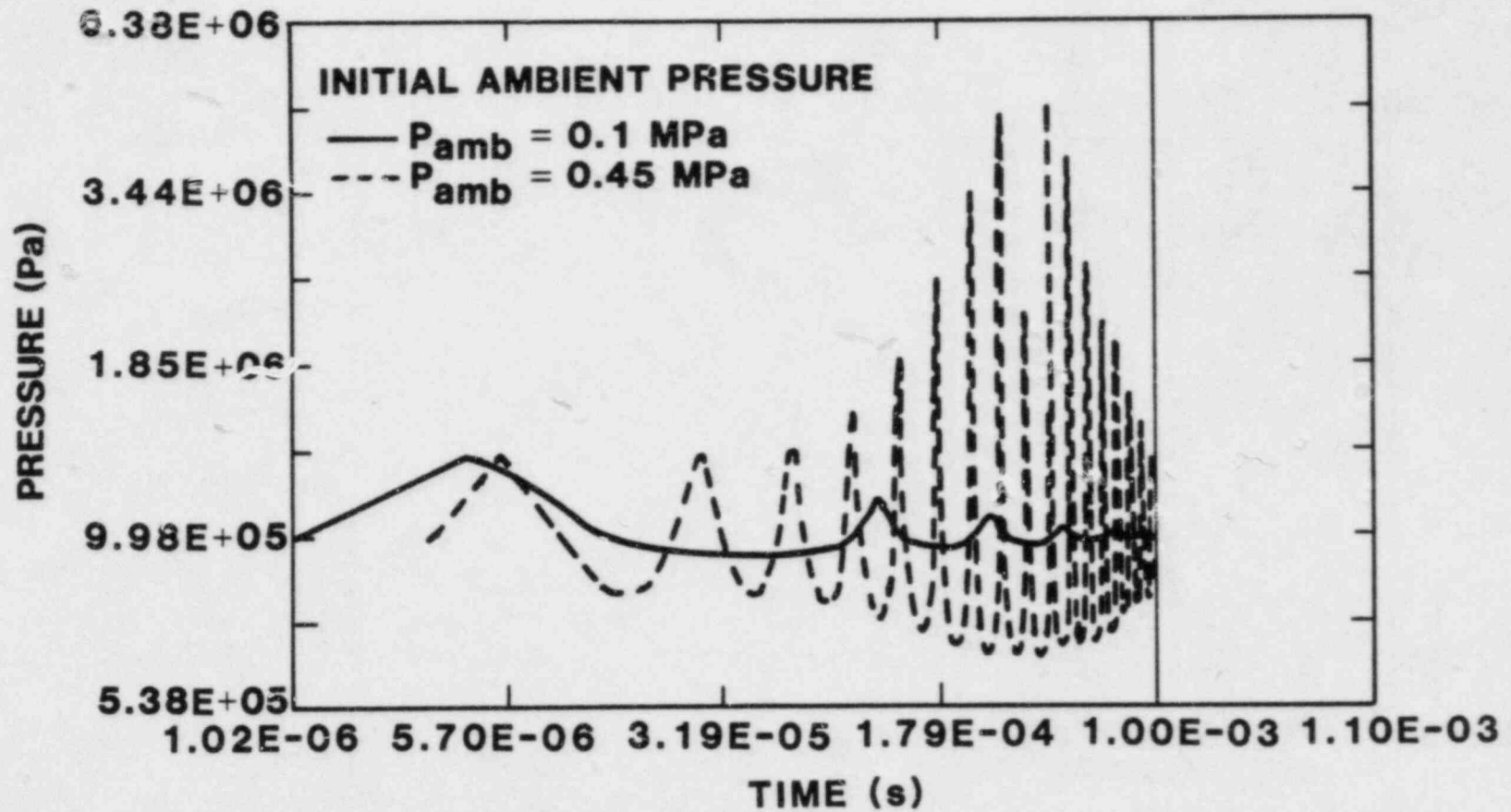


Figure 2.35. Effect of Initial Ambient Pressure on Vapor-Film Pressure

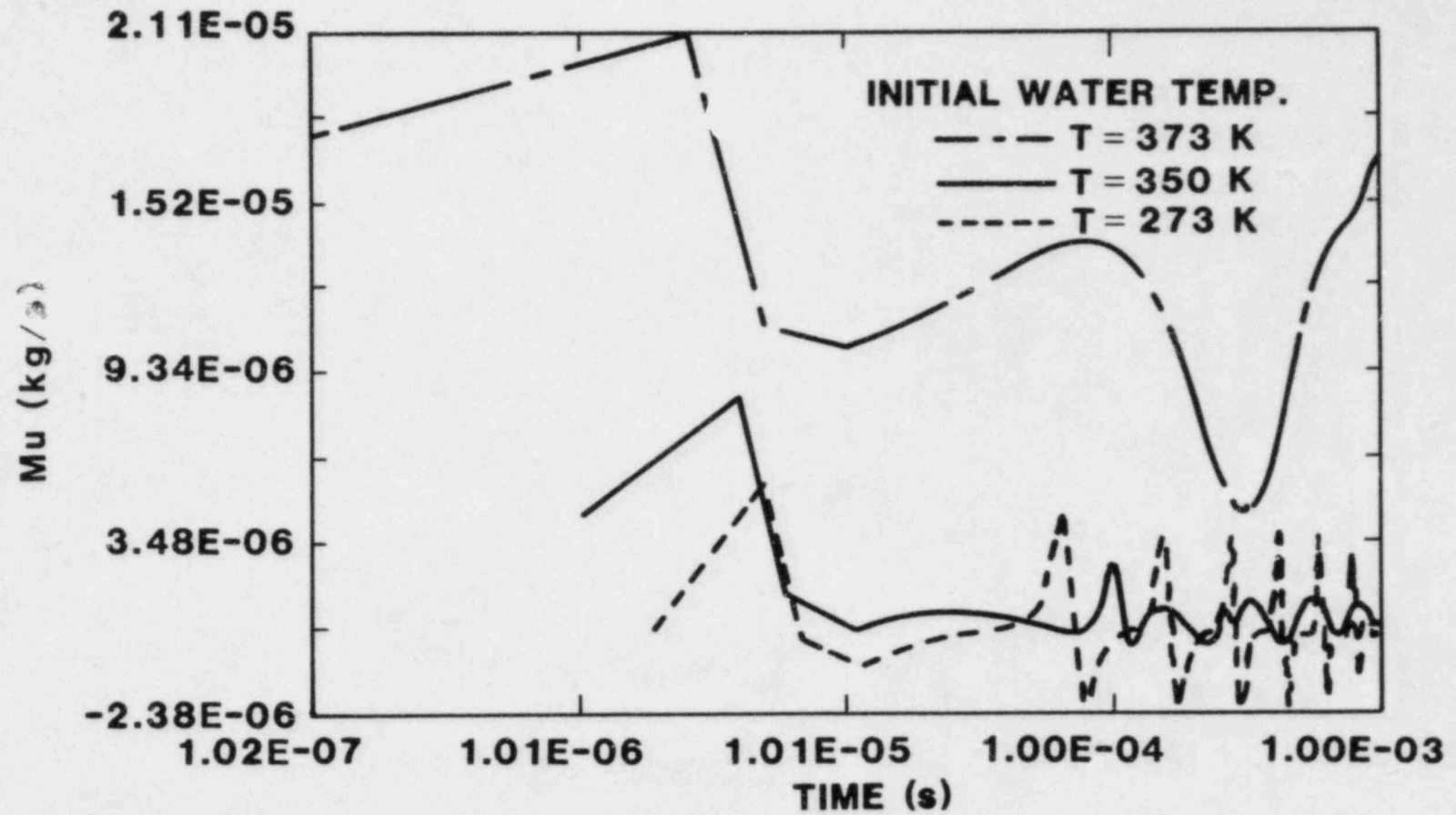


Figure 2.36. Effect of Coolant Temperature on Evaporation Rate

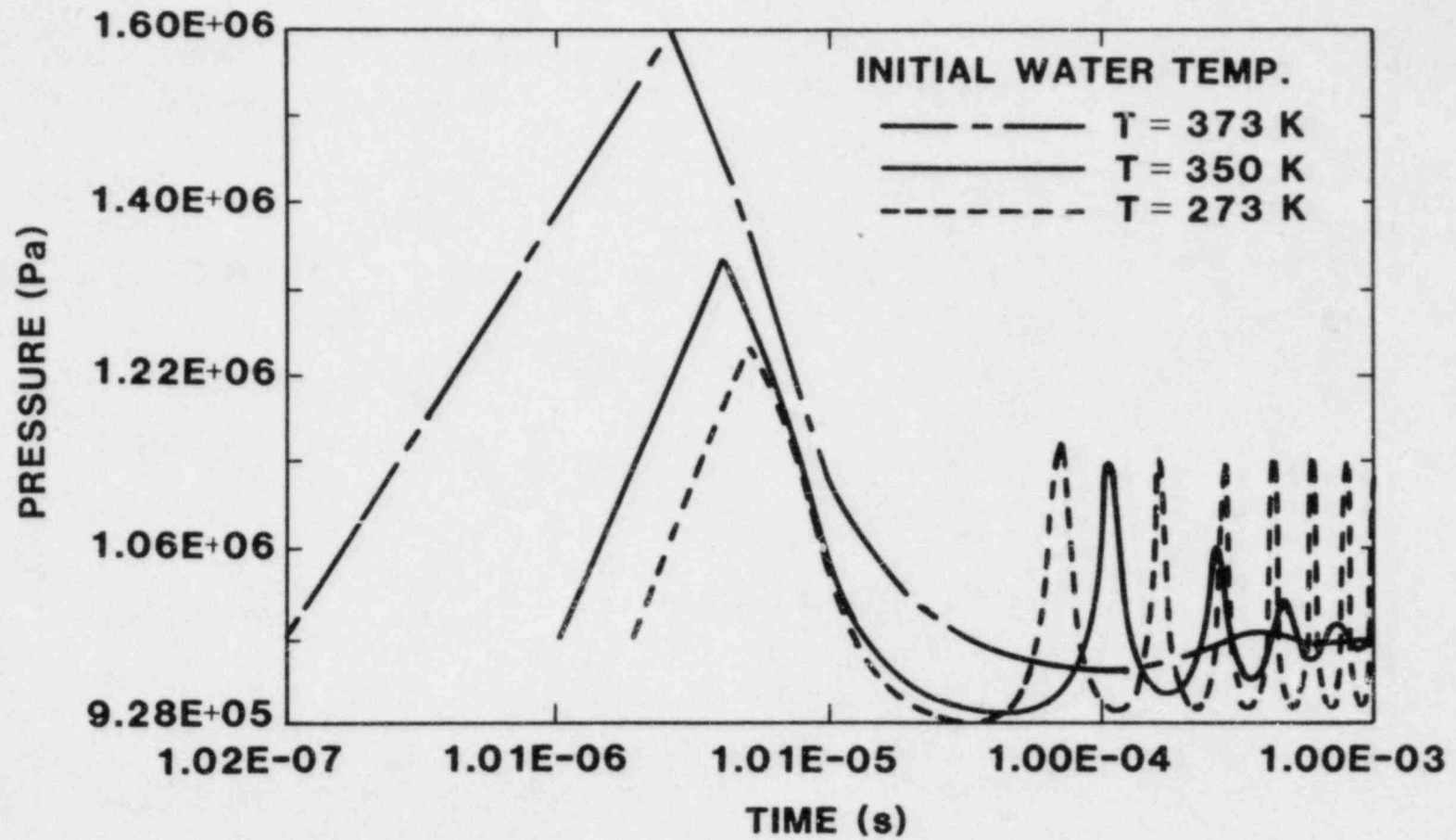


Figure 2.37. Effect of Coolant Temperature on Vapor-Film Pressure

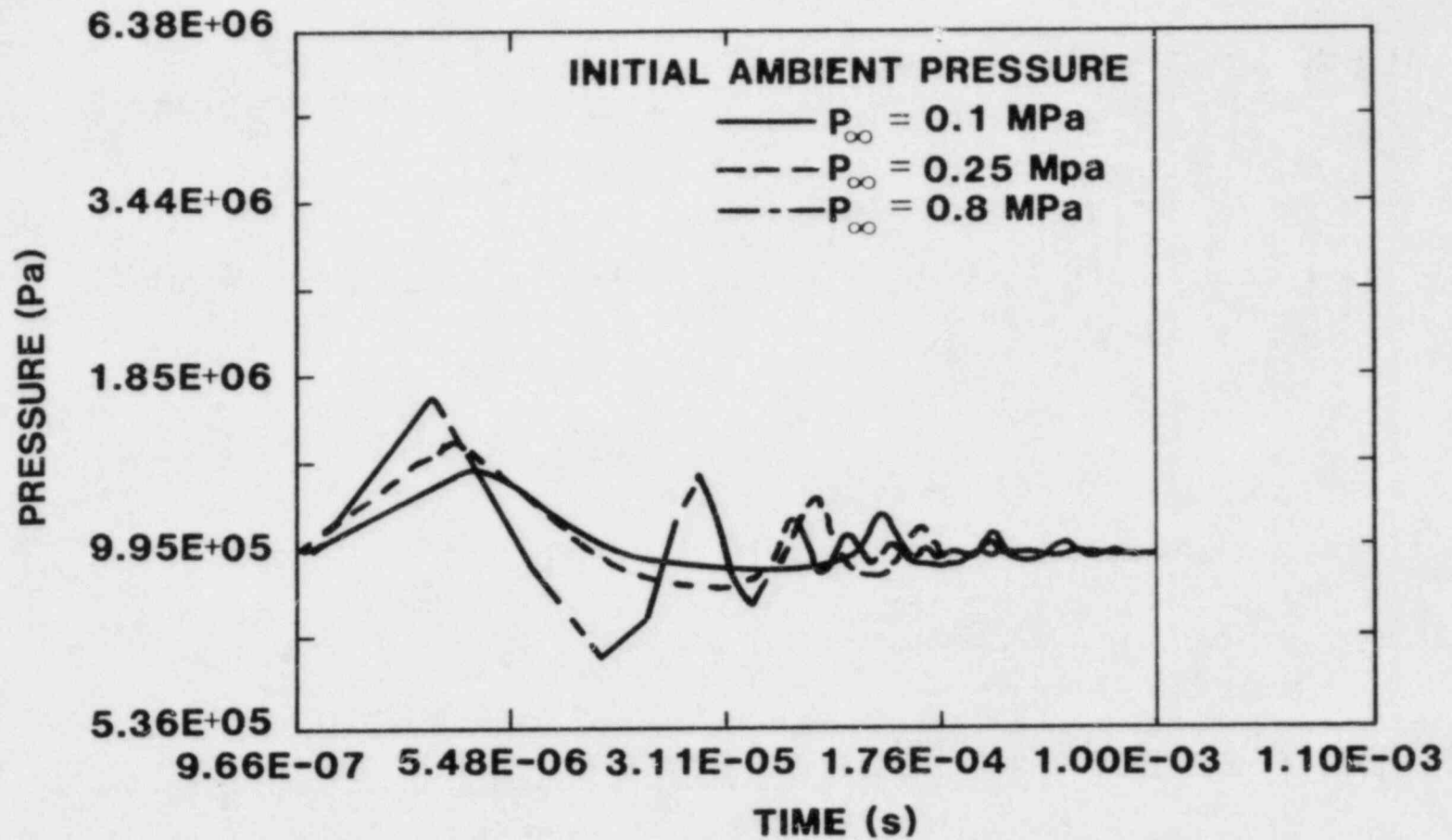


Figure 2.38. Effect of Constant Subcooling on Vapor-Film Pressure

pressure is higher, the amplitude of the pressure pulse is initially higher and quickly damps out. This suggests that constant subcooling allows for more coolant vaporization even at higher ambient pressures, compensating for the increased stiffness of the film due to the increased ambient pressure.

### 2.3.2.2 Conceptual Picture of Explosion Triggering and Molten-Fuel Fragmentation

During the cycle of vapor film growth and subsequent collapse around the fuel droplet, the coolant vapor-liquid interface undergoes repeated acceleration toward the fuel and then, toward the coolant liquid. Once the acceleration is directed outward toward the coolant liquid, the interface distorts due to a Rayleigh-Taylor instability. The growth of the instability can be estimated by using linear analysis.

$$\eta/\eta_0 = \cosh (nt) \quad (2.10)$$

$$\text{where } n = \left( \frac{2\pi}{\lambda_m} \frac{a(\rho_c - \rho_v)}{\rho_c + \rho_v} \right)^{1/2} \quad (2.11)$$

and  $\eta/\eta_0$  = ratio of instability amplitude to initial amplitude

- $\lambda_m$  = wavelength
- $a$  = acceleration
- $\rho_c$  = density of coolant liquid
- $\rho_v$  = density of coolant vapor

This representation of the instability is valid for  $\eta \leq \lambda$ .

Coolant liquid-fuel contact would occur during film collapse when the acceleration is large enough to cause the distorted vapor-liquid interface to traverse the film thickness,  $\delta$ ; this would most likely occur when the film thickness is at a minimum. The time required to have a fuel/coolant contact is given by

$$t = \frac{1}{n} \left[ \cosh^{-1} \left( \frac{\delta_{\min}}{\eta_0} \right) \right] \quad (2.12)$$

Also, it is quite possible for the coolant to continue to penetrate the fuel surface like a jet if the kinetic energy of the instability is larger than the inertia of the fuel (viscous and form drag). Since the acceleration is a direct function of vapor-film pressure, one can cause the penetration of the fuel surface by altering certain initial conditions such as ambient pressure, coolant temperature, etc. However, we cannot directly evaluate the exact nature of the jet because a direct link cannot be made between instability growth and film collapse due to the unknown  $\eta_0$  and  $\lambda_0$ .

The initial wavelength  $\lambda_0$  can only be bounded from Taylor's theory, and  $\eta_0$  is not known a priori.

Once a coolant jet of velocity  $U_c$  has been directed toward the fuel, the penetration velocity,  $U_p$ , is given by a simple momentum balance as

$$U_p = \frac{U_c}{\frac{\rho_f}{\gamma_e \rho_c} + 1} \quad (2.13)$$

where  $\gamma_e$  is a breakup factor to account for the change in the potential flow area of the coolant jet after penetration. The depth of penetration and the amount of radial dispersion of the jet would be a function of the size and kinetic energy of the coolant jet (length and diameter) and the ratio of the coolant density to the fuel density. Once jet penetration has occurred, the jet would break up into discrete masses, and this coolant liquid would now be entrapped within the fuel near its surface.

The behavior of these entrapped coolant droplets could be understood by applying the vapor-film dynamics model previously developed in a slightly modified geometry, i.e., coolant droplet surrounded by a vapor film in a continuum of fuel. Figures 2.39 to 2.41 show the results for a coolant droplet entrapped in iron-oxide fuel at atmospheric pressure. The coolant-droplet radius is estimated from film-collapse calculations of Nelson's test at Sandia. Notice that, for a constant ambient pressure, the film grows rapidly, and the coolant droplet rises to its saturation temperature exhibiting only modest pressures. For these conditions, it is not likely that the coolant droplet evaporates completely below the fuel surface; rather, in the middle of the vaporization and expansion process, the expansion of the vapor causes the "blowing-out" of the surrounding fuel and coolant liquid. This probably results in additional smaller fuel droplets dispersed in the coolant. Now the process would start again from the beginning of the intermixing. This cyclic behavior is qualitatively observed in Nelson's low-ambient-pressure, single-drop tests. We intend to continue this modeling as we analyze the single droplet experiments.

### 2.3.3 Explosion Phase -- A Parametric Model

One can conceptually subdivide an energetic FCI (steam explosion) into four phases of energy transfer:

- (1) Fuel/Coolant Mixing
- (2) Triggering
- (3) Propagation
- (4) Expansion

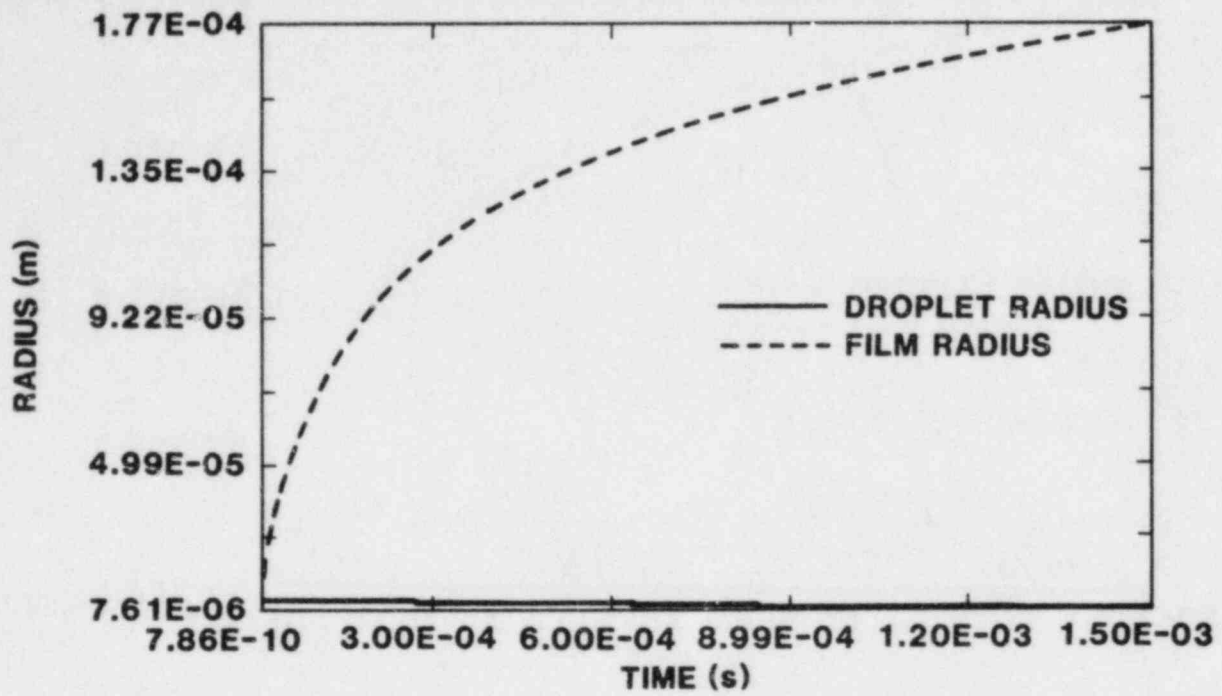


Figure 2.39. Radius History of Coolant Droplet in Fuel. Initial conditions similar to Nelson.

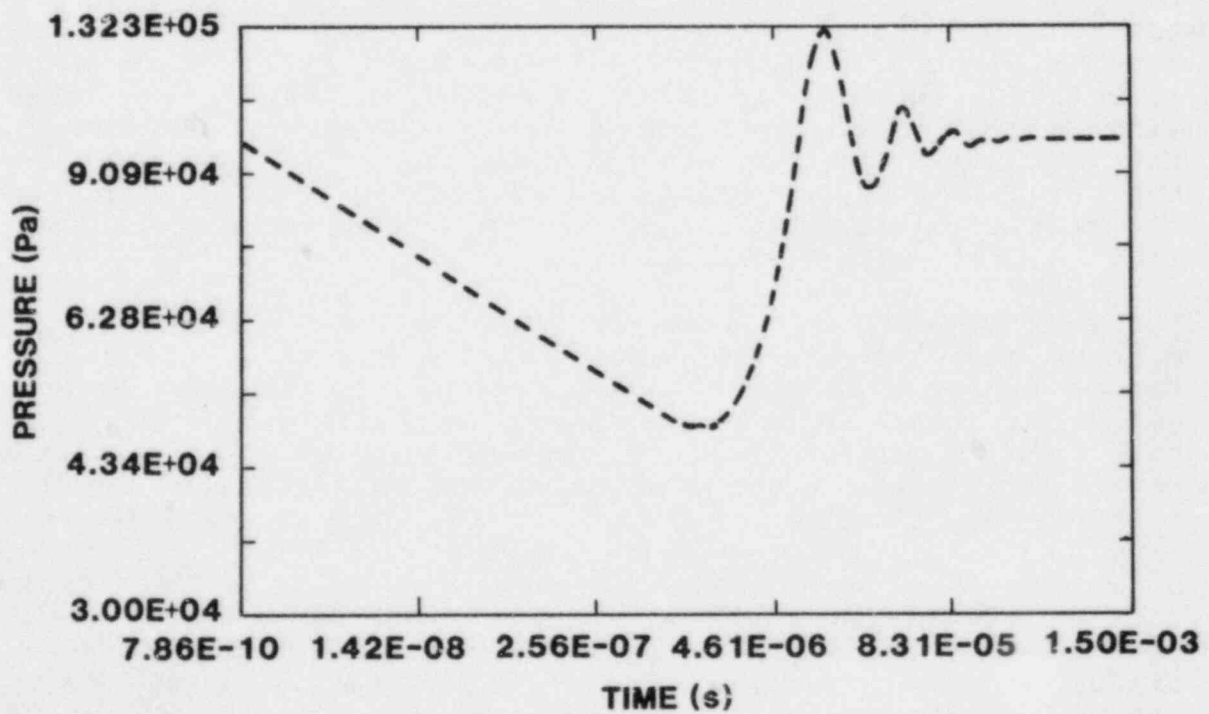


Figure 2.40. Pressure History of Vapor Film in Fuel



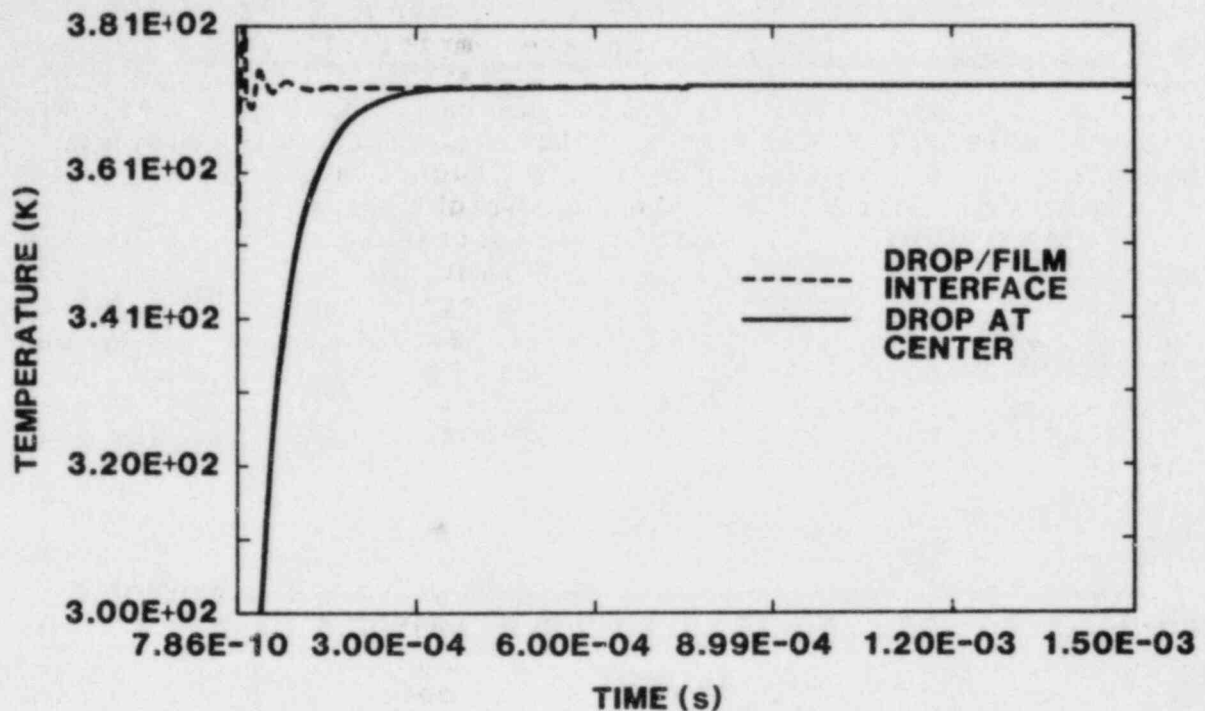


Figure 2.41. Temperature History of Coolant Droplet in Fuel

Fauske originally proposed that spontaneous nucleation upon contact of the hot and cold liquids is a necessary condition for the first three stages.[16] Board and Hall proposed the additional concept that a steam explosion during its propagation is analogous to a chemical detonation.[17] The contact temperature between the hot fuel and water coolant in an LWR exceeds the spontaneous nucleation temperature; therefore, the spontaneous nucleation criterion is satisfied for the LWR. This criterion represents the minimum temperature needed for stable liquid-liquid film boiling and assures the initiation of fuel/coolant mixing.

Earlier thermodynamic analyses were used to estimate the maximum theoretical explosion work that may cause structural damage or generate steam and hydrogen.[18] But the thermodynamic approach is a conservative upper limit and does not take into account any rate processes involved in the FCI that would limit the fuel or coolant masses participating or the rate of energy exchange (area or heat-transfer coefficient).

D. H. Cho et al developed a parametric model of FCI for LMFBR safety assessments that incorporates various limiting rate processes.[19,20,21] The rate processes (i.e., pressure history, coolant vapor produced, slug kinetic energy) were included in the model as input parameters for the parametric study of an FCI.

For the FITS experiments, the rate of fragmentation and the final debris-size distribution are empirically known from small and intermediate-scale experiments (e.g., Reference 22). Using these empirical data, we have developed a lumped-volume parametric model to predict the integral explosion behavior in an FCI for light-water reactor applications. It is similar in concept to the Cho-Wright parametric model. Our purpose in developing this parametric model is to assess which initial conditions are important in determining the explosion conversion ratio of fuel thermal energy to mechanical energy, steam generation and pressure history. Once we have accomplished this task we plan to use this model to develop a one-dimensional propagation model that will aid us in determining the proper input for more complex 2-D calculations.

### 2.3.3.1 Description of the Parametric Model

Suppose the molten fuel has fallen into the coolant and premixed to some specified diameter and volume fraction. If a steam explosion is triggered, the molten fuel rapidly fragments and transfers its energy to the coolant around the fuel particles within a short time ( $\ll 1$  s).

Consider the fuel fragmentation picture in Figure 2.42:

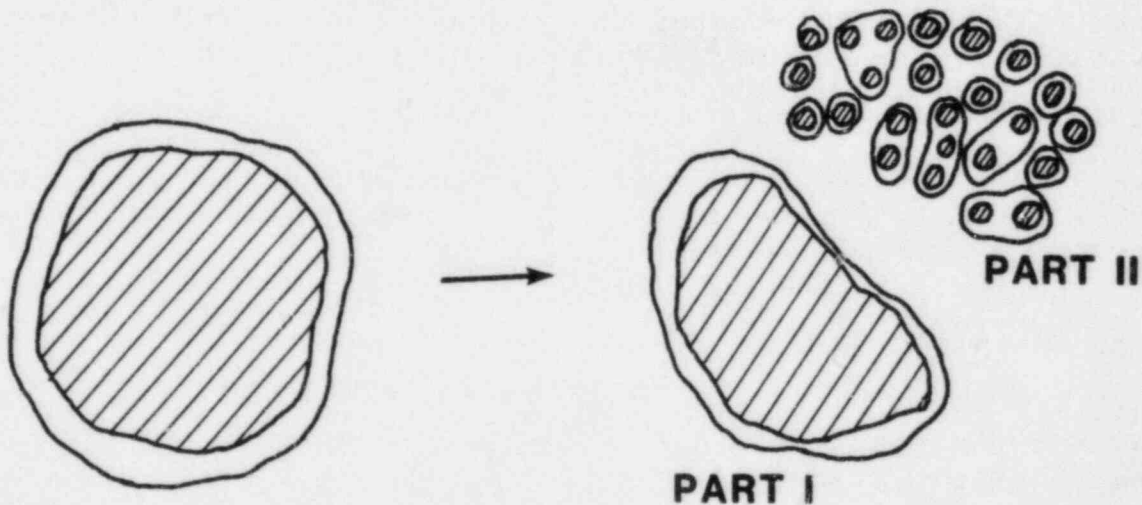


Figure 2.42. Fuel Fragmentation Mechanism

The initial fuel mass (or masses) at the premixed size can be subdivided into two parts:

Part I: This part is the remainder of the initial lumped fuel mass at time  $t$  and is further fragmented as time goes on.

Part II: This part is the fragmented fuel particles characterized by some fuel diameter.

Now consider a conceptual system geometry that consists of three parts (Figure 2.43):

Part I: Fuel/coolant interaction zone.

Part II: Overlying slug noninteraction zone.

Part III: Expansion volume.

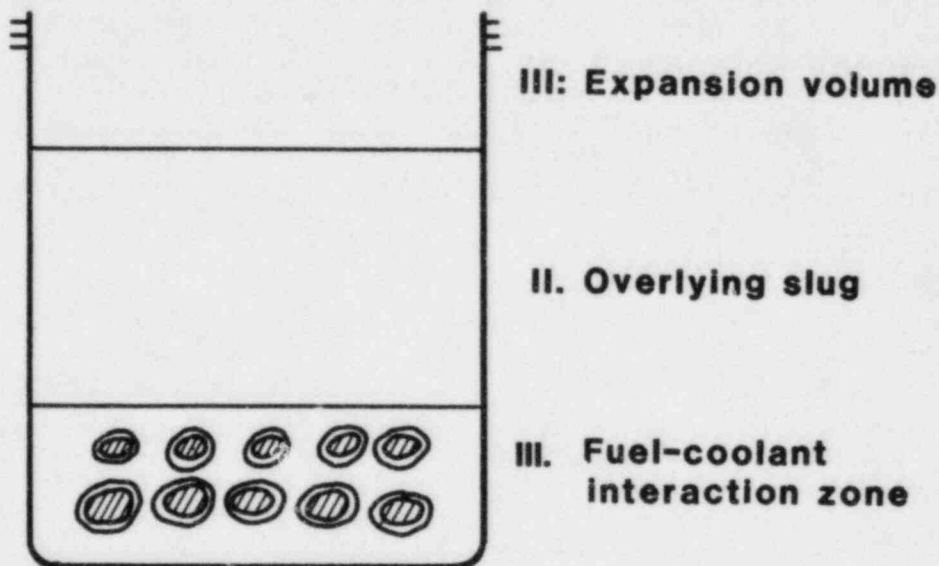


Figure 2.43. One-Dimensional System Geometry

The primary assumptions of this model are

- (1) There is no heat and mass transfer between the system (fuel/coolant and slug) and the environment.
- (2) All the coolant in the interaction zone is involved in the explosion.
- (3) There is no mixing between the slug and the interaction zone; this assumption can be relaxed, but we have chosen this to keep the current model unambiguous.

- (4) The fuel particles are uniformly dispersed in the coolant as a result of initial molten-fuel/coolant mixing.
- (5) The materials within the system are described by lumped-parameter mass and energy balance equations.
- (6) The fuel has constant thermophysical properties.

### Conservation Equations

We formulate the mass and energy balance equations for the one premixed fuel and the fragmented fuel particles separately in a lumped-parameter fashion. For the premixed fuel, we have the mass balance

$$\frac{dm_f}{dt} = -\dot{m}_{fr} \quad (2.14)$$

and the energy balance

$$\frac{dE_f}{dt} = -\dot{Q}_{cf} + \dot{m}_{fr} v_f P - \dot{m}_{fr} i_{fr} \quad (2.15)$$

For the fragmented fuel, we have the mass balance

$$\frac{dm_{fr}}{dt} = \dot{m}_{fr} \quad (2.16)$$

and the energy balance

$$\frac{dE_{fr}}{dt} = -\dot{Q}_{cfr} - \dot{m}_{fr} v_{fr} P + \dot{m}_{fr} i_{fr} \quad (2.17)$$

where

- $m$  = mass of fuel
- $\dot{m}$  = fragmentation rate
- $E$  = energy of fuel
- $\dot{Q}_c$  = heat-transfer rate to coolant
- $i$  = enthalpy
- $v$  = specific volume
- $P$  = pressure

and the subscripts  $f$  and  $fr$  refer to the premixed fuel and the fragmented fuel, respectively.

In a similar manner, the conservation equations for the coolant are

$$\frac{dm_c}{dt} = 0 \quad (2.18)$$

$$\frac{dE_c}{dt} = \dot{Q}_{cf} + \dot{Q}_{cfr} - P\dot{V}_c \quad (2.19)$$

where  $\dot{V}_c$  = rate of change of coolant volume.  
 $P$  = coolant pressure (since fuel-vapor pressure is negligible.)

As the fuel breaks up, the fuel particles transfer more of their energy to the coolant in the mixing zone. The heated coolant expands against the inertia of the unheated slug and the mixing zone. In our current model, we consider a planar inertial constraint; however, one could easily alter this to a spherical or cylindrical geometry and maintain its one-dimensional nature.

The macroscopic momentum balance equation for the slug is given by

$$\frac{dV_s}{dt} = -g + \frac{A}{m_s} (P - P_o) - \left( \frac{1}{2} V_s^2 \frac{f}{R_h} \right) \quad (2.20)$$

where  $V_s$  = slug velocity  
 $g$  = acceleration due to gravity  
 $m_s$  = slug mass  
 $P$  = pressure at bottom of slug  
 $P_o$  = ambient pressure  
 $f$  = friction factor  
 $R_h$  = hydraulic radius of coolant chamber

#### Constitutive Relations for Transport Terms

We model the rate of fuel fragmentation based on two empirical parameters of fragmentation time,  $\tau$ , and the final debris size,  $D_o$ .

$$\dot{m}_{fr} = -\left( \frac{m_{fi} - m_o}{\tau} \right) \exp\left(-\frac{t}{\tau}\right) \quad (2.21)$$

where  $m_{fi}$  = initial mass of premixed fuel

$$m_o = \text{final mass of premixed fuel} = \rho_f \frac{\pi}{6} D_o^3$$

The energy lost by the premixed and fragmented fuel due to heat transfer is given by the general relation

$$\dot{Q}_i = U_i A_i (T_f - T_c); \text{ for } i = f \text{ or } fr \quad (2.22)$$

where  $U$  = overall heat-transfer coefficient  
 $A$  = surface area of fuel  
 $T_f$  = fuel temperature  
 $T_c$  = coolant temperature

Basically the overall heat-transfer coefficient  $U$  is composed of conductive resistance in the fuel,  $h_{fuel}$ , convective  $h_{film}$ , radiative resistance,  $h_{rad}$ , in the vapor film. Thus  $U$  is given by

$$U^{-1} = h_{fuel}^{-1} + h_{film} + h_{rad}^{-1} \quad (2.23)$$

The heat-transfer coefficient in the fuel is

$$h_{fuel} = \max \left( \frac{K_f}{R_f}, \sqrt{\pi \alpha_f t} \right) \quad (2.24)$$

The heat-transfer coefficient through the film is

$$h_{film} = \frac{K_f}{\max \left( \frac{V_g}{A_f}, \delta_o \right)} \quad (2.25)$$

where  $V_g$  = volume of vapor in total coolant volume  
 $A_f$  = surface area of fuel  
 $K_f$  = thermal conductivity of fuel  
 $\delta_o$  = initial film-boiling thickness  
 $\alpha_f$  = fuel thermal diffusivity

The film-boiling thickness is approximately given by

$$\delta_o = 2 \left[ \frac{K_v \mu_v D_f (T_f - T_{sat})}{\rho_v (\rho_c - \rho_v) g i_{fg}} \right]^{1/4} \quad (2.26)$$

and  $K_V$  = thermal conductivity of vapor  
 $\mu_V$  = viscosity of vapor  
 $D_f$  = diameter of fuel  
 $\rho_V$  = density of vapor  
 $\rho_C$  = density of coolant  
 $C_{pV}$  = heat capacity of vapor  
 $i_{fg}$  = latent heat of vaporization

The radiative coefficient is given by the radiation energy transfer between two gray surfaces in the single system:

$$h_{\text{rad}} = \frac{F\sigma(T_f^4 - T_{\text{sat}_c}^4)}{T_f - T_{\text{sat}_c}} \quad (2.27)$$

where  $\sigma$  = Stefan-Boltzmann constant  
 $F$  = view factor

The view factor between the two gray surfaces is

$$F = \frac{1}{\frac{1-\epsilon_f}{\epsilon_f} + 1 + \frac{A_f(1-\epsilon_c)}{A_c\epsilon_c}} \quad (2.28)$$

where  $\epsilon_f$  = emissivity of fuel  
 $\epsilon_c$  = emissivity of coolant  
 $A_f$  = surface area of fuel  
 $A_c$  = surface area of coolant

The energy lost by both the premixed and fragmented fuel is given by these constitutive relations.

### 2.3.3.2 Numerical Solution and Representative Results

These simultaneous first-order nonlinear differential equations can be solved by many numerical integration techniques. Because the time scale in the present model calculations is very small ( $\sim 1 \mu\text{s}$ ), the simple Euler integration technique could not give us stable and accurate solutions without large numerical computation times. Thus these differential equations and their constitutive relations were solved by a more sophisticated numerical technique which is a modification of the fourth-order Runge-Kutta integration technique with a self-adjusting time-step size.

The mass and energy calculations for each component were checked to verify that the total mass and energy were conserved; this occurred with less than 0.1% error.

The "STEAM" subroutine package was developed to solve the full water/steam equation of state from the fundamental equations. This routine gives one accurate thermodynamic properties over a wide range of densities and energies. A sample calculation was performed using the parametric model for a set of nominal conditions from the FITS experiments: mass of iron/alumina fuel,  $m_f = 5$  kg; mass of water coolant involved,  $m_c = 1$  kg; mass of slug,  $m_s = 200$  kg. The results are presented in Figures 2.44 to 2.46 for the interaction zone pressure history, slug kinetic energy, and the conversion ratio of the fuel's internal energy (i.e., the proportion of that energy transferred to the coolant, expressed as a fraction of the fuel's total initial energy).

### 2.3.3.3 Design of Sensitivity Study

In an overall sensitivity study, it is desirable to ascertain the few really important parameters from a large number of possible variables with a minimum of testing.

A Plackett-Burman Screening Design uses a specific fraction of the  $2^P$  factorial design that allows efficient estimation of the variables under study.[23] The ranges of input variables for the calculation were obtained from the MD, MDC, FITS A, FITS B, FITS C, and FITS G series of experiments and from our own physical intuition (Table 2.10). The seven independent variables would require 128 independent calculations for an overall sensitivity study. But the Plackett-Burman Screening Design technique reduces the total number of tests to 12, a more manageable number (Table 2.11). In this case, the statistical significance level is 0.90.

A ranking of the assigned factor effects provided us with a best estimate of the relative importance of these parameters:

- (1) Diameter of fragmented fuel
- (2) Mass of coolant slug and the fuel/coolant mass ratio
- (3) Temperature of the coolant
- (4) Characteristic fragmentation time
- (5) Temperature of the fuel

In our future work we plan to focus on the first few parameters and attempt to determine reasonable parametric values that empirically match the FITS data. Also, we can use this lumped-parameter model as a beginning for a one-dimensional calculation of the explosion propagation phase. In this way we hope to supply a prediction of the empirical constants to be used in more detailed two-dimensional calculations.

### 2.3.4 Reactor Application: "Steam Spike" Phenomena

The purpose of this current work was to delineate the phenomena that may contribute to rapid steam generation that occurs during a core-melt accident when the reactor vessel fails and



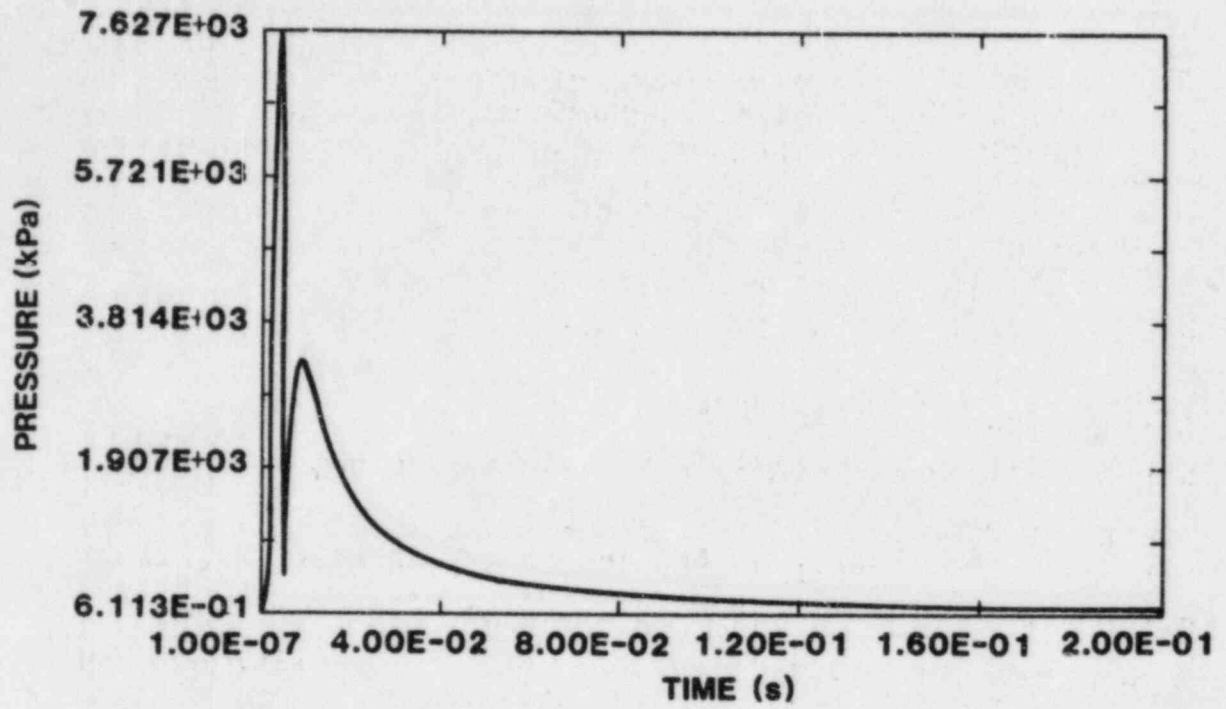


Figure 2.44. Pressure History in Explosion Zone

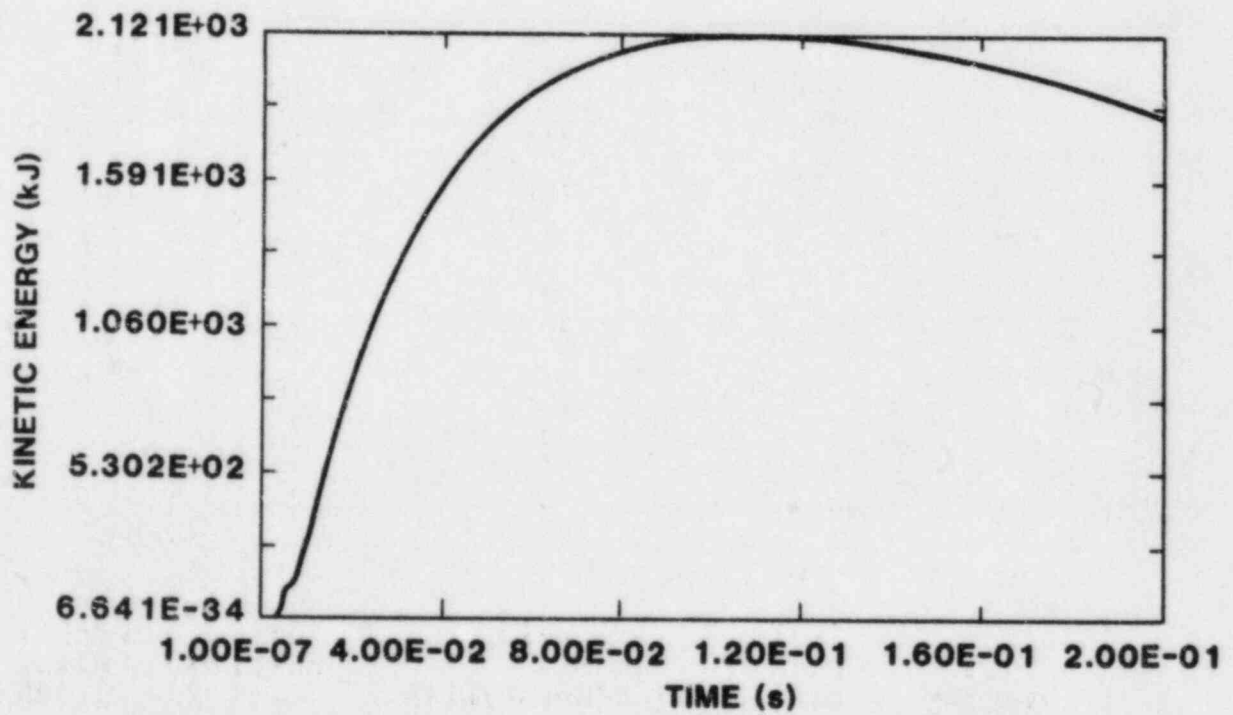


Figure 2.45. Kinetic Energy of Explosion Mixture

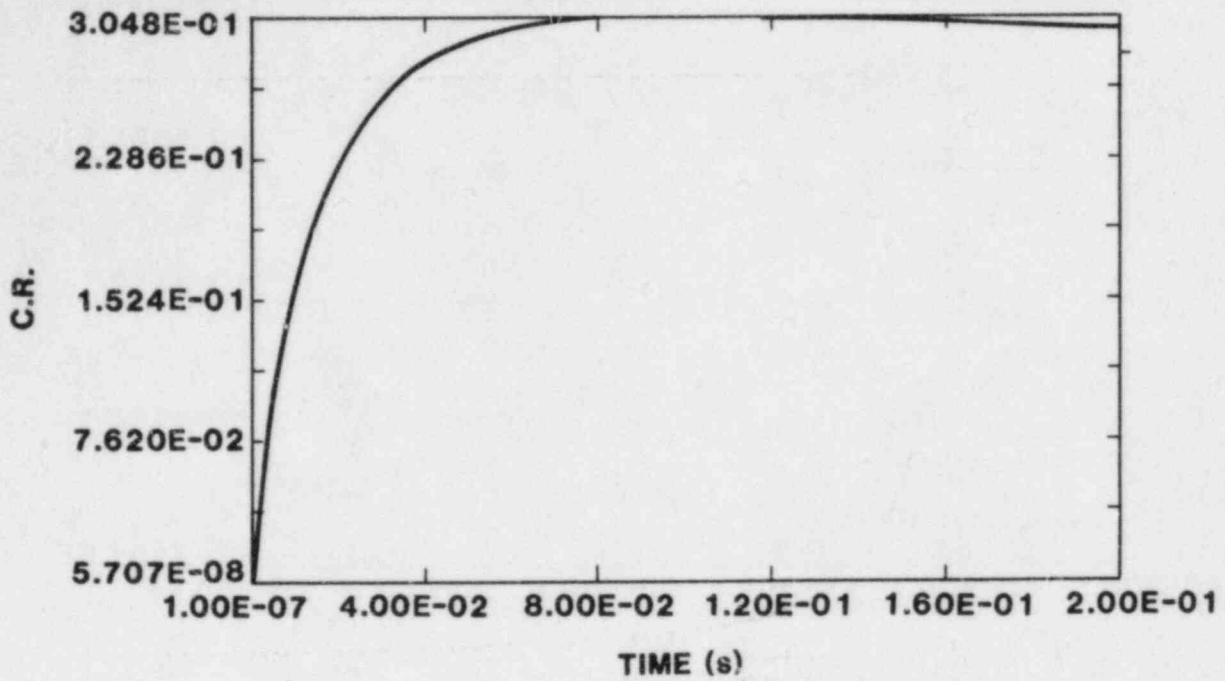


Figure 2.46. Conversion Ratio of Fuel Internal Energy

Table 2.10

Ranges of Input Variables

	$m_f$ (kg)	$m_c$ (kg)	$m_s$ (kg)	$T_{ci}^a$ (K)	$T_{fi}^b$ (K)	$D_o$ (m)	$\tau$ (s)
Upper Bound	20	200	300	373.13	2900	$10^{-3}$	$10^{-3}$
Lower Bound	0.5	0.5	40	283.13	2700	$10^{-5}$	$10^{-5}$

<sup>a</sup> $T_{ci}$  = coolant initial temperature

<sup>b</sup> $T_{fi}$  = fuel initial temperature

Table 2.11

Matrix of Input Data for Parametric FCI Model  
Using Randomized Plackett-Burman Screening Design

Run No.	Trial No.	MASSFI X1	MASSC X2	MASSLUG X3	TEMPCI X4	TEMPFI X5	DIAFI X6	TAUFI X7
1	5	20	200	40	283.13	3266	$10^{-3}$	$10^{-5}$
2	12	0.5	0.5	40	283.13	3266	$10^{-5}$	$10^{-5}$
3	10	20	0.5	300	373.13	3266	$10^{-3}$	$10^{-3}$
4	7	0.5	0.5	40	373.13	3266	$10^{-3}$	$10^{-3}$
5	4	20	200	300	283.13	3266	$10^{-5}$	$10^{-3}$
6	8	0.5	0.5	300	283.13	3666	$10^{-3}$	$10^{-5}$
7	11	0.5	200	300	283.13	3666	$10^{-3}$	$10^{-3}$
8	9	0.5	200	40	373.13	3666	$10^{-5}$	$10^{-3}$
9	1	20	200	40	373.13	3666	$10^{-3}$	$10^{-5}$
10	3	0.5	200	300	373.13	3266	$10^{-5}$	$10^{-5}$
11	6	20	0.5	40	283.13	3666	$10^{-5}$	$10^{-3}$
12	2	20	0.5	300	373.13	3666	$10^{-5}$	$10^{-5}$
Nominal Case		5	5	100	293.13	3466	$10^4$	$10^4$

Note: The fuel is Fe/Al<sub>2</sub>O<sub>3</sub>.

The temperature of fuel contains the effect of fuel freezing  $T_{f_i} = T_{f_i} + \Delta T_{\text{freezing}}$

the molten fuel (and possibly gas) is discharged into the reactor cavity. One can identify a number of phenomena that could individually or in combination contribute to the rapid pressure rise in the containment subsequent to vessel failure:

- (1) Fuel/Coolant Mixing: As the fuel is discharged from the vessel, it pours into the water pool and breaks apart primarily because of hydrodynamic forces (there are other factors that may be operative in certain circumstances, e.g., dissolved gases or an in-vessel FCI). The fuel pour-stream fragments into smaller sizes and transfers its energy to the coolant by radiation and convection while in film boiling. This then produces steam and some hydrogen.
- (2) Energetic Fuel/Coolant Interaction (Steam Explosion): As the fuel mixes with the coolant, a steam explosion may be spontaneously triggered. This explosion will more rapidly produce steam (and hydrogen) as the fuel is fragmented to sizes one to two orders of magnitude smaller than would be present during fuel/coolant mixing. This steam production may eject the fuel and surrounding coolant out of the cavity if the explosion is energetic enough, thereby limiting the occurrence of further events by the rate of fuel and coolant reentry. In experiments multiple explosions have been observed, and it seems quite likely that this will also occur here. Another consequence of the explosion is that the finer fuel debris generated will probably make debris bed coolability much more difficult in the longer term.
- (3) Gas Discharge and Entrainment: Once the fuel discharge (or fuel and coolant) has occurred at high reactor-coolant-system pressures, residual gas (mainly superheated steam and hydrogen) will be discharged from the vessel. This gas discharge can do two things. First, it will pressurize the containment simply from its added mass and energy; this is a straightforward effect that can be easily estimated (e.g., for the Zion plant under TMLB' conditions this would add approximately 0.8 bars to the containment pressure, ~12 psia). Second the blowdown of these gases is quite violent and would, depending on the cavity geometry, cause some of the fuel and coolant remaining in the cavity to be entrained and carried out of the cavity. This could do two things: First, the containment atmosphere could be directly heated by the fuel as it quenches, and second, steam could be produced from the entrained water.
- (4) Molten-Core Concrete Interactions (MCCI): As the fuel stratifies on the cavity base, it would begin to thermally attack the concrete, producing gases (CO, CO<sub>2</sub>, H<sub>2</sub>O, H<sub>2</sub>). In addition to this, a water pool would

likely be present above this molten pool and would also be receiving energy from the fuel. This stratified fuel/coolant interaction may generate a substantial amount of steam. This could occur by means of fuel/coolant interactions in a stratified geometry; also, gases generated by the MCCI (their integral total over two hours would not appreciably affect the containment pressure) could cause convective mixing at the fuel/coolant interface and allow water to quench the top layer of fuel at some rate and flow downward, continually quenching the molten mass. This downward quenching of the molten core could rapidly produce steam that also could add to the "steam spike" (Reference 24; Theofanous contends that this rate of quenching may be large).

Besides these four phenomena, recent experiments at Sandia National Laboratories (HIPS tests) conducted by Tarbell et al. indicate that high-pressure fuel and gas discharge from the vessel may occur simultaneously, causing phenomena (2) and (3) to become intermixed.[25] We do not specifically consider this newly observed phenomena at this time, although it should be noted that an integral coupling of (2) and (3) is quite possible.

We have completed a sensitivity analysis of the "steam spike" that considers these four phenomena for the SARRP work being conducted by A. Benjamin at Sandia and for the Containment Loads Working Group (CLWG). We used the first standard problem as defined by the CLWG as our basic reference design (Appendix) and considered twelve sensitivities from TMLB' and LOCA base-case calculations for our initial conditions (Tables A.1 and A.2 in the appendix). We identify the low, nominal, and high amounts of steam contributing to the "steam spike" based on the physical phenomena that may occur. For the low value of the "steam spike," we consider that only fuel/coolant mixing would occur without steam explosions, gas entrainment, or core quenching during an MCCI (Table 2.12). For the nominal value of the "steam spike," we consider fuel/coolant mixing and multiple steam explosions to occur in the cavity, again neglecting gas entrainment or an MCCI core quench (Table 2.13). Finally, for the high value we consider the final two physical processes: gas entrainment and an MCCI core quench (Table 2.14). For the low and nominal values we used the dynamic FCI model being developed at Wisconsin (WISCI, the MI module in MEDICI). It considers the fuel/coolant mixture as a lumped-parameter system and performs transient calculations for mixing and steam explosions. For the high value cases we performed parametric calculations for the three stated fuel masses and attempted to estimate the characteristic time of each event. In all the cases performed, we did not calculate directly the rate of hydrogen produced, but rather estimated it based on the phenomena that occurred.

Table 2.12  
Lowest Possible Steam Spike<sup>a</sup>

Cases	Steam Mass (kg)	Hydrogen Mass (kg)	Characteristic Time (s)	Debris Size	Pressure Rise <sup>b</sup> (kPa)
Base TMLB'	30	<0.1	4	(MP) <sup>c</sup>	0.1
A.1	300	<1	3	(MP)	1.0
B.1	30	<0.1	1.33	(MP)	0.1
C.1	10	<10	1.33	(MP)	<0.1
D.1	2	<<0.1	3	(MP)	<0.1
E.1	200	<1	2	(MP)	1.0
F.1	110	<1	4.6	(MP)	<1.0
G.1	30	<0.1	4.6	(MP)	0.1
H.1	1	<<0.1	2	(MP)	<0.1
Base LOCA	40	<0.1	5	(MP)	0.1
A.2	41	0.1	1.7	(MP)	0.1
B.2	22	<0.1	4	(MP)	<0.1
C.2	50	0.1	4	(MP)	0.2
D.2	5.6	<<0.1	1.7	(MP)	<0.1

<sup>a</sup>The effect of concrete type is not included; we assume no MCCI during this time of interest.

<sup>b</sup>Pressure rise =  $m_{st}RT_{st}/V_{cont}$ ;  $V_{cont} = 80\ 000\ m^3$

<sup>c</sup>MP = molten pool; no debris

Table 2.13  
Best Estimate Steam Spike<sup>a</sup>

Cases	Steam Mass (kg)	Characteristic Time to Empty Cavity (s)	Debris Size (kg/mm)	Pressure Rise <sup>b</sup> (kPa)	Steam Mass If Cavity Water Replenished <sup>c</sup> (kg)
Base TMLB'	360 (2) <sup>d</sup>	0.5	740/10	1	27000
A.1	750 (3)	0.75	2100/10	2	22000
B.1	500 (3)	0.85	2100/10	1	6230
C.1	130	-	(MP) <sup>e</sup>	<1	1625
D.1	100	-	(MP)	<1	2900
E.1	750 (3)	0.75	2100/10	2	9350
F.1	500 (3)	0.85	2100/10	1	14400
G.1	130	-	(MP)	<1	3770
H.1	100	-	(MP)	<1	1250
Base LOCA	580	0.55	(MP)	2	3350
A.2	2890	0.9	(MP)	7	5800
B.2	2900	1.4	(MP)	7	13150
C.2	580	0.55	(MP)	2	2400
D.2	550	0.75	(MP)	2	1100

<sup>a</sup>The effect of concrete type is not included; MCCI phenomena and its contribution to pressure is considered separately.

<sup>b</sup>Pressure rise =  $m_{st}RT_{st}/V_{cont}$ ;  $V_{cont} = 80\ 000\ m^3$

<sup>c</sup>We assume the water is always replenished to the same level as the problem started, for each new set of multiple explosions.

<sup>d</sup>Number of explosions to void cavity

<sup>e</sup>MP = molten pool; no debris

Table 2.14

Highest Possible Steam Spike<sup>a</sup>

## GAS ENTRAINMENT OF FUEL

- Direct heating of atmosphere (time scale ~60 s)

Percent of Fuel	Pressure Rise (kPa)
10%	75
33%	232
75%	484
100%	594

- Vaporization of available coolant (same time scale)

Percent of Fuel	Pressure Rise (kPa)
10%	61
33%	111
77%	206
100%	255

DOWNWARD QUENCHING OF MOLTEN CORE DURING MCCI<sup>b</sup>

- The absolute pressure rise in the containment would be similar to vaporization of available coolant above except that the time scale of quenching would be longer

$$\tau \sim \frac{m_f c_f \delta T}{q_{\text{BED DRYOUT}}} A \sim 4000 \text{ s for whole core}$$

<sup>a</sup>Here we use  $T_f = 3033 \text{ K}$  as the only value for purpose of illustration; lower temperatures reduce the pressure rise in proportion to sensible heat; also we again neglect the effect of the MCCI during this time.

<sup>b</sup>For downward pool quenching, we use the model suggested by Theofanous. [24]



The "steam spike" produced from fuel/coolant mixing only (Table 2.12) is quite small. The physical reason is that the fuel-pour diameter assumed in these calculations (radius = 14.5 cm and 46 cm, respectively) is rather large and the water-pool depth (nominal value ~1.5 m) is shallow. This combination causes the fuel to fall through the available water in a very short time without much breakup and heat transfer. The steam generation rate is quite small, as is the hydrogen rate (three orders of magnitude smaller, almost negligible). Notice that the total pressure rise in the containment is almost negligible from the total discharge of the fuel from the vessel.

The "steam spike" produced from a series of steam explosions (Table 2.13) is strongly dependent on the number of explosions that occur. In Table 2.13 the first four columns of results correspond to a few multiple steam explosions calculated in the cavity. After these few explosions, we physically expect most of the water in the cavity to be blown out by the explosions. This results in the pressurization being limited by the available water; this would occur when the water inventory is limited or the cavity geometry limits easy reentry. Conversely, if water can easily reenter the cavity during the fuel discharge, more fuel would be available from the vessel and would continue to mix with the water and undergo more multiple explosions. If this were the case, then steam explosions would occur throughout the fuel-discharge phase, and the total steam produced would be given by the last column in Table 2.13. The hydrogen produced from these steam explosions is estimated to oxidize approximately 20% to 30% of the molten metal available. One should consider these values for hydrogen produced as very rough approximations.

These final results on time scale indicate that an adiabatic boundary condition for the containment walls may be quite conservative in certain situations. If the time scale of the "steam spike" is fast relative to the thermal response time of the structure (e.g., a 60-s quench time will not allow time for heat transfer to concrete), then the containment walls will not have a large effect as a heat sink (only an 8 to 10 psi effect due to the thinwall steel plate). However, if the time scale is long, as in the case of molten core quenching (~60 minutes for quench model of Theofanous) from overlying water, then it appears a nonadiabatic boundary must be considered and would have a large effect in reducing the steam spike. Another large heat sink that would reduce the steam spike early in time is the molten-core/concrete interaction. The sensible energy of the core is taken up in decomposing concrete that reduces the net overall gas production rate early in time. This effect also becomes much more important as the time of molten core quenching increases.

2.3.5 A Critique of the Paper "Interpretation of Large-Scale Vapor Explosion Experiments with Application to LWR Accidents" by H. K. Fauske and R. E. Henry. (M. L. Corradini, M. Berman)

At the end of August the International Meeting on LWR Severe Accident Evaluation was held in Cambridge, MA. We presented a number of papers in the area of fuel/coolant interactions. Other researchers in this area presented their results and findings. One paper in particular was presented ("Interpretation of Large-Scale Vapor Explosion Experiments with Application to LWR Accidents," H. K. Fauske, R. E. Henry) that advanced some unique ideas on fuel/coolant mixing phenomena. At this time, we feel a brief critique of this work is needed.

The major tenets of this paper were that "large quantities (many tons) of the molten fuel and the coolant must be finely intermixed prior to any significant energy transfer," and that "premixing on such a scale can readily be ruled out on the basis of first-principle arguments." The basis of these conclusions is that "the presence of large subcooling (reflected in the increase in  $q_{CHF}$ ), relatively lower melting point (reflected by a decrease in  $q_{FB}$ ), and higher fuel superheat ( $\Delta T_S$ ) contribute to the large predicted difference in 'explosivity' potential between the current thermite/water system tests (i.e., referring to Sandia FITS tests) and the LWR system (i.e., corium/saturated water)." To examine these conclusions in detail one must look at the differences between the thermite/water systems used in the FITS experiments and the "actual" corium/saturated water LWR system. To do this let us first list the various constituents of each system, its properties, and possible initial conditions. Then let us look at each point in reverse order, i.e., first  $\Delta T_S$ , then  $q_{FB}$ , then  $q_{CHF}$ .

The properties of the two thermite fuel/water systems and the "actual" corium/saturated water LWR system are given in Table 2.15 along with what we presumed the authors of the paper assumed for their study.

Before we discuss the models presented in Fauske's paper, let us look at the "actual" corium fuel he seems to use in his calculations, at the fuel used in FITS tests, and at that which is likely to be in the reactor. Note first that a single melting point has been assigned to corium, namely 2800 K. According to Reference 26, the melting point of stoichiometric  $UO_2$  is 3133 K; stoichiometric  $ZrO_2$  melts at 2946 K. A eutectic melting point occurs at 2825 K. Hence, it appears that Fauske has assumed an approximately equal mixture (on a molar basis) of fully oxidized  $UO_2$  and  $ZrO_2$ . It is our belief that the MAAP code frequently predicts that only about 20% of the zirconium is oxidized

prior to core slumping for many accidents. Under those conditions, one would expect to find a melt composed of a non-stoichiometric ternary mixture of uranium, zirconium, and oxygen. Such mixtures show a range of melting temperatures from as low as 1800 K to as high as 3133 K.[26] One could also expect to find significant fractions of molten stainless steel in "typical LWR coriums." Hence, it is not an exaggeration to consider that the uncertainty in corium-melting temperatures covers a range in excess of 1300 K (excess depends on superheat), and that actual temperatures will depend on accident scenario.

Fauske assumes a maximum fuel superheat of 400 K, corresponding to a maximum  $T_f$  of 3200 K. If the mixture were indeed composed only of the two stoichiometric oxides,  $UO_2$  and  $ZrO_2$ , then the maximum melt temperature would not exceed 3200 K.[26] Four-hundred kelvin of superheat would correspond to  $T_f = 3600$  K. If unoxidized zirconium metal were available, temperatures could greatly exceed 3200 K if steam were available to oxidize the metal. The heat of reaction is significant and would be released coincident with the molten-fuel/coolant interaction. If steel were present, its rapid boiling at about 3200 K\* might tend to limit the maximum fuel temperature. However, the steel would also be available for exothermic reactions with steam. Furthermore, by neglecting the presence of stainless steel in the "corium," credit could not be taken for the latent heat of evaporation of the steel. Overall, we concluded that the fuel temperature could range from 1800 to 3600 K or higher.

The water used in the FITS and earlier Buxton-Benedick tests ranged from highly subcooled to saturated. Explosive and nonexplosive interactions were observed throughout all temperature ranges. Furthermore, melt composition played a major role. We note that an energetic double explosion was observed for a purely oxidic melt in saturated water (see Table 2.5).

Now let us address the other reasons individually. First, it is asserted that the length scale for premixing is on the order of 1 cm. Fauske bases this value on the notion that hydrodynamic fragmentation due to relative velocities causes the rapid fuel breakup ( $T^+ = 3$ ); see Eq. 1 of the Fauske/Henry paper. This is curious considering one still does not know the actual fuel fragmentation mechanism; in fact, Fauske has historically rejected hydrodynamic fragmentation and instead proposed a breakup mechanism due to spontaneous nucleation. Therefore, the quoted length scale is highly

---

\*We have reviewed eight references for the boiling point of iron and found values ranging from 3000 K to 3271 K. The National Bureau of Standards currently uses 3135 K, information received by telephone.

Table 2.15

## Fuel/Coolant Pairs Considered

Property	FITS Iron/Alumina	FITS Iron/Oxide	FITS Corium A+R	Actual Corium	Corium in Fauske Paper
Fuel	Fe-Al <sub>2</sub> O <sub>3</sub>	Fe <sub>3</sub> O <sub>4</sub>	UO <sub>2</sub> -ZrO <sub>2</sub> -SS	U-O-Zr, SS	UO <sub>2</sub> , ZrO <sub>2</sub>
Composition	55w/o, 45w/o		53w/o, 17w/o, 30w/o	Unknown <sup>a</sup>	Not Given
Melt temp (K)	1800, 2300	1800	2750-2800, 1800	1800-3100, 1800	2800
Density <sup>b</sup> (kg/m <sup>3</sup> )	3800	3500	7000	Depends on comp.	Not Given
Specific heat <sup>b</sup> (J/kg-K)	1060	880	587	Depends on comp.	Not Given
Thermal cond. <sup>b</sup> (W/m-K)	22	4	6.5	Depends on comp.	Not Given
Emissivity <sup>b</sup>	0.5-0.7	0.7	0.5-0.7	Depends on comp.	1
Heat of reaction (MJ/kg H <sub>2</sub> )	16		20	20 for SS 150 for Zr	Neglected
Fuel temp (K)	2700-3200	~2000	2700-3200	1800-3600	2800-3200
Coolant	Water		Water	Water	Water
Initial temp <sup>c</sup> (K)	280-367		280-300	298-620	373

<sup>a</sup>Actual corium may be a complex mix of the quaternary U-O-Zr-SS system, depending on the extent of zirconium oxidation before melting and stainless-steel structure melted.

<sup>b</sup>Homogeneous average quantities.

<sup>c</sup>In the FITS hot water tests the water temperature was raised to saturation at Albuquerque ambient pressure (0.83 b).

arbitrary because it depends on the mechanism and an assumed breakup time of 1 ms and a relative velocity of 100 m/s. We think that the premixing scale may be much larger or smaller depending on the initial conditions and geometry (1 mm to 0.2 m).

Second, Fauske contends that the time to solidification of the fuel surface must be considered as the limit to premixing. At that time premixing would stop because the fuel would begin to solidify. He suggests this time is given by his Eq. 2,

$$t = \frac{1}{\pi a_{tf}} \left( \frac{k_f (T_f - T_{fm})}{q_{FB}} \right)^2$$

where  $a_{tf}$  = fuel thermal diffusivity,  
 $k_f$  = fuel thermal conductivity,  
 $T_f$  = fuel temperature,  
 $T_{fm}$  = melting temperature,

and

$q_{FB}$  = boiling heat flux (Fauske/Henry paper, Eq. 4).

$$q_{FB} = \sigma \epsilon \left[ (T_{fm})^4 - (T_{sat})^4 \right] + h_f (T_{fm} - T_{sat})$$

where  $\sigma$  = Stefan-Boltzmann constant.  
 $\epsilon$  = fuel emissivity.  
 $T_{sat}$  = coolant saturation temperature.  
 $h_f$  = film boiling heat-transfer coefficient.

Now using his assumptions,  $\epsilon = 1$ ,  $T_f - T_{fm} = 200$  K for "actual," and  $q_{FB} \sim 3$  MW/m<sup>2</sup>, one concludes that the "actual" corium/saturated water system has much less time (factor of 60) than the thermite/water system for mixing. The emissivity is probably not 1 but rather  $\sim 0.5$ . The amount of superheat for the fuel could be as little as 200 K or as great as 1800 K for reasons discussed previously. The actual film-boiling heat flux is the same for both fuel systems because their temperature range and emissivities are similar (1.5 to 3 MW/m<sup>2</sup>). Now if one uses Fauske's criterion from Table 1 in the Fauske/Henry paper,

$$\left( \frac{q_{FB\_LWR}}{q_{FB\_THERMITE}} \right)^2 \left( \frac{(T_f - T_{fm})_{THERMITE}}{(T_f - T_{fm})_{LWR}} \right)^2$$

we find that the ratio of premixing time up to fuel solidification for thermite to "actual" corium ranges between 0.1 to 10. This implies that the available time for premixing can be more for corium or less when compared to the FITS thermite system.

As noted previously, the Fauske/Henry paper completely neglected the effects of chemical reactions. If we account for steel and zirconium oxidation, we must remember that the fuel can actually heat up rather than cool down due to metal oxidation. Nelson presented experimental evidence of this possibility at the Cambridge meeting. This suggests that realistically the "actual" corium could heat up and the limit to the mixing time would not be fuel solidification at all, at least for the metallic fraction.

Finally, Fauske compares the potential for intermixing for an "actual" corium/saturated water system and the thermite/water system by comparing the film-boiling heat flux,  $q_{FB}$ , and the pool boiling critical heat flux,  $q_{CHF}$ , for each system. His point is that because water is subcooled in some FITS tests (not all), then  $q_{CHF} > q_{FB}$  and mixing is allowed to occur; in the actual corium/saturated water system,  $q_{FB} > q_{CHF}$ , and mixing is not allowed. This conclusion is questionable on two counts. First, it is a dubious assertion that the pool-boiling critical heat flux is the proper measure against which to compare fuel-film-boiling heat flux. What is so important about  $q_{CHF}$ ? It is only important insofar as it represents a qualitative limit of steam outflow from the fuel/coolant mixture and water inflow (counter-current, one-dimensional). The actual limit to counter-current steam-water flow into the mixture is the vapor/gas mass flux, not the energy it carries. The major fallacy is that during mixing the fuel and coolant may not mix by counter-current steam outflow and water inflow. Rather, steam flows out the top of the mixture and water flows in from the sides and bottom of the mixture (an unambiguous experimental observation). This inherent difference calls into serious question the use of  $q_{CHF}$  as a measure of the ability of a fuel/coolant system to mix. Rather, fuel and coolant liquid fluidization by the steam mass flux upward may be the limit to mixing. We have already developed models for this situation indicating that substantially more mixing is possible than Fauske contends ("A Dynamic Model for Fuel/Coolant Mixing," M. L. Corradini, G. A. Moses, Cambridge Meeting).

Also, even if one assumes  $q_{CHF}$  is a reasonable measure of mixing with which to compare  $q_{FB}$ , one finds Fauske's comparison to be erroneous. Earlier, we emphasized that  $q_{FB}$

is actually the same for the thermite or "actual" corium system ( $1.5$  to  $3 \text{ MW/m}^2$  depending on  $\epsilon$ ); this is an obvious error in Fauske's analysis. Additionally, new experiments at Sandia (EXO-FITS CM and OM series, a total of 16 experiments to date, many with saturated water) indicate that mixing does occur with thermite/saturated water system even when  $q_{FB} > q_{CHF}$ . Steam explosions have also been observed in saturated water with oxide melts (OM tests) and iron-alumina (see Table 2.5). Thus, the supposed limit to mixing that requires  $q_{FB} < q_{CHF}$  for fuel/coolant system is invalidated.

This suggests to us that the thermite/water systems (subcooled and saturated water, iron-alumina and corium A+R) are excellent simulants for the "actual" corium in a core-melt accident.

One final comment should be made. In the final sentence of the paper, Fauske says that the "vanishingly low explosivity" potential indicated for the LWR system is consistent with experimental findings: no propagating vapor explosions have been observed with the corium/saturated water system." In fact, at the FITS facility, no such experiments have yet been attempted. Our observations of the explosivity and conversion ratios of corium A+R/cold water systems led us to believe that they were extremely similar to the iron-alumina/water systems. Explosions have been experimentally observed for iron-alumina/saturated water. Since corium tests are much more expensive than iron-alumina, such tests are performed less frequently. However, higher priority will be assigned to corium/saturated water tests in future experiment planning.

## 2.4 References for Section 2

1. L. S. Nelson, L. D. Buxton, H. N. Planner, "Steam Explosion Triggering Phenomena. Part 2: Corium-A and Corium-E Simulants and Oxides of Iron and Cobalt Studied with a Floodable Arc Melting Apparatus," NUREG/CR-0633, SAND79-0260, May 1980.
2. G. A. Greene, N. A. Park, S. B. Burson, J. Klages, J. Klein, Y. Sanborn, C. E. Schwarz, "Some Observations on Simulated Molten Debris-Coolant Layer Dynamics," Proceedings of the International Meeting on LWR Severe Accident Evaluation, August 28-September 1, 1983, Cambridge, MA.
3. The Explosion at Appleby-Frodingham Steelworks, Scunthorpe, 4 November 1975, A report by HM Factory Inspectorate, Health and Safety Executive, Crown copyright 1976, ISBN 0 11 880331 X.
4. Fauske and Associates, "Key Phenomenological Models for Assessing Explosive Steam Generation Rates," IDCOR Technical Report 14.1A, Burr Ridge, IL, June 1983.
5. L. D. Buxton, Molten Core-Water Contact Analysis, SAND77-1842, Sandia National Laboratories (1979).
6. R. E. Henry et al, "Establishment of a Permanently Coolable State," Trans. Am. Nucl. Soc., 39, 368 (1981).
7. R. E. Henry and H. K. Fauske, "Core Melt Progression and the Attainment of a Permanently Coolable State," Proc. of Ther. Reac. Fuels Mtg., Sun Valley, ID (1981).
8. D. H. Cho et al, "Mixing Considerations for Large-Mass, Energetic Fuel-Coolant Interactions," 11, Proc. ANS/ENS Fast Reac. Safety Mtg., Chicago, IL, CONF-761001 (1976).
9. D. E. Mitchell, M. L. Corradini, and W. W. Tarbell, Intermediate Scale Steam Explosion Phenomena: Experiments and Analysis, SAND81-0124, Sandia National Laboratories (1981).
10. M. Berman, Light Water Reactor Safety Research Program Semi-Annual Report, October 1981-March 1982, SAND83-1572, NUREG/CR2841 Sandia National Laboratories (1982).
11. G. Wallis, One-Dimensional Two-Phase Flow, 2nd ed, McGraw-Hill, NY (1981).
12. J. B. Rivard, Report of the Zion/Indian Point Study, Chapter 6, Vol. 1, SAND80-0617/1, NUREG/CR-1410, Sandia National Laboratories (1980).



13. M. L. Corradini, "Phenomenological Modeling of the Triggering Phase of Small Scale Steam Explosion Experiments," Nuclear Science and Engineering, V78, 131 (1981).
14. M. S. Kazimi, "Theoretical Aspects of Fuel-Coolant Interactions," PhD Thesis, MIT-NE 155 (1973).
15. L. S. Nelson and P. Duda, Steam Explosion Experiments with Single Drops of Iron-Oxide Melted with a CO<sub>2</sub> Laser, SAND82-1105, NUREG/CR-2718, Sandia National Laboratories (1982).
16. H. K. Fauske, "Some Aspects of Molten Fuel-Coolant Interactions," Proc. Fast Reac. Safety Mtg., Beverly Hills, CA (1974).
17. S. J. Board, R. W. Hall, and R. S. Hall, "Thermal Detonation Model for Fuel-Coolant Interaction," Nature, 254, 319 (1975).
18. M. Berman et al, LWR Safety Semiannual Progress Report, October 1982 to March 1983, NUREG/CR-3734, SAND84-0688, Sandia National Laboratories, (March 1984).
19. D. H. Cho et al, A Rate-Limited Model of Molten Fuel/Coolant Interactions, ANL-7917, Argonne National Laboratory (1972).
20. D. H. Cho, W. L. Chen, R. W. Wright, A Parametric Study of Pressure Generation and Sodium-Slug Energy from Molten-Fuel-Coolant Interactions, ANL-7919, Argonne National Laboratory (1972).
21. W. L. Chen, D. H. Cho, and M. S. Kazimi, Recent Additions to the Parametric Model of Fuel-Coolant Interactions, ANL-8130, Argonne National Laboratory (1974).
22. D. E. Mitchell and M. L. Corradini, Intermediate Scale Steam Explosion Phenomena: Experiments and Analysis, SAND81-2131, Sandia National Laboratories (1981).
23. DuPont Co., Strategy of Experimentation (1975).
24. J. F. Meyer et al, Preliminary Assessment of Core Melt Accidents at the Zion and Indian Point Nuclear Power Plants and Strategies for Mitigating Their Effects, NUREG-0850, Vol. 1, USNRC Report (1981).
25. W. Tarbell et al, "Aerosol Source Term in High-Pressure Melt Ejection," 1st Proc. of Nuclear Thermal Hydraulics, ANS Winter Mtg, San Francisco, CA (1983).
26. Core-Meltdown Experimental Review, NUREG-0205, SAND74-0382, Revision, (March 1977).

APPENDIX TO CHAPTER 2

PWR "Steam-Spike" Standard Problem

Specifications for Comparison Calculation

- I. Mass of corium (exiting vessel)
- A. Mass of  $\text{UO}_2$ : 90,000 kg
  - B. Mass of steel: 22,000 kg
    - $\text{Fe} = 85 \text{ wt}\%$
    - $\text{Cr} = 10 \text{ wt}\%$
    - $\text{Ni} = 5 \text{ wt}\%$
  - C. Mass of zirconium: 22,000 kg  
(assume 50% has oxidized)
  - D. Total corium mass: 138,400 kg  
(exiting vessel)
- II. Temperature of corium (exiting vessel): 2533 K
- III. Type of concrete: Limestone
- 2400 kg/m<sup>3</sup>
- $\text{CaCO}_3$  80 wt%
  - $\text{Ca(OH)}_2$  15 wt%
  - $\text{SiO}_2$  1 wt%
  - Free  $\text{H}_2\text{O}$  3 wt%
  - $\text{Al}_2\text{O}_3$  1 wt%
- IV. Vessel/cavity/containment specification
- A. Dimensions for vessel/cavity: As shown in Figures A.1 and A.2
  - B. Containment: One volume, 80,000 m<sup>3</sup>, assumed adiabatic; total containment pressure at vessel failure 0.4 MPa; partial pressure of air 0.1 MPa; partial pressure of steam 0.3 MPa; temperature = 407 K

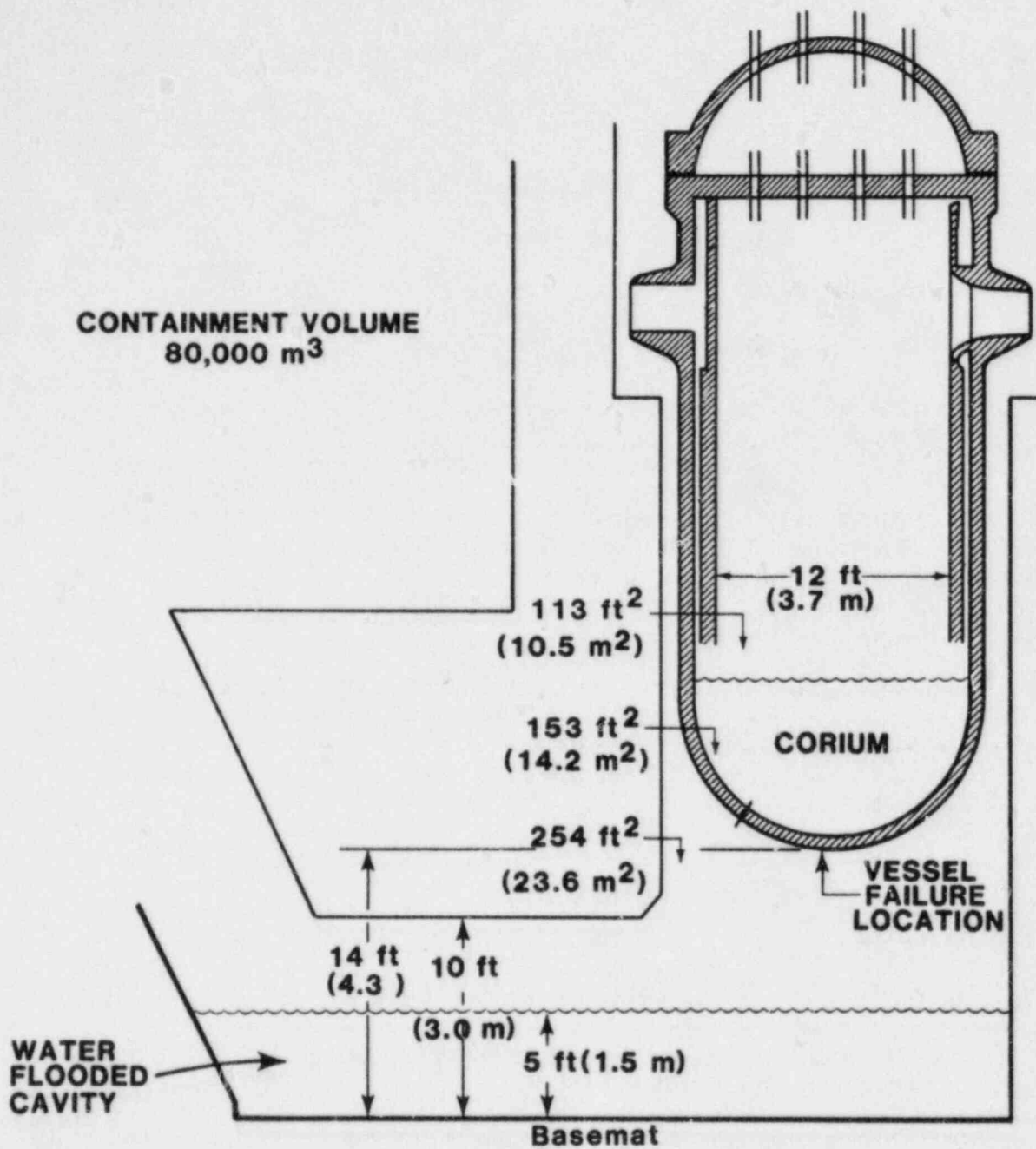


Figure A.1. Representation of the Reactor Vessel Situated Within the Reactor Cavity

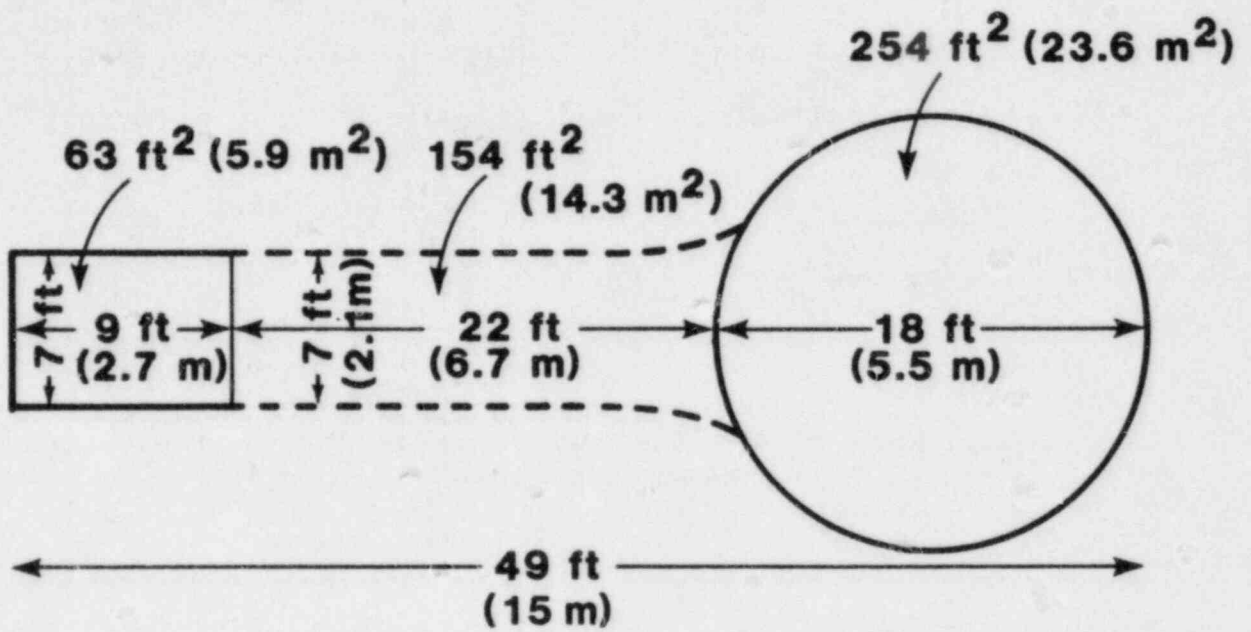


Figure A.2. Plan View and Typical Dimensions of Reactor Cavity and Keyway

- V. Type 1 ejection from vessel (high pressure) -- Specifications
  - A. Vessel and primary system pressure: 17 MPa
  - B. Vessel and primary system total volume: 340 m<sup>3</sup> (saturated steam plus 455 kg Hydrogen)
  - C. Vessel hole equivalent radius: 0.145 m (0.066 m<sup>2</sup> Area)\*
- VI. Type 2 ejection from vessel (low pressure) -- Specifications
  - A. Vessel and primary system pressure: 0.4 MPa
  - B. Vessel and primary system total volume: 340 m<sup>3</sup>
  - C. Vessel hole equivalent radius: 0.46 m (0.66 m<sup>2</sup> Area)
- VII. Water temperature (in cavity at vessel failure): 397 K
- VIII. Decay heat level: 30 Mw (1%)
- IX. For the two cases for ejection from the vessel calculate:
  - A. Mass flow rates and temperatures as a function of time for constituents being added to containment atmosphere, specifically for:
    - i. steam
    - ii. hydrogen
    - iii. carbon dioxide
    - iv. carbon monoxide
  - B. Enthalpies for the same
  - C. Pressure and temperature history in containment
  - D. Disposition of corium after 1-hour period
  - E. Size and size distribution of corium particulates/aerosols
  - F. Characterization of basemat penetration (if any)

(All of the above for 1 hour following vessel failure. Use international units.)

---

\*Do not assume any ablation. Hole diameter remains constant.

Table A.1

## Type 1, High Pressure Ejection From Vessel

Alternative Case	Corium Mass (kg)	Corium Temperature (K)	Type Concrete	Water Depth (m)	Primary Pressure (MPa)
A.1	106,133	3,033	Limestone	3.2	17
B.1	46,133	2,033	Limestone	3.2	17
C.1	46,133	3,033	Basaltic	0.5	17
D.1	106,133	2,033	Basaltic	0.5	17
E.1	46,133	3,033	Basaltic	3.2	7
F.1	106,133	2,033	Basaltic	3.2	7
G.1	106,133	3,033	Limestone	0.5	7
H.1	46,133	2,033	Limestone	0.5	7

## Table A.1 Notes:

1. The corium mass of 106,133 kg is composed of 90,000 kg  $UO_2$ , 7,333 kg steel, 7,333 kg zirconium, and 1,467 kg  $O_2$ . This represents a relatively low ratio of metal to total corium mass (i.e., 0.104) as compared to the standard problem.
2. The corium mass of 46,133 kg is composed of 30,000 kg  $UO_2$ , 7,333 kg steel, 7,333 kg zirconium, and 1,467 kg  $O_2$ . This represents the same ratio of metal to total corium mass as the standard problem (i.e., 0.238).
3. The corium temperatures are specified by the CLWG standard problem.
4. The types of concrete are from the CLWG standard problem.
5. The water depths are from the standard problem. The water depth in the cavity of 0.5 m means that the cavity is essentially dry when the corium drops into it and that the accumulator water is dumped onto the corium.
6. The primary system pressures are from the standard problem.
7. The vessel hole equivalent radius is 0.145 m for all alternative cases in Table A.1.

Table A.2

## Type 2, Low Pressure Ejection From Vessel

Alternative Case	Corium Mass (kg)	Corium Temperature (K)	Water Depth (m)
A.2	46,133	3,033	3.2
B.2	106,133	2,033	3.2
C.2	106,133	3,033	1.5
D.2	46,133	2,033	1.5

## Table A.2 Notes:

1. The masses of corium have the same compositions (i.e., ratios of metal to total corium mass), respectively, as in Table A.1.
2. The corium temperatures are from the standard problem.
3. The water depths are from the standard problem. For both water depths in Table A.2, the corium drops into the water.
4. The vessel hole equivalent radius is 0.46 m for all alternative cases in Table A.2.
5. The type of concrete is limestone for all alternative cases in Table A.2.

### 3. HYDROGEN PROGRAM

#### 3.1 Analysis and Code Development

##### 3.1.1 HECTR Analysis and Code Development

(S. E. Dingman, A. L. Camp, M. J. Wester, R. A. Watson)

During the past six months, we have added several new models to HECTR and have upgraded several existing models. We have also reformatted the code considerably to make HECTR easier to use and modify. We performed calculations for reactor containments and for experimental facilities. Results of some of these calculations were reported in the papers: "MARCH-HECTR Analysis of an Ice-Condenser Containment," and "Evaluation of HECTR Predictions of Hydrogen Transport." These papers were presented at the International Meeting on Light-Water Reactor Severe Accident Evaluation held in August. In addition, we are continuing to provide support for the MELCOR, SARP, SASA, and HBS programs.

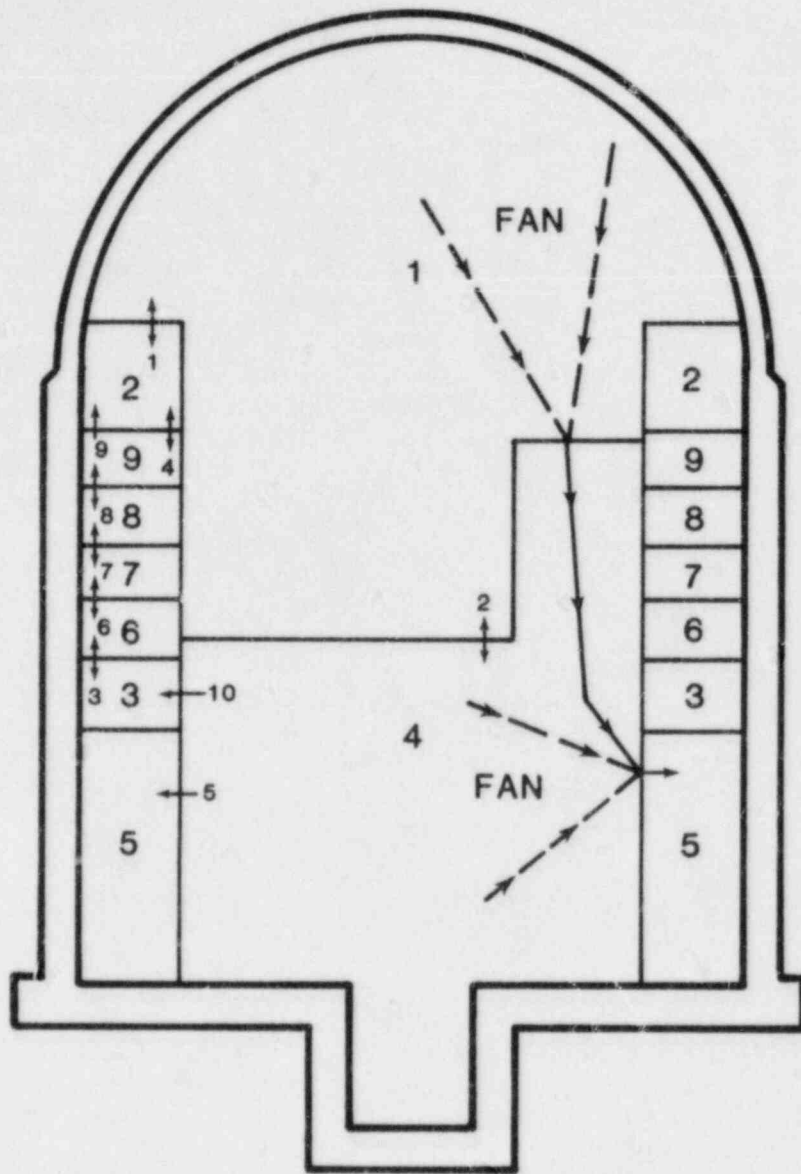
##### 3.1.1.1 Ice-Condenser Containment Analysis

We have completed our analysis of the pressure-temperature response of an ice-condenser containment for a variety of severe accidents. This work was a joint effort of the hydrogen behavior and SASA programs. Sequoyah was used as the reference plant for this work. A report describing this work has been prepared in draft and should be published during the next reporting period. The significant results from this study are summarized below.

The analyses were based on both the MARCH and HECTR computer codes. MARCH was used to model the primary system and provide hydrogen and steam source terms to containment. HECTR was used to model the containment pressure-temperature response, including the effects of hydrogen deflagrations. This work was the first major application of HECTR to an ice-condenser containment. The combined use of MARCH and HECTR represents a significant advance in the capability to model ice-condenser containments.

Sixteen different base-case accident scenarios were analyzed with MARCH to provide steam and hydrogen source terms for HECTR. Fifty-three different variations of the base cases were evaluated using HECTR. The compartmentalization used in these calculations is shown in Figure 3.1. The accident scenarios examined do not represent all possible contributors to risk. However, many of the highest contributors to risk are examined in this report. The cases evaluated are described in Table 3.1. Note that the case numbering system differs from that used in previous descriptions of this work.





KEY

- 1 - COMPARTMENT NUMBER
- 1 - FLOW JUNCTION NUMBER
- - ONE-WAY FLOW JUNCTION
- ↔ - TWO-WAY FLOW JUNCTION

Figure 3.1. HECTR Ice-Condenser Containment Model

Table 3.1  
Case Descriptions

Case No.	Accident* Seq. <sup>a</sup>	Restore ECC	Extent Oxid.	Spray Trains	Recirc. Fans	Cont. Vent	Ignit. Limits	Drain Temp.	Ice Condenser			Comments
									Htxfer Coeff	Extent Comb.	Flame Speed	
A.00	S2D,2"	yes	75%	2	2	no	8%	310	d	d	d	
B.00	S2D,2"	yes	35%	2	2	no	8%	310	d	d	d	
C.00	S2D,2"	yes	75%	2	2	no	8%	310	d	d	d	
D.00	S2D,2"	no	100%	2	2	no	8%	310	d	d	d	
E.00	S2D,2"	no	min	2	2	no	8%	310	d	d	d	
F.00	S1D,6"	yes	75%	2	2	no	8%	310	d	d	d	
G.00	S1D,6"	yes	37%	2	2	no	8%	310	d	d	d	
H.00	S1H,6"	yes	75%	2	2	no	8%	310	d	d	d	
I.00	S1HF,6"	yes	75%	2inj	2	no	8%	310	d	d	d	
J.00	S1HF,6"	no	100%	2inj	2	no	8%	310	d	d	d	
K.00	S1HF,6"	no	min	2inj	2	no	8%	310	d	d	d	
L.00	TMLU	yes	75%	2	2	no	8%	310	d	d	d	
M.00	TMLB'	yes	75%	2rcvr	2rcvr	no	8%	310	d	d	d	
N.00	TMLB'	no	100%	0	0	no	12%	310	d	d	d	
O.00	TMLB'	no	min	0	0	no	12%	310	d	d	d	
P.00	TMLB'	no	65%	0	0	no	12%	310	d	d	d	
A.01	S2D,2"	yes	75%	2	0	no	8%	310	d	d	d	
A.02	S2D,2"	yes	75%	1	1	no	8%	310	d	d	d	
A.03	S2D,2"	yes	75%	0	2	no	8%	310	d	d	d	
A.04	S2D,2"	yes	75%	0	0	no	8%	310	d	d	d	
A.05	S2D,2"	yes	75%	0	2	no	8%	310	d	d	d	Surface heat xfer coeff. x 5.
A.06	S2D,2"	yes	75%	2	2	no	6%	310	d	d	d	
A.07	S2D,2"	yes	75%	2	2	no	7%	310	d	d	d	
A.08	S2D,2"	yes	75%	2	2	no	9%	310	d	d	d	
A.09	S2D,2"	yes	75%	2	2	no	10%	310	d	d	d	
A.10	S2D,2"	yes	75%	2	2	no	8%	310	d	.75xd	d	
A.11	S2D,2"	yes	75%	2	2	no	8%	310	d	d	3xd	
A.12	S2D,2"	yes	75%	2	2	no	8%	310	d	d	d/3	

**Table 3.1**  
**Case Descriptions**  
**(Continued)**

Case No.	Accident Seq. <sup>a</sup>	Restore ECC	Extent Oxid.	Spray Trains	Recirc. Fans	Cont. Vent	Ignit. Limits	Drain Temp.	Ice Condenser			Comments
									Htxfer Coeff	Extent Comb.	Flame Speed	
A.13	S2D, 2"	yes	75%	2	2	no	8%	310	d	d	d	Suppress upper plenum ignition.
A.14	S2D, 2"	yes	75%	2	2	no	8%	310	d	d	d	Partial oxygen depletion.
A.15	S2D, 2"	yes	75%	2	2	no	8%	310	d	d	d	Ice condenser doors removed.
C.01	S2D, 2"	yes	75%	2	2	no	8%	328	d	85%	6 fps	Comparison to CLASIX base case. No propagation into ice cond.
C.02	S2D, 2"	yes	75%	2	2	no	8%	328	d	85%	6 fps	Comparison to COMPARE.
D.01	S2D, 2"	no	100%	2	2	yes	8%	310	d	d	d	
D.02	S2D, 2"	no	100%	2	2	no	8%	310	d	d	d	Partial oxygen depletion.
E.01	S2D, 2"	no	min	2	2	no	8%	310	d	d	d	Partial oxygen depletion.
F.01	S2D, 6"	yes	75%	2	2	no	8%	310	d	d	d	Partial oxygen depletion.
H.G1	SlH, 6"	yes	75%	2	2	no	8%	310	d	d	d	Partial oxygen depletion.
I.01	SlHF, 6"	yes	75%	2inj	2	no	8%	290	d	d	d	
I.02	SlHF, 6"	yes	75%	2inj	2	no	8%	330	d	d	d	
I.03	SlHF, 6"	yes	75%	2inj	2	no	8%	310	d/5	d	d	
I.04	SlHF, 6"	yes	75%	2inj	2	no	8%	310	dx5	d	d	
I.05	SlHF, 6"	yes	75%	2inj	2	no	8%	310	d	d	d	Surface heat xfer coeff. x 5.
I.06	SlHF, 6"	yes	75%	2inj	2	no	8%	310	d	d	d	Partial oxygen depletion.
J.01	SlHF, 6"	no	100%	2inj	2	yes	8%	310	d	d	d	
J.02	SlHF, 6"	no	100%	2inj	2	no	8%	310	d	d	d	Partial oxygen depletion.
K.01	SlHF, 6"	no	min	2inj	2	no	8%	310	d	d	d	Partial oxygen depletion.
L.01	TMLU	yes	75%	2	2	no	8%	310	d	d	d	Partial oxygen depletion.
M.01	TMLB'	yes	75%	2rcvr	2rcvr	no	8%	310	d	d	d	Partial oxygen depletion.
N.01	TMLB'	no	100%	0	0	yes	12%	310	d	d	d	
N.02	TMLB'	no	100%	0	0	no	12%	310	d	d	d	Partial oxygen depletion.
O.01	TMLB'	no	min	0	0	no	12%	310	d	d	d	Partial oxygen depletion.
P.01	TMLB'	no	65%	0	0	yes	12%	310	d	d	d	

Key: d - default, inj - injection, min - minimum, rcvr - recover  
<sup>a</sup>Dimensions following accident sequence designator indicate diameter of break.

Both degraded-core and core-meltdown scenarios were examined. The degraded-core scenarios postulated that emergency core cooling (ECC) was unavailable for a period of time long enough to allow significant zirconium oxidation, but short enough that core damage could be arrested when ECC was restored.

For degraded-core cases and for core-meltdown cases through the time of vessel failure, the source terms were generated by recording the rates of steam and hydrogen releases to containment (as calculated by MARCH) for each MARCH time step. These recorded values were then input to HECTR. After vessel breach, a coolable debris bed was postulated to form in the reactor cavity, because HECTR could not treat the carbon monoxide and carbon dioxide that would be produced during concrete attack by the hot debris. A sump model in HECTR then used MARCH heat transfer and hydrogen generation data to calculate steam and hydrogen source terms that were consistent with the HECTR-predicted sump temperature and containment atmosphere pressure.

#### 3.1.1.1.1 Results

Predicted peak pressures varied from 161.7 to 905.5 kPa (23.5 to 131.3 psia), depending on the particular accident scenario (Table 3.2). For cases involving failure of containment sprays, the pressure was still increasing at the end of the run. The estimated failure pressures for the type of ice-condenser containment analyzed in the report are 350 to 515 kPa (51 to 75 psia) for Sequoyah [1], and 929 to 1067 kPa (135 to 155 psia) for Watts Bar [2], which puts the maximum pressures tabulated in Table 3.2 in perspective.

The report addresses, in some detail, the effects of the following parameters on the results:

- source terms
- containment sprays
- recirculation fans
- combustion parameters (flame speed, ignition limits, and combustion completeness)
- ice-condenser parameters
- containment venting
- surface heat transfer coefficients
- partial oxygen depletion.

#### 3.1.1.1.2 Effectiveness of Igniter System

Based on our HECTR results, a glow plug igniter system is beneficial for many accident scenarios involving the release of hydrogen. Pressure rises were often decreased from what might be obtained from random combustion with no igniters present. However, a deliberate ignition system of the type installed at Sequoyah is not always beneficial. For example, the igniters at Sequoyah are ac-powered. DC-powered igniters

Table 3.2  
HECTR Results

Case	Number of Burns by Compartment									Maximum Pressure (kPa) and Comp. #	Maximum Temperature (K) and Comp. #
	1	2	3	4	5	6	7	8	9		
A.00	5	6	0	0	0	0	0	0	0	342.5 (1,2)	960 (2)
B.00	1	0	0	0	0	0	0	0	0	369.2 (1,2)	873 (1)
C.00	5	19	1	1	0	1	2	5	8	233.0 (1,2)	994 (2)
D.00	4	6	5	6	1	5	1	2	3	428.5 (1,2)	1226 (2)
E.00	2	6	0	0	0	1	2	1	3	249.8 (All)	1110 (2)
F.00	2	5	10	16	0	9	2	2	2	347.6 (1,2)	1242 (4)
G.00											
H.00	1	4	10	16	0	9	2	2	3	183.3 (1,2, 3,6,7,8,9)	1242 (4)
I.00	0	4	8	13	0	7	3	3	3	473.0 (All)	1210 (4)
J.00	3	8	6	8	0	6	6	6	8	519.8 (1,2)	1354 (2)
K.00	0	3	5	5	0	5	5	5	5	188.8 (All)	1071 (4)
L.00	5	12	2	2	0	2	2	0	0	360.7 (1,2)	981 (2)
M.00	4	9	2	2	0	2	1	1	6	355.3 (1,2)	1019 (4)
N.00	1	4	0	0	2	0	1	1	1	886.9 (1,2)	2025 (2)
O.00	0	2	0	0	0	0	1	2	2	201.0 (All)	1246 (2)
P.00	1	4	0	0	0	0	1	1	2	452.1 (1,2)	1410 (2)
A.01	2	24	0	0	2	0	0	2	6	521.3 (1,2)	1756 (2)
A.02	6	22	0	0	0	0	0	2	11	380.3 (1,2)	970 (2)
A.03	4	7	0	0	0	0	0	0	0	440.2 (All)	957 (2)
A.04	1	25	0	0	2	0	2	4	7	631.0 (1,2)	1363 (2)
A.05	5	10	0	0	0	0	0	0	0	381.0 (All)	946 (2)
A.06	8	43	1	1	0	1	0	0	0	217.8 (1,2)	760 (2)
A.07	7	16	0	0	0	0	0	0	0	278.8 (1,2)	832 (2)
A.08	4	3	0	0	0	0	0	0	0	383.9 (1,2)	1062 (2)
A.09	3	2	0	0	0	0	0	0	2	419.4 (1,2)	1144 (2)
A.10	8	9	0	0	0	0	0	0	0	286.1 (1,2)	831 (2)
A.11	5	5	0	0	0	0	0	0	0	404.7 (1,2)	1023 (1,2)
A.12	5	7	0	0	0	0	0	0	0	240.7 (1,2, 3,6,7,8,9)	924 (2)
A.13	3	2	2	2	2	2	2	2	2	414.7 (1,2)	1059 (2)
A.14	5	5	0	0	0	0	0	0	0	341.5 (1,2)	964 (2)
A.15	5	5	0	0	0	0	0	0	0	251.5 (All)	940 (2)
C.01	0	30	0	10	0	0	0	0	0	187.6 (All)	1006 (2)
C.02	0	19	0	6	0	2	7	12	17	175.2 (All)	881 (2)
D.01	4	7	5	6	2	5	1	2	2	384.8 (All)	1074 (4)
D.02	3	3	3	5	1	3	1	1	1	424.6 (1,2)	1075 (4)
E.01	2	5	0	0	0	1	1	1	2	308.9 (1,2)	1104 (2)
F.01	2	7	6	10	0	6	3	3	3	399.1 (1,2)	1303 (4)
H.01	2	6	6	10	0	6	2	2	3	360.5 (1,2)	1295 (4)
I.01	0	3	7	12	0	7	3	3	2	499.5 (All)	1187 (4)
I.02	1	6	8	13	0	8	3	3	3	458.6 (All)	1206 (4)
I.03	0	3	5	8	0	5	2	2	2	419.1 (All)	1142 (4)
I.04	0	5	9	16	0	8	3	3	4	498.1 (All)	1248 (4)
I.05	1	5	8	12	0	7	3	3	4	424.4 (All)	1142 (4)
I.06	2	5	5	8	0	5	3	3	3	475.1 (All)	1287 (4)
J.01	2	14	6	8	0	6	6	6	9	401.3 (1,2)	1312 (4)
J.02	2	5	6	6	0	6	5	5	5	460.3 (1,2)	1176 (4)
K.01	0	3	5	5	0	5	5	5	5	189.0 (All)	1074 (4)
L.01	5	12	1	2	0	1	0	0	0	357.3 (1,2)	976 (2)
M.01	4	10	1	1	0	0	1	7	10	354.1 (1,2)	977 (4)
N.01	2	5	0	0	2	0	1	3	3	699.3 (1,2)	1512 (2)
N.02	1	2	0	0	1	0	0	1	1	905.5 (1,2)	1508 (1)
O.01	0	3	0	0	0	0	0	1	2	209.5 (All)	1246 (2)
P.01	1	9	0	0	0	0	1	2	3	407.3 (1,2)	1532 (2)

Notes: 1. All pressures are absolute.  
 2. The pressure is still increasing at the end of cases A.03, A.04, A.05, and the "I" cases due to steam overpressure, although in case A.04 the peak pressure occurs earlier due to burns.

would be required to reduce the risk from accidents involving total loss of ac power. Also, for Sequoyah, no igniters are located in the ice regions. As a result, in some accidents high hydrogen concentrations can accumulate in the ice regions.

Finally, our calculations did not address the possibility of stable diffusion flames or of equipment failures as result of combustion events. Future considerations of these possibilities might alter the perceived benefits of deliberate ignition.

#### 3.1.1.1.3 Unresolved Issues

It was beyond the scope of this report to attempt to resolve several issues regarding hydrogen combustion in ice-condenser containments. Those issues were:

- (1) The potential for accelerated flames or local detonations in or near the ice condenser;
- (2) The effects of additional combustible (and noncondensable) gas generation from other metal-water reactions and molten core-concrete interactions;
- (3) The likelihood and effects of stable diffusion flames either near the hydrogen release point, in the ice condenser, or near the fan exits;
- (4) The response of safety-related equipment to combustion, particularly if diffusion flames are present; and,
- (5) Accidents in which the igniter systems may fail.

Work is in progress that will address most of the above issues. The potential for accelerated flames or detonations in the ice condenser will be addressed experimentally at Sandia in the FLAME facility. HECTR is now being modified to address combustion in the presence of the carbon monoxide and carbon dioxide formed during core-concrete interactions. Experiments are in progress to address diffusion flames, and models will be developed for future incorporation into HECTR. Equipment survival will be addressed in a subsequent report using boundary conditions obtained from the analyses described in this report. The feasibility of passive igniters that would function during an accident involving the total loss of AC power is also being studied at Sandia.

#### 3.1.1.2 Transport Analysis

We have completed an evaluation of HECTR's gas transport model and have written a topical report describing this analysis, titled "An Evaluation of HECTR Predictions of Hydrogen Transport" (NUREG/CR-3463, SAND83-1814). This report was sent to

be printed at the end of September. Its conclusions will be summarized here.

HECTR calculations were compared with experimental data and the results of other analytical models. The experimental data consisted of results from the Battelle-Frankfurt test series and the HEDL (Westinghouse-Hanford Engineering Development Laboratory) Standard Problems on Hydrogen Mixing and Distribution. The other analytical models were RALOC, a computer program with a gas transport model similar to HECTR's, and an earlier version of HECTR used to perform a complete transport/combustion analysis of a full-scale reactor containment (Grand Gulf). [3]

In general, HECTR was in satisfactory agreement with RALOC when performing analyses that used similar sets of input and for which no hydrogen combustion was allowed (RALOC does not currently model combustion). For the two sets of experimental comparisons, HECTR performed well, producing excellent quantitative agreement with the experimental results for the same experiments and good qualitative agreement for all cases (hydrogen concentration in the Battelle-Frankfurt tests and temperature and dry hydrogen concentration in the HEDL tests). It was especially noteworthy that HECTR performed quantitatively well in the HEDL standard problems since they incorporated several of the features of a possible accident scenario in a medium-scale representation of a portion of an ice-condenser nuclear power plant.

Finally, we observed that the current version of HECTR produced results quite similar to those generated in the Grand Gulf analysis [3] by the original version of HECTR for the two different two-compartment cases. However, dramatic differences occurred in the calculations of the five-volume compartmentalization. In the current analysis of the five-compartment case, the mixing was very thorough and hydrogen was distributed uniformly throughout the containment, resulting in large global burns. In the original analysis, the hydrogen was distributed very unevenly, promoting smaller local burns (mainly in the wetwell) and eventually leading to oxygen inerting of the lower compartments. An investigation revealed that the difference in the two analyses resulted from a numerical check in the time-step controller of the original version of HECTR, which set the flow through a junction to zero unless the pressure drop across that junction exceeded a certain threshold value. This, in turn, had acted to suppress buoyancy effects. These effects are important in compartmentalizations in which multiple convective mixing loops can form, such as the five-volume compartmentalization of Grand Gulf (Figure 3.2). The other major changes in the two versions of HECTR (changing the momentum equation from a steady-state algebraic equation to a time-dependent differential equation and changing the solution scheme of the conservation equations from an explicit to an implicit formulation),

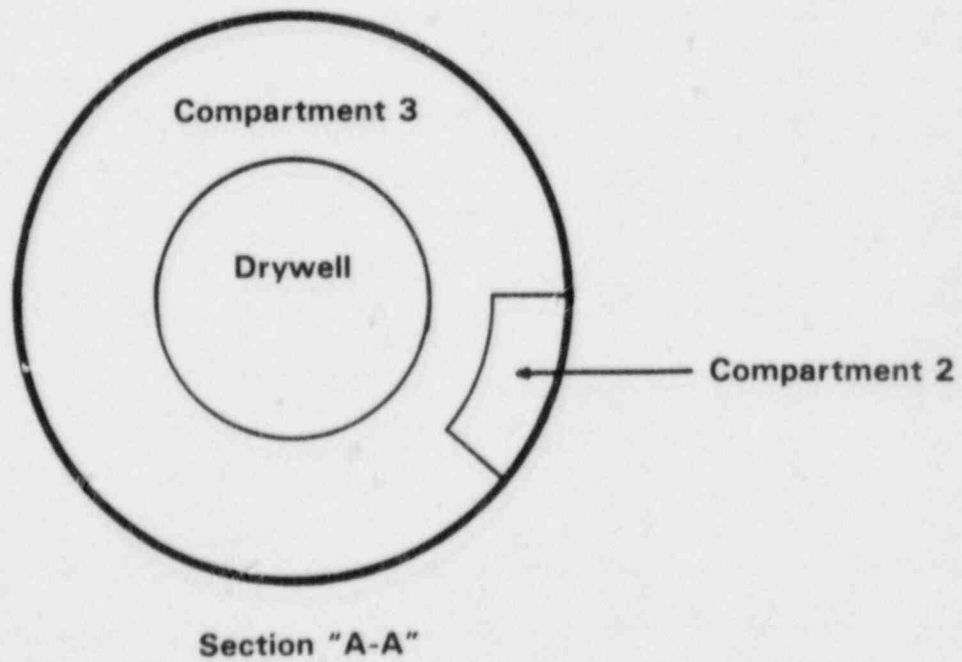
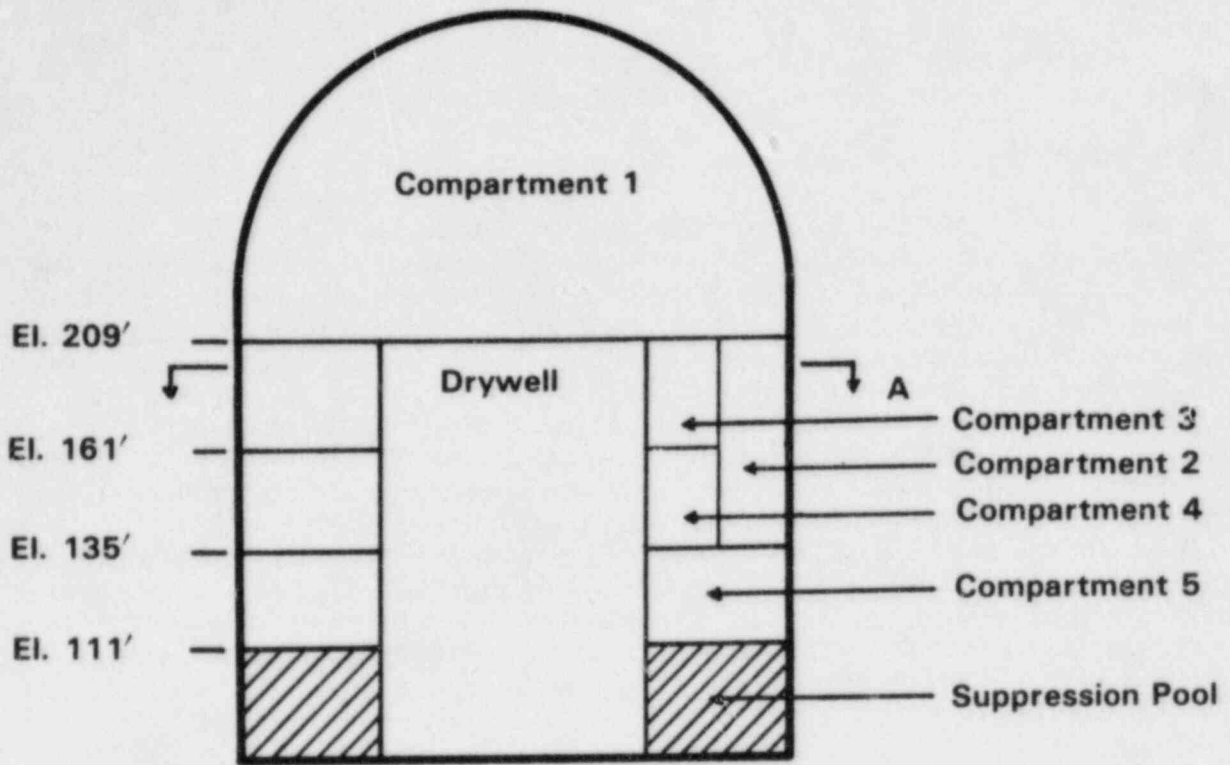


Figure 3.2. Five-Volume Compartmentalization of Grand Gulf



did not change the physics in the cases we compared, but did result in a substantial decrease in computer execution time. Further details can be obtained from the Grand Gulf report mentioned previously.

#### 3.1.1.3 NTS Calculations

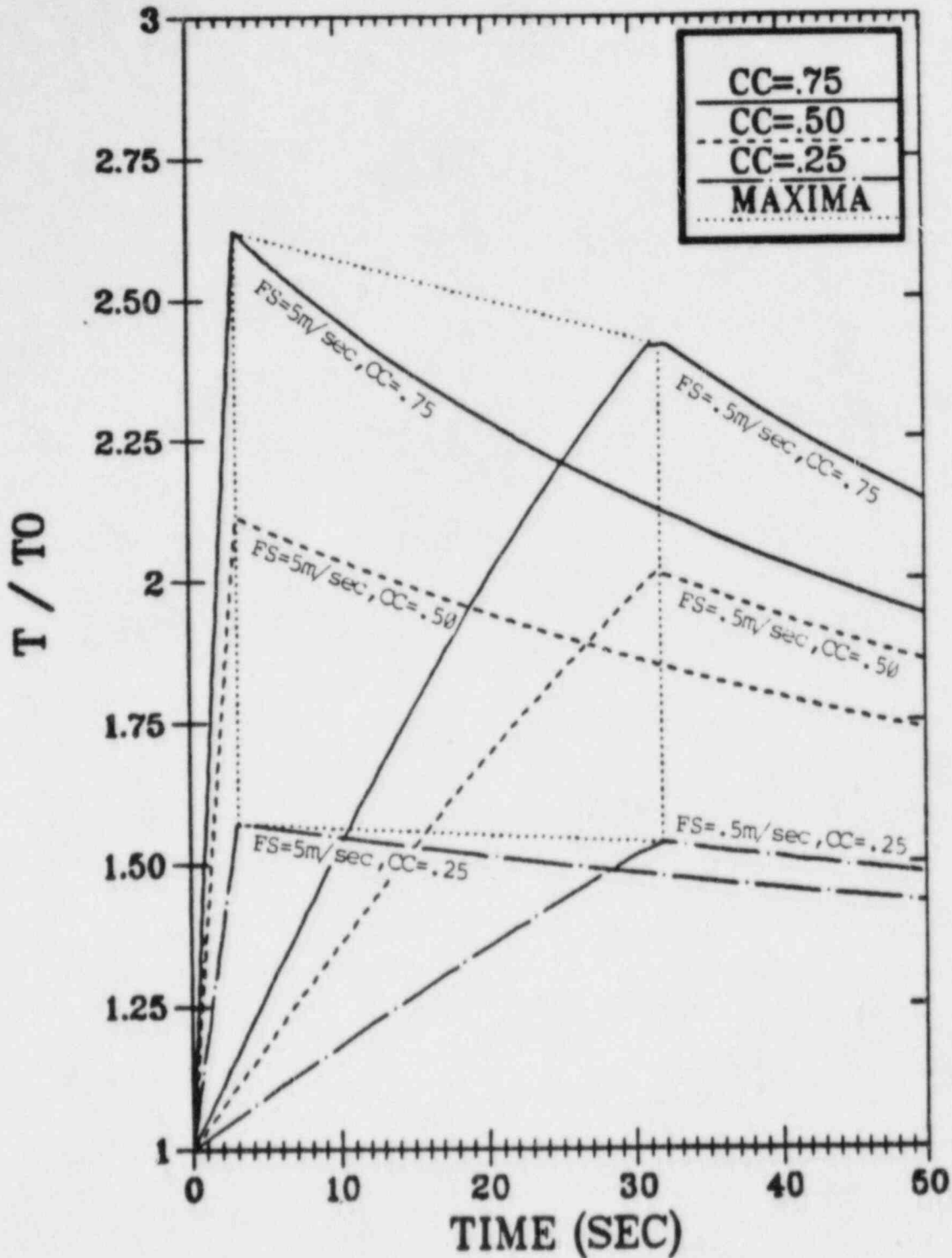
A series of large-scale experiments is being performed at the Nevada Test Site (NTS) under the sponsorship of the Electric Power Research Institute (EPRI). We performed pretest predictions for these experiments using HECTR. Because of the nature of the tests, (lean combustion with significant amounts of steam present), we feel that a great deal of uncertainty exists in the results. At smaller scales, combustion of lean mixtures can vary greatly from test to test. Because of these uncertainties, we chose to approach this problem parametrically and made several runs for each case, varying the important parameters. Flame speed (FS) and combustion completeness (CC) were varied in the one-compartment model used in the premixed test calculations. Figure 3.3 displays the temperature ratios during the burn of Test P-1. The dotted box brackets the region where the peak temperature ratio is expected to occur in the experiment. Figure 3.4 illustrates the peak temperature for P-1 as a function of the two parameters. Similar plots were generated for the rest of the premixed tests.

The same one-compartment model was used in a scoping study of the dynamic injection tests by including a global hydrogen ignition limit as an additional parameter. Although some insight was gained from these calculations, the strongest conclusion reached in this study was the necessity of a multicompartment model to predict more accurately the dynamic injection test results. Such a modeling effort will depend on the availability and usefulness of the experimental data.

Aside from the varied parameters, the greatest effect on peak temperature ratios was provided by water vapor and sprays. A high initial steam content, and the corresponding increase in gaseous heat capacity, lowered the peak temperature ratio on the order of a half of a percent per volume percent of steam. Additionally, the effect of flame speed was minor except for the spray cases, where the rapid cooling from spray evaporation was the dominant mode of heat transfer.

#### 3.1.1.4 BWR Mark III Models

We added several new models to HECTR that are needed for the Grand Gulf follow-up analysis and modified some existing models. We have also been reviewing the FSAR and containment drawings so that we can generate an input model for the analyses. The new models and modifications are described in the following paragraphs.



6% Hydrogen, 4% Steam, Bottom Ignition, FS = 5 & .5 m/sec

Figure 3.3. Temperature Ratios during Burn for Test P-1

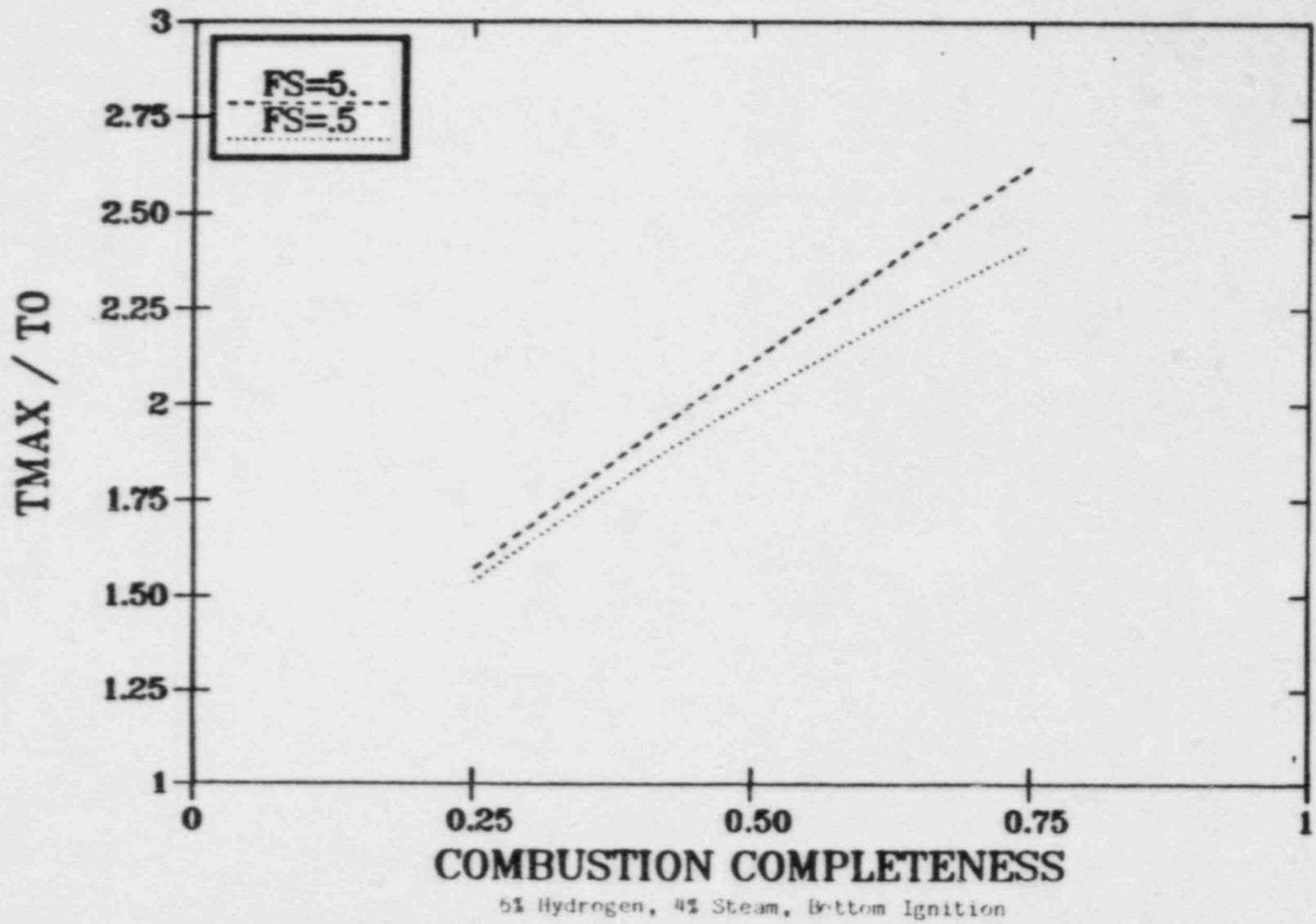


Figure 3.4. Maximum Temperature Ratios for Test P-1

We generalized the HECTR sump model so that we can model more than one sump in a calculation. Surface condensation and the liquid portion of the water sources injected into compartments can be transferred to any of the sumps. Only one sump may be specified as the source of spray and ECC recirculation water, but heat exchangers can be connected to any of the sumps to provide cooling. A sump is allowed to spill over into another sump if the capacity of the sump is exceeded.

To model the stuck-open relief valves (SORVs) in Grand Gulf, we added the capability to inject sources into a sump, instead of directly into the compartment atmosphere. We assume that any steam injected into a sump is condensed in the sump and that any noncondensable gas injected into a sump enters the connected compartment at the sump temperature.

The suppression pool is modeled as a special case of a sump. The mass and energy balances used in the sump model are used to calculate the volume and temperature of the suppression pool, but the pool motion (including the flow over the weir wall), vent flow, and upper pool dump, require additional models.

To model the suppression pool motion, we subdivide the suppression pool into nine control volumes. Conservation of mass and momentum are applied at each control volume, yielding differential equations for the velocity of the pool. These equations are then solved, giving the pool velocities and levels. The equations are valid for pool motion in both directions, so we can determine the amount of pressure relief through the suppression pool that would occur during a wetwell burn. Flow of water over the weir wall into a drywell pool and draining of this water back into the suppression pool, are modeled.

The gas flow through each suppression pool vent is modeled like a normal HECTR connection, except that the pressure at the vent outlet is modified to account for the static pressure head of the suppression pool water. Flow through the vents is not allowed to exceed the choked flow value.

The upper pool dump is modeled by transferring water from the upper pool to the suppression pool at a user-specified time in the calculation. The draining rate and minimum upper pool level are also specified by the user.

To model the purge-vent system in Grand Gulf, we added the option of inputting a head-flow curve for the fans, rather than using the default table. The vacuum breakers will be modeled as doors that open whenever the containment pressure exceeds the drywell pressure. The doors will open instantaneously to the full-open value, and will close when the pressure differential at the door reverses.

The suppression pool model is being checked by comparing against a sample problem in the CONTEMPT-LT manual and the CLASIX results for a drywell break. We do not currently have access to experimental data, so we cannot make experimental comparisons.

#### 3.1.1.5 Heat Transfer Upgrades

The heat transfer models were modified to include liquid layers on surfaces. Previously, water that condensed on a surface was instantaneously transferred to a sump, rather than being allowed to build up on the surface as a water layer. We added a model to HECTR that calculates a liquid layer thickness, which increases as water condenses on a surface and decreases as water evaporates from it. The resistance of this liquid film is included in the conduction heat-transfer calculations.

The finite difference, slab heat conduction model has been generalized to accept stacked layers of different materials. Essentially, the new method involves converting the various layers into one thermally equivalent layer of steel by scaling the layer thicknesses and thermal conductivities with the square root of the thermal diffusivity. Improvements were also made in the automatic scheme for noding finite-difference calculations. Additionally, the back side of the slab may now have an insulated, constant-temperature, or convective boundary condition.

#### 3.1.1.6 Additional Upgrades and Preparation for Code Release

We expect to release HECTR on a limited basis during the next reporting period. To accomplish this, we have begun a code cleanup effort to insure the efficiency and transportability of the coding in HECTR. The changes will make HECTR easier to run and will make the coding easier to understand. The input requirements have been modified, making the code more user-friendly. We also have expanded the output capabilities, improved the error messages, and restructured some of the sub-routines for convenience. We have generalized the modeling of sources to allow any of the gases modeled in HECTR to be injected into a compartment or sump. We expanded the saturation property tables to give greater accuracy and modified the spray model to make it computationally more rugged. We have also started drafting a user's manual to accompany the code.

#### 3.1.2 Vortex Dynamics Modeling of Flame Acceleration

(P. K. Barr, W. T. Ashurst, and J. F. Grcar)

The computer code for studying flame acceleration using the discrete vortex dynamics method has been rewritten to model flame propagation in a multichamber channel. Unlike the previous version, which investigated the interaction of the flame

with large recirculation regions within a single rectangular chamber [4], internal baffles can now be placed arbitrarily within the channel.

This model simulates flame propagation in a premixed hydrogen:air mixture confined within a two-dimensional multichamber channel. Results of flame acceleration are presented in Figure 3.5, which contains five frames from a computer-generated movie.[5] As shown in the top frame in Figure 3.5, the combustible mixture was ignited along the left wall at the closed end of the channel. The combustion of the mixture, modeled with a zero-thickness reaction front that propagates into the unburned fluid at the laminar burn velocity, results in a constant pressure expansion that forces the gas to flow over the obstacles and out the open end. This flow creates turbulent recirculation regions downstream from the obstacles, which are simulated with the discrete vortex dynamics technique. The individual vortices are shown in the figures by dashed lines, scaled to the local velocity vector. As the flame propagates into these regions, the surface area increases, which in turn increases the overall burning rate and thus enhances the flow past succeeding obstacles and leads to flame acceleration.

The various components of this computer code have been tested for accuracy and smoothness.[6] The calculated solution for flow over various obstacle geometries has been compared with exact solutions and shown to be quite satisfactory. The flame propagation algorithm, which keeps track of the movement of an interface between two fluids, has been tested for distortion of the interface shape when used to compute the movement resulting from convection of the interface, combustion at the interface at constant density, or a combination of convection of the flame as it consumes the unburned fluid.

Recent work has focused on the comparison of computational results with experimental results obtained by Calvin Chan and John Lee at McGill University in Montreal.[7,8] The experiment investigates flame propagation over several obstacles in a rectangular cross section channel, the same geometry that the code is designed to handle. The experimental results were obtained in a channel 60 cm long with a square cross section 12.7 cm on a side. The obstacles were arranged in a staggered fashion, as shown in Figure 3.6(a), and produce a blockage ratio of 0.6 at each baffle. The side walls are transparent so that high speed Schlieren photography can be used.

Figure 3.6(b) shows a Schlieren photograph of flame propagation in this experimental apparatus. In this case, the combustible gas mixture was 10.6% hydrogen:air by volume and was ignited with 13 point sources located on the left wall. Since only a portion of the geometry can be photographed in each run, the results from two experiments are shown as a composite photo.

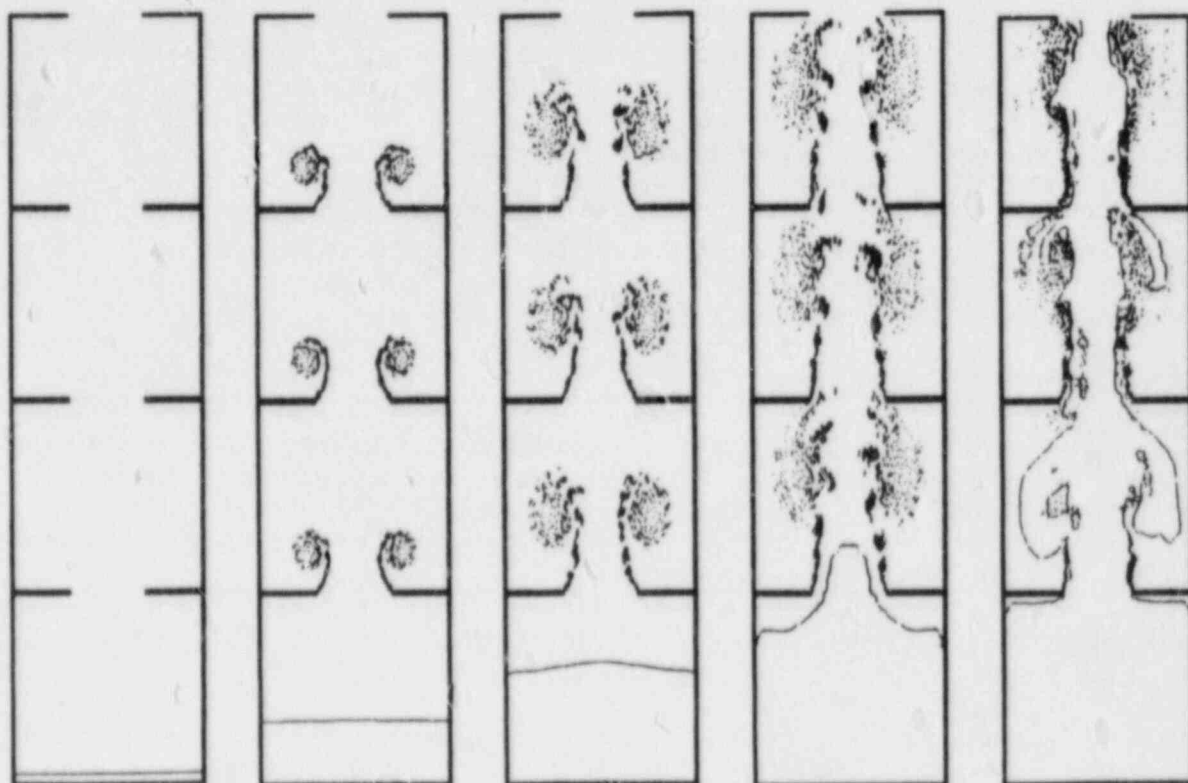


Figure 3.5. Flame acceleration through a four-chamber configuration. The distortion in the flame shape as it approaches the first set of obstacles increases the flow velocity which, combined with the vorticity, further increases the flame surface. Parameters are: volume expansion ratio of 6, flame speed of 0.2 L/t, and blockage ratio of 0.6, described on a 163-by-40 mesh. Frames are at constant intervals of 0.25 t following the initial condition.

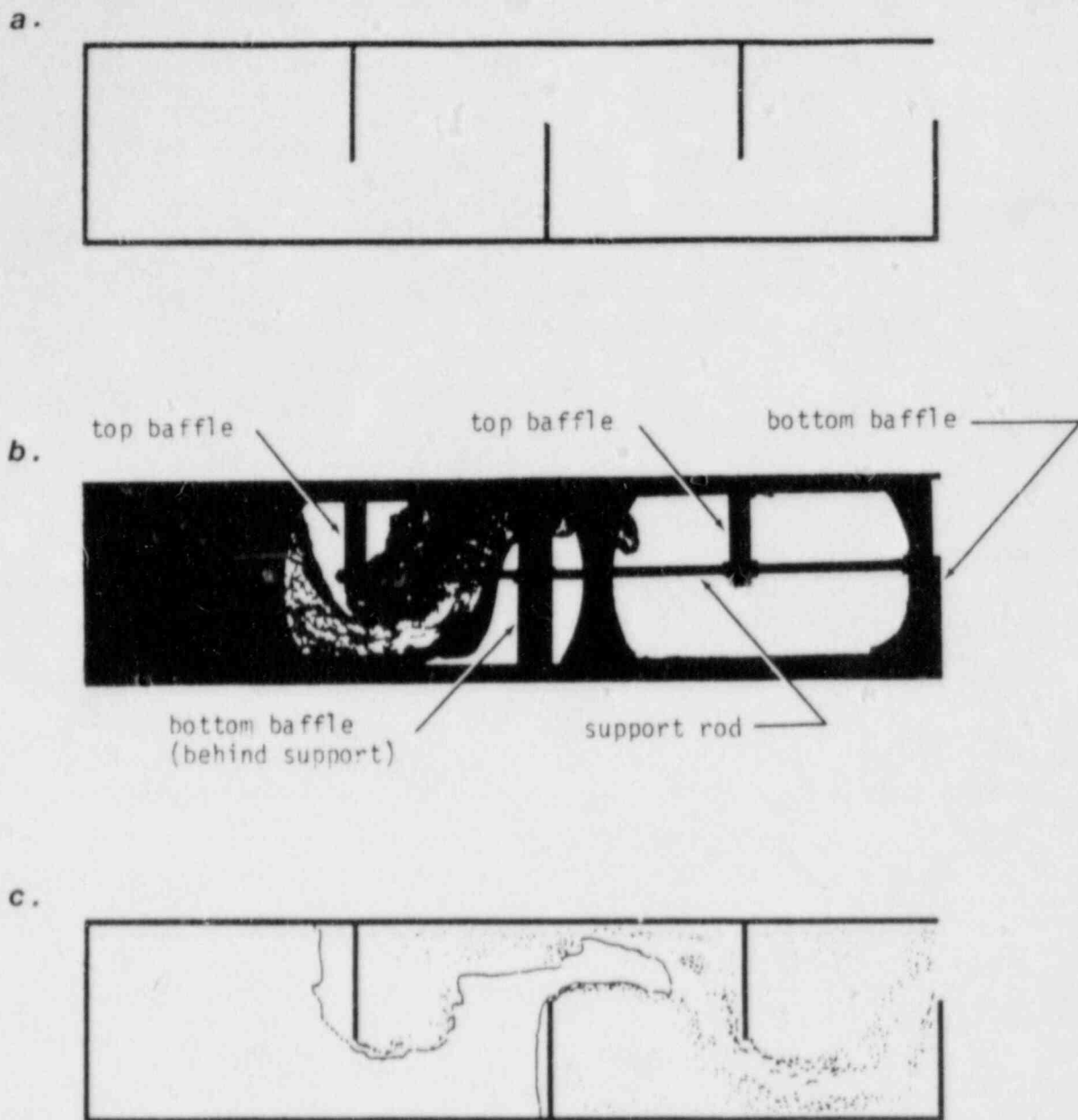


Figure 3.6. Geometry of channel and resulting flame configurations. Figure 3.6(a) shows the geometry used in both the experiments and the computations. The Schlieren photograph shown in Figure 3.6(b) represents the following conditions: 10.6% hydrogen:air and multipoint ignition along the left wall. This was simulated with the computer code by using a volume expansion ratio of 3.8 and planar ignition along left wall. Although the computed flame front shown in Figure 3.6(c) has advanced to the same downstream position as that of the experiment, the burnout within the chambers is much less.



The flame propagation through a similar configuration is computed using our vortex dynamics code. In this case, the combustible mixture is defined to have a volume expansion ratio of 3.8, corresponding to the hydrogen:air mixture in the experiment. A flame contour obtained with this model is shown in Figure 3.6(c). Note that although the flame front has advanced to approximately the same location as the experimental result shown in Figure 3.6(b), the amount of burnout in the region behind the baffle in the second chamber is much less; estimates of the amount of fluid burned in this chamber indicate that in the experimental result 70% (by volume) is burned, whereas only 50% is burned in the computational result.

The vortex dynamics model has only included what we thought to be the important effects for this application. Future work will look at whether the cause of these small-scale structures might be phenomena we have not included, such as vorticity creation by the combined action of density and pressure gradients, flame instabilities (dependent on the Lewis number), or perhaps stream-wise vorticity. This will be aided by the comparison with other experimental results.

McGill University and Sandia Livermore are continuing to exchange results. Many questions have yet to be answered; the results presented here are preliminary. For this phase of the study, we are varying our numerical parameters within physical ranges in order to test the sensitivity of our results.

### 3.1.3 Comparison of CONCHAS-SPRAY and Vortex Dynamics Flame Acceleration Calculations (K. D. Marx, P. K. Barr, and W. T. Ashurst)

The CONCHAS-SPRAY computer code has been used to simulate hydrogen flame behavior in the first four chambers of a flame acceleration experiment. The computational domain is a cylindrical tube 5.2 cm in diameter, with obstacles placed every 5 cm. The blockage ratio is 0.62. Hence, the geometry corresponds closely to some of the experiments performed at McGill University.[9] The tube is initially filled with a stoichiometric hydrogen:air mixture that is ignited by depositing energy uniformly in the first layer of zones in the closed end of the tube. This leads to an initially flat flame.

The chemistry model consists of a one-step reaction. The kinetics are defined by performing a one-dimensional adiabatic calculation with CONCHAS-SPRAY and adjusting the Arrhenius coefficients to yield a flame velocity corresponding to the experimental burn velocity of 270 cm/s for a free flame.[10] These same coefficients are then used in a two-dimensional calculation, and are assumed to produce the same burn velocity.

Isotherms are plotted in Figure 3.7 at various times during the progress of the flame. The heavy black lines correspond to a concentration of isotherms, and are an indication of the artificially increased flame thickness.[11] (The apparent flame thickness is augmented somewhat by the plotted letters H and L, which correspond to the high and low temperatures.) The high temperature contours lie very near the flame zone, rather than some distance behind the flame, where one would expect them. The reason for this is that the temperature tends to run away at the high temperature side of the flame front because of a numerical overshoot. This can be corrected by increasing the flame thickness. We believe that it has only a small effect on the flame velocity in this calculation.

This computation was carried out on a 13 x 125 finite-difference grid. Such coarse zoning resolved only the gross features of the flame. We have improved the calculation somewhat by refining the zoning (see below), and further resolution can be obtained implicitly by modeling the effects of turbulence. It should be emphasized that this is strictly a laminar calculation. The Subgrid-Scale (SGS) turbulence model, which is available as an option in the code, has been turned off for this calculation.

In addition to applying standard turbulence models (SGS,  $k-\epsilon$ , etc.), we intend to use vortex dynamics to obtain information on the effects of the larger scales of turbulence (e.g., flame folding or wrinkling). In turn, the CONCHAS-SPRAY code will supply the vortex dynamics calculation with information on compressibility effects.

Because of the intended interaction between the two computational methods, obtaining a comparison of their performance is of interest in a test calculation such as this. Hence, the simulation illustrated in Figure 3.7 was repeated with the vortex dynamics code (Figure 3.8). The only significant difference between the configurations in the two calculations was that CONCHAS-SPRAY assumed axisymmetric cylindrical coordinates, whereas vortex dynamics dealt with a rectangular geometry, which was infinite in the span-wise direction. (Also, the blockage ratio was 0.6 and the ratio of obstacle spacing to diameter was unity in the vortex dynamics calculation. However, these latter differences are virtually unnoticeable.)

Figure 3.9 shows the farthest position of the flame front as a function of time for the two methods. The lower of the two solid lines corresponds to a grid in which the spacing is halved (so the grid is 26 x 250). For both grids, CONCHAS-SPRAY predicts a more rapid acceleration of the flame early in the computation, while Vortex Dynamics catches up near the end. When the flame reaches the fourth obstacle, Vortex Dynamics predicts a flame speed of about 500 m/s compared to that of 200-300 m/s for CONCHAS-SPRAY. Note that the sound

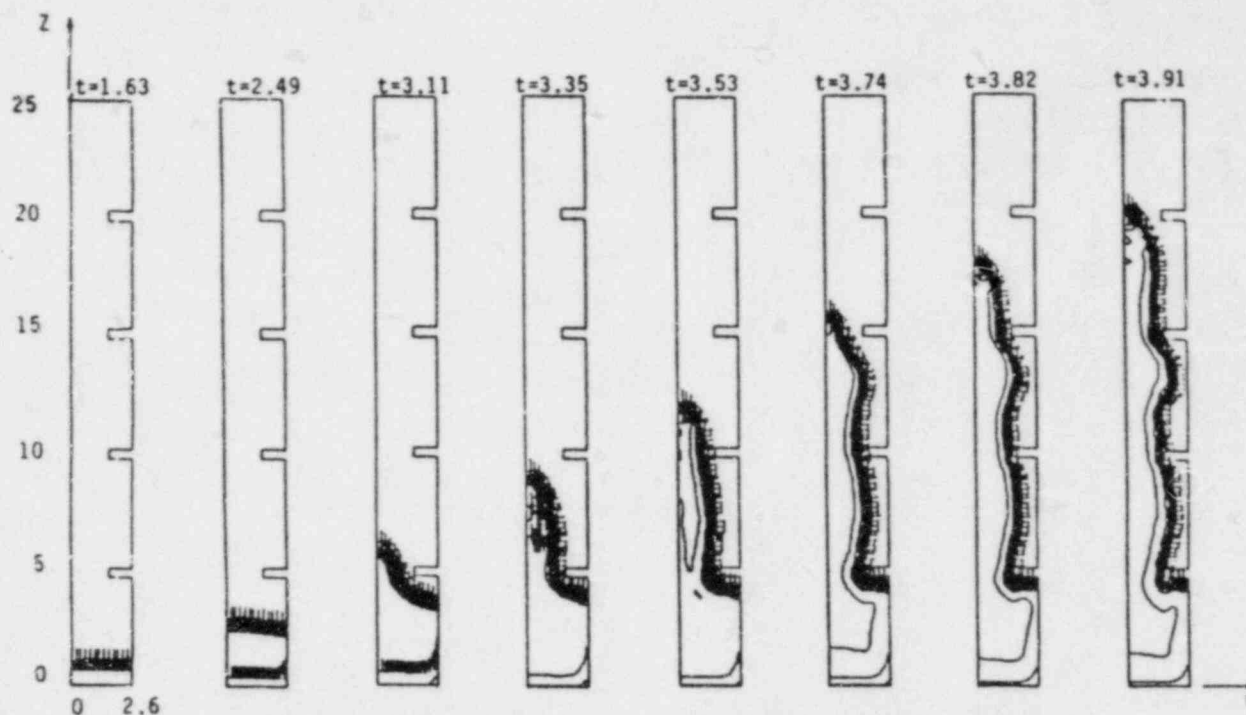


Figure 3.7. Simulation of a portion of the hydrogen flame propagation in a small-scale experiment. The combustion takes place in a tube 5.2 cm in diameter x 25 cm long. Four washer-shaped obstacles of inside diameter 3.2 cm (blockage ratio = 0.62) are spaced 5 cm apart in the tube. The plots show isotherms at times (given in milliseconds) increasing to the right. The coordinate system is cylindrical, with radial and axial dimensions given in centimeters on the first frame.

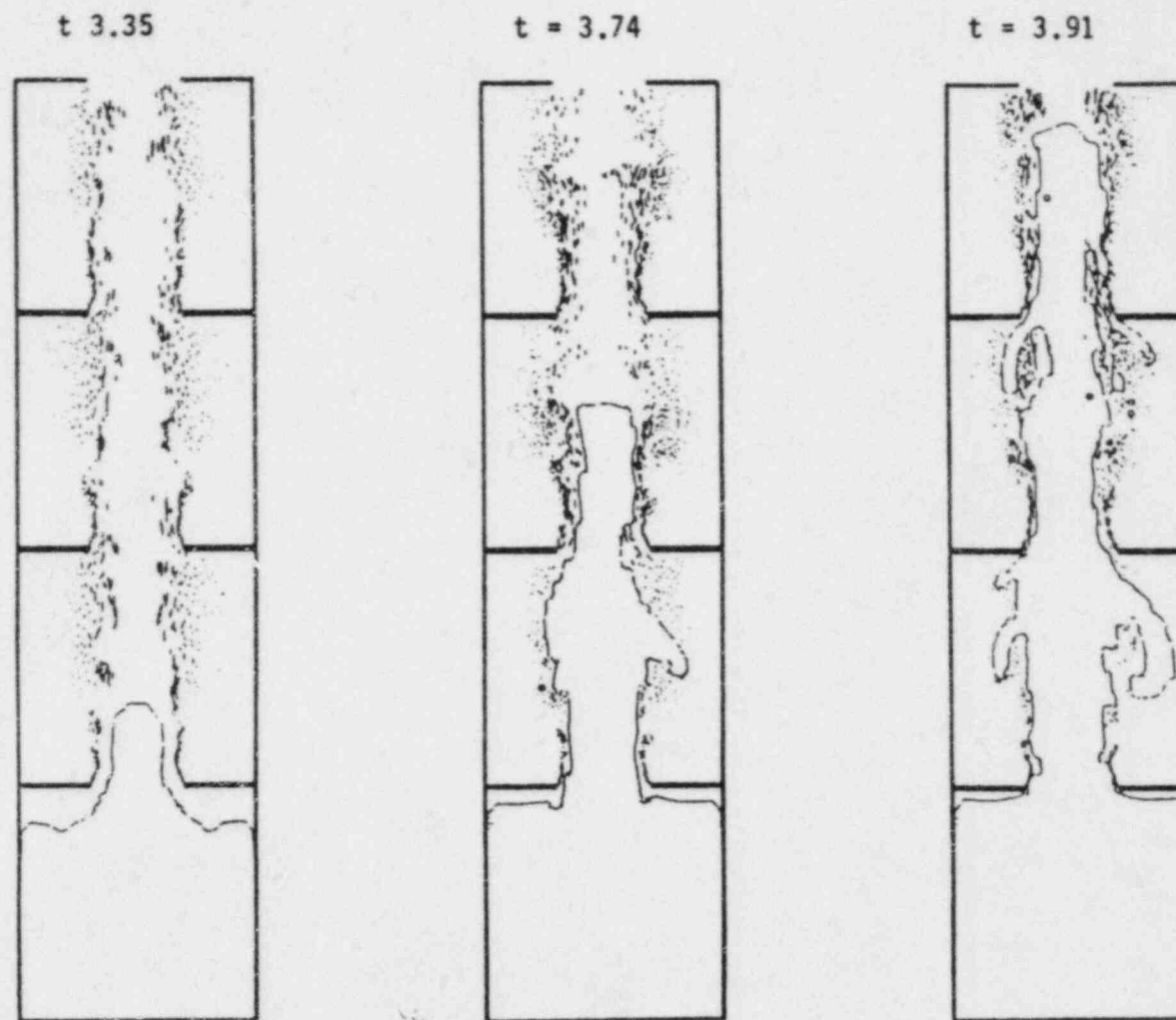


Figure 3.8. Vortex dynamics simulation of the configuration of Figure 3.7. Note the following differences: the geometry is rectangular, the width of the channel is 5.0 cm, and the blockage ratio is 0.6.

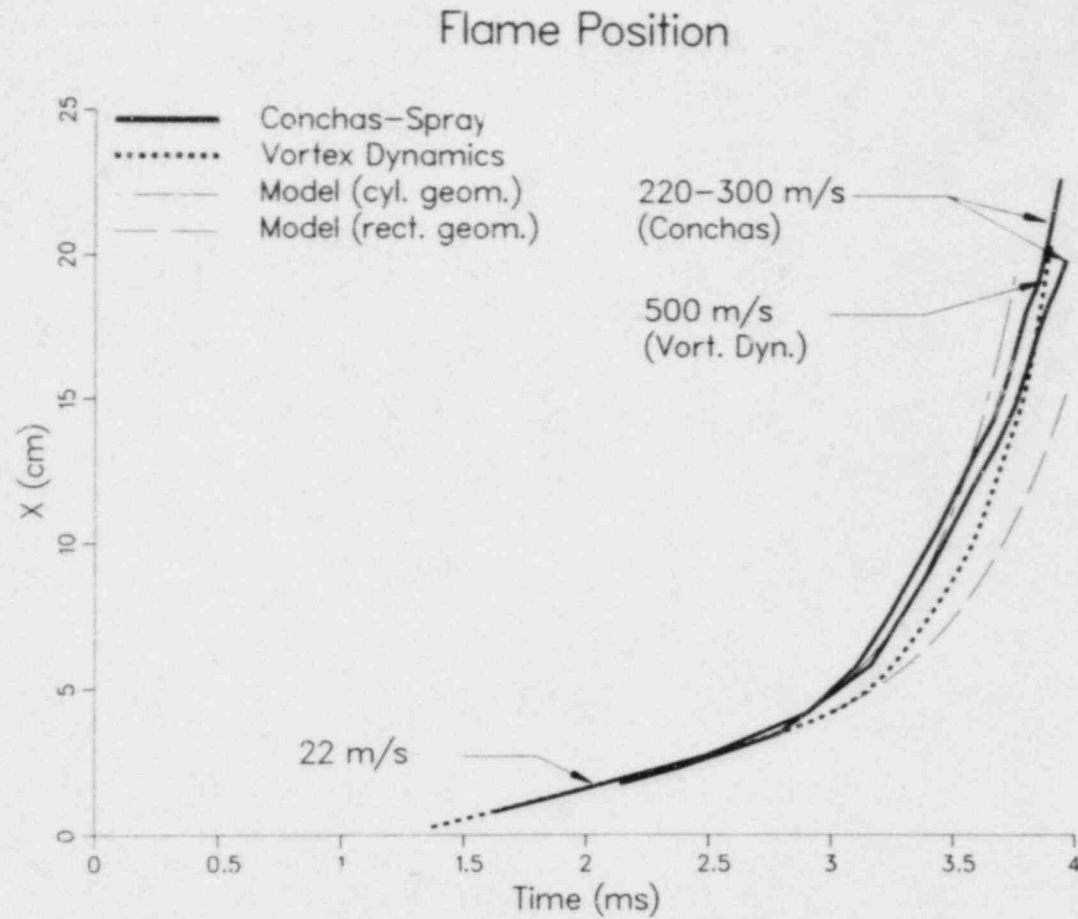


Figure 3.9. Comparison of CONCHAS-SPRAY, vortex dynamics, and simple models for the calculation of Figure 3.7. The horizontal dotted lines represent the positions of the obstacles, and the vertical dotted lines indicate the times at which the flame front passes the obstacles in the fine-mesh CONCHAS-SPRAY calculation. The flame velocities shown are those for all three computer calculations just after ignition and at the time of passing the fourth obstacle.

speed in the unburned gas is 400 m/s, so the exit gas velocity becomes supersonic at about that time. The reasons for the early rapid acceleration of the CONCHAS-SPRAY calculation are the following:

- (1) There is a difference between cylindrical and rectangular geometry.
- (2) Numerical diffusion in CONCHAS-SPRAY caused by the coarse mesh increases the flame speed. This was alleviated by refining the mesh.

The reasons for the more rapid acceleration of the vortex dynamics calculation at late times are as follows:

- (1) Vortex dynamics provides an increased overall burning rate due to flame-front distortion and large-scale turbulence.
- (2) The compressibility of the gas is ignored by vortex dynamics. This results in supersonic flow velocities which actually exceed the range of applicability of the vortex dynamics code. In the CONCHAS-SPRAY run, this flow tends to choke, and the pressure in the first chamber rises to nearly 1.4 atmospheres (regardless of mesh size) by the time the flame reaches the fourth obstacle. Hence, the density is allowed to increase by essentially that factor, thereby diminishing the flow rate from that predicted by the vortex dynamics assumption of incompressible flow.
- (3) The artificial flame thickening in CONCHAS-SPRAY is achieved by an artificial increase in thermal conductivity, which may be enhancing the heat loss to the walls.

The computer times (on the CRAY-1) required for these results were: 25 min for the coarse-grid results with CONCHAS-SPRAY, 2.8 h for the fine grid, and 40 min for vortex dynamics. The dependence on zoning is consistent with the estimate that halving the mesh size should result in an increase in run time of a factor of eight. There are factors of two for each dimension, and another factor of two because of the necessity to decrease the time step. (However, the time step remains above the Courant limitation that would hold for standard explicit methods.)

Further insight into the phenomena depicted in Figure 3.9 can be obtained by considering a very crude model. The details of the model were presented in Ref. 12. It simply calculates the position of the flame front by accounting for conservation of mass and for the volume expansion of the gas as it passes through the flame. The result is that exponential behavior is predicted for the flame velocity and the flame position

after the flame passes the first obstacle. The acceleration time constant  $t_a$  is

$$t_a = \frac{\sqrt{1 - B} R}{2 \left( \frac{T_a}{T_0} - 1 \right) u_b}$$

where  $R$  is total tube radius,  $B$  is blockage ratio,  $u_b$  is burn velocity,  $T_a$  is adiabatic flame temperature, and  $T_0$  is initial gas temperature. For the parameters used in the CONCHAS-SPRAY computation, we obtain  $t_a = 0.400$  ms.

Results of applying the simple model are shown by the chain-dashed plot in Figure 3.9. The initial conditions for the model are defined by assuming that the flame trajectory up to the time of passing the first obstacle is that of the fine-mesh CONCHAS-SPRAY calculation. The model is very sensitive to these initial conditions, so no precise quantitative judgments are possible. However, the important point is that the model predicts greater flame acceleration in the long run than does CONCHAS-SPRAY, regardless of when it started. The reasons for this are the same reasons 2 and 3 above for the same effect noted for vortex dynamics.

The above formula for the time constant is not valid for comparison with vortex dynamics, because that formula assumes cylindrical geometry. The derivation of the model, when carried out for rectangular coordinates, predicts the same exponential behavior but with the time constant given by

$$t_a = \frac{(1 - B) R}{\left( \frac{T_a}{T_0} - 1 \right) u_b}$$

where  $R$  is to be interpreted as half the width of the channel. Then  $t_a$  is equal to 0.521 ms; the resulting curve for this model is given by the chain-dotted plot in Figure 3.9. It lags the vortex dynamics computation considerably. This provides a better indication of the amount of flame acceleration that can be attributed to the wrinkling of the flame front, and illustrates the difference between rectangular and cylindrical geometry. However, not all the differences between the model and the vortex dynamics calculation can be attributed to flame distortion, because the above time constants have been computed under the assumption that the transverse dimension of the flame is equal to the inside dimension of the obstacles. A more realistic model would account for the transverse propagation of the flame into the chambers as time elapses. This would shorten the flame acceleration time constant  $t_a$ , and yield a model prediction somewhat closer to that of the numerical calculation.

In the future, we will continue to work toward an effective interaction between the CONCHAS-SPRAY and vortex dynamics approaches to the simulation of flame acceleration. As noted above, this will involve investigating ways to simulate turbulence, including the application of the Subgrid Scale,  $k-\epsilon$ , and other models. We will also define the capability of these codes to progress from the study of small-scale experiments to the larger scales of, for example, the FLAME facility.

#### 3.1.4 One-Dimensional Flame Propagation Code ODFLAME (K. D. Marx and A. E. Lutz)

The ODFLAME code has been used to model flame-water droplet interactions over a range of stoichiometries and droplet sizes.[13] The results are given in Ref. 13, and are summarized in what follows. Calculations have been performed for stoichiometric hydrogen:air mixtures and for mixtures containing 15% and 20% hydrogen by volume. Droplet diameters of 20, 100, and 400  $\mu\text{m}$  have been studied.

Figure 3.10 gives burn velocities for the different hydrogen concentrations and droplet sizes. As the volume fraction of water increases, the burn velocity decreases, until the flame is finally extinguished. This defines the propagation limits, which are given in Table 3.3 in the form of volume fraction of water required to extinguish the flame for given hydrogen concentrations and droplet diameters. The limiting volume fraction increases dramatically with droplet diameter, which agrees with experimental results.[14] This is because, for a given volume, more surface area is presented by the smaller droplets, thereby providing more effective heat transfer. Two cases that require a volume fraction of at least 2% are indicated in the table. These were not included in Figure 3.10 because the production of such large volume fractions is deemed impractical. The modeling of these cases was discontinued after determining the lower bounds of 2%.

In obtaining these results, it has been assumed that the gas exerts zero drag on the 100- and 400- $\mu\text{m}$  droplets (free-slip assumption), while the 20- $\mu\text{m}$  droplets flow with the gas without slipping. Solutions of the equation of motion for the droplets in typical gas flow velocity environments indicate that these assumptions introduce significant error in the droplet velocity only in the 20- $\mu\text{m}$  case. The no-slip assumption implies that the drops move through the flame zone faster than they actually do, thereby reducing their effect in cooling the flame. This means that the results shown here somewhat overpredict the burn velocity and the volume fraction required to extinguish the flame in the 20- $\mu\text{m}$  case.



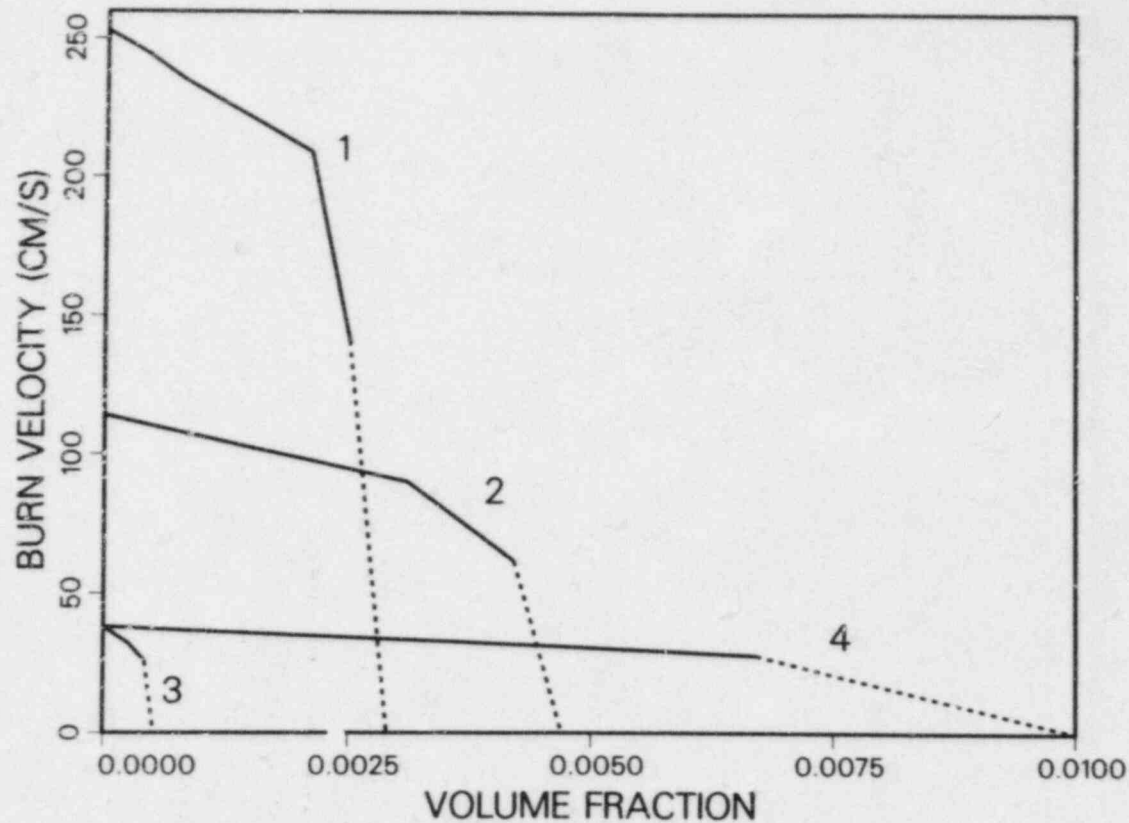


Figure 3.10. Flame velocities vs volume fraction of water for the following droplet sizes and hydrogen concentrations: 1--20  $\mu\text{m}$ , 29.5% hydrogen by volume (stoichiometric); 2--100  $\mu\text{m}$ , 20%; 3--100  $\mu\text{m}$ , 15%; and 4--200  $\mu\text{m}$ , 15%. The dashed lines represent uncertainty in the propagation limits due to the fact that only a relatively small number of computer runs have been carried out so far. Each dashed line connects the point at the largest volume fraction for which a computation predicted propagation to the point at the smallest volume fraction which resulted in extinction. Note that the rightmost point on the abscissa represents a volume fraction of 1%.

Table 3.3

Volume Fraction of Water Required to Extinguish Various  
Hydrogen:Air Droplet Configurations

% Hydrogen	$D_d$ ( $\mu\text{m}$ )	$f_v$
29.5	20	0.0029
	100	> 0.02
20	100	0.0047
	400	> 0.02
15	100	0.00052
	400	0.01

The following comments can be made regarding the accuracy of these calculations. The code has been used to simulate flames in dry hydrogen:air mixtures, and the burn velocities have been compared with both experiment [15,16] and other calculations.[16,17] There is about a 30% spread in the experimental data, and the calculations in Refs. 16 and 17 fall within that range. The burn velocities obtained in this work are about 15% greater than those in Ref. 17, but still lie within the range of the experimental data. The difference between the calculations is caused by the numerical diffusion inherent in the upwind differencing method used. It could be alleviated by refining the finite-difference grid at the expense of additional computer time. The burn velocities that we obtain for moist air are consistent with those of Liu and MacFarlane [15], but no direct comparisons can be made.

Recent experiments on fogs and sprays at intermediate scales indicate results very different from those shown in Figure 3.10. The turbulence created by the larger droplets actually results in a significant increase in flame speeds and completeness of combustion. In the absence of a model for droplet-induced turbulence, the code predictions for flame extinction are not valid for droplet sizes of tens or hundreds of microns. As in much of the flame acceleration research, the experimental data indicate that combustion is strongly affected by three factors: chemistry, fluid mechanics, and heat transfer. For propagation of a flame through a droplet-filled combustible atmosphere, the fluid mechanical effects have been shown to dominate for droplet sizes and densities of interest in reactor safety. Hence, based on current experimental data, the ODFLAME code is of limited applicability; no further development of this code is anticipated.

### 3.1.5 CSQ Detonation Calculations (R. K. Byers)

Four CSQ calculations were performed with an axisymmetric model for the wetwell and upper compartment regions of the GESSAR II containment design. Mixtures of dry, sea-level air and hydrogen were assumed to fill the containment model; initial hydrogen mole fractions were 0.18 and 0.22. For each mixture, ignition was specified to occur at a point at the center of the drywell head, or in a ring near the center of the wetwell approximately 5 m above the surface of the suppression pool. All boundaries were defined as impermeable, and the region of interest was divided into square cells 0.36 m on a side. Figure 3.11 shows the boundaries and ignition locations for the two pairs of calculations. As in the Grand Gulf analysis, the wetwell boundaries were made irregular because of the various obstructions to flow. Table 3.4 contains the thermodynamic parameters of interest for the two mixtures. These hydrogen concentrations in the volume modeled would require the release of about 532 and 684 kg of hydrogen.

Figures 3.12 and 3.13 display pressure histories at the center of the dome for the richer mixture and the two ignition locations. In the case of the central detonation in the upper compartment (Figure 3.12), a familiar phenomenon is observed: interaction of reflected waves after complete detonation produced the maximum pressure at the center of the dome. With ignition in the wetwell, the converging detonation wave in the upper compartment yielded the peak pressure (again at the dome center) on its arrival at the boundary. Impulse histories at the dome center for these two calculations are shown in Figures 3.14 and 3.15; the 9.5 ms interval over which the impulse was calculated is very probably shorter than a quarter-period for this structure, but this value was already incorporated in the relevant plot program. The smaller regions, and "obstructions," in the wetwell produced fairly complicated pressure histories, as shown in Figure 3.16. The results for the calculations with the leaner mixture were of course quite similar to those already described, differing only in magnitudes and timing. Table 3.5 summarizes a few of the results of all four calculations.

It is difficult at this time to assess the threat posed by the pressures observed in the CSQ results. Note, however, that the Sequoyah upper compartment--which is also a virtually free-standing shell--has been quoted by Mark as being able to withstand a total pressure of roughly 0.36 MPa in static loading.[18] The difference in minimum shell thicknesses (~ 13 mm for Sequoyah and ~ 32 mm for GESSAR) would indicate a corresponding value of about 0.9 MPa in this case; the late-time pressures in the calculations are not far from this. In addition, the period of the reverberations in the upper compartment may be near that of the fundamental breathing

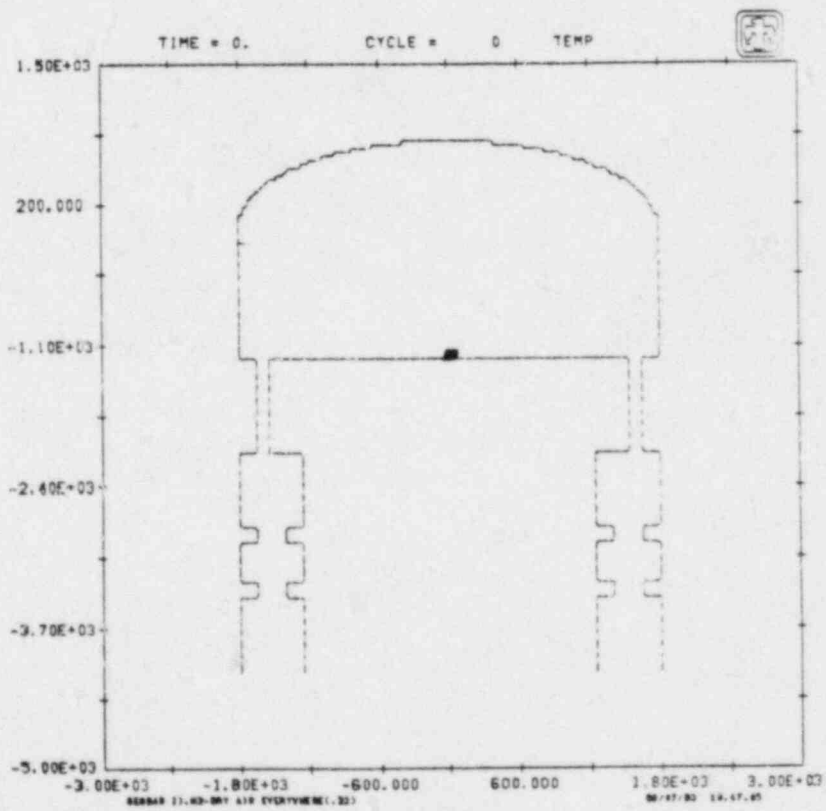
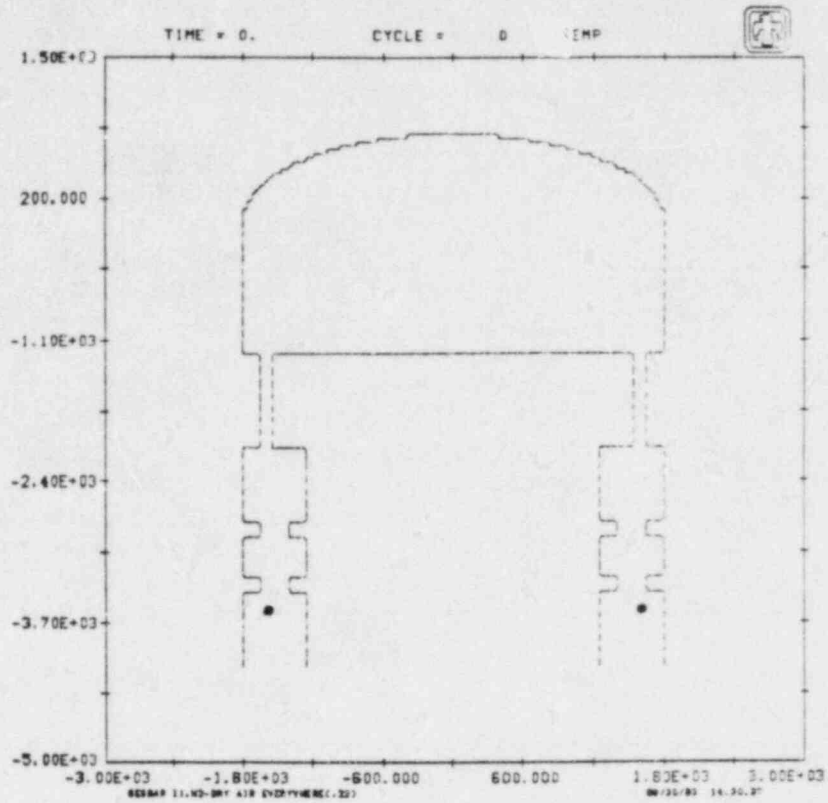


Figure 3.11. CSQ Model for GESSAR II and Ignition Locations

Table 3.4

## Thermodynamic States for Hydrogen: Dry Air Mixtures

	Initial Hydrogen Mole Fraction ( $\phi$ )	
	0.18	0.22
<u>Initial Conditions<sup>a</sup></u>		
Temperature (K)	315	315
Pressure (MPa)	0.135	0.142
Density (kg/m <sup>3</sup> )	1.245	1.250
<u>Isochoric Burn</u>		
Temperature (K)	2057	2364
Pressure (MPa)	0.804	0.885
<u>Chapman-Jouquet Detonations</u>		
Temperature (K)	2277	2589
Pressure (MPa)	1.548	1.842
Density (kg/m <sup>3</sup> )	2.164	2.204
<u>Isentrope from C-J State to Initial Density</u>		
Temperature (K)	1991	2295
Pressure (MPa)	0.778	0.923

<sup>a</sup>Air partial pressure is 0.1 MPa.

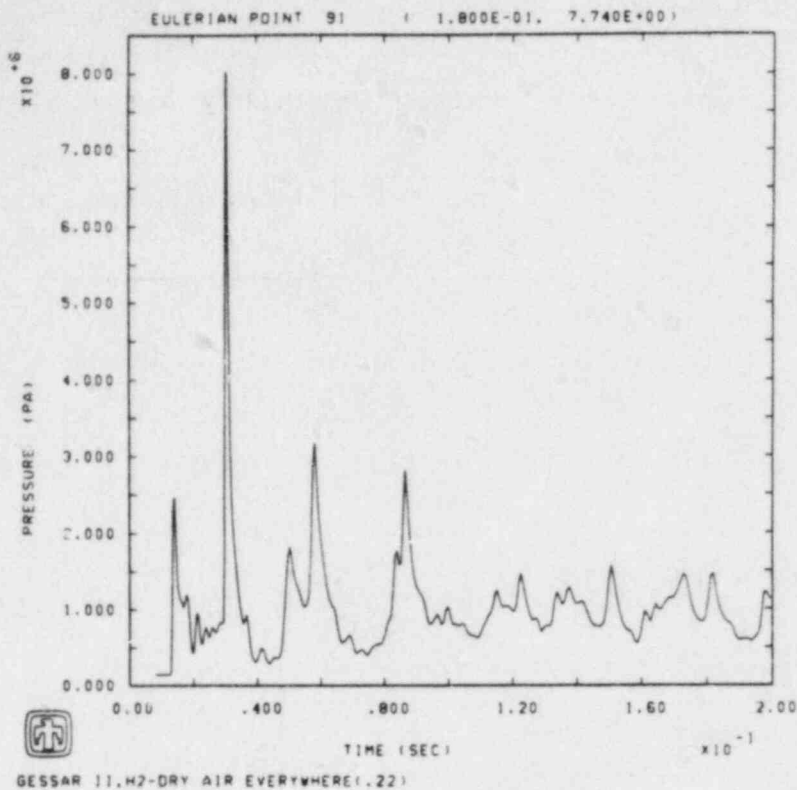


Figure 3.12. CSQ Pressure at Center of Dome (Central Ignition)

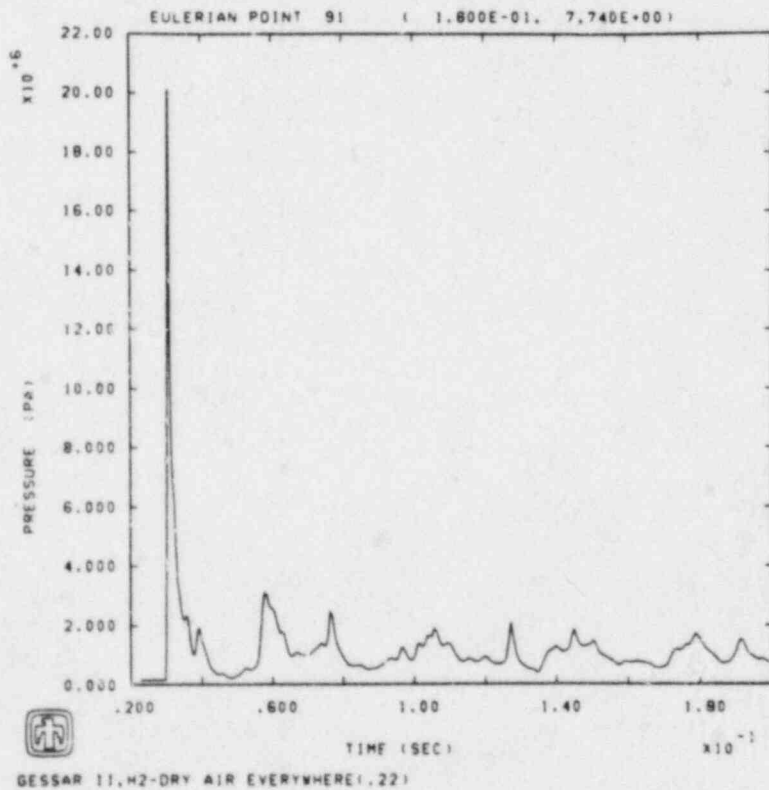


Figure 3.13. CSQ Pressure at Center of Dome (Wetwell Ignition)

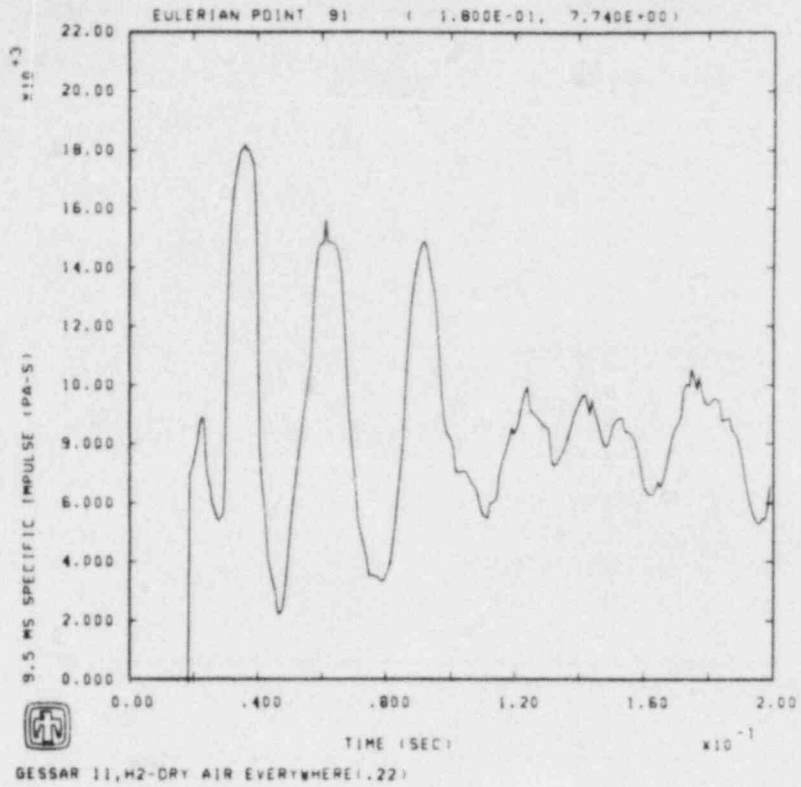


Figure 3.14. CSQ Specific Impulse at Center of Dome (Central Ignition)

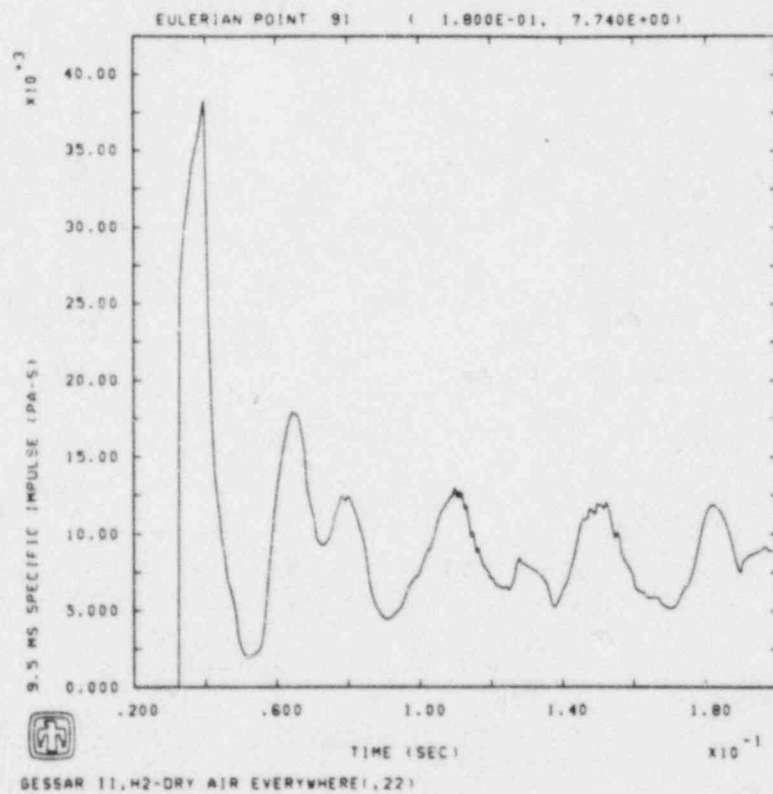


Figure 3.15. CSQ Specific Impulse at Center of Dome (Wetwell Ignition)

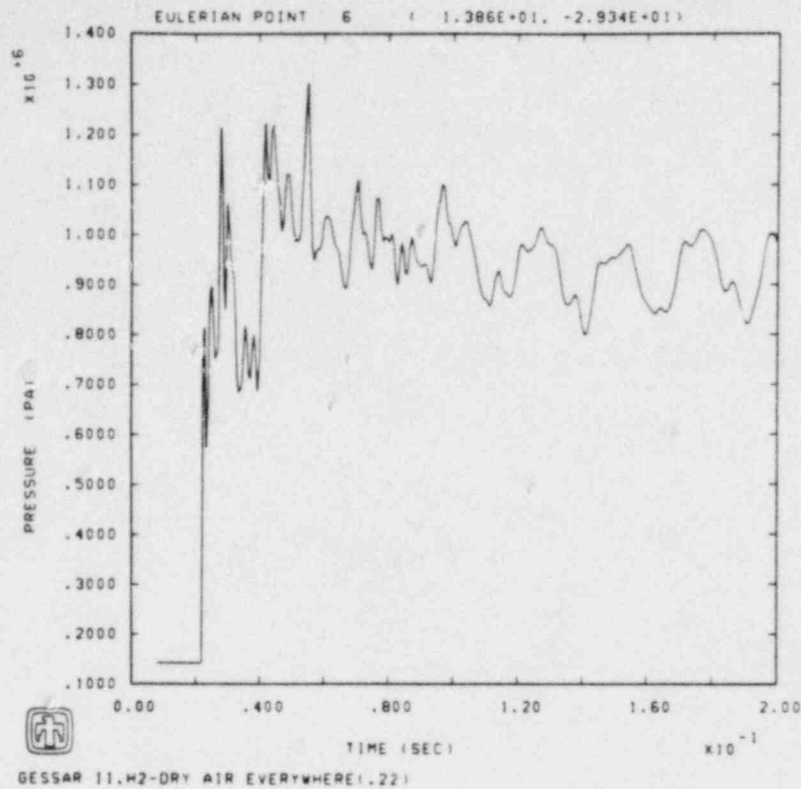


Figure 3.16. CSQ Pressure in Wetwell

Table 3.5

GESSAR II CSQ Calculations  
Hydrogen: Dry Air Mixtures at Hydrogen Mole Fractions  
of 0.18 and 0.22

	Dome Center		Dome Wall Joint		Center of Drywell Roof	
	Peak Pressure (MPa)	Impulse (kPa•s)	Peak Pressure (MPa)	Impulse (kPa•s)	Peak Pressure (MPa)	Impulse (kPa•s)
Detonation at Center of Drywell Roof <sup>a</sup>						
Hydrogen Mole Fraction						
0.18	6.2	16	3.5	11	4.5	19
0.22	8.0	18	3.6	13	5.3	22
Detonation in Wetwell						
0.18	13.5	33	1.7	10	4.7	14
0.22	20	38	2.0	11	5.9	16

<sup>a</sup>Impulses are for 9.5 ms intervals; very probably too short.



mode of the structure. As has so often been the case, it appears that some dynamic structural analyses are called for.

A "release package" containing our special version of CSQ and related codes is being prepared so that similar detonation calculations may be performed outside Sandia. Work on documenting the use of these codes is also in progress.

### 3.2 Experimental Facilities, Tests, and Plans

#### 3.2.1 FITS Facility

(B. W. Marshall and A. C. Ratzel)

During this semiannual period, two areas of testing were pursued at the FITS facility. The hydrogen:air:steam flammability series of combustion tests for the Hydrogen Combustion Behavior program continued. Sixty-two combustion tests were conducted consisting of hydrogen volume percentages ranging from 5 to 60% and steam percentages of 9 to 48%. All tests were conducted in a turbulent (fans on) environment, with air partial pressures of approximately 82.7 kPa (12 psi) and pre-ignition temperatures of 110°C or above. In Figure 3.17, the preliminary flammability results of these combustion tests are shown, where "O" represents a mixture that ignited and "X" represents an inerted mixture.

The second area of testing at the FITS facility addressed the importance of a thermal barrier to the operation of three pressure transducer types used in past combustion testing. In particular, the effectiveness of felt metal as a thermal barrier in the hydrogen combustion atmosphere was of interest. The three transducer types evaluated include (1) the Precise Sensor model 111-1, which had been used almost exclusively in the Hydrogen Behavior Program's (HBP) first series of combustion tests and in the series of tests performed for the Hydrogen Burn Survivability (HBS) program, (2) the Precise Sensor model 141-1, which was used primarily in the second and the third series of burns for the HBP, and (3) the Kulite model XT-190, which has been used periodically throughout all of the test series at the FITS facility.

Multiple gauge protection (with and without felt metal flame arresters), different tank locations, and various gas cooling conditions for the Precise Sensors were evaluated in an effort to isolate any thermal responses induced by the combustion. The testing was divided into two major segments. The first of these was an evaluation of two Kulite transducers (felt metal employed on both) and four Precise Sensor model 141-1 gauges (two of the gauges protected and the other two gauges unshielded from the hot gases). In the second segment of testing, one Kulite transducer with thermal protection (i.e., with felt metal), two Precise Sensor model 141-1 gauges and two Precise Sensor model 111-1 gauges with and without thermal protection were compared. A complete report outlining the

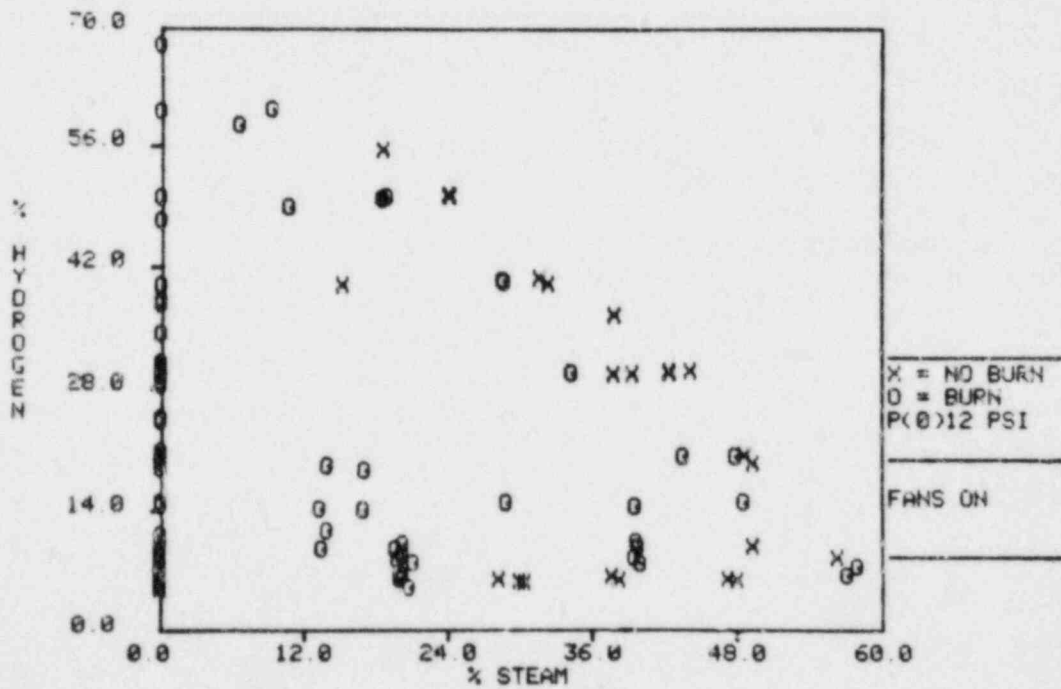
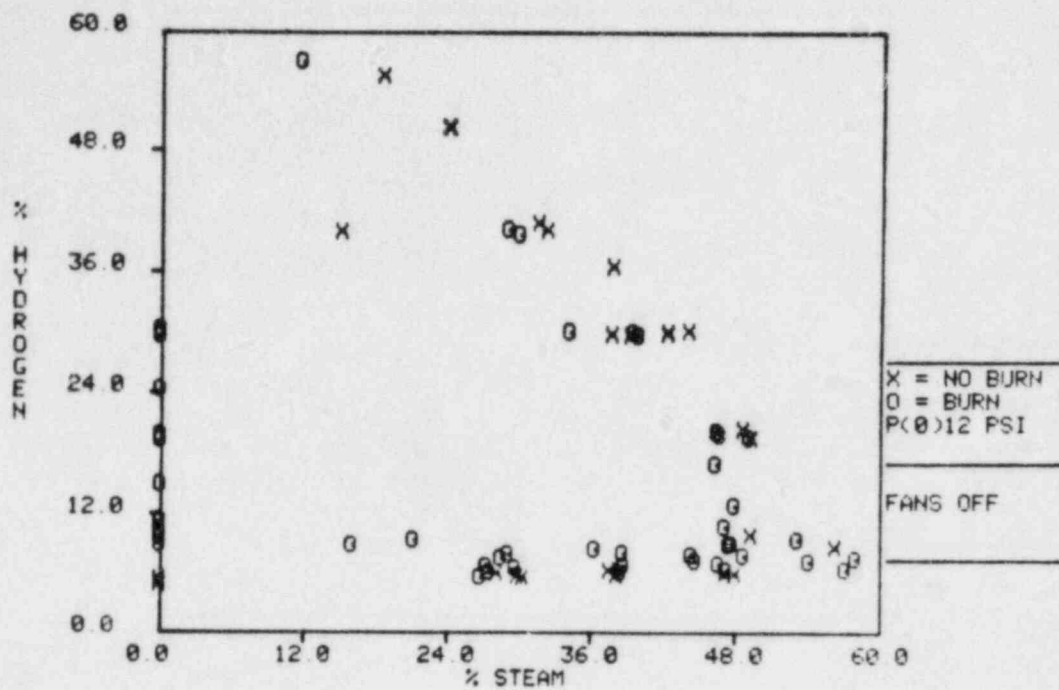


Figure 3.17. Hydrogen:Air:Steam Flammability Limits

experimental procedures, gauge set-ups in the FITS tank, and discussion of the results is being prepared. The preliminary conclusions drawn from this pressure transducer testing are:

- (1) The Kulite model XT-190 gauges record data that is relatively independent of tank location, as one would expect. Additionally, these gauge responses approach, but never exceed, the Adiabatic Isochoric Complete Combustion (AICC) calculations as hydrogen concentrations approach stoichiometry, again as would be expected. These gauges must always be thermally shielded from the hot gases of combustion.
- (2) The Precise Sensor model 111-1 gauges appear to be much more sensitive to the combustion gas temperatures than are the other two gauge types. The unprotected model 111-1 records a thermally induced output in addition to the combustion pressure-induced response. When thermally protected, this gauge type matched the pressure responses of the Kulite and Precise Sensor 141-1 gauges reasonably well.
- (3) The Precise Sensor model 141-1 gauges record data that is consistent with the thermally shielded Kulites and model 111-1 gauges, whether thermal protection is employed or not. The data recorded by this gauge appears to be relatively independent of tank location and approaches the AICC predictions as hydrogen concentrations approach stoichiometry, again as would be expected.

As a result of this study, we now believe that we know how to use the thermally protected Kulite gauges and the Precise Sensor model 141-1 gauges (with or without thermal protection) to record consistent, believable combustion pressure data. The model 141-1 gauge appears to provide reasonable pressure traces with or without thermal protection, although the felt metal protection would be advantageous in all future testing. The felt metal protection does not significantly change the shape of the transient combustion pressure trace, the peak pressure magnitude, or the associated burn time, based on the test data recorded for protected and unprotected model 141-1 Precise Sensors. The felt metal seems to be a very good thermal barrier as shown by the model 111-1 Precise Sensor results, and should be used whenever possible with all transducer designs. Based on this work, in fact, the Precise Sensor model 111-1 and Kulite XT-190 transducers should always be thermally shielded from the residual hot gases of combustion to obtain consistent believable results.

The Steam Explosion program moved into the FITS tank in mid-September for a series of tests. The HBP is tentatively scheduled back into the FITS tank in the spring of 1984.

### 3.2.2 Review of the HCOG and NTS Hydrogen Combustion Experiments

(J. C. Cummings and J. E. Shepherd)

As technical consultants for the Research and Regulatory Branches of the U.S. NRC, we are reviewing the Hydrogen Control Owner's Group (HCOG)\* and the Nevada Test Site (NTS) large-scale experimental programs on hydrogen combustion. The HCOG program consists of igniter tests in hydrogen-rich environments, a 1/20-scale facility for flow and flame visualization, and a 1/4-scale facility for accident simulation. The NTS program consists of both premixed and continuous-injection (of steam and hydrogen) tests in a heated, 52-ft-diameter steel dewar. We are assisting in the technical review of the program plans as well as assessment of experimental results and analyses. Extrapolation of results to full-scale reactor containment accidents is the ultimate goal of both programs.

We previously reviewed the HCOG proposal and documented our comments in a report to the NRC. HCOG submitted a progress report to the NRC that addressed several of our concerns. The NRC asked us to comment on this HCOG submittal and to determine if our previous concerns had been adequately resolved. We responded with a letter to the NRC discussing the HCOG proposals for small-scale igniters and chamber venting in the 1/20-scale facility. The issue of heat transfer scaling laws (HCOG has proposed the use of Froude modeling to scale results) was also considered. We noted the significant differences that can exist between local and global heat transfer coefficients.

We also attended review meetings at NRC in Bethesda, Maryland, and at EPRI in Palo Alto, California. Experimental data from the HCOG 1/20-scale tests and the NTS preliminary test series were presented and discussed at these meetings. We are writing a letter report to the NRC regarding our assessment of the HCOG 1/4-scale test plan and the thermal environment analyses used to address equipment survivability questions (based upon heat flux and temperature data from the 1/20-scale tests). We anticipate attending future NTS meetings in order to assist in the definition of their experimental test matrix.

### 3.2.3 Velocity Measurements in a Hydrogen Combustion Tank (J. C. Cummings, J. E. Shepherd, and O. B. Crump)

We are preparing to measure average velocities and turbulence intensities as a function of spatial location inside a tank used to conduct hydrogen:air combustion experiments. Two fans are often employed during combustion experiments to create a

---

\*The HCOG is a consortium of owners of Mark III BWRs.

"turbulent environment" into which the flame propagates. Consequently, one of our near-term objectives will be to characterize that preburn environment.

We have completed our hot-wire and hot-film anemometer calibrations in a new wind tunnel apparatus. Calibrations were recorded over a velocity range of 30-150 cm/s and a temperature range of 20-30°C. Mean flow velocities were referenced to pitot-probe data and also compared to velocities computed from vortex shedding frequencies (using a circular cylinder upstream of the anemometer). We have designed and constructed a traversable "rake" to hold six hot wires or hot films. This device will be inserted into the VGES tank in the near future. Preparation of our data acquisition system and software has also been completed.

#### 3.2.4 Combustible Gas in Containment Program (V. Loyola)

The Combustible Gas in Containment Program was started in FY80 to investigate the production of hydrogen gas in containment buildings following a LOCA. This program was specifically intended to focus on hydrogen production from corrosion of Zn in contact with ECCS solutions at post-LOCA conditions. The emphasis in the program was changed in January of 1982 after it was discovered that, even in minor LOCA's, other sources of hydrogen (core reactions, concrete reactions, etc.) within containment dwarfed the contribution from zinc. The change focused more attention on the production of solid products, which could foul sump pumps and/or other parts of the ECCS, and less on the reactions of Zn and ECCS solutions.

During the period April through September, 1983, the program focused on the production of hydrogen and solid products from reactions of ECCS solutions and zinc rich coatings (paints) which are typical of those used in nuclear power plants. Two series of coatings were tested: one which consisted only of a zinc-rich primer coat; another which consisted of the same primer coat, but which had a modified phenolic top coat. The coatings were tested in two different environments: one in which the samples were completely immersed in the solution of interest; another in which the samples were suspended above the solution and subjected to a continuous exposure to steam and droplets (i.e., spray) of the solution of interest.

The results of the testing in immersed conditions show that at temperatures  $\geq 132^\circ\text{C}$ , the conditions are too severe for both series of coatings and that drastic failure can be expected. The primer coat alone fails by releasing large quantities of reaction product (X-ray diffraction and photoelectron spectroscopy indicate that it is ZnO) which settles to the bottom of our test vessel when not agitated. The top-coated samples fail via a delamination of the phenolic coat and also produce large quantities of solid product. The

results of the testing in spray conditions show that failure again occurs at  $\geq 132^{\circ}\text{C}$ . The topcoated samples exhibit a high degree of cracking of the topcoat and areas where large bubbles form; however, the topcoat has a tendency to remain attached to the substrate and very little solid product is found in the bottom of our vessel. The primer-coated samples show evidence of rust coming through the primer coat, suggesting corrosion at the steel substrate, but very little solid product is found in the vessel. A more detailed discussion of our results will be forthcoming in a final topical report.

Funding for the Combustible Gas Program was discontinued as of the end of FY83, formally ending the program. The only remaining activity is the compilation of the results in a final report.

### 3.2.5 Effects of Aerosols on Hydrogen:Air Combustion (L. S. Nelson and W. B. Benedick)

Eight scoping experiments were performed in the VGES tank to study the effects of aerosols on hydrogen:air combustion. The aerosols used were iron oxide or aluminum oxide powders. The powders were dispersed with a commercial dry chemical fire extinguisher placed at the bottom of the VGES tank with the nozzle directed upward. Experiments were performed in 10% and 20% hydrogen:air premixtures at local atmospheric pressure (0.083 MPa). Pressure transducers and a tree of thermocouples were used as active diagnostics during the combustion. An exploding wire was used to ignite the mixtures.

The hydrogen:air mixtures were ignited exactly at the time the wire exploded, indicating that: (i) static charges generated during the powder discharge did not cause early ignition; (ii) catalytically-caused preignition did not occur as the aerosol was injected into the chamber; and (iii) ignition was not delayed because of the presence of the aerosol in the chamber.

The presence of the aerosol during the combustion apparently caused a modest decrease of the peak pressure recorded during the combustion, as shown in Figure 3.18. However, the presence of the aerosol significantly reduced the maximum temperature recorded on the thermocouples immersed in the combusting gases, as shown in Figure 3.19. The reduction in temperature seems to be proportional to the weight of powder discharged for both combustible mixtures, as is shown in Figure 3.20. Note that the recorded peak temperature rises decreased approximately linearly with increasing aerosol concentration for both the 10% and 20% mixtures. Moreover, the changes do not seem to depend on the chemical nature of the aerosol (when iron oxide and aluminum oxide are compared). Experiments similar to these, both field and laboratory scale, are planned for the next year.

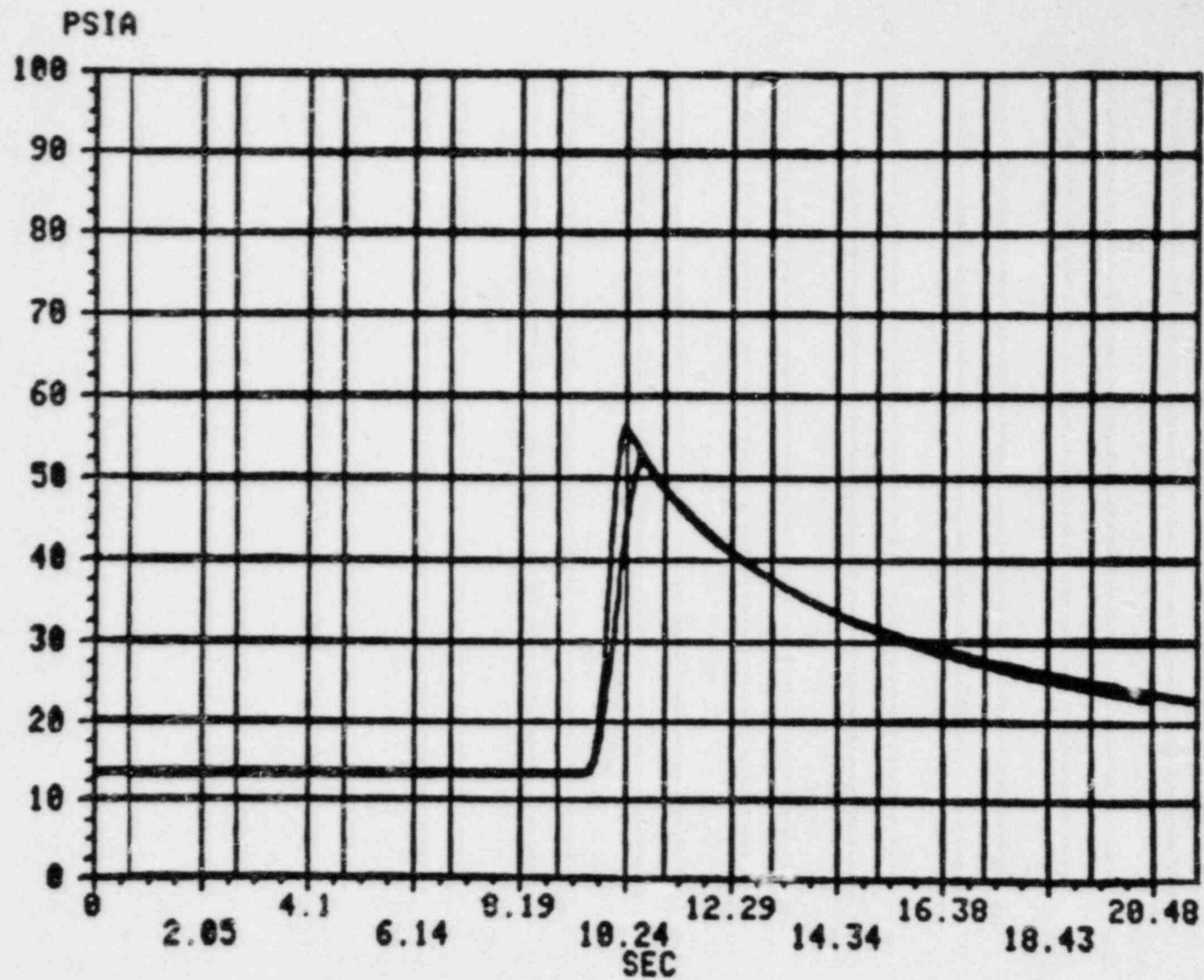


Figure 3.18. Comparison of pressure records (P2A) made during hydrogen combustion with (14-45-1; B11H12) and without (14-43-1; B9H12)  $\text{Fe}_2\text{O}_3$  aerosol, lower and upper traces, respectively.

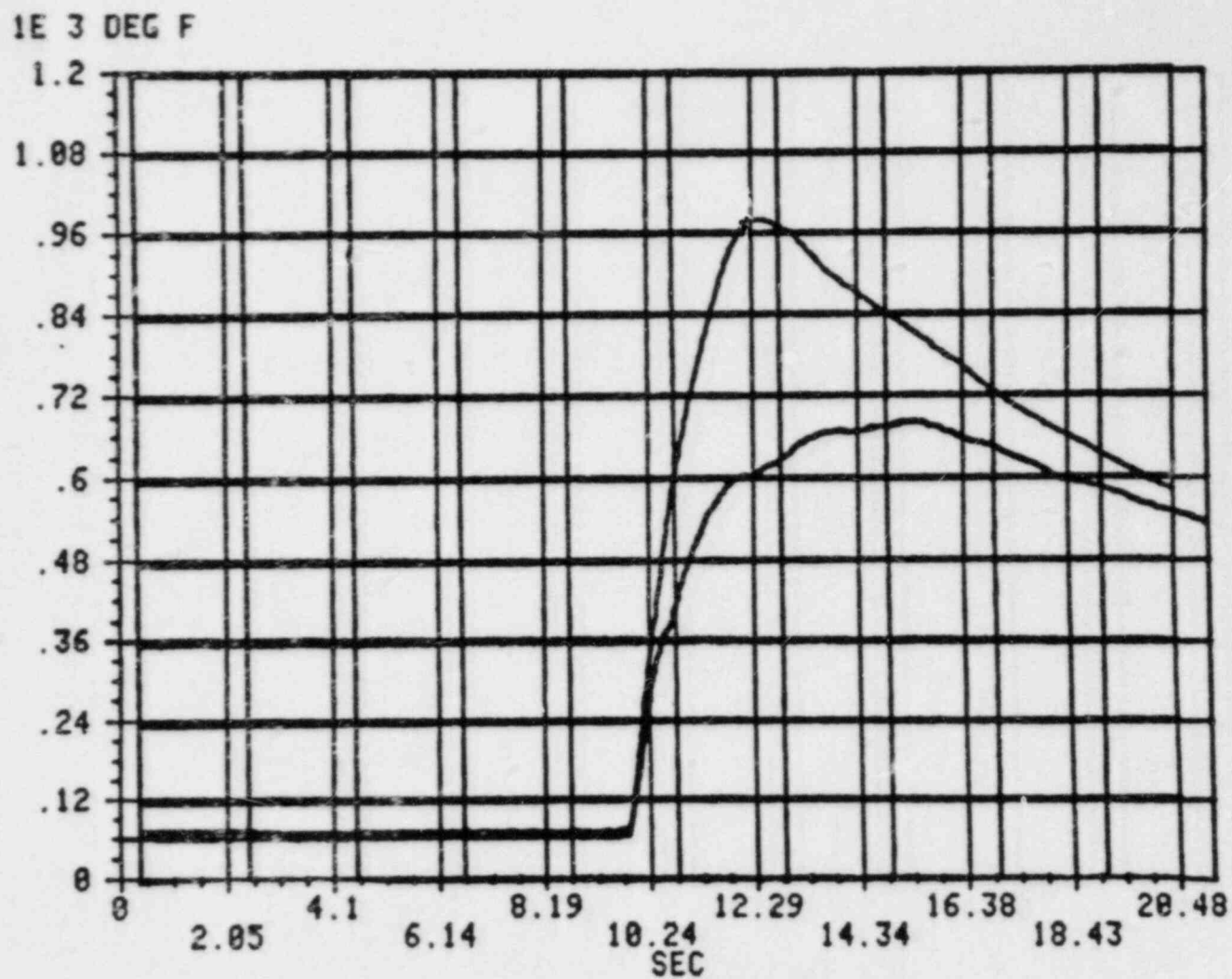


Figure 3.19. Comparison between thermocouple records (TC241) made during hydrogen combustion with (14-45-1; B11H12) and without (14-43-1; B9H12)  $Fe_2O_3$  aerosol, lower and upper traces, respectively.



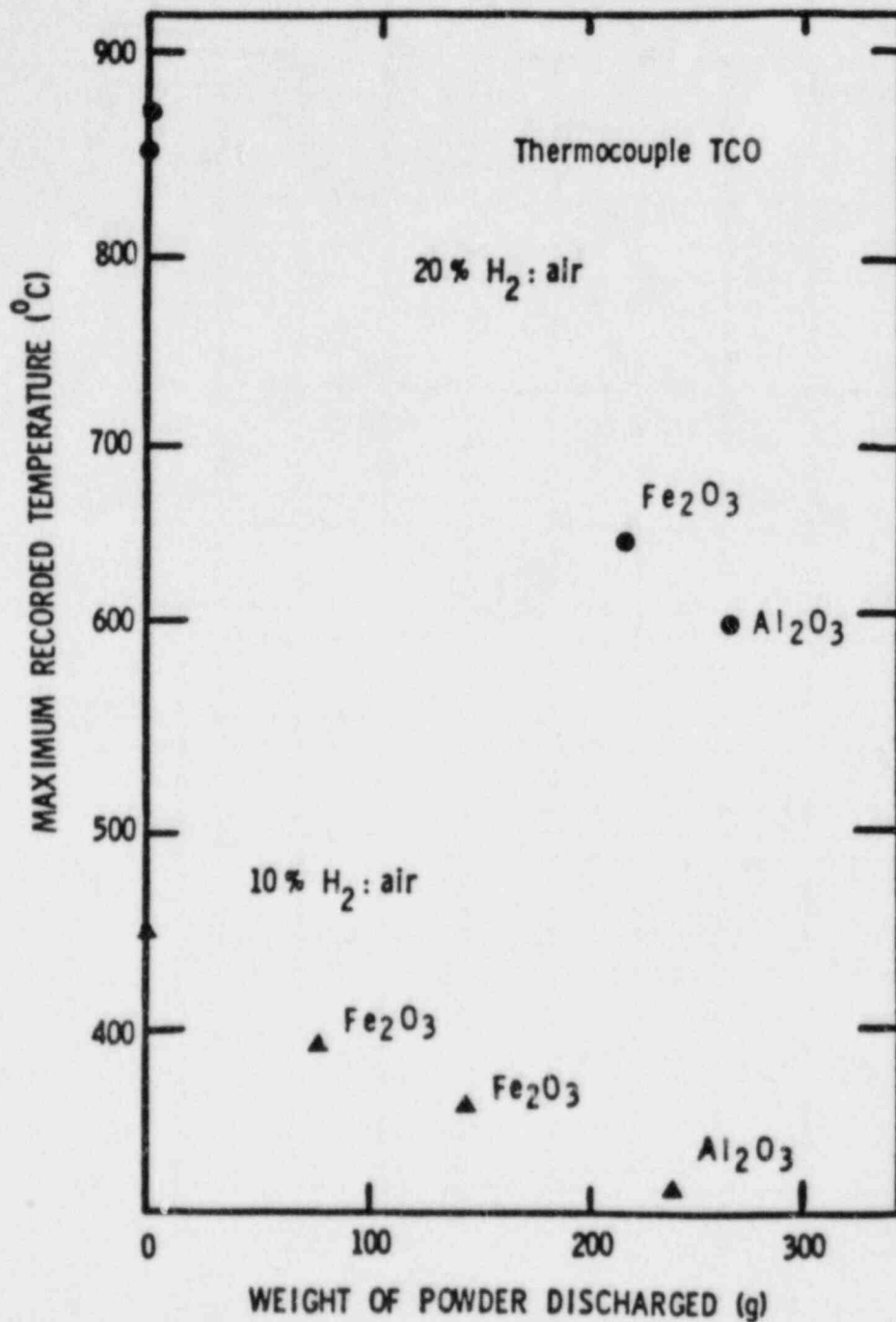


Figure 3.20. Maximum Recorded Temperatures vs Weight of Powder Discharged in VGES Tank Experiments; Thermocouple TCO

### 3.2.6 Effects of Hydrogen:Air Combustion on Aerosols (L. S. Nelson and W. B. Benedick)

Several distinct chemical changes were observed during the exposure of aerosols to the hydrogen combustion. In one of the experiments described in the previous section, iron oxide ( $\text{Fe}_2\text{O}_3$ ) was exposed to the combustion of a 20% hydrogen:air mixture. After this experiment, significant quantities of a black powdery material were observed on various surfaces in the tank. We attributed this change to the transition from the red-brown hematite,  $\text{Fe}_2\text{O}_3$ , to magnetite,  $\text{Fe}_3\text{O}_4$ , which is black. The thermal decomposition of hematite occurs at temperatures above 1720 K (2637°F) with liberation of gaseous oxygen.[19]

The other chemical change was observed in two experiments in the VGES tank in which 30 to 36 g of a 50% alumina-cesium iodide aerosol was exposed to the combustion of a stoichiometric (29%) hydrogen:air mixture. The combustion was vigorous. Upon removal of the head of the VGES chamber after about 20 min, we detected a strong halogen-like odor above the chamber. Also, a yellowish aerosol lingered in the chamber. Moreover, silver coupons exposed to the combustion gained weight and a heavy concentration of iodine on their surfaces was detected by X-ray fluorescence; the same technique indicated essentially no cesium on the surface, however.

In the second experiment, gas analyses were attempted after approximately 15 min. The species of interest were gaseous hydrogen iodide (tested with silver nitrate solution) and elemental iodine (tested with the starch/iodine reaction). Both analyses were negative; in spite of these negative results, the formation of the iodine-containing layer on the silver indicates strongly that at least one of these gases was present in the chamber at some point in the combustion. This is because cesium iodide is unreactive towards silver, while both iodine and hydrogen iodide react quantitatively with the metal.

We are planning to improve the analytical procedures and perform both field and laboratory scale experiments during the coming year.

### 3.2.7 Water Drop Diagnostics (L. S. Nelson)

We have used direct drop sampling successfully for the analysis of water sprays produced by small flow nozzles in repetition of the work of Camp.[20] The sampling was done with tinted polyvinyl alcohol-coated microscope slides [21]; later the slides were examined by Quantimet optical image analyses as discussed previously.[22]

Recently, we have been analyzing drops from large flow nozzles similar to those used in nuclear reactor containment. We considered the hollow cone nozzle, Spraco Model 1713A, and two full cone nozzles, Spraco Models 1126-1814, and 1108-1214. These nozzles produce total water flows up to 60 l/min compared to those studied by Camp which have flows of about 1 l/min. When we attempted direct drop sampling with the large flow nozzles, the fast-shuttered samplers were flooded, yielding unusable images. A secondary pneumatically-operated wiper-type cover over the shutter synchronized to fire with it did little to produce better images.

As an alternate method for drop diagnostics, we have used high speed 16 mm motion pictures recorded with back lighting. A thin vertical plane of drops is isolated for these photographs by using an appropriate slit arrangement placed in the spray. A photograph reproduced from one of these 16 mm films is shown in Figure 3.21. Note the presence of very large drops, some of which were up to 1 cm across. Films such as these are analyzed for droplet velocity-diameter relationships and droplet diameter distributions using appropriate optical imaging techniques. We measured both spray fluxes and total flows with interception samplers and stopwatch timing.

Water drop diagnostics will be continued in support of the water drop programs described below.

### 3.2.8 Tests of Monodisperse Water Drop Generator (L. S. Nelson and C. N. Richards)

We performed two brief series of tests with a prototype spinning disk water drop generator [23] supplied by Atmospheric Physics, Inc. This was a four-disk unit with 20-cm (8-in) diameter disks shown schematically in Figure 3.22. The unit was operated in a quiescent atmosphere with its hollow shaft placed horizontally. Approximately 0.5 l/min of water was delivered by each disk. Again, water drop sampling was performed with tinted polyvinyl alcohol-coated microscope slides.

The drop diameters were calculated according to the governing equation:

$$d = 3.8(\sigma/D\rho)^{1/2}/\omega$$

where

- $\sigma$  = surface tension of liquid
- $D$  = diameter of disk
- $\omega$  = angular velocity of disk
- $d$  = diameter of drops

Using this relationship, when the unit was operated at 2300 rpm, the calculated drop diameter was 295  $\mu\text{m}$ .

3-45

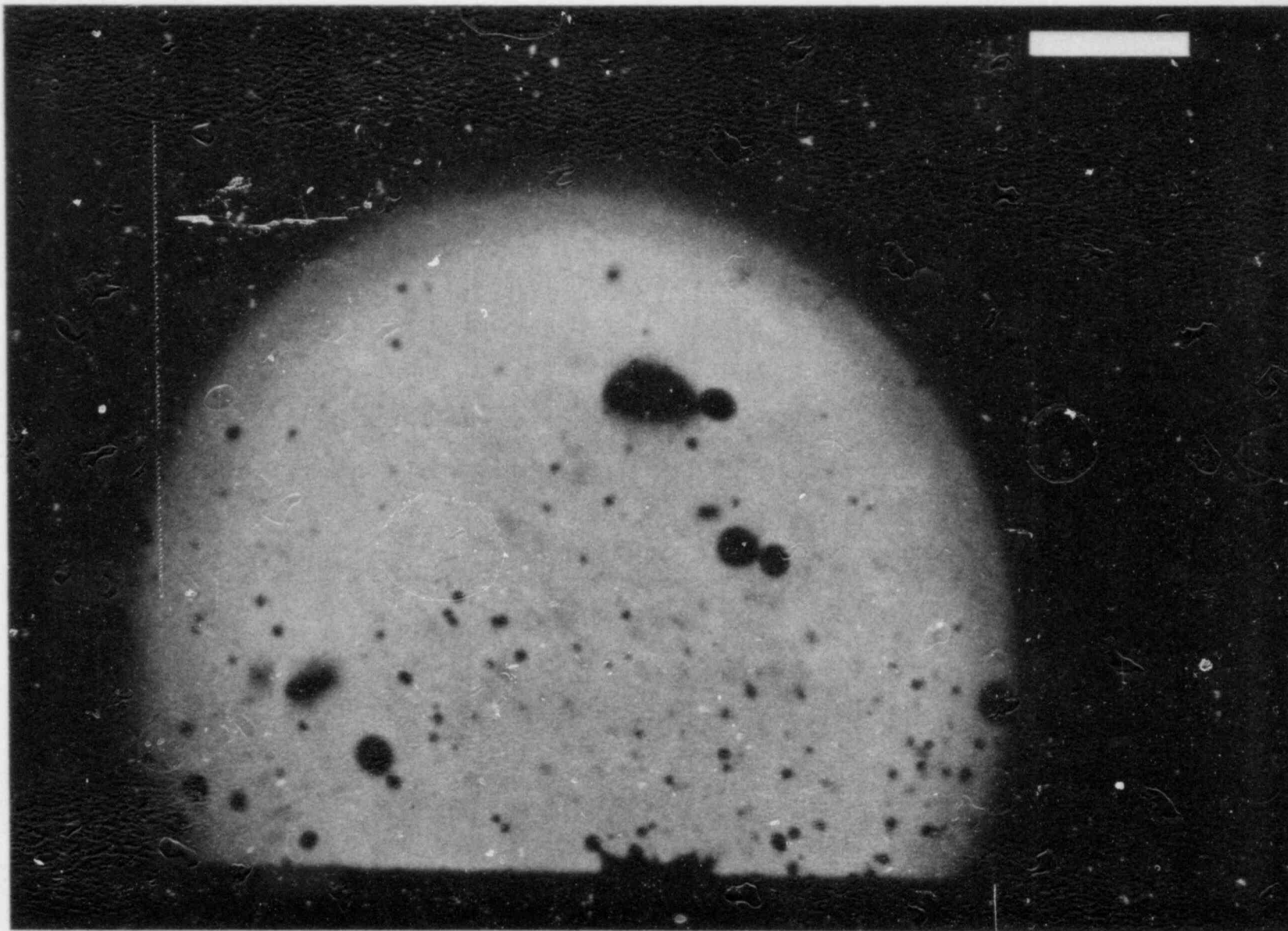


Figure 3.21. Images of spray drops recorded 1.2 m below a Spraco 1126-1314 solid cone nozzle. Bar is 10 mm long. (17-90-1-2-L).

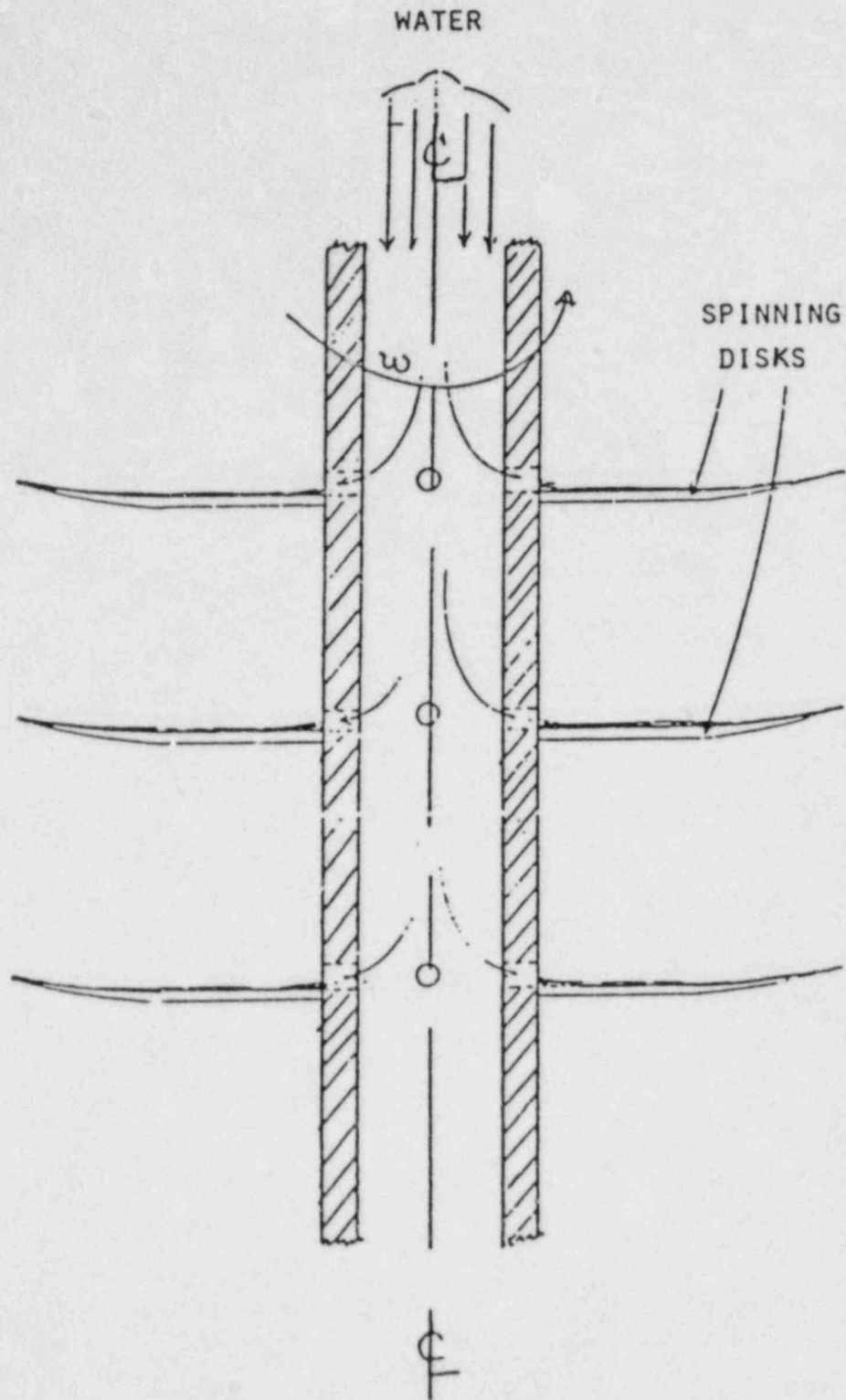


Figure 3.22. Sketch of a Cross Section of Spinning Disk-Type Generator of Monodisperse Water Drops

Images of the drops on the microscope slides were analyzed with the Quantimet optical image analyzer. The result of the analysis for drops produced at 2300 rpm are shown in Figure 3.23. Note the narrow distribution of drop diameters shown in the histogram (less than a twofold spread). Also compare the measured mean diameter of 293  $\mu\text{m}$  with the calculated diameter of 295  $\mu\text{m}$ .

The narrow distribution shown in Figure 3.23 provides an interesting contrast with the broad distributions typical of nozzle-generated drops; see, for example, Figure 3.60 in Ref. 22.

A pair of spinning disk drop generators has been ordered. We intend to use them to investigate the effects of water drops on hydrogen combustion in the FITS facility next year.

### 3.2.9 Operability of Tayco Igniters in a Water Spray Environment

(L. S. Nelson, W. B. Benedick and P. G. Prassinis)

Ten field-scale experiments were performed in the VGES hydrogen combustion facility (volume 5  $\text{m}^3$ ) to determine whether 6% hydrogen:air mixtures can be ignited reliably with a Tayco helical igniter in a water spray environment. We addressed the following questions: Will the device ignite the lean hydrogen:air mixture while exposed directly to a spray flux of 38.3  $\text{l}/\text{m}^2\text{-min}$  (0.915  $\text{gal}/\text{ft}^2\text{-min}$ ), prototypical [24] for a nuclear plant spray system? If not, will the placement of a horizontal plate spray shield above the igniter enable it to function properly in this flux even though there may be a horizontal gas flow that might drive spray drops beneath the plate? (The flow of gas is intended to simulate turbulent fluctuations that might be experienced during spray operation in the containment of a nuclear power plant during a hydrogen-producing accident.)

We used the Spraco Model 1108-1214 solid-cone nozzle to simulate the prototypical spray using a gas pressurizing unit to drive the water. The spray was characterized first in a calm indoor location to determine drop diameter distribution (100 to 1000  $\mu\text{m}$ ), total flux (given in previous paragraph) and drop velocities (1 to 3  $\text{m}/\text{s}$ , spanning terminal velocity within a factor of 2).

The arrangement of nozzle, igniter and spray shield in the VGES facility are shown in Figure 3.24. A fan was placed horizontally next to the igniter to induce horizontal gas flows up to 6  $\text{m}/\text{s}$ . These flows are thought to exceed the horizontal component of turbulent fluctuations in a nuclear reactor containment.[25]

NUMBER OF DROPS

DROP DIAMETER IN MICRONS

0	
10	0
12.5893	0
15.8489	0
19.9526	0
25.1189	0
31.6228	0
39.8107	0
50.1187	0
63.0957	0
79.4328	1
100	0
125.893	0
158.489	0
199.526	0
*****	18
251.189	***** 104
316.228	***** 29
398.107	* 3
501.187	0
630.957	0
794.328	0
1000	0

Figure 3.23. Histogram Generated by the Quantimet for Optional Image Analyzer for Water Drop Images Produced in a Tinted Polyvinyl Alcohol-Coated Microscope Slide by a Monodisperse Water Drop Generator

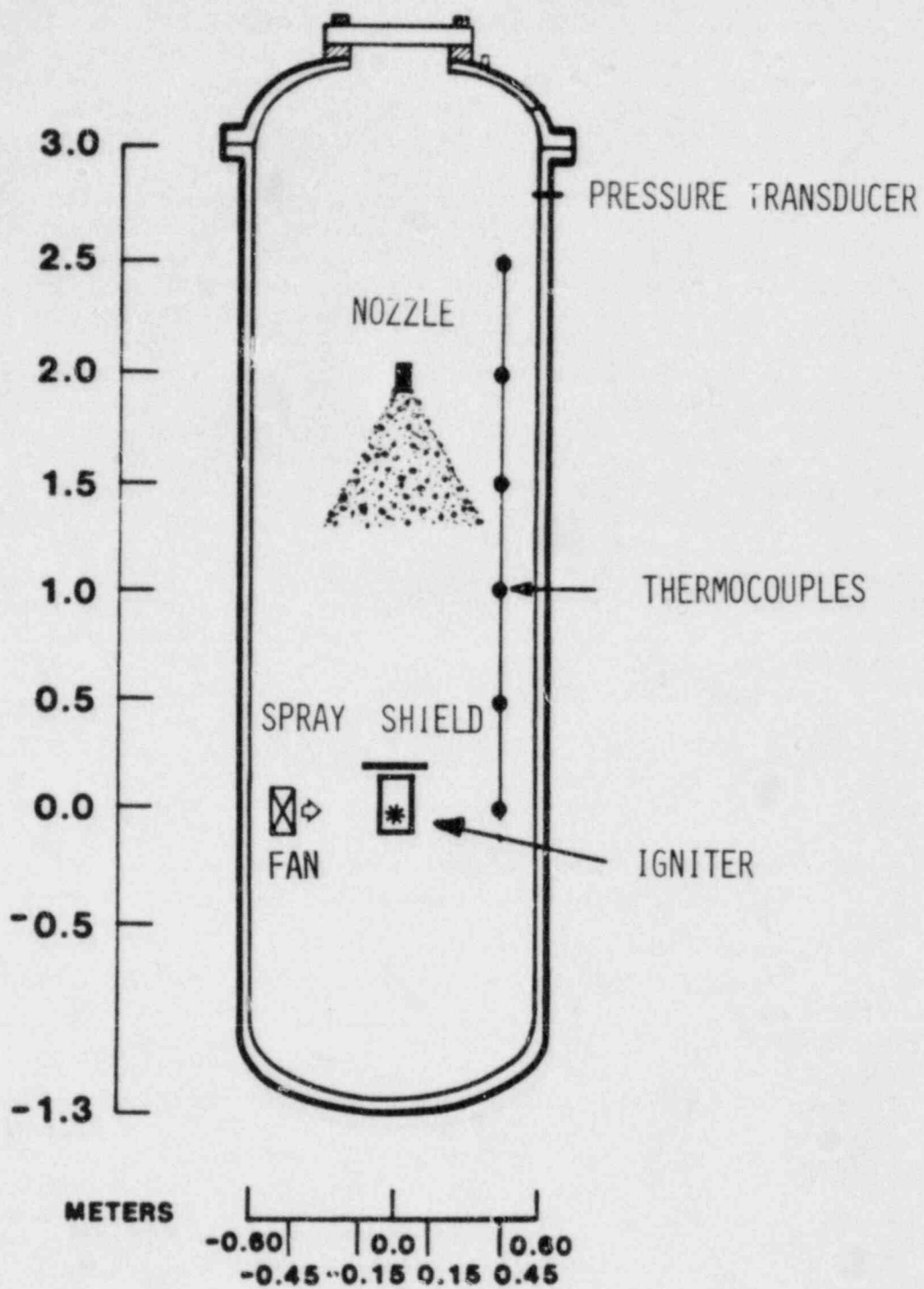


Figure 3.24. Experimental Arrangement of the VGES Facility Used to Study the Operability of a Tayco Igniter in a Water Spray Environment



The igniter, as it was mounted in the tank, is shown in Figure 3.25. The spray shield is visible in this figure. The igniter was powered with 120 Vac from the local mains. Thermocouples were spot-welded to the bottom of the helical igniter to determine surface temperatures during the experiments. The experiments were performed in four ways: (i) spray, spray shield and fan off; (ii) spray on, spray shield and fan off; (iii) spray and spray shield on, fan off; and (iv) spray, spray shield and fan on (several velocities up to 0.5 m/s). Of the four types of experiments performed, only those in which the igniter was exposed directly to the spray (i.e., (ii) above) failed to ignite within the first 40 seconds after the igniter was energized. This difference in time to ignition can be explained by the cooling effect of the spray and gas flow on the igniter coil. This is illustrated in Figure 3.26, in which thermocouple-time traces are compared for the shield on and shield-off cases (ii and iii above). Note that without the shield, the thermocouple readings remain at approximately the local boiling point of water until the spray is turned off; at this time the igniter begins to heat as in the shield-on situation and ignites the mixture.

We have reached the following tentative conclusions for the situation in which a Tayco igniter was located in a water spray flux of  $38.3 \text{ l/m}^2\text{-min}$  ( $0.915 \text{ gal/ft}^2\text{-min}$ ) in the VGES combustion chamber that contained a 6% hydrogen:air mixture: (i) ignition did not occur when the igniter was exposed directly to the full spray; (ii) ignition did occur when a horizontal plate spray shield was placed above the igniters; and (iii) with the spray shield in place, horizontal gas flows up to 6 m/s caused only minor delays in the times to ignition.

Analogous experiments with GMAC 7G glow plug igniters are planned during the last quarter of 1984.

#### 3.2.10 Modification of Plant Atmospheres

(L. S. Nelson, P. G. Prassinis, and E. W. Shepherd)

We have been investigating the modification of containment atmospheres to reduce or eliminate the risks from hydrogen combustion. Among the schemes we have studied is the partial depletion of oxygen in a nuclear reactor containment to the lowest concentration permissible for safe breathing during continuous work (14% oxygen). We have also studied the use of storage of large quantities of inert gas in unused spaces in a nuclear reactor containment building separated from other portions of the building by a rupturable membrane. According to this scheme, upon rupture of the membrane, the inert gas would be released and could lower the oxygen level dramatically within the containment without increasing the total pressure. Moreover, the inert gas could be chosen to reduce the risk of detonation as well as to lower the peak temperatures reached by safety-related equipment exposed to a hydrogen burn.

3-51

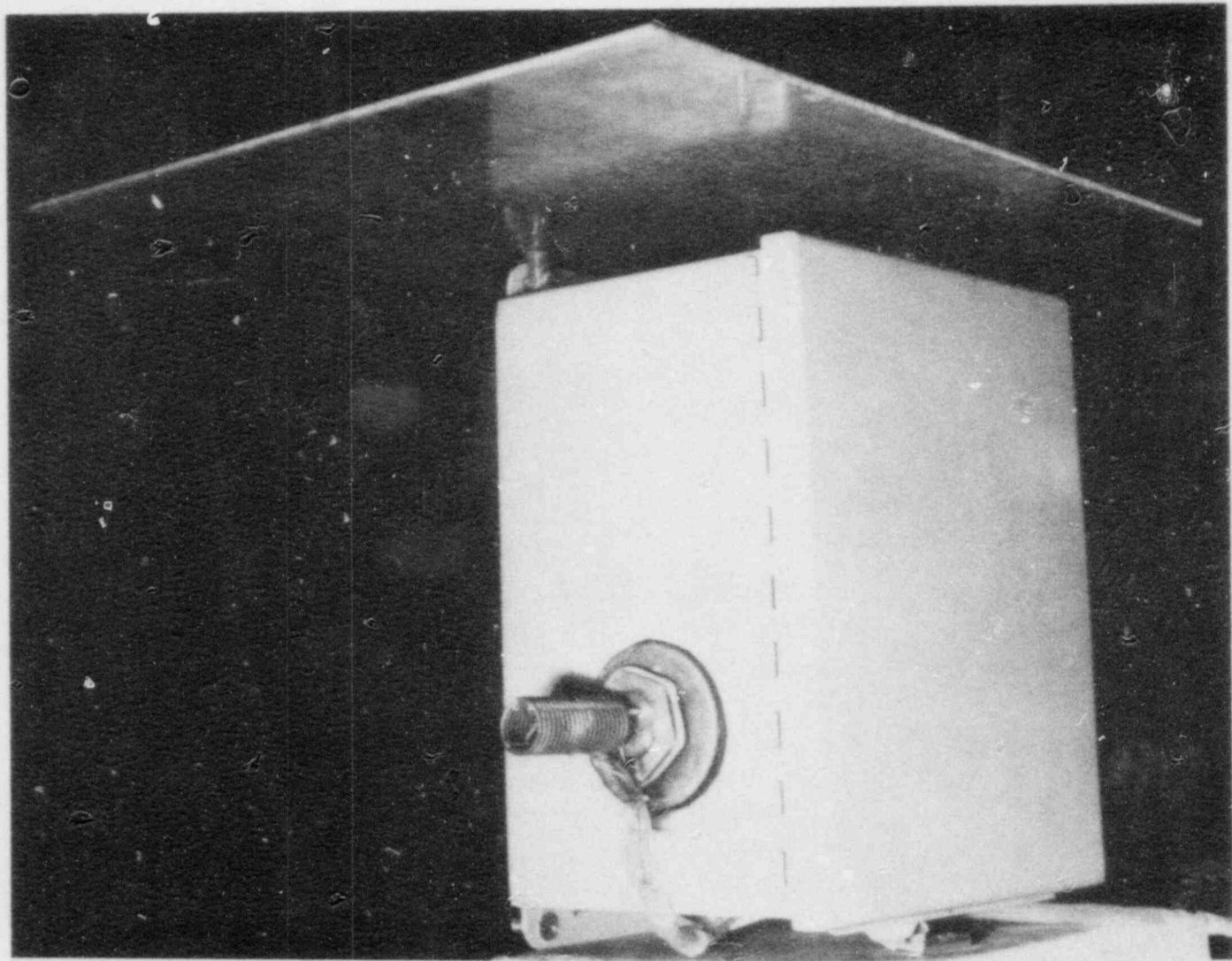


Figure 3.25. Tayco Helical Igniter Installed in Box with Spray Shield (Sheet Metal at Top of Photo). Box is 26 cm tall.

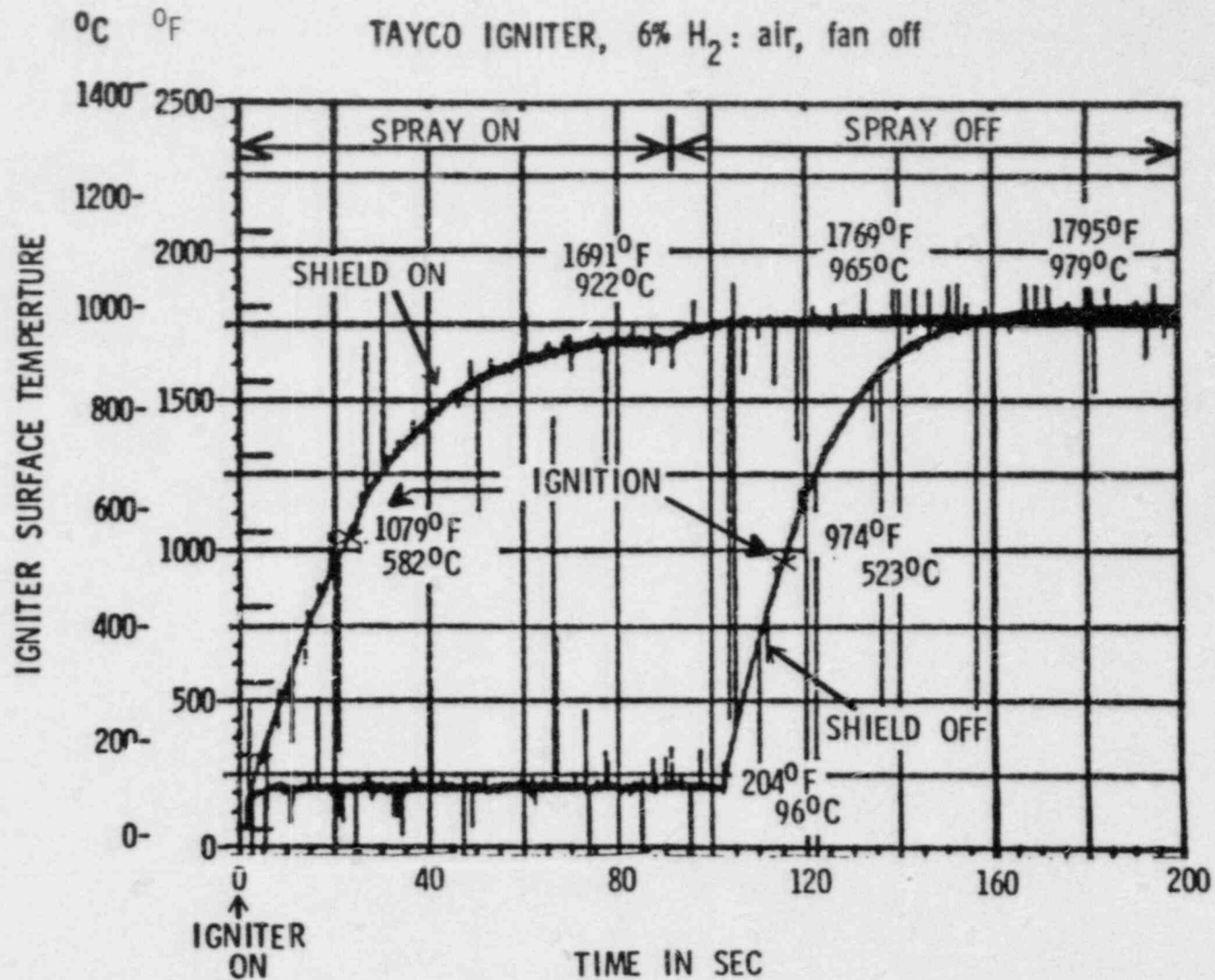


Figure 3.26. Records of Thermocouple Spot-Welded to Tayco Igniter Exposed to Prototypical Water Spray with and without Spray Shield during Hydrogen Combustion Experiments in the VGES Facility.

We have completed a series of analyses via an AICC code to determine the worst case peak pressures and temperatures that might be produced in a large dry containment using normal and depleted air prior to the accident, and with carbon dioxide added to the containment via a rupturable membrane. The inert gas was assumed to fill 40% of containment. Some of the analytical results are summarized in Table 3.6. Note the dramatic reductions in peak pressures and temperature that can be achieved by these procedures.

Table 3.6

Effects of Partial Depletion of Oxygen on Pressure and Temperature Rises (Large Dry Containment)

Containment Air Normal (21% O <sub>2</sub> )	Air Depleted (14% O <sub>2</sub> )	Postaccident Dilution CO <sub>2</sub> from "bag"	AICC Estimates <sup>a</sup>	
			P <sub>max</sub> (atm)	T <sub>max</sub> (K)
X			11.5 <sup>b</sup>	2771
	X		9.0	2348
X		X	7.1	1873
	X	X	5.6	1651

<sup>a</sup>Assumes excess of hydrogen is present. AICC = adiabatic isochoric complete combustion.

<sup>b</sup>Far exceeds design pressure; possible containment failure

### 3.2.11 FLAME Facility

(M. P. Sherman, S. R. Tieszen, and J. Fisk)

In this period of time most of the systems required to run FLAME were installed and one test was conducted. In the next semiannual period regular testing should begin.

The FLAME structural work was completed in April with the repair of defective concrete sections with high-strength grout. The structure was inspected and approved by Sandia inspectors. Several months later some superficial cracking of the thin feather edges of some of the patches was found and repaired by the construction contractor, Cardenas Construction Co.

A Safety Operating Procedure (SOP) was written and approved. A tower overlooking the site was erected and a television camera was installed on top, with the ability to rotate 360°, tilt up or down, and zoom in on a view. We can examine the site from inside the blockhouse control room, building 9920.

With the completion of the SOP and the installation of the TV system, we have approval from our safety inspectors to run FLAME.

Our first test was conducted on June 28 with a 12.4% hydrogen: air mixture, 50% top venting, and no obstacles in the channel. We used the DAASY system to back up our CAMAC data acquisition system. The DAASY system is limited to 40 data channels, the number we used in the test. Instrumentation included two vertical rakes each with 12 thermocouples, several thermocouples at the walls, lithium niobate gauges, pressure transducers, and germanium photodiodes. The pressure gauges indicated a negligible pressure rise. The thermocouples have excellent data on the time of arrival of the flame. The flame was observed to propagate down the channel at speeds of 5 to 7 m/s, with the front near the floor lagging the flame near the top (Figure 3.27). The test gave us valuable experience as well as useful data.

The test had been conducted with temporary signal lines laid on the ground. We have since dug trenches and installed permanent signal lines and power lines.

The test was conducted with other temporary systems. For example, the hydrogen used was supplied by gas bottles. We have since completed a permanent hydrogen transfer system consisting of a hydrogen trailer, buried lines, a hydrogen flow meter, flame arresters, and pressure regulators. Other systems installed include air-driven mixing fans inside FLAME, and ignition systems. As hydrogen enters FLAME, a collapsed 4 mil virgin polyethylene bag expands outward. A system of guy wires to control the bag and tarpaulins to act as a wind-break was installed.

A version of the computer software to run our data acquisition system was completed and used in the initial test. We are continuing to extend this program to include elements that would be useful and modify our data acquisition system.

### 3.2.12 Heated Detonation Tube (M. P. Sherman, S. K. Tieszen, and J. Fisk)

During this period, most of the work required to make the facility operational was completed, and a series of shakedown tests was conducted. The next semiannual period will see the completion of the preparation and the start of regular testing.

The tests conducted were at ambient temperature and at hydrogen mole fractions of 20, 18, and 16%. Air was mixed in the detonation tube until the temperature was uniform, and the pressure in the tube was measured. Hydrogen was injected,

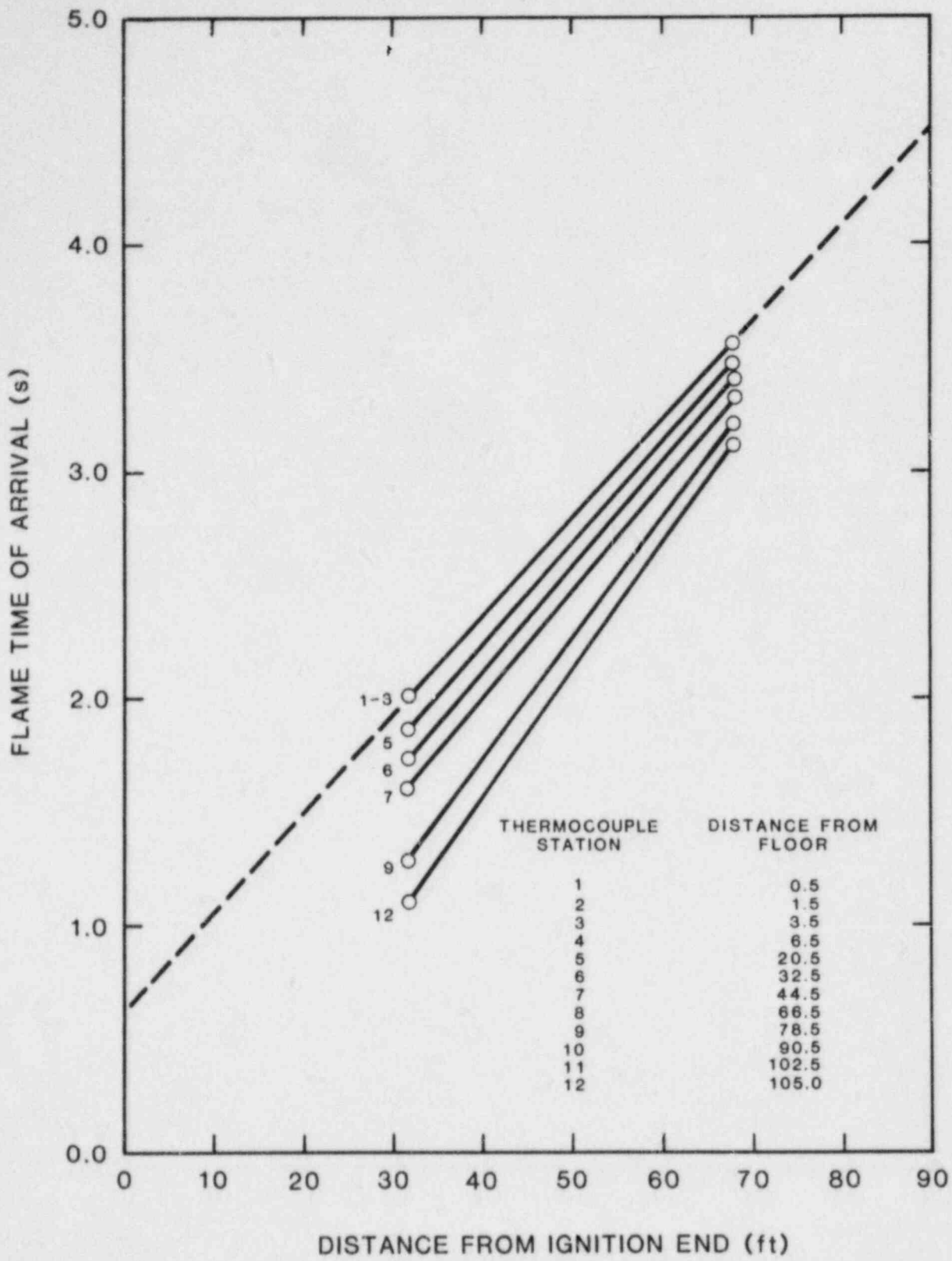


Figure 3.27. Flame Test 1, June 28, 1983

and the hydrogen:air mixture was again mixed. The concentration of hydrogen was determined from the two pressures. Difficulties with the high-explosive ignition system were overcome.

The instrumentation for the tests included six fast response Kistler 211B3 pressure transducers. These were used to measure the time of arrival of the detonation and the pressure behind the detonation. The quality of the signals was degraded by noise that travelled up the tube from the ignition end at a speed somewhat faster than the detonation. Before the onset of the noise, the inherent noise in the system was low. We believe that the noise was caused by mechanical vibrations of the tube, which travelled through the brass bushings holding the pressure transducers. We discussed this problem with our consultants at McGill University, Profs. Lee and Knystautas. They use Delrin plastic bushings to minimize the transmission of such vibrations to the transducers. The higher compliance material slows and reduces the transmission of such motions. Delrin is listed as being marginally able to withstand the initial temperatures we wish to use in the heated detonation tube. As a consequence we have manufactured bushings of Delrin and of Nylon. The Nylon withstands high temperatures better, but is considerably more difficult to machine.

The other instrumentation in the tube consisted of a thin steel plate placed circumferentially around the inner surface of the tube at the end farthest from the ignition. The inner surface of the plate was smoked with soot from fuel-rich hydrocarbon flames. Such "smoked foils" are used to record the passage of the detonation wave, which is composed of transverse shock wave Mach intersections, and hence the detonation cell size. The lines on the smoked foil were distinct. In our initial measurements, the cell sizes determined were much smaller than those measured by other researchers. Initially, we were concerned that we had overdriven the detonation wave by using too large a high explosive ignition source. This may have been true, and we will have to be careful to avoid overdriving the detonation in the future by checking that the results are invariant to changes in ignition source strength at the strength levels used. However, during a meeting with Prof. J. Lee of McGill University, he expressed concern that we had been reading "overtones" and not the fundamental detonation cell size. We expect to have Prof. R. Knystautas, a world expert in carrying out these measurements, visit us in January to examine our results and teach us how to perform the measurements.

### 3.2.13 McGill Work

(C. Guirao, C. Chan, J. Lee, R. Knystautas)

#### 3.2.13.1 Hydrogen:Air Deflagration Studies

Freely propagating flames are very sensitive to the gas dynamic flow structure that they generate. The interaction between such a flow field and the flame front can cause the burning rate to increase to many times the normal (or laminar) burning rate. As a result of such an interaction, a freely expanding flame can accelerate to very high flame speeds and even transit to detonation under appropriate conditions. However, the coupling between gas dynamics and combustion in transient situations is far from being understood. The research at McGill is designed to elucidate such a coupling mechanism and deduce some empirical relationships and scaling laws so that one can assess in a realistic way the hazards of a hydrogen:air explosion as a result of a loss-of-coolant accident in a light water nuclear reactor.

##### 3.2.13.1.1 Flame Acceleration in Multiple Chambers

For a freely expanding flame, the combustion process and the flow field are intimately coupled in that the specific volume increases across the flame produce the unburned gas flow. In the presence of obstructions, this flow will generate turbulence leading to an increase in the rate of burning caused by enhancement in the local transport of mass and energy. Furthermore, the flame will be distorted and stretched in the nonuniform flow field leading to an increase in flame surface area. The increase in the total burning resulting from these effects depends on the flow velocity ahead of the flame, which in turn is controlled by the burning rate itself. This coupling leads to the establishment of a strong feedback mechanism which continuously accelerates the flame. It has been demonstrated in small-scale experiments [26] as well as large-scale field tests [27] that turbulence induced in the unburned flow ahead by the presence of obstacles can cause a propagating flame to accelerate to very high flame speeds and even transit to quasi-detonation under appropriate conditions.[28]

To study the phenomena associated with flame propagation in multiple chambers, experiments are performed in a 60-cm-long square channel (12.7 cm x 12.7 cm). To simulate interconnected chambers, rectangular baffle-type obstacles are mounted perpendicular to the side walls with blockage ratio equal to 0.6 and are used as partition walls. To provide a wide range of flow situations, the chambers are connected together in consecutive fashion with openings on the opposite corners of the walls. Due to structural limitations imposed by the apparatus, only very lean hydrogen:air mixtures were tested (up to 12% hydrogen). Ignition is by 13 weak electrical sparks located at the closed end of the channel, to



provide a planar flame front. As the flame propagates from one chamber to another, the flame structure is observed using Schlieren cinematography. The pressure development in each chamber is monitored by piezoelectric pressure transducers. The outlet velocity at the exit of each chamber is measured by laser doppler velocimetry.

Figure 3.28 shows a series of Schlieren movies of a flame (10.6% hydrogen) propagating through a series of interconnected chambers. The configuration of the partition is also shown at the beginning of the sequence in the same figure. The structure of the flame as it propagates into adjacent chambers is clearly shown. Between the first and second chamber, the flame front is observed to follow the unburned flow field ahead as it is entrained into the developing eddy at the wake of the opening. The increase in flame surface area attributable to stretching of the flame surface is clearly shown. Because of the increase in the total burning rate, the leading flame front is convected into the next chamber at a much higher velocity. The flame development in the third and the fourth chambers is quite different in that intense burning occurs along the shear layer created by the venting flow. The mixtures in these chambers are quickly

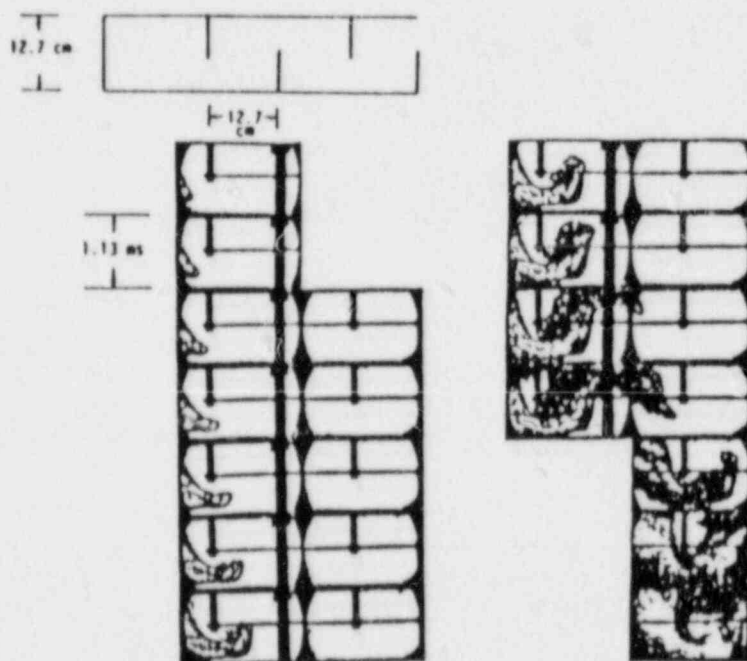


Figure 3.28. Schlieren Movies for Flame Propagation in Multiple Chambers

consumed in this highly turbulent region. Small-scale wrinkles on the flame surface indicate that it consists mainly of fine-scale turbulent structures.

Figure 3.29 shows the profile of the speed (relative to a fixed observer) of the leading flame front measured from the Schlieren movies. The flame accelerates very rapidly as it propagates from one chamber to the next for this configuration. At the exit of the fourth chamber, which is located only 50 cm from the ignition source, the flame speed is of the order of 65 m/s. Because of the jetting effect at the opening between chambers, the flame does not accelerate smoothly.

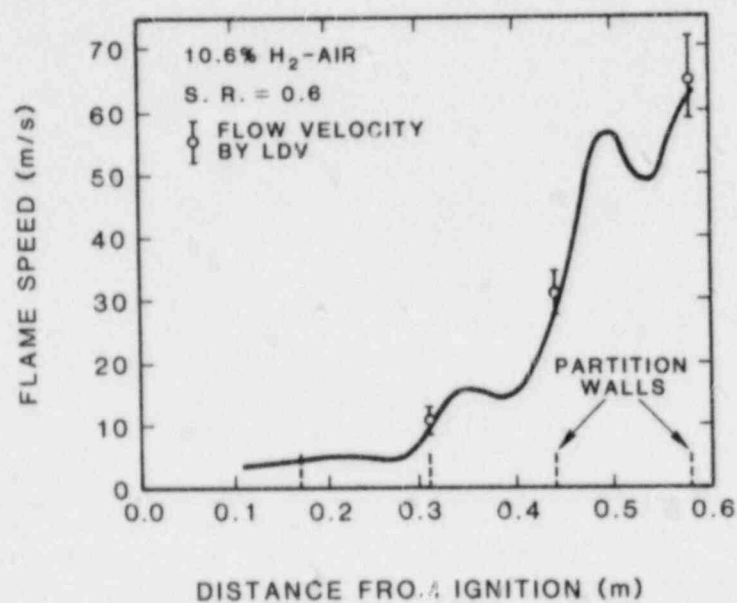


Figure 3.29. Flame Speed Profile for Flame Propagation in Multiple Chambers

A good qualitative understanding of the phenomena associated with flame propagation in multiple chambers has been obtained through Schlieren cinematography and LDV measurement of the flow field. Comparing experimental results to the prediction from a numerical code developed at the Sandia National Laboratories based on the concept of "vortex dynamics," shows that the code can qualitatively describe the flame development reasonably well. However, further refinement to include the effects of fine-scale structure in the flow field on the flame is required to provide better quantitative agreement. This work was described previously in Sections 3.1.2 and 3.1.3.

### 3.2.13.1.2 High Speed Turbulent Deflagrations and Transition to Detonation

Several studies [26, 27] have been carried out in recent years on the influence of obstacles on the acceleration of propagating flames in premixed gases. In all these studies, the apparatus was too short to permit steady-state conditions to be achieved at the end of the flame travel. Hence, the maximum turbulent flame speed for a given obstacle configuration is not reached, and important information on whether transition to detonation is possible cannot be deduced from these experiments. This section reports some recent experimental results on flame acceleration in long tubes ( $L/D > 200$ ) in the presence of multiple obstacles.

The experiments are conducted in tubes having three different diameters (5 cm, 15 cm, 30 cm). This enables us to investigate the scaling effects. These tubes are filled with orificial obstacles having blockage ratios ranging from 0.4 to 0.6. The spacing of the obstacles is set equal to the diameter of the corresponding tube. Besides studying flame acceleration for various hydrogen:air mixtures, experiments are also conducted with hydrocarbon fuels ( $\text{CH}_4$ ,  $\text{C}_3\text{H}_8$ ,  $\text{C}_2\text{H}_4$ ,  $\text{C}_2\text{H}_2$ ) for comparison.

Figure 3.30 shows the maximum (or steady-state) flame speed in the obstacle section for various hydrogen concentrations. Results from the 5-cm and 15-cm tube are plotted in the same figure. Note that for all cases, a sharp jump in the turbulent flame speed occurs around 13% hydrogen. For hydrogen  $< 13\%$ , the flame speeds are less than 200 m/s. For hydrogen  $> 13\%$ , the flame speeds increase sharply to values of the order of the sound speed of the mixture (500 m/s to 800 m/s). At around 25% hydrogen, another sharp jump to detonation velocities of about 1600 m/s occurs. For lean mixtures (hydrogen  $\leq 13\%$ ), the steady-state turbulent deflagration velocity appears to result from the balance between the positive effect of turbulence in augmenting the volumetric combustion rate via flame folding and the negative effect of quenching as the flame stretches. At about 13% hydrogen, flame temperatures increase to values of the order of 1300 K. From kinetic considerations, the competing reaction between the  $\text{H} + \text{O}_2 + \text{M} \rightarrow \text{H O}_2 + \text{M}$  and  $\text{H} + \text{O}_2 \rightarrow \text{OH} + \text{O}$  appears to change over at around 1300 K in favor of the more rapid OH branching reaction. In the region where the flame speeds are of the order of the sonic velocity, (i.e.,  $13\% \leq \text{hydrogen} \leq 25\%$  for the particular obstacle configurations investigated), it appears that frictional choking sets the limiting condition. For sufficiently intense combustion, autoignition attributable to either local shock heating and/or violent turbulent mixing occurs. This gives rise to the second sharp increase in which transition to the detonation regime occurs. Turbulent flame speeds are almost identical for both tubes although for the case of the larger tube, the detonation velocity is found to be slightly below that of the smaller tube. The variation of

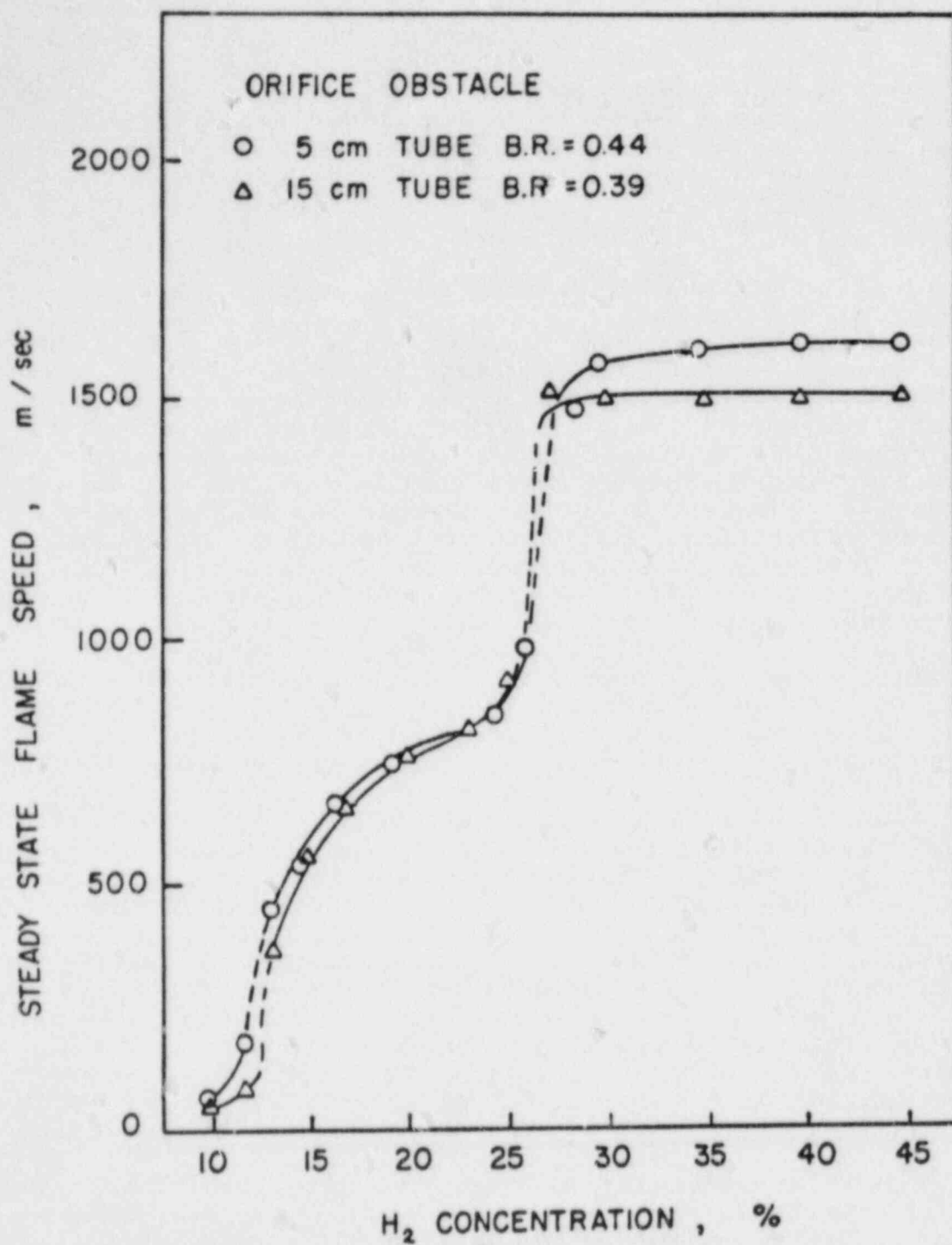


Figure 3.30. Steady State Flame Speeds for Hydrogen:Air Mixtures

the peak overpressure with hydrogen concentration for the 5 cm and 15 cm tubes is shown in Figure 3.31. Almost identical results are obtained for the turbulent deflagration regime. However, the detonation pressure for the larger tubes is slightly higher than the corresponding case for the smaller tubes.

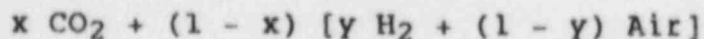
The results obtained thus far for the two tubes indicate that larger scales appear to increase the acceleration rate, but the influence on the final steady-state turbulent flame speed is minimal. Future experiments in the 30-cm-diameter tube and in the 4-ft-diameter VGES facility at Sandia should be of great value for the lean mixtures.

### 3.2.13.1.3 Influence of CO<sub>2</sub> on Hydrogen:Air Deflagration

One of the schemes proposed to desensitize a combustible mixture of hydrogen and air is dilution with CO<sub>2</sub> or N<sub>2</sub>. It has been demonstrated that CO<sub>2</sub> is a promising desensitizer or inhibitor for detonative-mode combustion.[29] Small amounts of CO<sub>2</sub> (i.e., 5% of the total volume) in stoichiometric hydrogen:air mixture increase the size of detonative cellular structure by roughly 40% and the minimum energy required for initiation of detonation by almost 300%. However, the role of CO<sub>2</sub> in deflagrative-mode combustion, in particular, its influence on the sensitivity of fuel:air mixtures to flame acceleration, has not been assessed.

The study on the influence of CO<sub>2</sub> on hydrogen:air deflagration is subdivided into two parts. The first part of the program is to investigate its influence on the normal burning velocity. In the second part, its influence on the steady-state turbulent flame speed in an obstacle field is investigated. The first part of the experiment is performed in a constant volume combustion apparatus in which optical observations can be made. The normal burning velocity is obtained by monitoring the initial rate of growth of the flame kernel, after ignition by a weak spark, using high-speed Schlieren cinematography. Experiments for the second part of the study are performed in a long circular tube (15 cm diameter and 15 m long). Multiple orifice plates of blockage ratio of 0.39 are placed in the first 5 m of the tube as turbulence-producing obstacles. The spacing of the obstacles is 15 cm. The mixture is ignited by a weak electrical spark. The flame speed (relative to a fixed observer) is measured using ion probes.

For mixtures less than 15% hydrogen and mixtures which are highly diluted with CO<sub>2</sub>, the flame speeds are measured using thin thermocouples (0.075-mm-diameter chromel-alumel). The pressure development in the tube is measured using piezoelectric pressure transducers. The composition of the diluted mixture is defined by the relation:



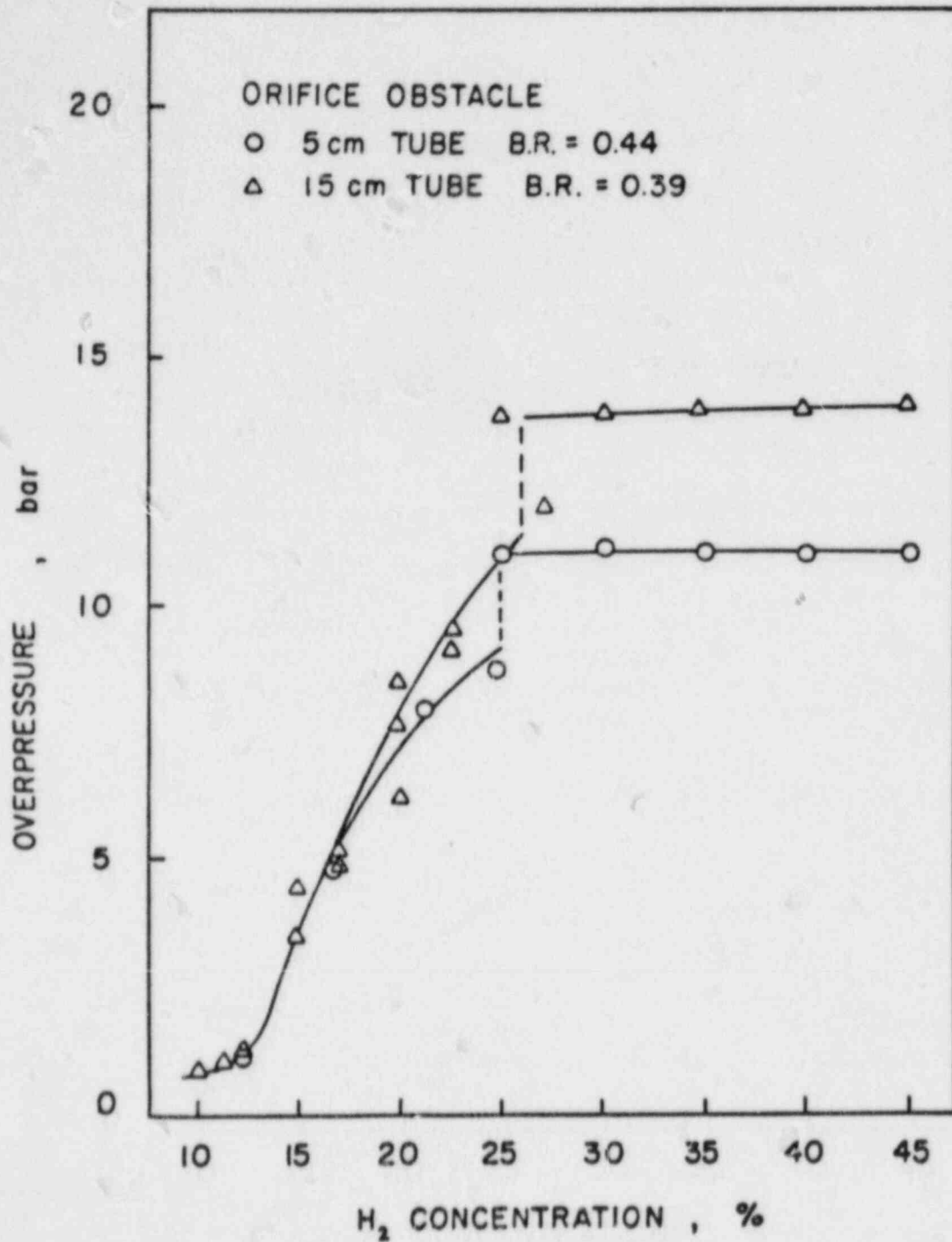


Figure 3.31. Overpressure at Steady State Flame Speeds for Hydrogen:Air Mixtures

where  $y$  is the fuel mole fraction in the undiluted hydrogen:air mixture and  $x$  is the mole fraction of  $\text{CO}_2$  diluent in the diluted mixture. The dilution range extends from  $x = 0.0$  to  $x = 0.15$  in increments of 0.05. Only lean hydrogen:air mixtures (i.e.,  $0.1 \leq y \leq 0.3$ ) have been examined.

The normal burning velocities obtained by dividing the rate of increase of the flame radius by the density ratio across the flame are plotted in Figure 3.32. Results show that the normal burning velocity is affected significantly by the addition of  $\text{CO}_2$ . For the range of hydrogen:air mixtures considered ( $0.08 \leq y \leq 0.3$ ), addition of 5%  $\text{CO}_2$  ( $x = 0.05$ ) lowers the normal burning velocities by roughly 40%. For  $x = 0.1$ , the normal burning velocity is lowered by almost 60%. To compare the influence of other diluents to that of  $\text{CO}_2$  on the burning velocity, similar experiments are performed using  $\text{N}_2$  as diluent. These results are also shown in Figure 3.32. With 10%  $\text{N}_2$  ( $x = 0.1$ ), as indicated by the solid symbols, approximately a 15% reduction in the normal burning velocity is observed. Also plotted on the same figure is the result obtained by Liu and MacFarlane on the normal burning velocity of hydrogen:air:steam mixtures (indicated by the dot-dashed line). [15] Similarly to the addition of  $\text{N}_2$ , addition of 10% steam ( $x = 0.1$ ) results in roughly a 15% reduction. These results clearly indicate that  $\text{CO}_2$  plays a different role in influencing the normal burning velocity than does  $\text{N}_2$  or steam. Further studies are needed to be able to identify more precisely the mechanisms of  $\text{CO}_2$  dilution effects in hydrogen:air mixtures.

To study the influence of  $\text{CO}_2$  on flame acceleration, the maximum flame speeds for hydrogen:air: $\text{CO}_2$  flames are examined in a 15 cm tube filled with orifice-ring obstacles. Figure 3.33 shows the maximum flame speeds for various hydrogen:air mixtures under different degrees of  $\text{CO}_2$  dilution. With 5%  $\text{CO}_2$  ( $x = 0.05$ ), the maximum flame speeds range from less than 100 m/s for 15% hydrogen ( $y = 0.15$ ) to slightly less than 900 m/s for stoichiometric hydrogen:air mixtures. An interesting note is that even with only 5%  $\text{CO}_2$ , the flame fails to transit to quasi-detonation. Because of the cubic-power dependence of initiation energy on detonation cell size, 5% addition of  $\text{CO}_2$  in stoichiometric hydrogen:air mixture will increase the energy required to initiate detonation by three times. The transition from deflagration to detonation, as a result of flame acceleration is, therefore, highly improbable. If transition to detonation does not occur, the maximum flame speed results from the gas-dynamic choking of the flow ahead. Gas-dynamic choking sets an upper limit on the flow velocity ahead of the flame, which, in turn, sets a limit on the turbulence intensity and reaction rate in the combustion zone. Therefore, the maximum flame speeds in this regime are directly related to the local sonic velocities.

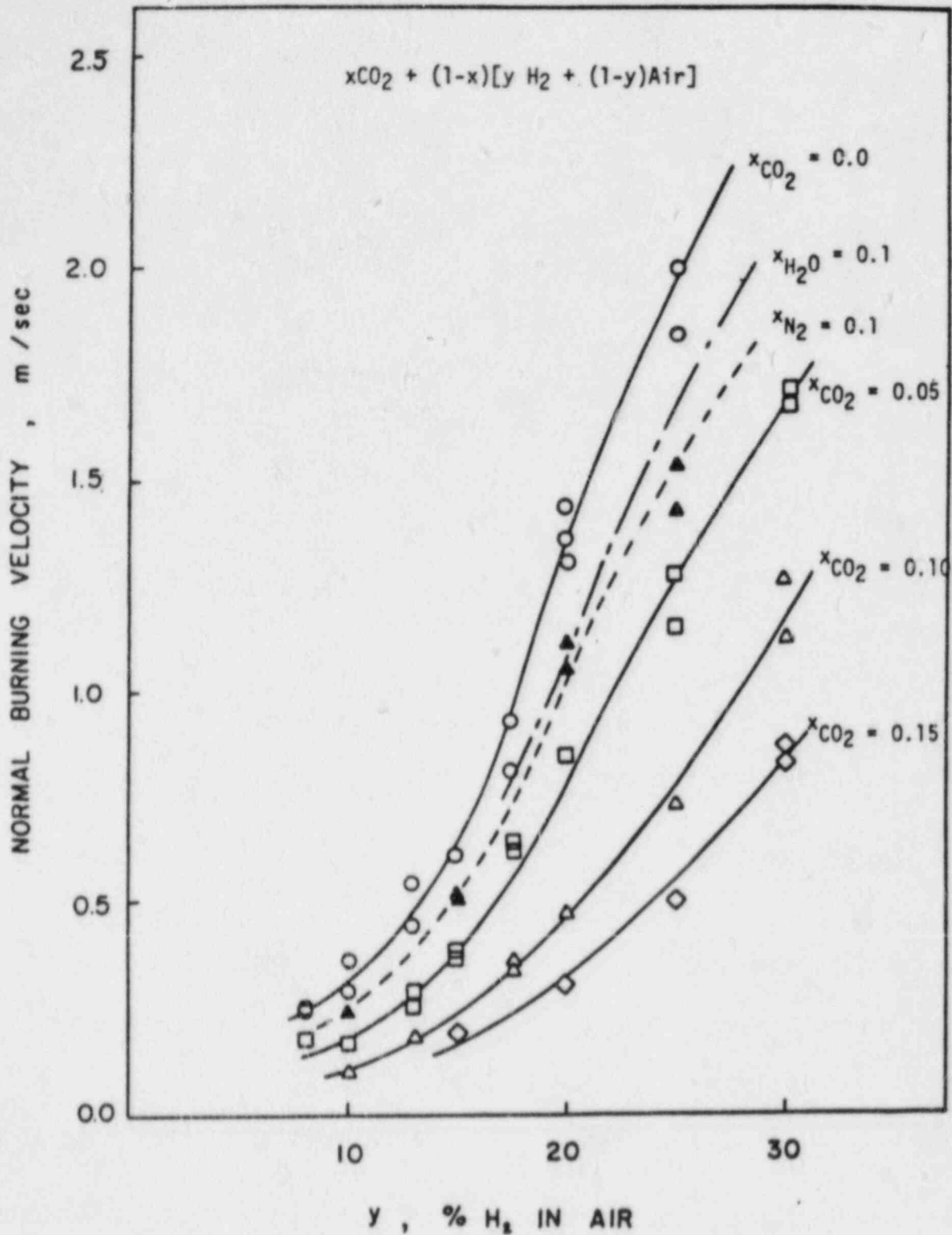


Figure 3.32. Normal Burning Velocity for Hydrogen:Air:CO<sub>2</sub> Mixtures



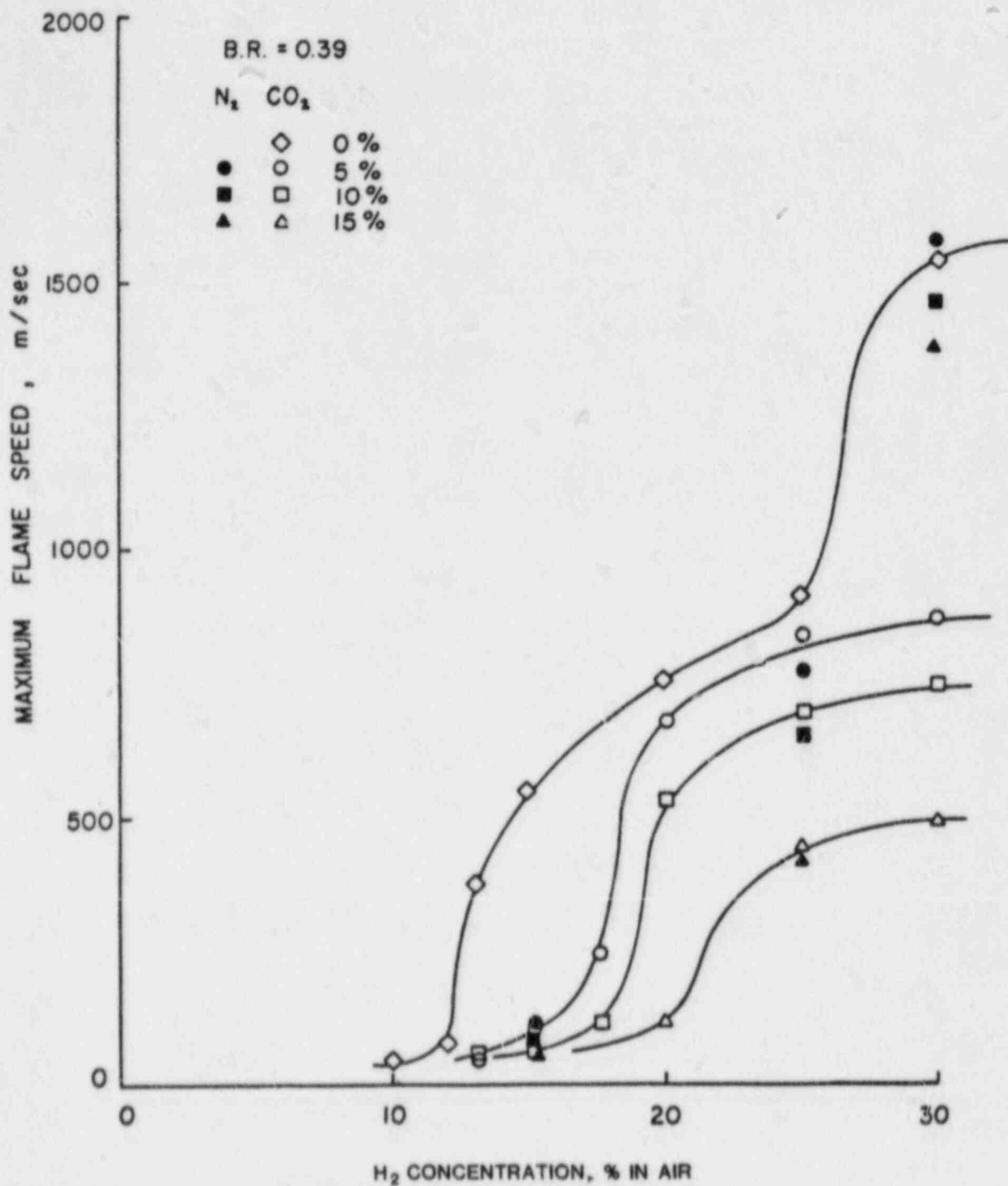


Figure 3.33. Steady-State Flame Speeds for Hydrogen:Air:CO<sub>2</sub> Mixtures

To examine the effects of  $N_2$  as a diluent, similar experiments are performed for some selected conditions. Results are also shown in Figure 3.33. In general, the effects of  $N_2$  and  $CO_2$  are similar below 25% hydrogen, indicating that both of them act as pure diluents in the reaction zone resulting in a lowering of flame temperature and lowering of the laminar burning velocity. However, for more sensitive mixtures such as stoichiometric hydrogen:air,  $N_2$  has little effect on the maximum flame speed. Even with 15% dilution, the maximum flame speed is still of the order of 1400 m/s. Unlike  $CO_2$ ,  $N_2$  does not prevent the flame from transiting to a quasi-detonation state.  $N_2$  is a stable molecule and dissociates only under extremely high temperatures. (Characteristic dissociation temperature for  $N_2 = 113,000$  K).  $N_2$  is, therefore, less efficient as a mitigation agent.

#### 3.2.13.1.4 The Interaction of a Vortex Ring with a Spherical Flame

The fundamental problem in turbulent flames is the complex coupling between the flame front and the vorticity in the unburned flow ahead. The present study isolates this basic mechanism and investigates the interaction of a simple vortex ring with a flame front. The flame-vortex interaction mechanism also plays an important role in the flame acceleration process past multiple obstacles [30,31,32], as well as in the transition from deflagration to detonation.[33] The dynamics of vortex rings have been studied by Lamb [34], Maxworthy [35,36,37], and reviewed by Saffman.[38] Interesting studies of combustible vortex rings have also been reported by McCormack.[39,40]

The experiments were performed in a 20 x 20 cm cylindrical chamber (Figure 3.34). Stoichiometric mixtures of methane and propane with air at atmospheric pressure were used. The mixtures were prepared in a continuous flow system with the fuel:air concentration controlled by standard flowmeters. Ignition was produced by a spark at the middle of the vessel. The vortex rings were produced in two different ways, as shown in Figure 3.34:

- To obtain strong turbulent vortex rings, a shock tube was used. The driver section consisted of a very small volume ( $\sim 3$  cm<sup>3</sup>) that could be pressurized.
- To obtain weak vortex rings, a piston was inserted in the driven section and a sharp-edged orifice fixed at the entry of the chamber.

Using a time delay between the rupture of the shock tube diaphragm by the plunger and the ignition by the spark, the size of the flame when the interaction with the vortex occurred could be varied. The diagnostics for the experiment were

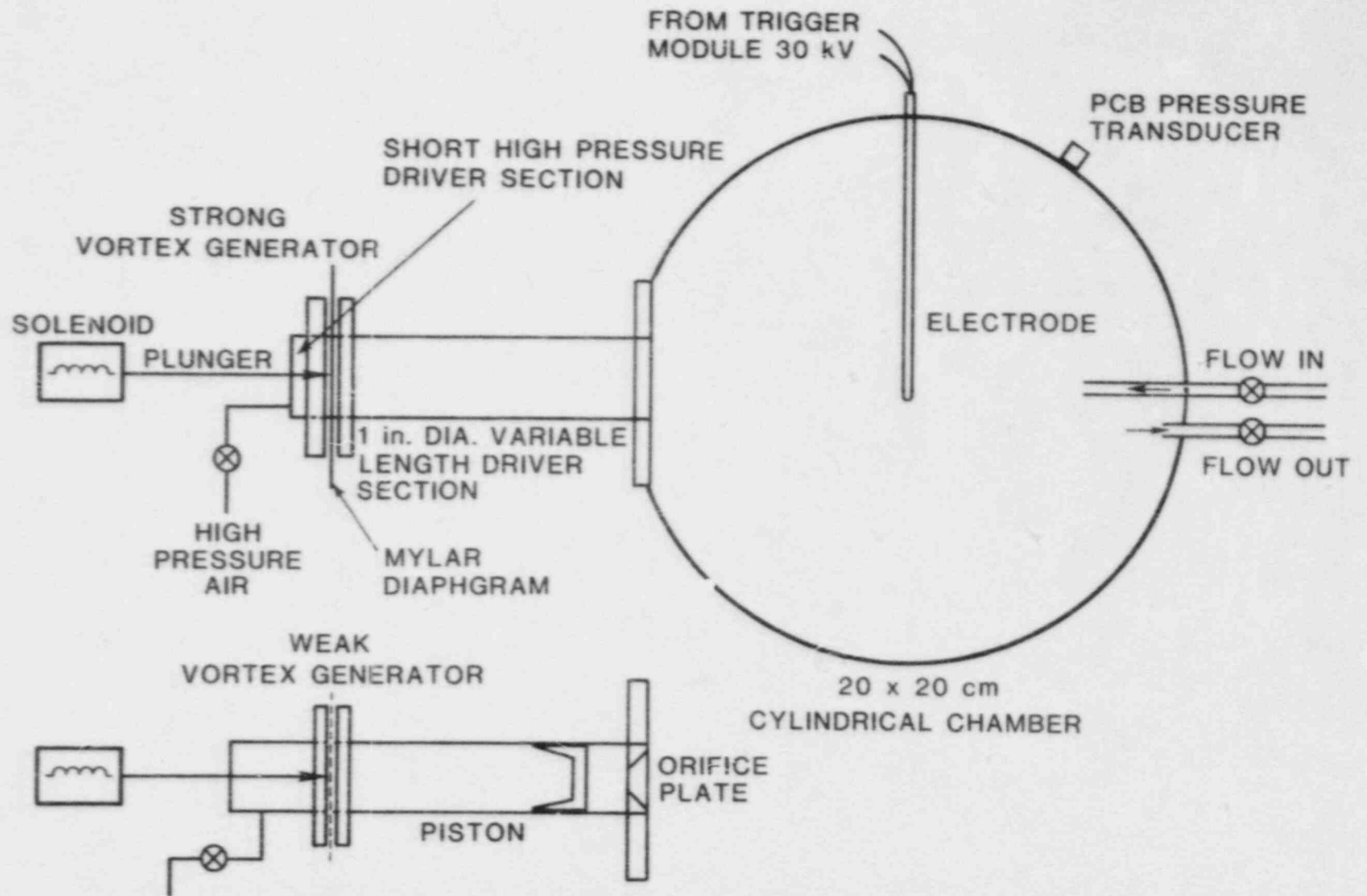


Figure 3.34. Apparatus

pressure-time records (PCB pressure transducer) and high-speed Schlieren movies (Hycam Camera: 5,000 frames per second).

The typical interaction phenomenon between a vortex ring and the spherical flame is shown in the sequence of the frames from the high speed Schlieren movie in Figure 3.35. The vortex ring, traveling from left to right, is just in front of the flame in the first frame. The flow following the diverging weak spherical shock that precedes the vortex ring causes the spherical flame to "flatten out" at the upstream site. The vortex ring penetrates into the flame ball and leaves it at the downstream site. The entire flame surface takes on a fine scale turbulent structure as a result of the interaction. A significant increase in the burning rate occurs resulting in a shorter burnout time of the volume of mixture in the vessel. If the size of the spherical flame is small compared with the diameter of the vortex ring, the rapid turbulent mixing of the cold unburned gases of the vortex ring and the hot gases in the flame burned during the interaction results in quenching. The sequence of Schlieren photographs (Figure 3.36) clearly illustrates the quenching phenomenon. The quenching criteria are found to depend on the relative sizes of the vortex ring and the flame kernel as well as the vortex strength. For a strong turbulent vortex, quenching occurs when the diameter of the flame kernel is less than the vortex ring diameter. Typical records of the pressure-time development in the vessel are shown in Figure 3.37.

The present study demonstrates that a significant increase in the turbulent burning rate occurs when a laminar flame interacts with a vortex. The experimental scheme employed permits detailed diagnostics to be made during the interaction process. The simplicity of the model of isolating a single vortex ring to interact with a laminar front also permits theoretical analysis to be carried out.

### 3.2.13.2 Influence of Obstacles on Detonation Propagation

The ultimate objective of our study of hydrogen:air detonations is to achieve a priori predictions of the dynamic detonation parameters such as detonation limits, critical initiation energy, conditions for transition from deflagration to detonation, and transmission criteria (critical tube diameter, critical channel width, etc.). Progress in detonation research of the past few years has resulted in the establishment of the detonation cell size as the fundamental parameter from which all dynamic detonation parameters can be derived (either through the use of theoretical models or empirical laws).[41] Thus, in the hydrogen program over the past couple of years, considerable attention has been devoted to the experimental measurement of cell size in hydrogen:air detonations. However, cell-size measurement is not without difficulties, as discussed below.

\* Acceleration

time between pictures : 1.2 ms



Figure 3.35. Interaction of Vortex Ring with a Spherical Flame (Acceleration)

3-70

\* Quenching

time between pictures : 0.8 ms

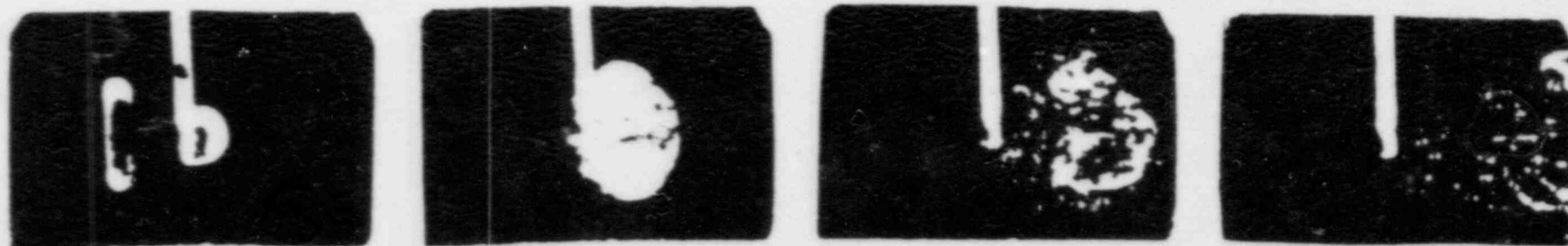


Figure 3.36. Interaction of a Vortex Ring with a Spherical Flame (Quenching)

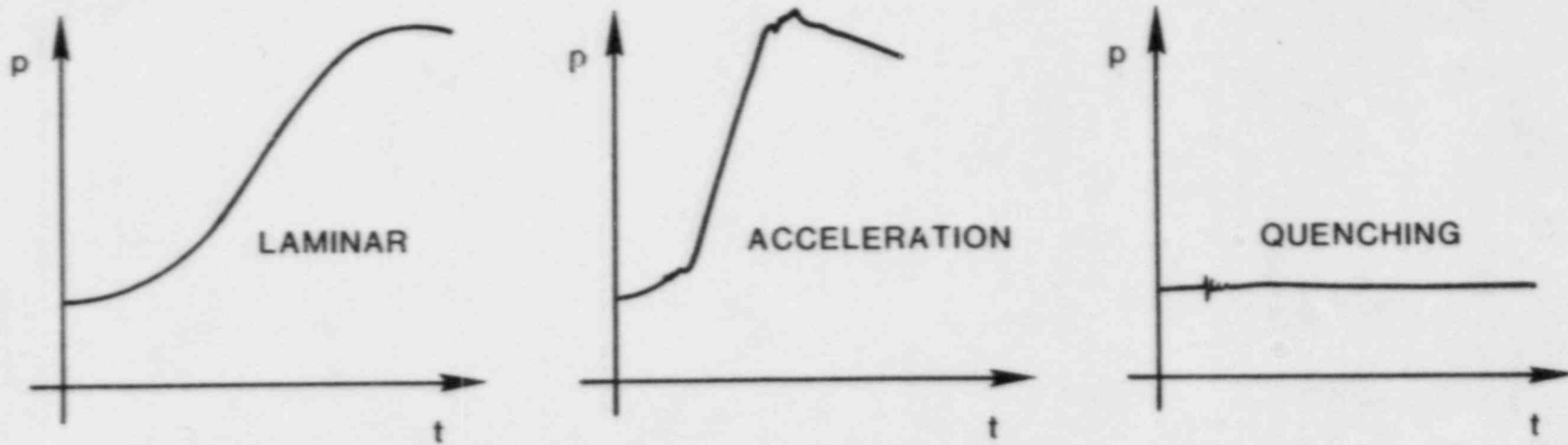


Figure 3.37. Pressure-Time Records

This report summarizes the results obtained to date. They are preliminary in nature but we feel that they should be included now to reflect the current state of the art. Important conclusions and implications of these results are currently being followed up to establish more definitive results to be reported later.

The presence of obstacles (e.g., equipment) in the path of a detonation can result in detonation quenching. Therefore, appropriate obstacles may be used as detonation traps. The aim of the present investigation is to study the mechanisms associated with the interaction of a detonation with obstacles in order to formulate adequate detonation quenching criteria.

Experiments were performed in a cylindrical tube (2.64 m long and 5.5 cm in diameter) containing stoichiometric mixtures of hydrogen-oxygen and ethylene-oxygen initially at subatmospheric pressures in the range from 20 to 150 torr. Detonation was initiated by a spark located at one end of the tube. Obstacles in the form of perforated plates of porosity (defined as the ratio of the open area to total area) ranging from 0.34 to 0.53 and screens of porosity in the range 0.38 - 0.81 were placed halfway along the tube from the tube ignition end. Detonation cell sizes were recorded on smoked foils located in front of and behind the obstacle.

The smoked foil records showed that detonation-obstacle interaction can occur in four different ways:

- (1) No visible interaction.
- (2) Increase of cell sizes over a certain distance after passage of the detonation through the obstacle followed by a return to the cell size observed ahead of the obstacle.
- (3) Detonation quenching upon passage through the obstacle followed by deflagration propagation over a certain distance and detonation reinitiation.
- (4) Same as (3), except that no detonation reinitiation was observed (i.e., reinitiation distance greater than 50 cm).

Depending on the type of obstacle (perforated plate or screen) two quenching criteria can be defined from the variation of reinitiation distance  $\Delta$  (i.e., the distance behind the obstacle where detonation cells return to their original size before interaction with the obstacle, i.e., cases (1), (2), and (3)) with the obstacle characteristic dimension (i.e., hole diameter  $d$  for perforated plate and wire spacing  $h$  for screen) plotted in Figures 3.38 and 3.39. All variables ( $\Delta$ ,  $d$ , and  $h$ ) have been normalized using the cell size  $\lambda$ . The

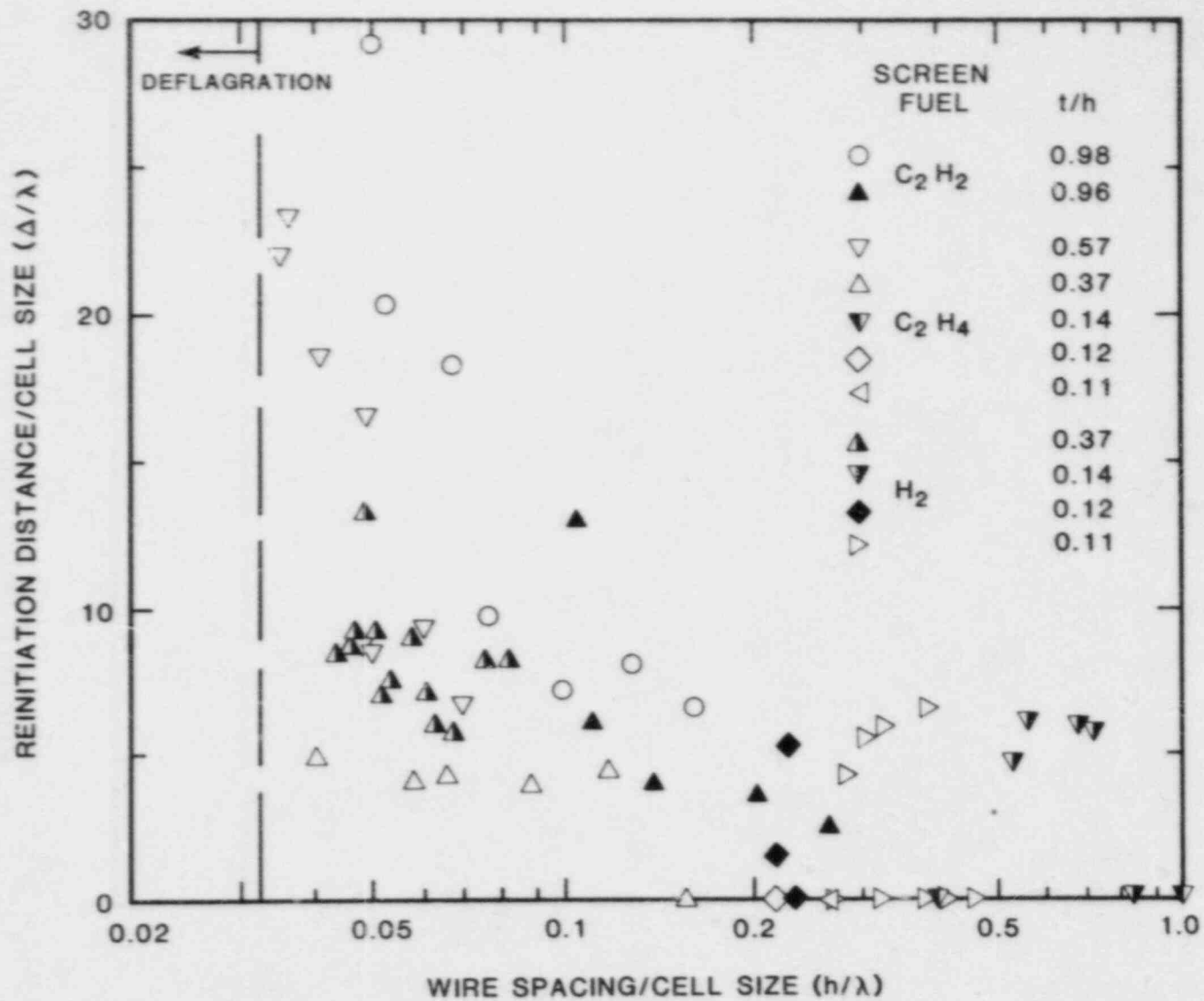


Figure 3.38. Reinitiation Distance vs Hole Diameter



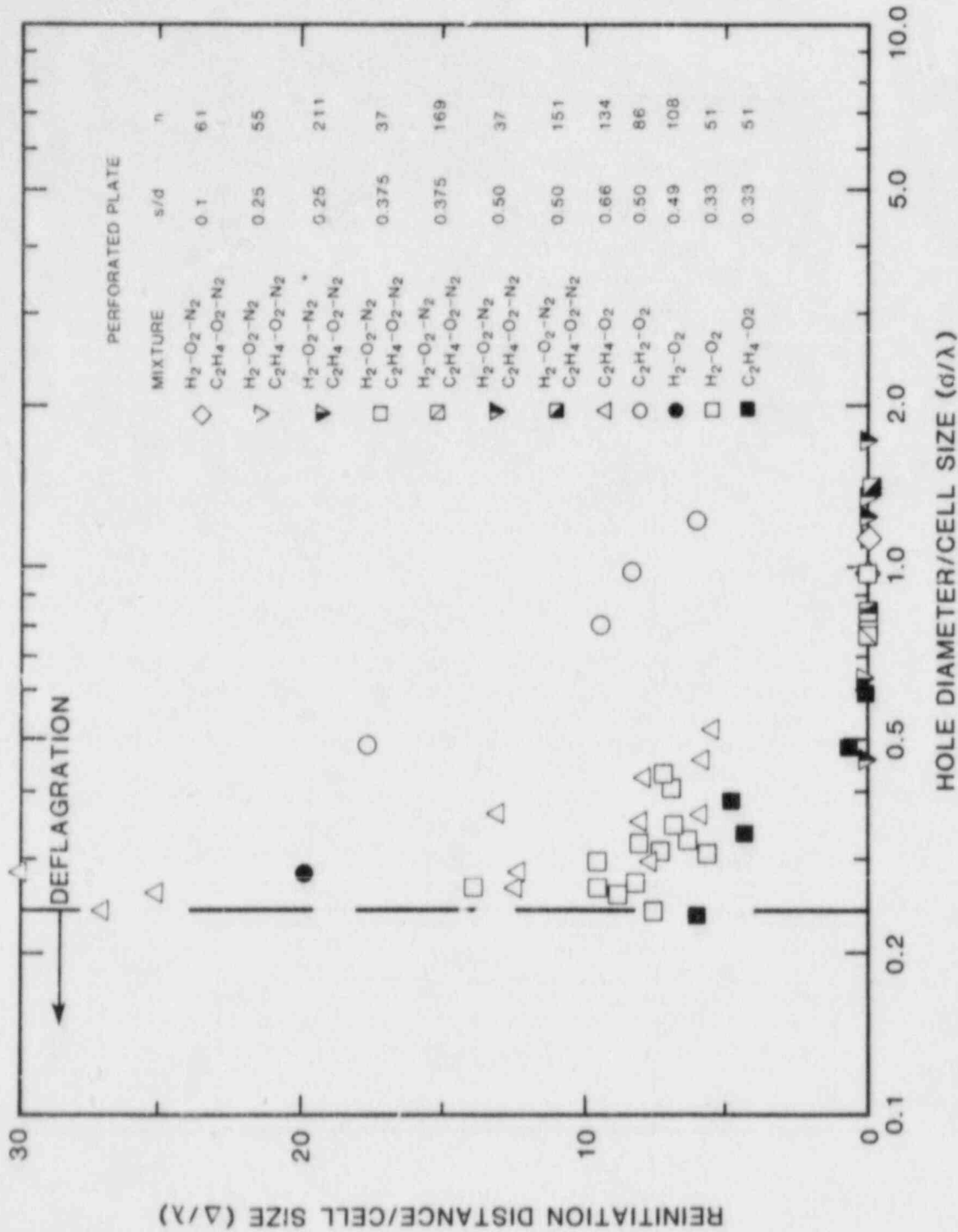


Figure 3.39. Reinitiation Distance vs Wire Spacing

present results shown in Figure 3.38 indicate that detonation quenching by perforated plates occurs for ratios of hole diameter to cell size less than about 0.25 (i.e.,  $d/\lambda \sim 0.25$ ). In the case of perforated plates, the smaller quenching diameter results from the interaction of the diffracted shocks upon transmission of the detonation through the holes.

The present preliminary results indicate that detonation quenching by obstacles in a confined environment strongly depends on the nature of the obstacle. For perforated plates of  $s/d$  ratios (where  $s$  is the hole spacing) ranging from 0.3 to 0.7, the quenching diameter is less than approximately one quarter of a cell size (i.e.,  $d/\lambda \sim 0.25$ ). For screens with  $t/h$  ratios (where  $t$  is the wire thickness and  $h$ , the wire spacing) ranging from about 0.1 to 1, the quenching wire spacing is less than approximately 3/100 of a cell size (i.e.,  $h/\lambda \leq 0.03$ ). In other words, the quenching efficiency of screens is about one order of magnitude smaller than that of perforated plates and approximately two orders of magnitude smaller than that of boundary layer development in constant-area tubes. Additional studies are currently being carried out to provide more physical insights into the mechanisms governing the transmission through obstacles and reinitiation of detonation waves in confined environments.

#### 3.2.13.3 Transmission of Detonations Into Unconfined Environments through Multiple Openings

The transmission of a confined detonation into an unconfined environment through openings is of major concern in risk analyses of detonation hazards. The present study is concerned with the transmission of detonations through multiple openings. The experiments were performed in the same apparatus used for the detonation transmission studies through a single opening, and a schematic of the apparatus is shown in Figure 3.40. The openings consisted of two-hole plates of hole diameters  $d = 2$  inches with spacing ranging from  $s = 0.03d$  to  $s = 1.75d$ , as well as multiple-hole plates of hole diameters  $d = 0.50$  inch and  $0.25$  inch with spacing ranging from  $s = 0.1d$  to  $s = 0.5d$ . Stoichiometric mixtures of oxygen:hydrogen and  $C_2H_4-O_2$  diluted with  $N_2$  initially at atmospheric pressure were tested. The detonation was initiated in the detonation tube by means of an exploding wire. Its subsequent propagation in the detonation tube ahead of the perforated plate was monitored by a pressure transducer. Successful transmission or failure in the detonation chamber (the unconfined environment) was recorded by a pressure transducer on the end wall of the detonation chamber.

The variations of critical hole diameter  $d$  with hole spacing  $s$  for two-hole plate plotted in Figure 3.41 exhibit a continuous increase from  $d \approx 5.5\lambda$  when  $s/d \approx 0.03$  to  $d \approx 13\lambda$  for  $s/d \geq 0.6$ . Such behavior results from the collisional interaction of the diffracted shocks generated by the transmission

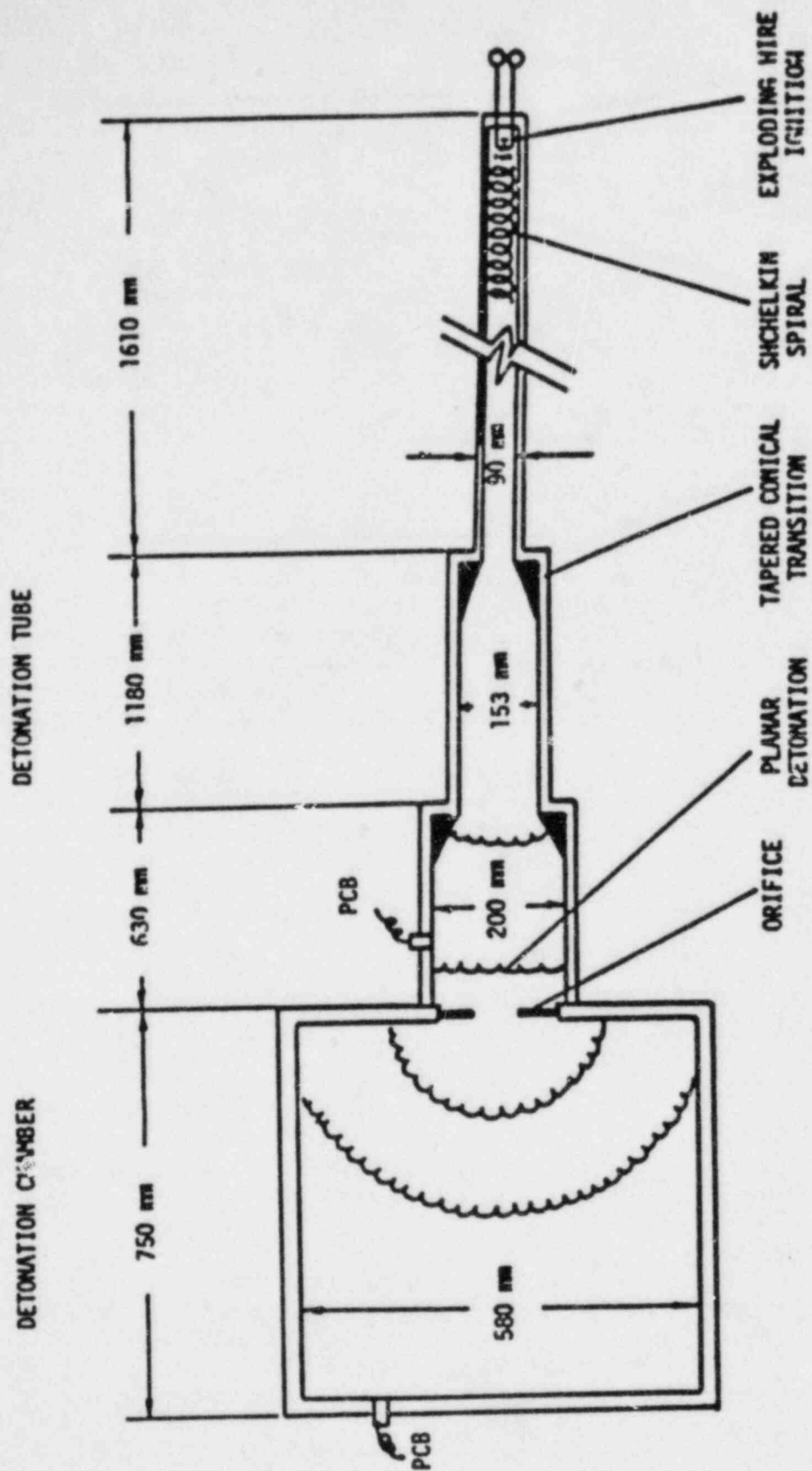


Figure 3.40. Experimental Apparatus

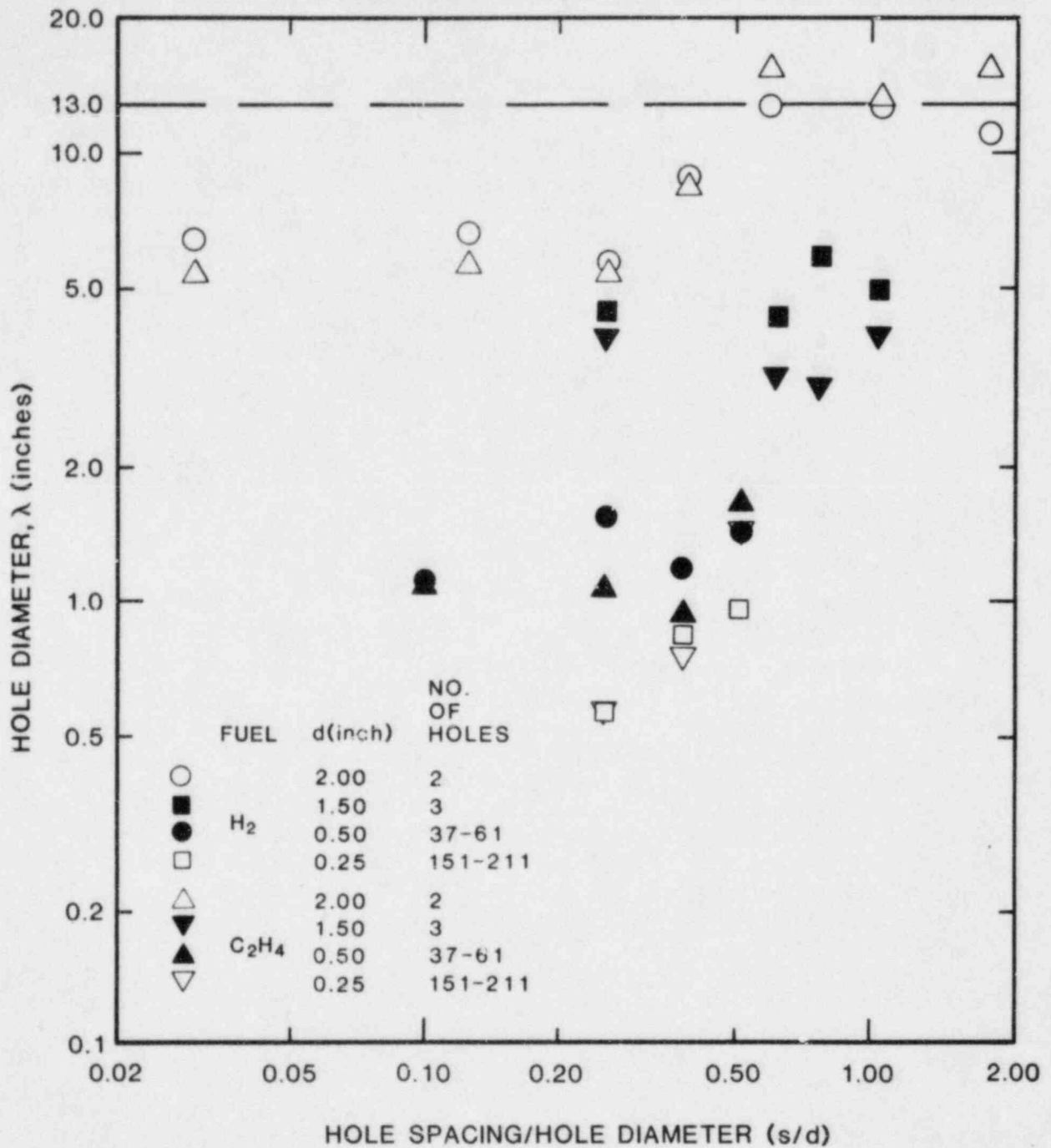


Figure 3.41. Variations of Critical Hole Diameter with Hole Spacing for Two-Hole Plate

of the detonation through each hole. As the hole spacing increases from  $s/d = 0$ , the collision of the diffracted shocks occurs at later times when the shock strengths are smaller and the collision process can no longer serve to assist detonation transmission. Therefore, for a given hole diameter, as the hole spacing increases, successful detonation transmission requires a more sensitive mixture characterized by a smaller cell size  $\lambda$ . When the hole spacing is greater than approximately half a hole diameter, the present results indicate that each hole behaves like a single opening and the critical hole diameter must be at least of the order of the critical tube diameter, i.e.,  $d = d_c \approx 13$ . Furthermore, when the hole spacing  $s$  approaches zero, the critical hole diameter ( $d \approx 5.5\lambda$ ) for a two-hole plate with aspect ratio  $L/W = 2d/d = 2$  does not differ appreciably from the critical channel width  $W/\lambda \approx 7$  for a rectangular slot of same aspect ratio.

Detonation transmission through a three-hole plate is achieved in less reactive mixtures as shown in Figure 3.41, where for  $s/d$  ratios ranging from 0.5 to 1, a 50% reduction in critical hole diameter to cell size ratio  $d/\lambda$  is observed. Increasing the number of holes up to about 200 by decreasing the hole diameter by a factor of 4 results in an order of magnitude reduction in  $d/\lambda$  for the range of  $s/d$  ratios tested so far (i.e.,  $0.25 \leq s/d \leq 0.5$ ). This reduction in critical hole diameter may be ascribed to the enhancement of the interaction of the diffracted shocks.

#### 3.2.13.3.1 Transmission of Detonations Through Diverging Channels

It has been found experimentally [42] that the detonation propagation limit in a two-dimensional channel of thickness  $W$  is when the cell size  $\lambda \approx W$ . On the other hand, Benedick's experiments on the transmission of a two-dimensional detonation into unconfined spaces showed that  $W \approx 3\lambda$  for successful transmission. This is to be compared to the three dimensional case of a round tube where successful transmission requires  $d_c \approx 13\lambda$ . [43] In order to elucidate the two-dimensional transmission mechanism, experimental studies were carried out in which the divergence of the channel may be varied from  $0^\circ$  (corresponding to a confined propagation along the straight duct) to  $90^\circ$  (corresponding to the unconfined case). Thus we would expect the failure criteria to vary between  $\lambda \leq Wc \leq 3\lambda$ .

The present experiments use a rectangular channel of aspect ratio  $L/W = 12$ . The detonation channel of rectangular cross section ( $L = 12$  in,  $W = 1$  in) is 10 ft long. Stoichiometric oxygen:hydrogen mixtures at subatmospheric pressures ranging from 50 torr to 250 torr were tested. Controlled expansions in a square detonation chamber, at the exit end of the detonation channel, were achieved by two-hinged steel plates, whose angles can be varied from  $\theta = 0^\circ$  to  $90^\circ$  (unconfined detonation). Detonation velocities were monitored by two ion probes

in the rectangular channel and a pressure transducer in the expansion chamber. The cellular structure of the detonation was recorded on smoked foils located in the rectangular channel for all divergence angles and in the expansion chamber for the 90° divergence case. In the present study, it has been postulated that successful transmission has occurred if the wave velocities in both rectangular channel and expansion chamber do not differ by more than 200 m/s.

The variations of the critical number of detonation cells across the channel width  $W/\lambda$  with divergence angle  $\theta$  plotted in Figure 3.42 show a sharp increase from  $W/\lambda = 1$  to about 5.5 when  $\theta$  increases from 0° to 40°. For  $\theta = 90^\circ$ ,  $W/\lambda \approx 4$  seems to suggest that a critical expansion exists (i.e., a critical angle of divergence) beyond which the critical number of cells remains constant. The present results are in qualitative agreement with the previous results of Bowick [44], which are also plotted in Figure 3.42. The short length (3 ft) of the rectangular channel used by Bowick may be responsible for the quantitative disagreement of both sets of data. The present result for the 90° expansion ( $W/\lambda \approx 4$ ) agrees with the earlier results ( $W/\lambda \approx 3$ ) obtained by Liu et al. [45] and Benedick et al. [46] for aspect ratios  $L/W > 7$  in fuel:air and fuel:oxygen:nitrogen mixtures at atmospheric pressure, initially.

#### 3.2.13.3.2 The Chapman-Jouguet Surface Location as an Alternative Measure of the Detonation Cell Size

The classical one-dimensional model of a self-sustained detonation wave (i.e., a Chapman-Jouguet (or C-J) detonation) postulates the existence of a sonic plane (the C-J plane) behind the shock front separating the burnt from the unburned gases. In the one-dimensional reactive model of Zeldovich, von Neumann, and Doering (ZND model), the location of the sonic plane is of the order of the chemical reaction length. The existence of a sonic surface in a real self-sustained (i.e., three-dimensional) detonation wave was demonstrated by Vasiliev et al. with experiments on the interaction of a detonation wave with a thin plate.[47] Vasiliev et al. concluded that the location of the sonic surface behind a detonation wave varies between one and three cell lengths  $L$ , i.e., approximately between two and six cell diameters  $\lambda$ . A similar conclusion was reached by Edwards et al.[48] In view of these data, the location of the C-J surface could provide an alternative way to estimate detonation cell size, especially in mixtures with poor cell regularity.

To extend the validity of these earlier results, preliminary experiments were performed in undiluted and diluted stoichiometric oxygen:hydrogen mixtures at initial pressures ranging from 60 to 200 torr. Both helium and carbon dioxide were

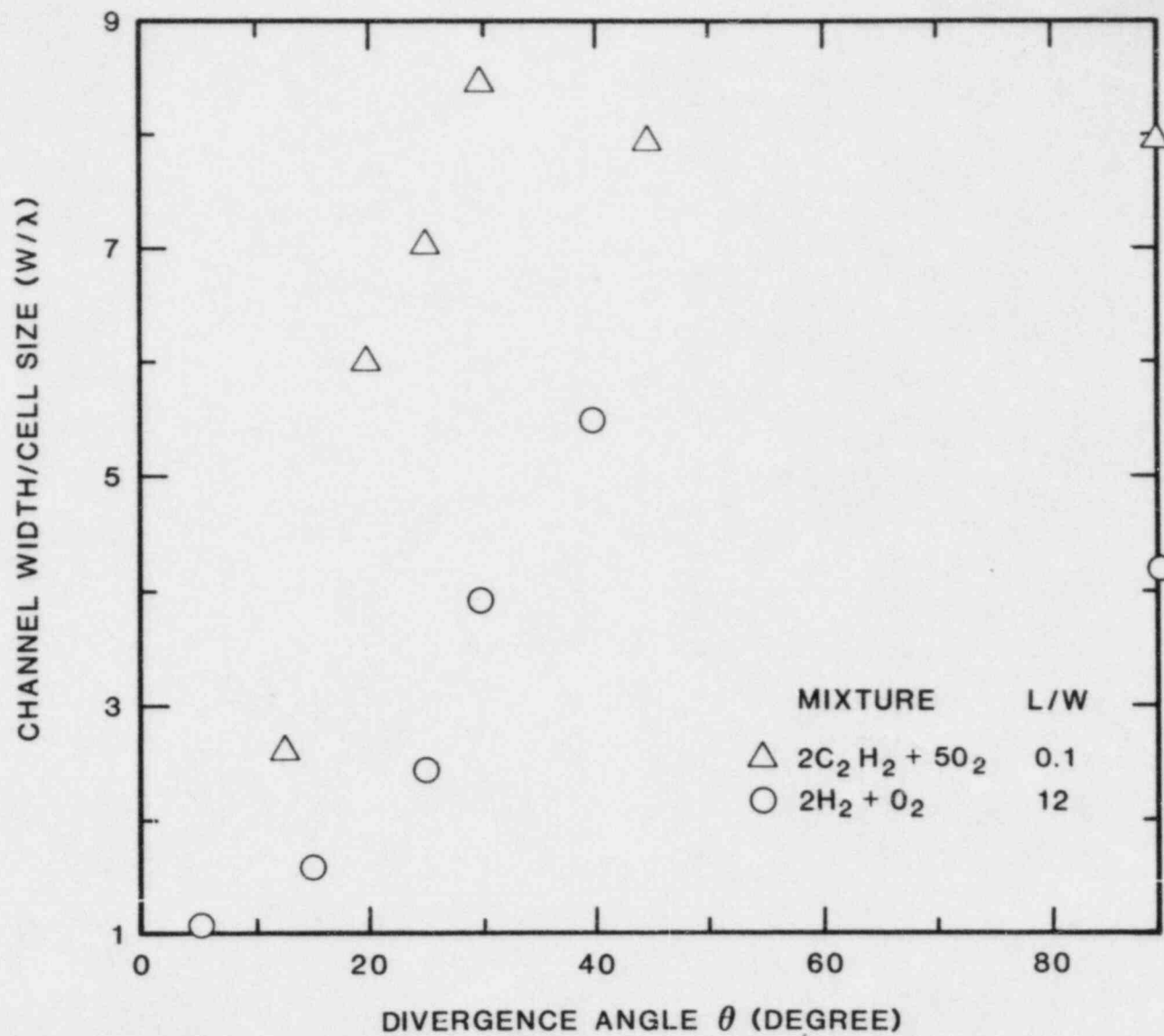


Figure 3.42. Variations of the Critical Number of Detonation Cells Across the Channel Width with Divergence Angles

used as diluents. Detonations were initiated by an exploding wire in a cylindrical tube, 15 cm in diameter, 3.7 m long. Plastic and metallic smoked foils (15 cm x 20 cm) recorded the cellular structure of the detonation. A piezoelectric pressure transducer located 2.3 m from the ignition end of the tube monitored the pressure decay behind the detonation front. The location of the C-J surface was associated with the last pressure oscillation on the pressure record.

Our present preliminary results indicate that the location of the C-J surface of a multidimensional detonation wave is not a unique multiple of the detonation cell size in contrast with earlier results reported by Vasiliev et al. and Edwards et al. for a limited range of mixtures and initial conditions. We found that the location of the C-J surface depends significantly on the tube diameter and initial pressure. Therefore, the measurement of the C-J surface location does not seem a valid alternative to the measurement of detonation cell size.

### 3.2.13.3.3 Influence of the Ignition Source Characteristics on the Direct Initiation of Gaseous Detonations

Direct initiation of gaseous detonations requires the generation of free radicals for the oxidation reactions. In conventional initiation techniques, free radicals are generated by thermal dissociation in the shock wave created by the ignition source. However, Lee et al. have demonstrated that the use of chemical sensitizers (like  $\text{NO}_2$ ) and flash photolysis provide alternative initiation methods without the initial presence of strong shock waves.[49] Similarly, direct initiation of detonations in fuel:oxygen mixtures by rapid turbulent mixing of a jet of hot combustion products with a cold explosive mixture was also achieved by Knystautas et al.[50] To provide a better understanding of the initiation phenomena, initiation studies were conducted with two initiation sources, namely, an electrical spark and a cold turbulent jet of fluorine molecules.

#### 3.2.13.3.3.1 Electrical Spark Initiation

The present study intends to generate cylindrical critical energy data using an electrical spark discharge. The experiments were conducted in a 20-cm-diameter steel sphere equipped with 6-mm brass rod electrodes. Flanged and pointed electrodes, as well as spherical electrodes made of copper or steel, were used. The range of electrode spacing was restricted by experimental limitations. For spacings greater than about 3.5 cm, the spark becomes highly nonlinear. A pressure transducer mounted on the sphere wall detected direct initiation by sensing the time of arrival of the combustion wave, as well as the magnitude of the pressure wave itself. As described in detail in Refs. 49 to 51, the spark energy is calculated from the discharge current which is measured with a Pearson current transformer.



Several varied experiments were carried out with  $C_2H_4-O_2$  mixtures. These results will be reported in detail in future topical reports. Preliminary studies were also carried out in  $2H_2 + O_2$  mixtures and  $2H_2 + O_2$  mixtures diluted with 2% and 5%  $CO_2$ . Direct initiation of cylindrical detonation in the undiluted stoichiometric mixture was achieved at an initial pressure of 570 torr with a spark gap  $L = 2.5$  cm, i.e. at  $L/\lambda \approx 12$ . The corresponding critical energy  $E_C = 1.86$  J/cm indicates that  $2H_2 + O_2$  mixtures are less reactive than  $C_2H_4 + 3O_2$  mixtures, a well-known result from cell size measurements.[52] An interesting note is that the present results indicate that the direct initiation energy of cylindrical detonations in stoichiometric oxygen:hydrogen mixtures is about three orders of magnitude smaller than the initiation energy of spherical detonations in stoichiometric hydrogen:air mixtures. On the other hand, direct initiation of a stoichiometric oxygen: hydrogen mixture diluted with 2%  $CO_2$  at 570 torr initially requires an initiation energy in excess of 7.8 J/cm for the same spark gap ( $L = 2.5$  cm). Furthermore, no direct initiation could be achieved with 5%  $CO_2$  dilution using the maximum energy available, namely 30 J/cm.

In summary, the present preliminary results indicate that direct initiation of cylindrical detonations by an electrical discharge requires a spark gap at least of the order of 10 detonation cell sizes.

#### 3.2.13.3.3.2 Direct Initiation of Spherical Detonations by Cold Turbulent Jet Mixing

Whereas conventional initiation techniques rely on the shock wave generated by the ignition source to initiate chemical reactions in the explosive mixture, in shockless initiation chemical reactions are initiated by flash photolysis, chemical sensitizers, or turbulent jet mixing. The present study deals with shockless initiation by turbulent jet mixing of cold chemical species with a cold explosive mixture. Because the success of this initiation technique depends strongly on turbulent mixing in a transient jet, a poorly understood mechanism, preliminary studies on transient jet behavior were carried out simultaneously to provide fundamental data on transient jet phenomena which are also relevant to flame acceleration studies.

##### 3.2.13.3.3.2.1 Transient Jet Studies

Among the parameters which characterize transient jet behavior (e.g., jet penetration, entrainment rate, mixing rate, turbulence intensity, etc.), the present studies were restricted to the measurement of jet penetration in unobstructed and obstructed environments. Such a parameter, which requires the formation of a critical volume for successful shock amplification, is critical for shockless initiation studies.

Transient jet experiments were carried out in cylindrical vessels of lengths  $L = 11$  cm, 20 cm, 30 cm, and 45 cm and diameters  $D = 6$  cm and 10 cm. One of the cylinders was sealed by a diaphragm, which was ruptured by pressurizing the vessel with cold air in the pressure range from 60 psig to 350 psig. Upon rupture of the diaphragm, a transient turbulent jet of cold air was ejected into the ambient atmosphere. The diagnostics consisted of (i) a barium titanate crystal to detect the diaphragm rupture time, hence the time  $t = 0$  for cold air ejection, and (ii) a hot wire anemometer to measure the time of arrival of the jet tip at various locations downstream from the vessel exit. The influence of obstacles on jet penetration was also investigated using a perforated plate with blockage ratio  $BR = 0.44$  located just ahead of the diaphragm.

For a given initial pressure ( $p_0 = 140$  psig) and a given vessel length ( $L = 20$  cm), an increase in vessel diameter by a factor of 1.7 does not significantly affect the jet penetration distances. The influence of vessel length on jet penetration is shown in Figure 3.43, where jet trajectories for a given initial pressure ( $p_0 = 140$  psig) and a given vessel diameter ( $D = 6$  cm) have been plotted. The maximum jet penetration distance (i.e., when the pressure in the vessel drops to the ambient pressure) increases with increasing vessel length because the rarefaction waves traveling inside the vessel propagate longer before the vessel pressure drops to ambient pressure. For the range of vessel pressures studied in the longest vessel ( $L = 45$  cm) with the same diameter ( $D = 6$  cm), the jet penetration time at a fixed location ( $x = 20$  cm,  $X/D = 3.3$ ) shows a very weak dependence on vessel pressure with a minimum time ( $t \approx 0.55$  ms) around  $p_0 = 180$  psig. The influence of obstacles on jet penetration is shown in Figure 3.44 where for a fixed vessel pressure ( $p_0 = 140$  psig) in a given vessel ( $L = 20$  cm,  $D = 10$  cm), a perforated plate (blockage ratio  $BR = 0.44$ ) slightly increases the time of arrival of the jet at a fixed location downstream up to distances  $x \approx 7.5D$  (i.e.,  $x = 75$  cm). Beyond that distance, the obstacle seems to decrease the time of arrival of the jet. The present results suggest that the fine-scale turbulence associated with the small eddies generated by the multiple jets, created by the perforated plate slightly inhibits the jet penetration. Although better entrainment is provided by large-scale eddies, fine-scale turbulence remains responsible for the mixing process.

### 3.2.13.3.3.2.2 Shockless Initiation Studies

Direct initiation of fuel:air detonations by turbulent mixing of a cold jet of highly reactive chemical species (fluorine molecules) was investigated in both small-scale (laboratory) and large-scale (field test) experiments. The small-scale experiments were carried out in two in-line vertically mounted cylindrical chambers separated by a steel diaphragm. A schematic of the apparatus is shown in Figure 3.45. The

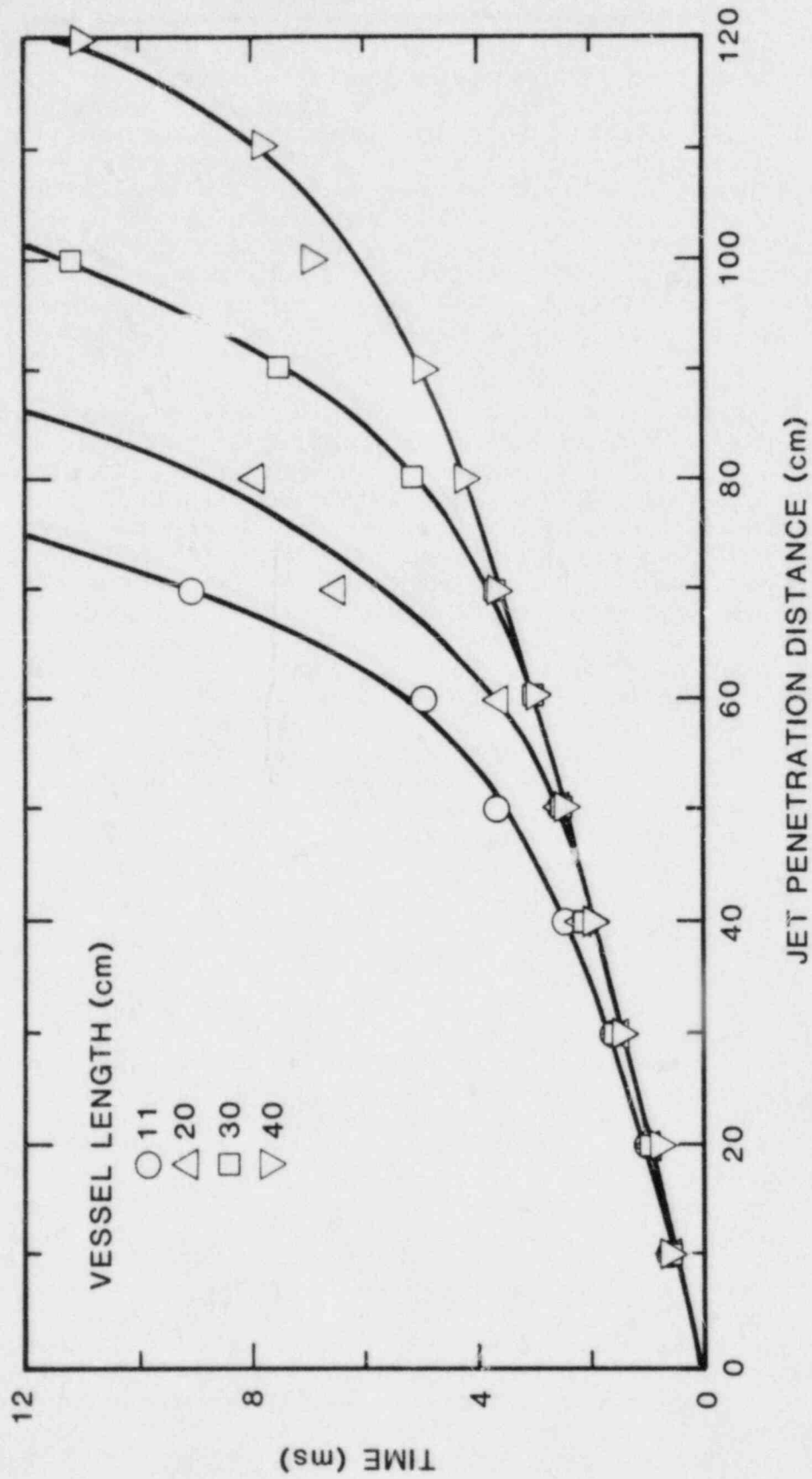


Figure 3.43. Influence of Vessel Length on Jet Penetration

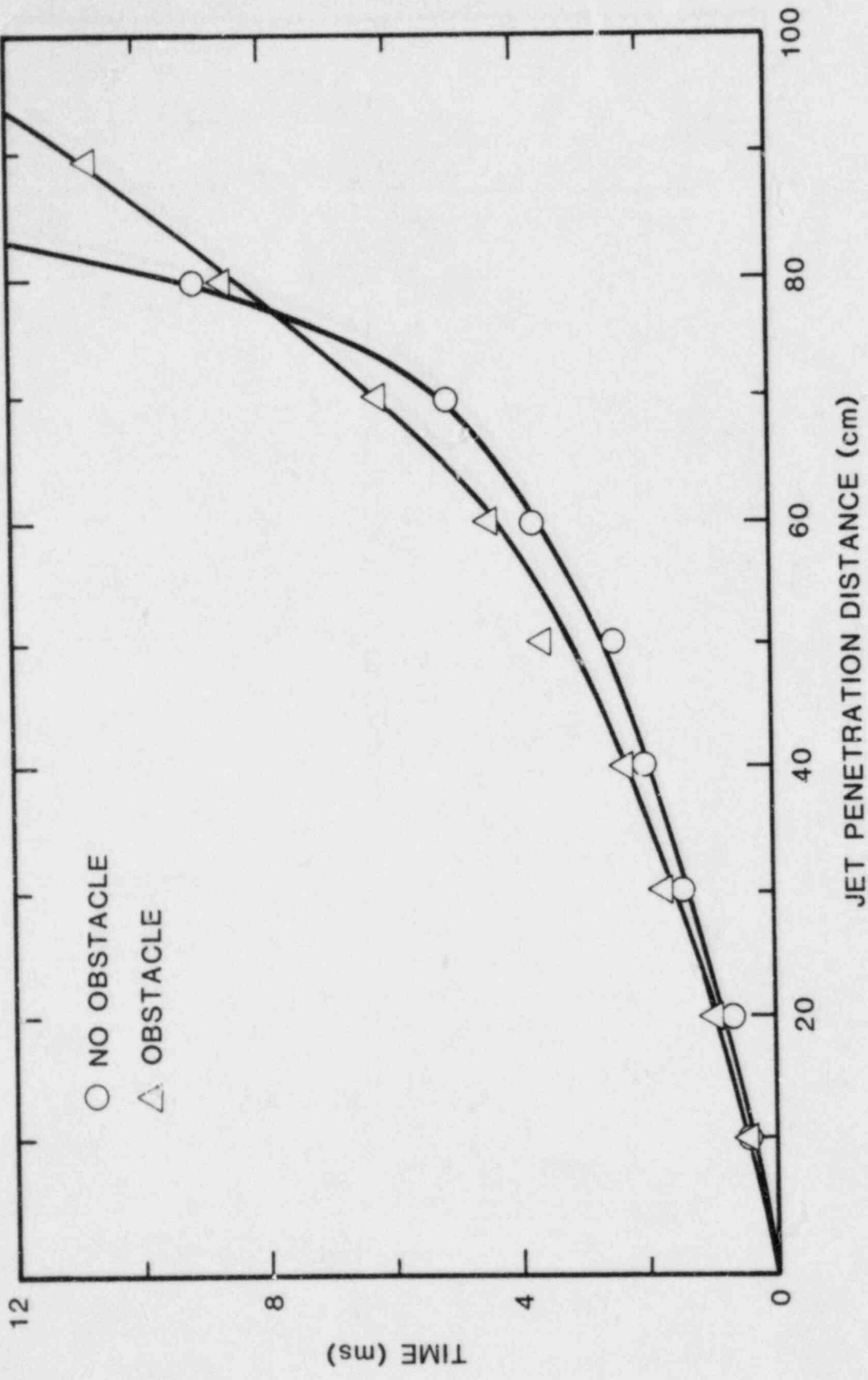


Figure 3.44. Influence of Obstacles on Jet Penetration

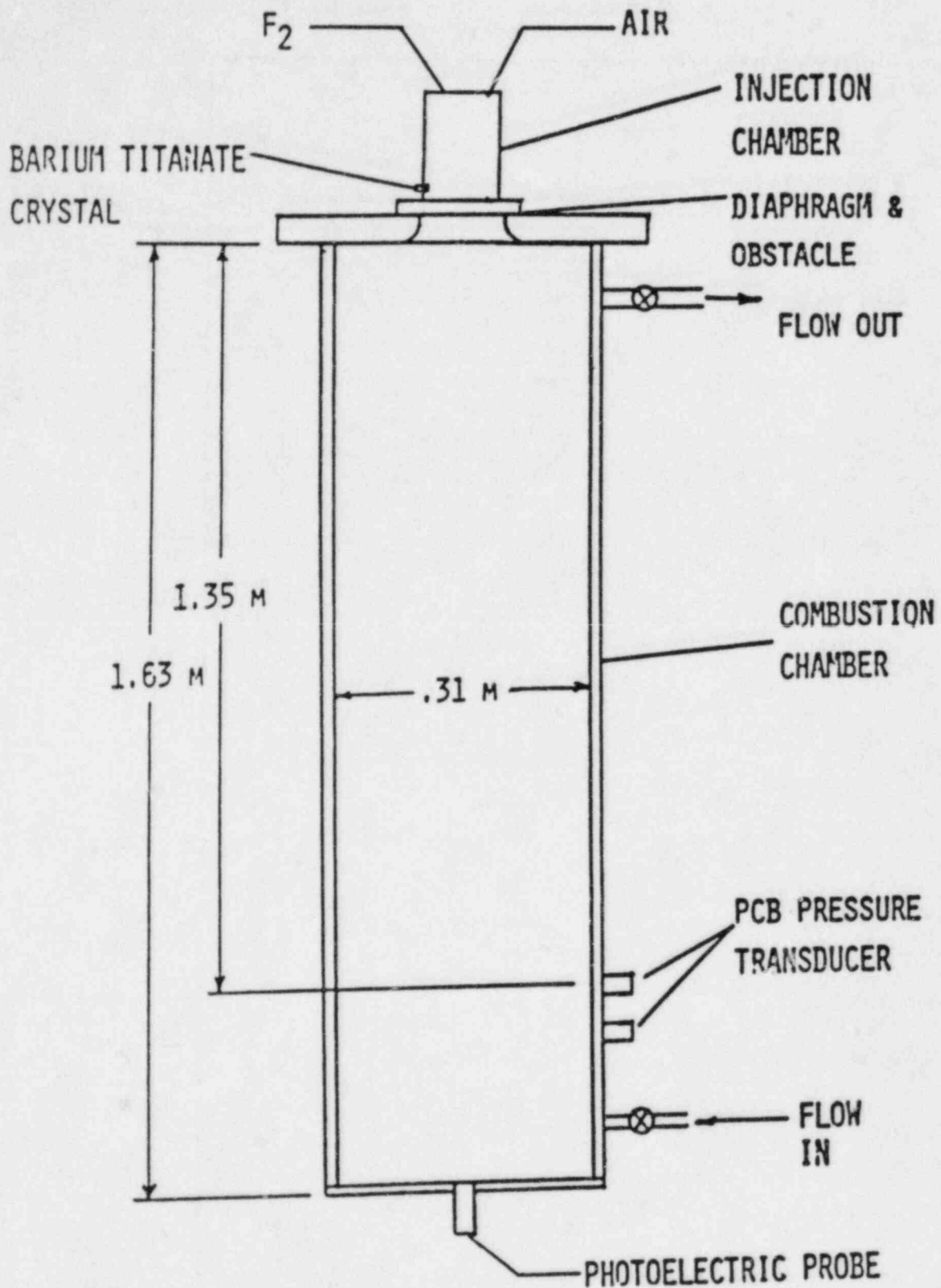


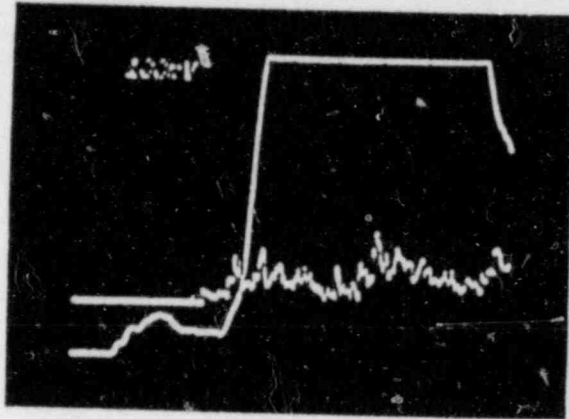
Figure 3.45. Schematic of Apparatus for Shockless Initiation Studies

injection chamber (i.e., the upper chamber, 5.1 cm in diameter, 10.2 cm in length) contained fluorine:air mixtures pressurized at 105 psia and 265 psia. Stoichiometric fuel:air mixtures at atmospheric pressure were loaded into the detonation chamber (i.e., the lower chamber, 31 cm in diameter, 1.63 m in length). Different obstacle configurations (perforated plates) were mounted at the exit of the injection chamber to control the turbulence scale of the fluorine:air jet. The diagnostics consisted of (i) a barium titanate crystal close to the diaphragm to provide a zero-time basis for the event, (ii) a photoelectric probe at the bottom of the detonation chamber to record the combustion wave luminosity, and (iii) two piezoelectric pressure transducers to monitor the pressure in the detonation chamber so that successful initiation could easily be identified. Smoked foils were also placed in the detonation chamber to record the detonation cellular structure.

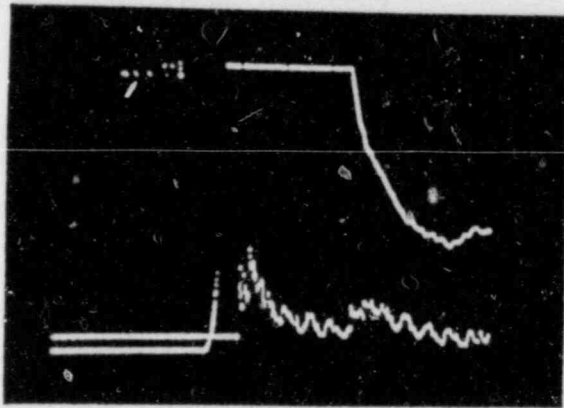
Direct initiation of detonation in both stoichiometric hydrogen:air and  $C_4H_{10}$ -air mixtures was achieved whereas stoichiometric  $C_3H_8$ -air mixtures could not be initiated. Typical pressure and luminosity records are shown in Figure 3.46. In the hydrogen:air tests, the minimum fluorine concentration in the injection chamber necessary to initiate detonation is 20%. Detonations were initiated in hydrogen:air mixtures with fluorine concentrations ranging from 20% to 30% with or without obstacles at the injection chamber exit. The presence of obstacles decreases the initiation time (i.e., the time between the rupture of the diaphragm and the onset of luminosity). Therefore, it seems that obstacles at the injection chamber exit increase the vorticity and turbulence intensity at the head of the jet, hence decrease the mixing time and the induction delay.

In the large-scale experiments (performed at the DRES facility in Alberta), hydrogen:air mixtures containing 30% and 42% hydrogen were tested. The explosive mixture was contained in plastic bags (9.4 m in length, 0.9 or 1.8 m in diameter). Fluorine:air mixtures at 200 psig were injected into the bag from a cylindrical chamber (0.3 m in length, 0.15 m in diameter). Diagnostics included pad-mounted pressure transducers and three high-speed motion picture cameras viewing from the side,  $30^\circ$  from the bag axis, and directly in line with the bag. Direct initiation was achieved with fluorine concentrations of 20% and 25%.

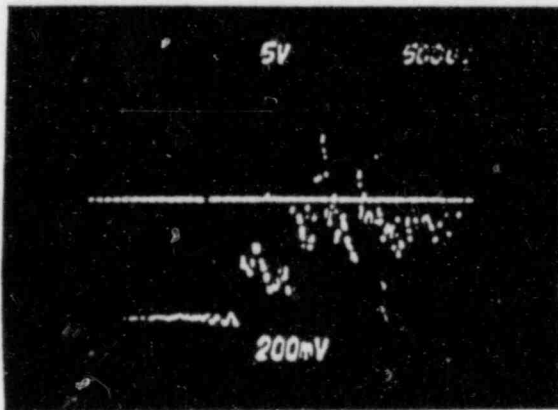
To optimize the shockless initiation process, several parameters must be properly adjusted. For example, to generate an adequate free radical gradient, the mixing time should be of the order of the induction time of the fluorine:fuel reactions, otherwise, deflagration will occur before a suitable amplification gradient has been created. Additional studies on transient turbulent jets are in progress to provide a



30 % F<sub>2</sub>  
 105 PSIA  
 H<sub>2</sub>- AIR



20 % F<sub>2</sub>  
 103 PSIA  
 H<sub>2</sub>- AIR



42% F<sub>2</sub>  
 265 PSIA  
 PROPANE- AIR

Figure 3.46. Typical Pressure and Luminosity Records

better quantitative understanding of jet development for optimizing shockless initiation parameters.

### 3.2.13.3.3 Effects of Additives on Detonation Propagation

Among the various procedures to mitigate explosion hazards, the use of additives seems very attractive. In previous studies conducted at McGill University on the desensitization of hydrogen:air detonations [53],  $\text{CO}_2$  was proven a very effective agent for hydrogen:air mixtures. Adding 15%  $\text{CO}_2$  to a stoichiometric hydrogen:air mixture results in a detonation cell size  $\lambda$  increase of almost an order of magnitude and a corresponding increase of about three orders of magnitude in critical initiation energy,  $E_c \sim \lambda^3$ . Theoretical modeling of detonation cell size using a detailed kinetic scheme for the oxidation of  $\text{H}_2$ - $\text{CO}_2$  mixtures [53] has indicated that  $\text{CO}_2$  acts as an inert diluent rather than a chemically active species. To further the understanding of detonation desensitization by additives, two studies were conducted on detonation propagation in subatmospheric stoichiometric oxygen:hydrogen mixtures diluted with rare gases (argon and helium),  $\text{CO}_2$  and halogenated compounds ( $\text{CH}_3\text{Br}$ ,  $\text{CH}_3\text{Cl}$ , and  $\text{CF}_3\text{Br}$ ).

The first study involving rare gas and  $\text{CO}_2$  addition was carried out in a 15-cm-diameter, 3.7-m-long tube. Stoichiometric oxygen:hydrogen mixtures in the pressure range from 60 torr to 250 torr were studied. Detonation was initiated by an exploding wire. The diagnostics consisted of a piezoelectric pressure transducer (located 2.23 m from the ignition end) to monitor the detonation pressure, 5 ion probes (spaced 25 cm apart) to measure detonation velocity, and smoked foils (15 cm x 20 cm) to record the detonation cellular structure.

The variations of detonation cell size  $\lambda$  with initial pressure  $p_0$  plotted in Figures 3.47 through 3.49 for undiluted and diluted  $2\text{H}_2 + \text{O}_2$  mixtures obey a power law of the form  $p_0 = K\lambda^\alpha$  where the constants  $K$  and  $\alpha$  depend on the mixture composition. On the same plots, the solid line represents the cell sizes derived from Matsui and Lee's critical tube diameter ( $d_c$ ) experiments [54] using Mitrofanov and Soloukhin empirical relationship ( $d_c \approx 13\lambda$ ) [53]. As shown in Figure 3.49,  $\text{CO}_2$  remains the most efficient diluent for oxygen:hydrogen mixtures because a 20%  $\text{CO}_2$  dilution increases the cell size of the undiluted mixture by almost a factor of 3. However, the loss of cell regularity with  $\text{CO}_2$  dilution makes it more difficult to measure cell size without ambiguity.

The second study investigated the influence of small amounts (5%) of halogen compounds ( $\text{CH}_3\text{Br}$ ,  $\text{CH}_3\text{Cl}$ , and  $\text{CF}_3\text{Br}$ ) on the propagation and transmission into unconfined space critical tube diameter experiments of detonations in stoichiometric oxygen:hydrogen mixtures initially at subatmospheric pressures



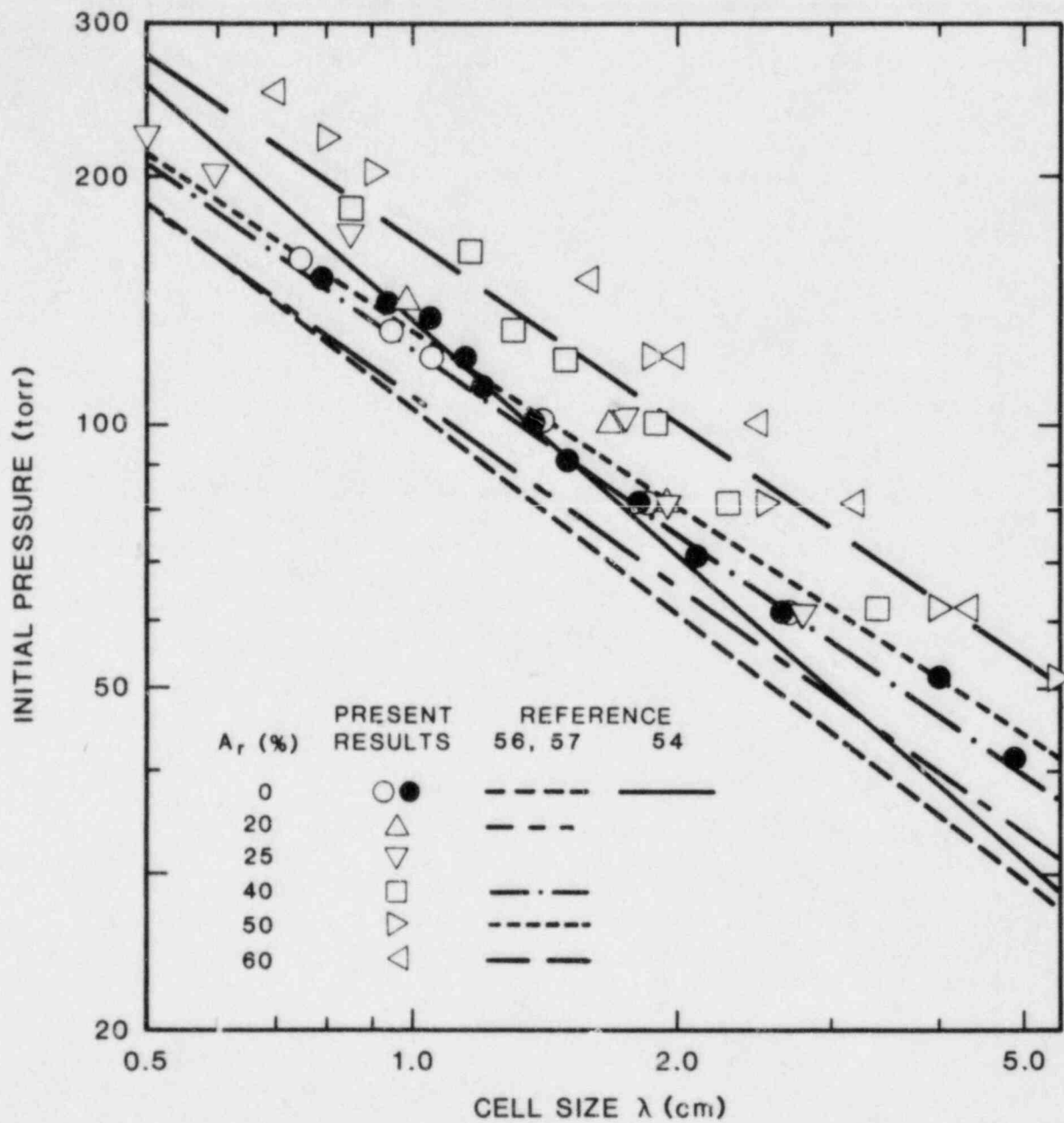


Figure 3.47. Variations of Detonation Cell Size with Initial Pressure for  $2\text{H}_2 + \text{O}_2$  Undiluted and Diluted with Argon

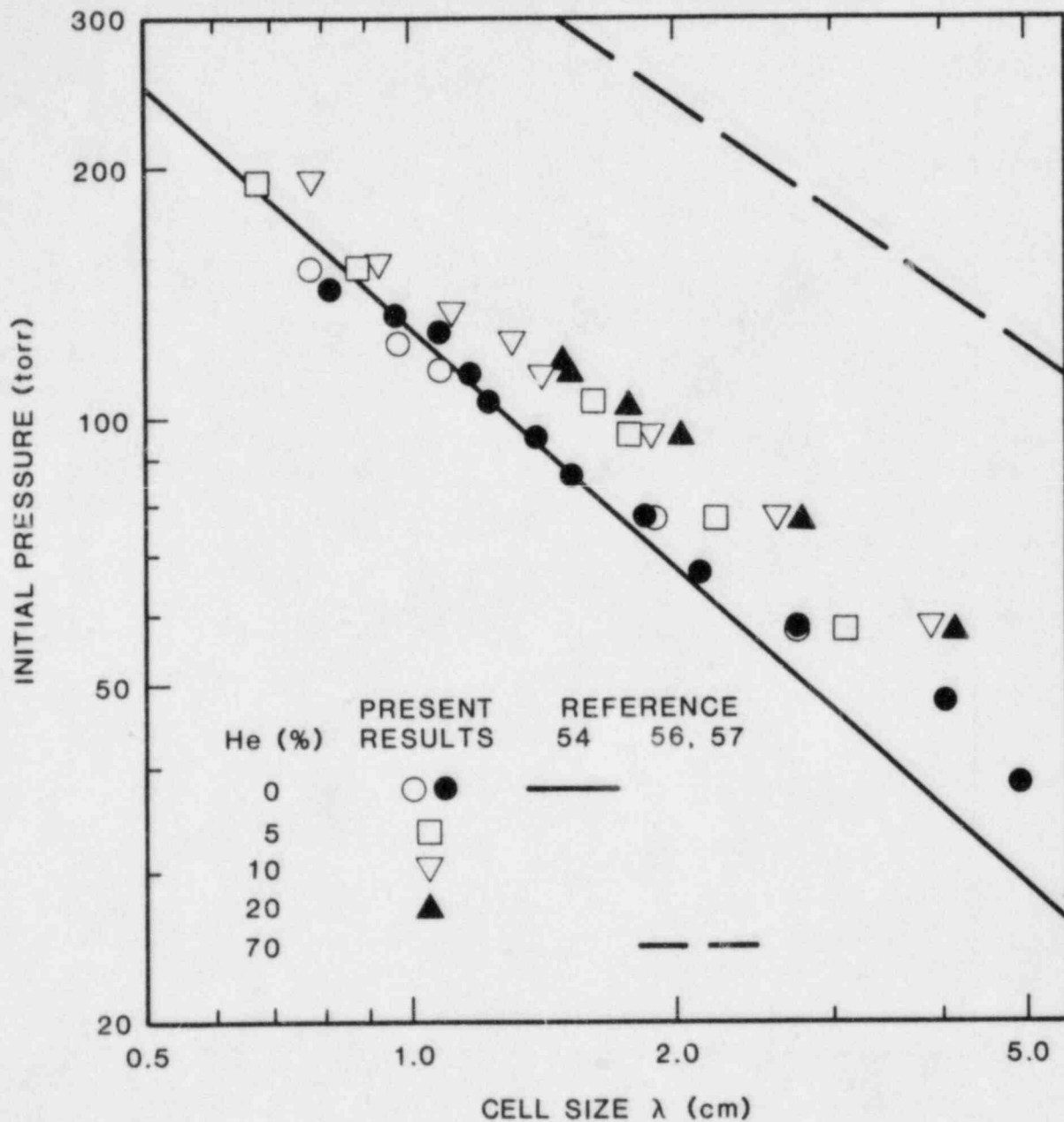


Figure 3.48. Variations of Detonation Cell Size with Initial Pressure for  $2\text{H}_2 + \text{O}_2$  Undiluted and Diluted with Helium

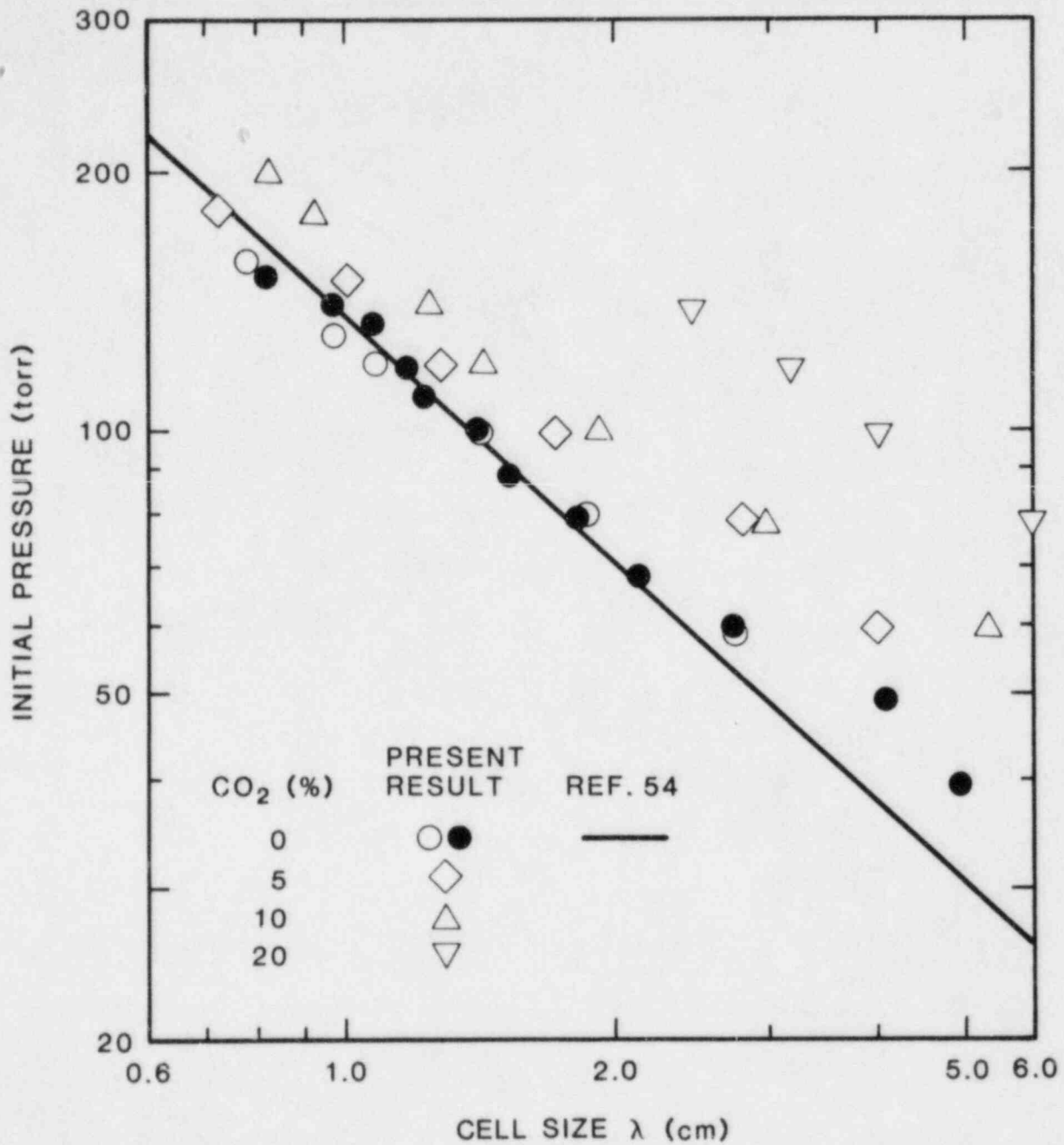


Figure 3.49. Variations of Detonation Cell Size with Initial Pressure for  $2\text{H}_2 + \text{O}_2$  Undiluted and Diluted with  $\text{CO}_2$

ranging from 75 torr to 1.200 torr. The present experiments also included 5%  $\text{CO}_2$  dilution for direct comparison with halogenated compounds. Critical-tube-diameter experiments for detonation failure were carried out in two detonation tubes (1.3 m long, 2.5 cm, and 4 cm in diameter, respectively) opening into a detonation chamber (the unconfined environment) 15 cm in diameter and 20 cm in length. Spark ignition was used along with a Shchelkhin spiral to ensure consistent detonation initiation. The diagnostics in the detonation tube consisted of 2 ion probes (0.5 m apart) to measure detonation velocity, a piezoelectric pressure transducer (0.5 m from the last ion probe) to monitor the pressure development and smoked foils near the entrance of the detonation chamber to record the detonation cellular structure. Success or failure of detonation transmission was detected in the detonation chamber by a piezoelectric pressure transducer mounted on the end wall. Both pressure transducers provided an estimate of the velocity of the transmitted wave, which was then compared to the detonation velocity measured in the detonation tube. A difference in wave velocities less than approximately 300 m/s was considered a successful transmission for a given initial mixture pressure and tube diameter. Although the critical pressure (i.e., the initial pressure of the mixture below which failure occurs) was not determined exactly, a range of pressure was established, the upper and lower limits of which characterize consistently successful transmission or failure, respectively.

Addition of 5%  $\text{CH}_3\text{Cl}$  or  $\text{CH}_3\text{Br}$  to  $2\text{H}_2 + \text{O}_2$  mixtures increases the cell size of the undiluted mixture by a factor of about 0.5 to 2 as the initial pressure decreases from 800 torr to 100 torr (Figure 3.50). Cell sizes were not measured for  $\text{CF}_3\text{Br}$  and  $\text{CO}_2$  additives. However, for the lower pressure range (100-200 torr), the  $\text{CO}_2$  data (also plotted in Figure 3.50) show a smaller desensitizing effect than the halogenated compounds. At higher pressures,  $\text{CO}_2$  remains the most effective additive to reduce the detonation sensitivity of  $2\text{H}_2 + \text{O}_2$  mixtures. In order of decreasing effectiveness,  $\text{CO}_2$  ranks first by increasing the critical pressures of the undiluted mixture in the 4 cm and 2.5 cm diameter tubes by about 62% and 75%, respectively. With 31% and 44% increases in critical pressures (for the 4 cm and 2.5 cm diameter tubes, respectively),  $\text{CH}_3\text{Cl}$  is the second most effective additive and is followed by  $\text{CH}_3\text{Br}$  with 23% and 17% increases in critical pressures. On the other hand, the well-known flame retardant  $\text{CF}_3\text{Br}$  is found to sensitize oxygen:hydrogen detonations by lowering the critical pressures by about 10% for both cases. The detonation sensitizer  $\text{CF}_3\text{Br}$  causes the largest velocity reduction followed by  $\text{CH}_3\text{Br}$  and  $\text{CO}_2$ .  $\text{CH}_3\text{Cl}$  has almost no influence on the detonation velocity of the undiluted mixture.

In summary, the present preliminary results indicate that  $\text{CO}_2$  is far more efficient than rare gases (argon and

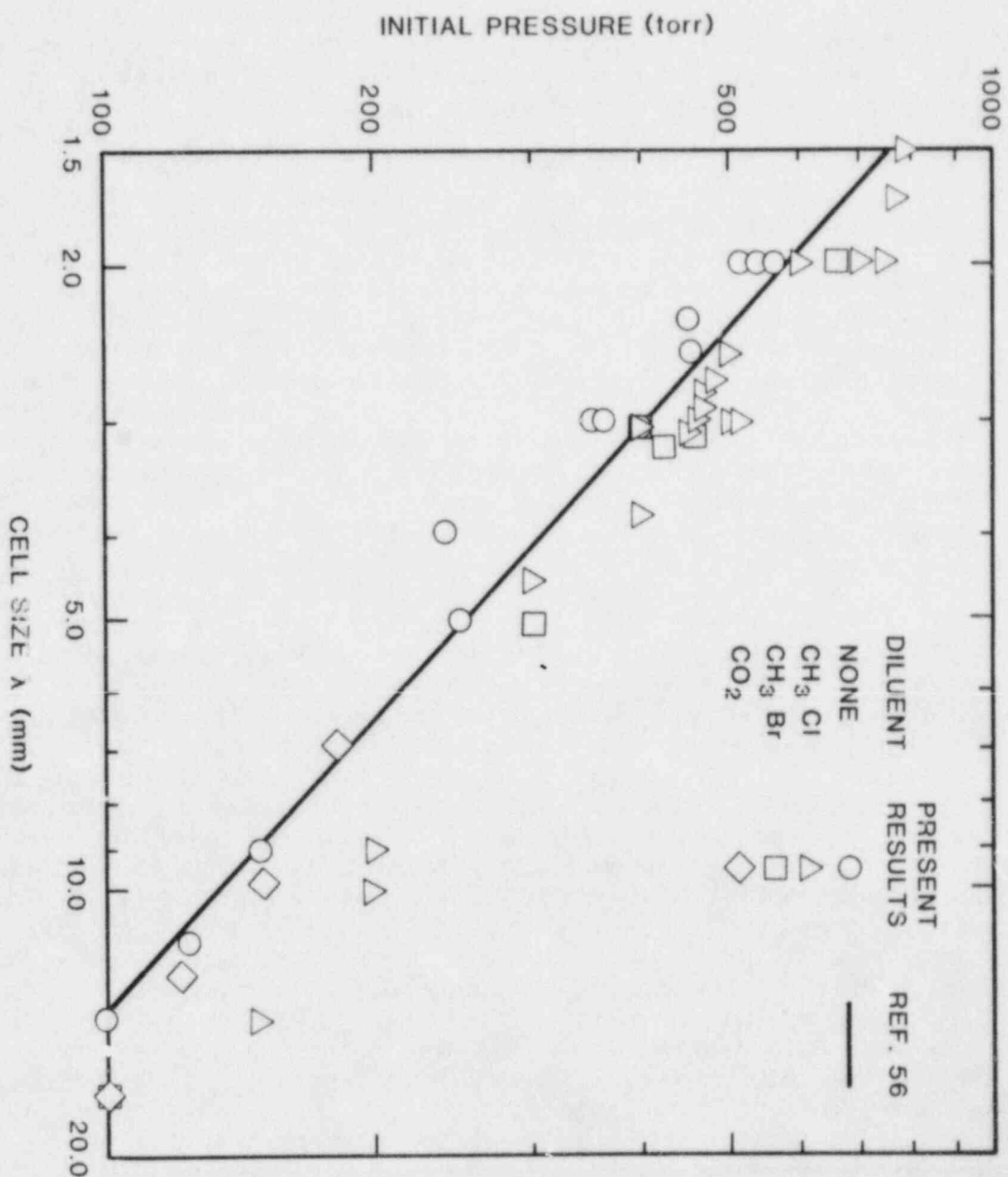


Figure 3.50. Increase in Cell Size of the Undiluted Mixture and Decrease in Initial Pressure Upon Addition of 5%  $\text{CH}_3\text{Cl}$  or  $\text{CH}_3\text{Br}$  to  $2\text{H}_2 + \text{O}_2$  Mixtures

helium) or halogenated compounds ( $\text{CH}_3\text{Cl}$  and  $\text{CH}_3\text{Br}$ ) for desensitizing subatmospheric stoichiometric oxygen:hydrogen mixtures to detonations. However, the well-known flame retardant  $\text{CF}_3\text{Br}$  is found to sensitize oxygen:hydrogen detonations.

#### 3.2.14 Steam:Hydrogen Flame Jet (J. E. Shepherd, and O. B. Crump)

Experiments have been carried out to examine concerns about the ignition process in the dynamic injection tests planned for the Nevada Test Site (NTS). The closest ignition source will be located about five feet above the point of injection and a question exists about whether the jet or plume of hydrogen and steam will ignite promptly. Several experiments have been performed in the Sandia hydrogen:steam jet to address this question.

For a pure hydrogen jet at room temperature, a glow plug located more than about 25 in downstream of a 0.25-in-diameter nozzle will not ignite the jet for a flowrate of 80 slpm. This is approximately the location of the end of the flame when the jet is burning, or about 100 nozzle diameters downstream. For turbulent jets, this location should scale roughly like the nozzle diameter because the entrainment will be similar if the Reynolds numbers are high enough. Because the jet nozzle is 5 inches in diameter at NTS, this suggests that the jet will ignite promptly in that configuration.

However, another configuration exists that will be used in those dynamic injection tests. A diffuser 50 inches in diameter will be mounted on the end of the injection pipe and the source will be more plume-like than jet-like. The steam:hydrogen jet facility at Sandia is not set up to address plume problems at this time, several models of plume mixing are available which could be used to evaluate the potential for ignition. One drawback is that all of these models assume the source is discharging into an infinite atmosphere.

A contract has been written for Professors Zukoski and Kubota of Caltech to modify their existing room fire code [58] to include a convective heat transfer model. The modified code will be used to analyze small-scale experiments and to make predictions for reactor-scale fires. The contract is in the process of being placed and the finished product will be available in May or June, 1984.

#### 3.2.15 BWR Mark III and HCOG Activities (J. C. Cummings, J. E. Shepherd, and A. Camp)

We have studied several issues related to combustion in the wetwell of the Mark III BWR reactors. John Cummings, Alan Camp and Joe Shepherd attended the HCOG meeting on June 29 and listened to presentations on the results of 1/20-scale experiments by John Hosler of EPRI. Hydrogen flow rates

were determined by Froude scaling of calculated (by codes such as MARCH) full-scale release rates. Froude modelling is appropriate for buoyancy-controlled flows and is based upon keeping the Froude number,  $Fr$ , (the ratio of inertial to buoyancy forces) constant;

$$Fr = \rho_0 U^2 / (\rho_0 - \rho_a) g U.$$

This implies that the scaled flowrates are equal to  $s^{5/2}$  times the full-scale flowrates, where  $s$  is the linear scaling factor.

Continuous flames were observed in the 1/20-scale model for equivalent full-scale hydrogen flowrates above about 0.18 kg/s; this was through 9 spargers, 8 ADS (automatic depressurization system) and 1 SORV (stuck-open relief valve). For the base case of 0.36 kg/s through 9 spargers, videotapes of the combustion indicated that the flames were about 25 cm high, equivalent to the first equipment level (HCU floor) in the wetwell of the full-scale containment. Note that for large enough initial flowrates, the flame length should scale linearly with the model size when Froude modelling is used. For example, unconfined, buoyant hydrocarbon flames obey the approximate relation [59]:

$$L = 0.23Q^{0.4}$$

where  $L$  is the flame length in meters and  $Q$  is the energy release rate in kW. Despite the confining effects of the wetwell geometry, the observed flame lengths do not differ greatly from what this would predict. The base-case flowrate results in a 4.8 MW fire above each sparger in the full-scale containment or a 2.7 kW fire in the model.

In the model, the most vigorous combustion was observed above the spargers located at 312°; this corresponds to the location of the greatest vertical open space above the wetwell. Down-drafts were observed in other regions above the wetwell and the flow above the suppression pool appeared to be lateral, transporting the atmosphere from the location of the down-drafts to the updrafts. The flames were very unsteady in appearance, flickering rapidly both vertically and horizontally. Gas temperatures of 600 K and heat fluxes of 1.3 W/cm<sup>2</sup> were observed at the level of the KCU floor over the region of the most vigorous combustion (with the base-case flowrate). At the base-case flowrate, the measured flux was 80% convective, 20% radiative; at higher flowrates, radiation becomes a larger fraction, up to 50% at 0.9 kg/s (full-scale equivalent). These temperatures and fluxes are in reasonable agreement with predictions based on a fire plume model of Zukoski et al. [59] and experiments of You and Faeth.[60]

A crucial issue is the technique used to predict the component temperatures in the full-scale containment. A major difficulty is that all techniques must rely on data from the 1/20-scale experiments and the absolute size of that model is so small that the flows are primarily laminar as opposed to the turbulent flows expected at full scale. This results in the introduction of ad hoc corrections and associated uncertainties in the scaling. A 1/4-scale Mark III BWR combustion test facility is being constructed by Factory Mutual Research Corporation and it is hoped that these questions will be answered in those tests.

One of the simplest techniques to obtain quantitative data is to place an instrumented, scaled-down component (scaled both in size and thermal properties) in a model experiment and record the temperature history as a function of time. The measured temperature history will be the same as that in full scale with a time scale compressed by  $s^{1/2}$ . Alternatively, the heat flux history on the surface of the model could be measured and multiplied by  $s^{1/2}$  to determine the full-scale value. This flux history, with an expanded time scale, could be used as an input to a heat transfer calculation to determine the component temperature history. Note that this scaling is global and does not account for the specific heat transfer mechanism and the particular scaling that it may imply. For example, the global scaling always implies that the heat flux increases with size, but the stagnation-point heat flux directly above the fire will scale like  $s^{-1/5}$ , i.e., decreasing with increasing size.

A third method, used by EPRI and MP&L, is to scale the gas velocity, temperature, and radiative flux measured in the 1/20-scale experiment and use this thermal environment as an input to a heat transfer calculation. This was carried out for an igniter box located immediately below the HCU factor. The base-case full-scale environment they defined was a gas temperature of 600 K, a radiant heat flux of  $2.0 \text{ W/cm}^2$  from below and a gas velocity of 11 m/s. Inside the igniter box, the transformer reached 530 K after about 10 min of exposure to this environment.

#### 3.2.16 FITS Test Analysis

(S. N. Kempka, A. C. Ratzel, A. W. Reed, and J. E. Shepherd)

Data reduction and analysis of FITS tests has continued. In support of B. W. Marshall's efforts to understand pressure gauge thermal response, several recent tests were analyzed and comparisons made between different transducers and protection methods. The first steps have been taken to transfer the data reduction codes to the Building 823 VAX and link them directly to the FITS data retrieval package. This task will be completed when the tape drive is installed at the FITS site and data can be transferred directly to the VAX.



A major deficiency of the data reduction package now in use is the inability to account properly for the effects of condensation during the postcombustion cooldown stage. We have developed an improved data reduction package which includes this process, and we are in the process of comparing tests with and without condensation ("cold" wall vs "hot" wall tests) to determine the effect of condensation on the heat transfer. In order to analyze cold wall tests and separate the convection and condensation contributions to the heat transfer, the bulk water vapor content must be known as a function of time. Because there are no measurements of the bulk gas composition as a function of time, an analytical model is necessary.

The model is based on a classic film analysis (Bird, et al. [61]). The relation between heat and mass transfer is described by the Chilton-Colburn analysis extended to high mass-transfer rates. These elements are combined into the data reduction procedure so that, for a given pressure, temperature, and pressure-time derivative, the heat and mass transfer rates or coefficients can be determined as functions of time.

Heat transfer coefficients for two tests with the same hydrogen concentrations but different initial wall temperatures are compared in Figure 3.51. Initial conditions for the tests were 10% hydrogen by volume, hot test (H10H) temperature 110°C, cold test (H10C) temperature 23°C. The top curve labeled "cold wall" reflects the enhancement attributable to the mass transfer, while the center curve labeled "cold wall" is the coefficient that would have been observed had no condensation taken place. The lowest curve labeled "hot wall" is the coefficient determined from the hot wall test where no condensation took place. Comparing the center curve to the hot wall test indicates that the difference is not due solely to the condensation but that the wall temperature must also be important.

Individual components of the heat flux in the cold wall test are shown in Figure 3.52. Condensation heat transfer (labeled QCOND) constitutes only 10 to 20% of the total heat transferred to the walls (QTOT). Convective (QCW) and radiative (QRAD) heat transfer, in that order, are clearly the dominant mechanisms.

Figure 3.53 shows the mole fraction of steam in the cold wall test as a function of time. The decrease from 10% to 4% indicates that the limited effect of condensation is not due to an underprediction of the condensation rate. For this test, large increases in the predicted condensation rate would only cause a slight difference in the computed heat transfer rates.

This condensation model is now being used to analyze additional pressure data from sets of hot and cold wall FITS

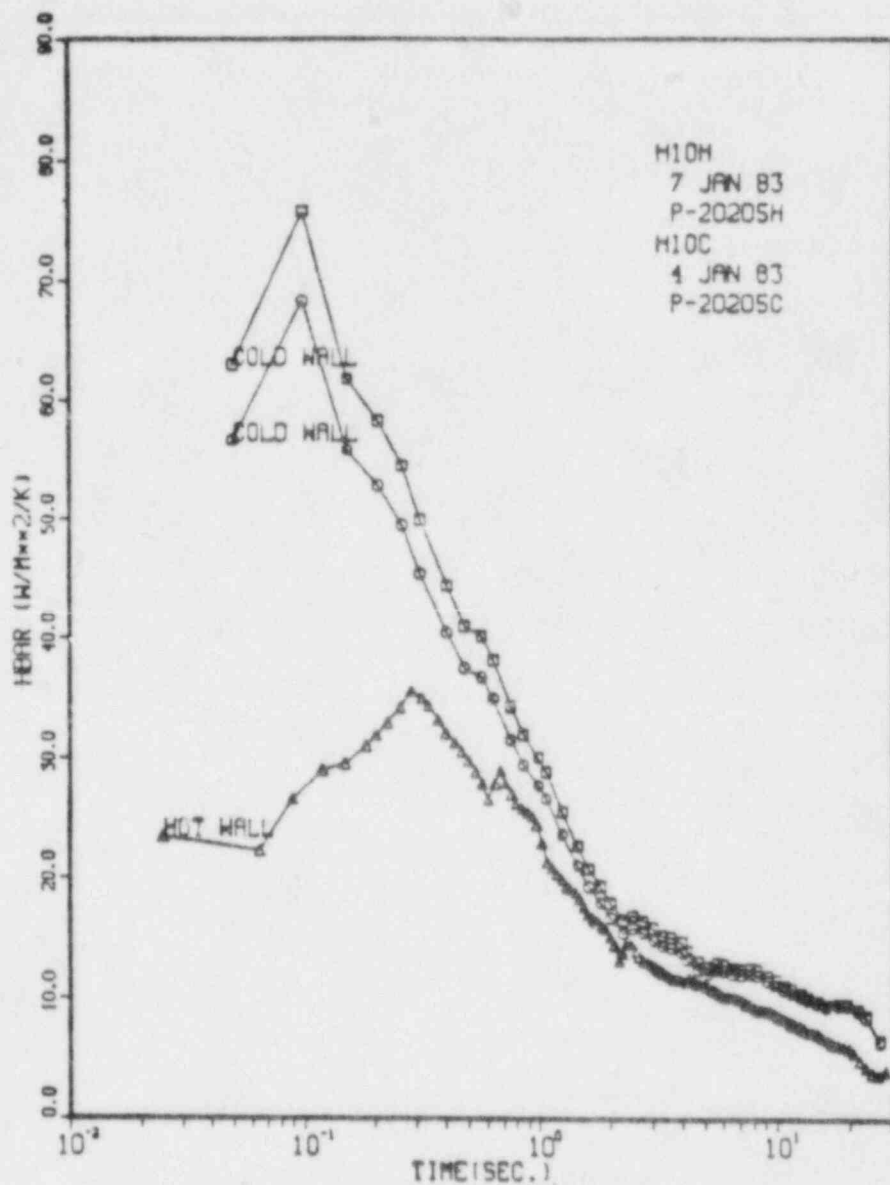


Figure 3.51. Comparison of Heat Transfer Coefficients Deduced for Cold and Hot Wall, 10% Hydrogen FITS Tests H10C and H10H. Upper curve, cold wall test including condensation; center curve, cold wall test with the effect of condensation subtracted out; lower curve, hot wall test (no condensation).

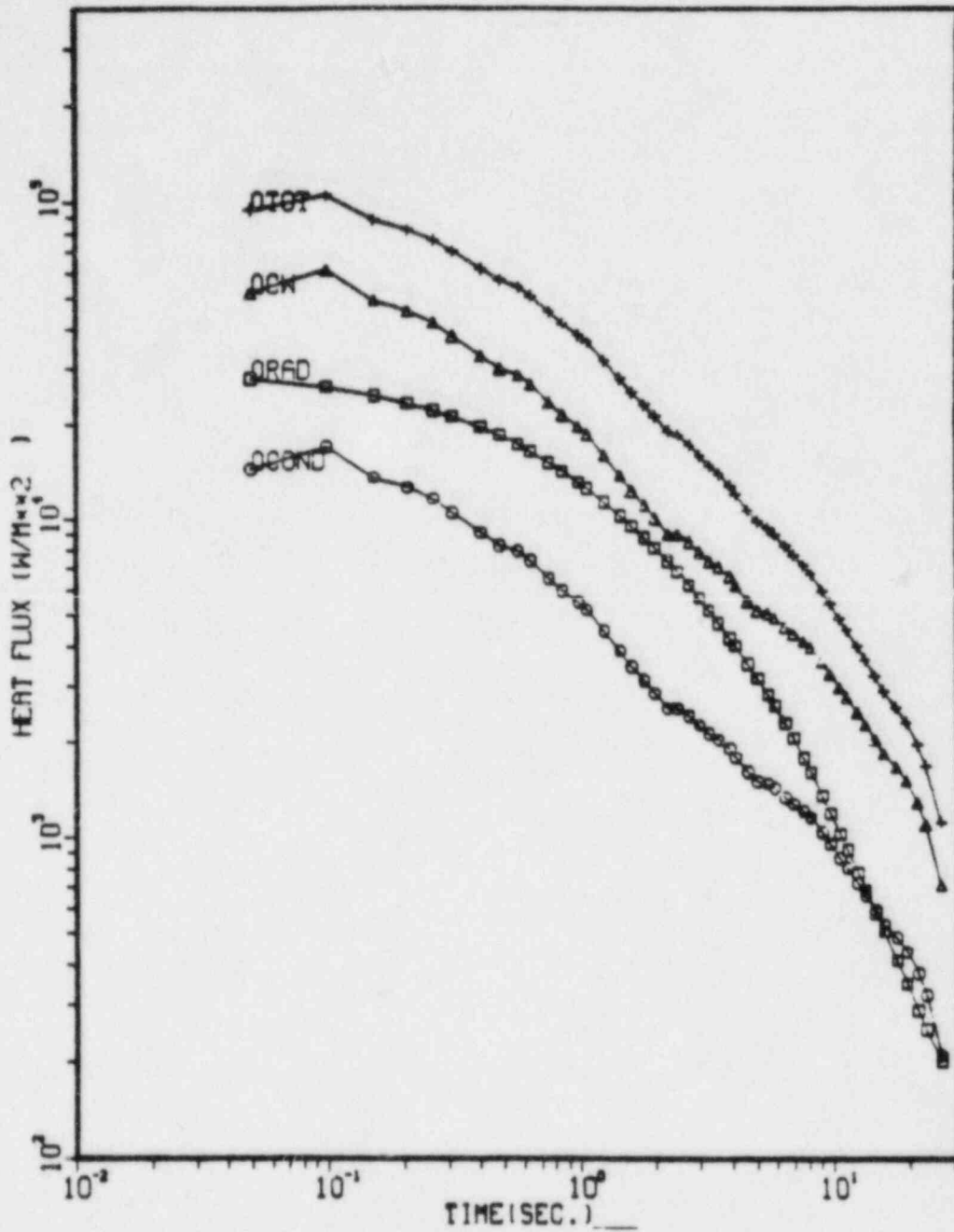


Figure 3.52. Components of the Wall Heat Flux in the Cold Wall Test H10C. Labels: QTOT, total heat flux; QCW, convective heat flux; QRAD, radiative heat flux; QCOND, condensation heat flux.

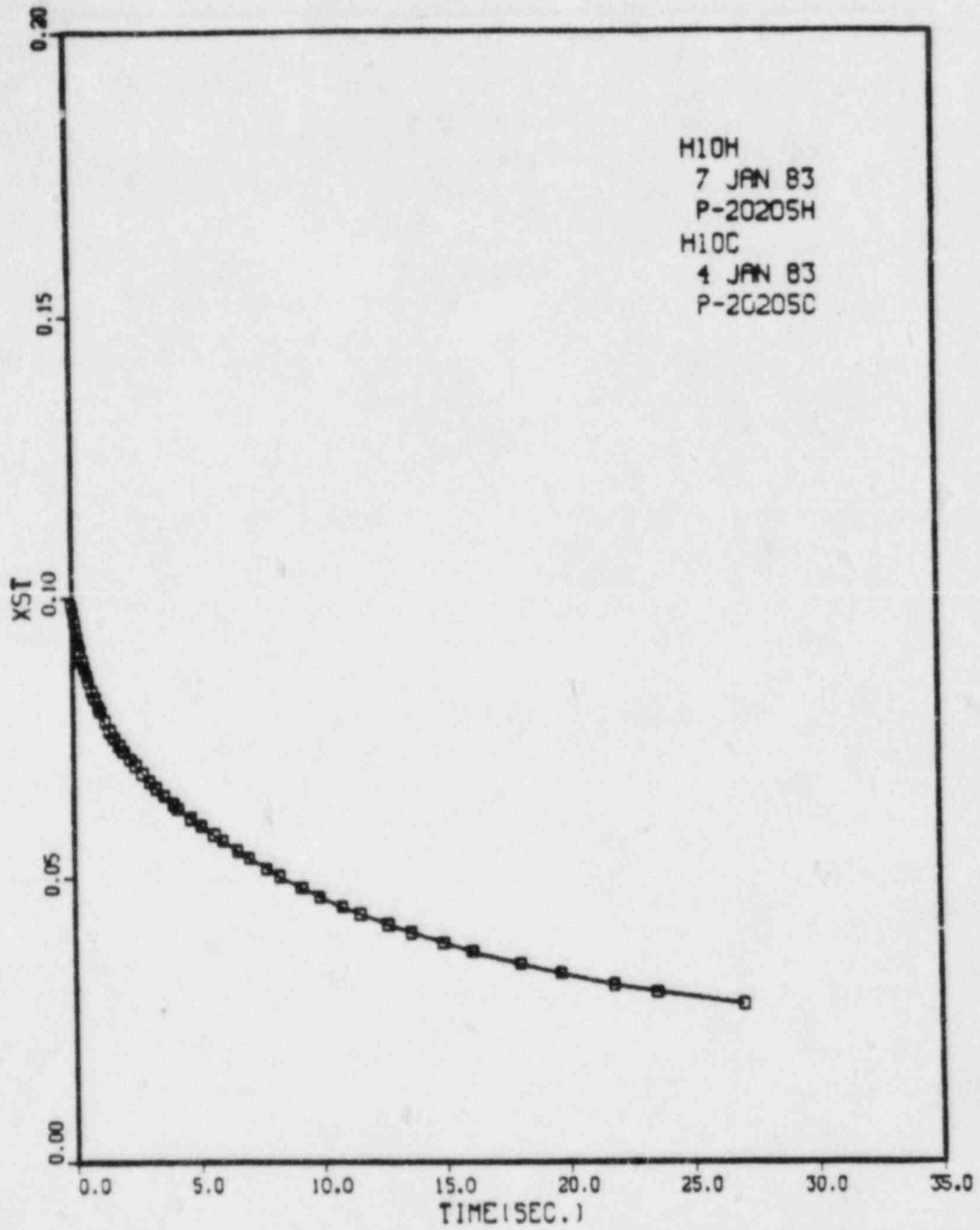


Figure 3.53. Computed Steam Fraction as a Function of Time in the Cold Wall FITS Test H10C

tests. We would like to incorporate the results of these analyses into a general correlation for the convective heat transfer during the postburn stage. The effects of condensation could then be included in heat transfer predictions through a modified analogy to the convective heat transfer.

### 3.2.17 EPRI NTS Experiments

(J. E. Shepherd and O. B. Crump)

Installation and checkout of the Sandia gauges inside the dewar at the NTS have been completed. A document describing the Sandia instrumentation, calibration, and data reduction has been prepared and distributed to those involved. A final pretest checkout of the Sandia equipment was made on June 19. Several potential problems with the data-point specification files in the data acquisition system software were identified and corrected.

Felt-metal protective covers and additional heat sinks were installed on the pressure transducers. An improved manifold and indicator were installed on the vacuum system for the radiative gauges. A ground-fault interrupter was placed in the lines for the heaters on the radiative gauges. This will prevent high voltage ac from arcing inside the tank if the wiring insulation fails.

Following the noncombusting checkout tests, the first burn was conducted on July 28. The initial conditions were 6.5% hydrogen and 4.8% water vapor, temperature 30°C and pressure 13.6 psia. One glow plug located about 3 m above the bottom was used to ignite the mixture. Excellent video images were obtained on the four infrared-sensitive TV cameras. The burn propagated upward as an expanding fireball which then burned back down the side of the tank after reaching the top. Ignition took place 18.8 s after current was applied to the glow plug, the fireball reached the top of the tank 6 s later and the combustion appeared to be over 22 s after ignition. The pressure peaked at 30.5 psia about 17.7 s after ignition. Complete data were obtained from the Sandia pressure transducers and slug calorimeters. The thin-film gauges were operating but the high-resolution data were lost because of data acquisition error.

Five more tests have been run since the first test and more are planned in the coming months. Data from all but the latest test have been transferred to Sandia on tape and a summary is presented here. The preliminary values for the initial conditions and selected burn results are given in Table 3.7. Plots of pressure and total calorimeter temperature histories are shown in Figures 3.54 through 3.58. These data are from the Sandia installed gauges P105 and H104; the P105 pressure data appear to be in good agreement with the other transducers (P101-103) installed in the dewar.

Table 3.7  
Initial Conditions and Burn Parameters

Test	P1	P2	P3	P4
Initial Pressure (psia)	14.4	13.0	14.15	14.53
Initial Temperature (°C)	31.0	52.5	54.2	34.3
Initial H <sub>2</sub> (%)	5.97	~6.5	~6	~8
Initial H <sub>2</sub> O (%)	5.0	~15	~15	~5
<u>Pressure Results (SANDIA - P105):</u>				
Pressure Risetime (s)	61.45	5.29	12.74	7.50
Pressure Peak (psia)	21.34	28.24	25.24	46.23
Pressure Ratio	1.48	2.17	1.78	3.18
<u>Calorimeter Results (SANDIA - H104):</u>				
Total Energy Deposition (J/cm <sup>2</sup> )	19.18	89.5	102.0	256.1
Peak Total Flux (W/cm <sup>2</sup> )	0.86	5.54	3.96	6.43
<u>Gardon Gauge Results (EPRI - H106):</u>				
Total Energy Deposition (J/cm <sup>2</sup> )	60	42.1	63.1	219.8
Peak Total Flux (W/cm <sup>2</sup> )	1.5	3.15	1.12	>10.0
<u>Computed Adiabatic, Isochoric, Complete Combustion Results:</u>				
Pressure Ratio	3.05	2.51 <sup>a</sup>	2.84	3.76
Total Energy Deposition (J/cm <sup>2</sup> )	151.7	136.1 <sup>a</sup>	140.9	201.8
Peak Temperature (K)	947	771 <sup>a</sup>	950	1143

<sup>a</sup>Assuming 0.005% by volume suspended liquid water.

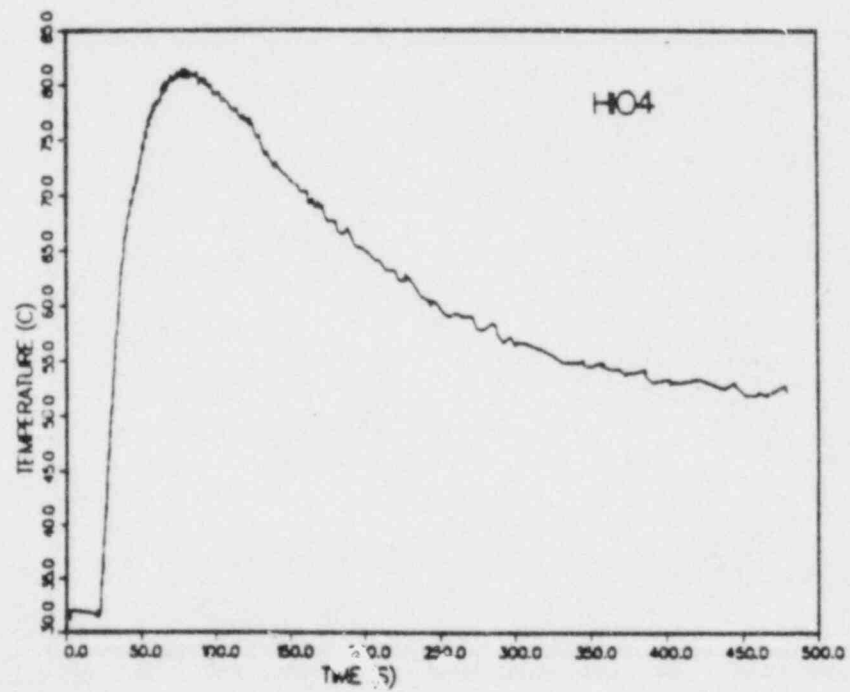
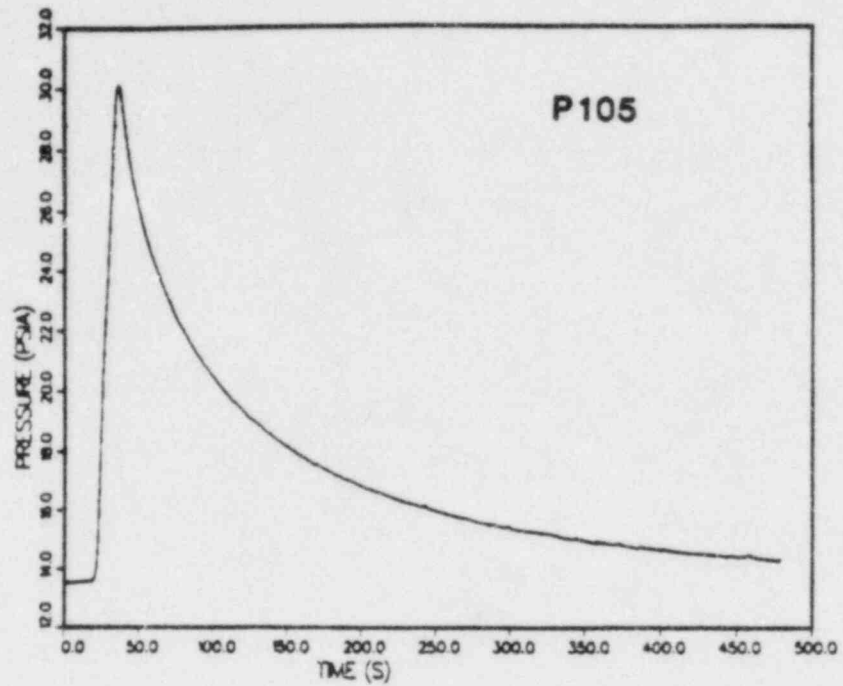


Figure 3.54. Pressure and Calorimeter Temperatures from July 28 Test (Shakedown Test).

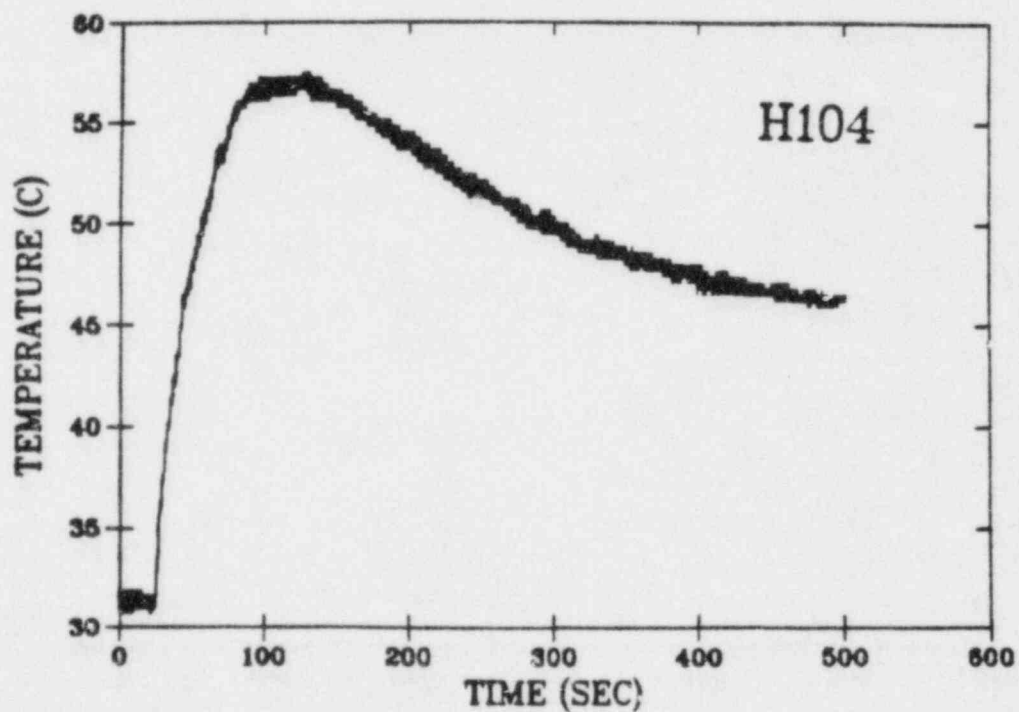
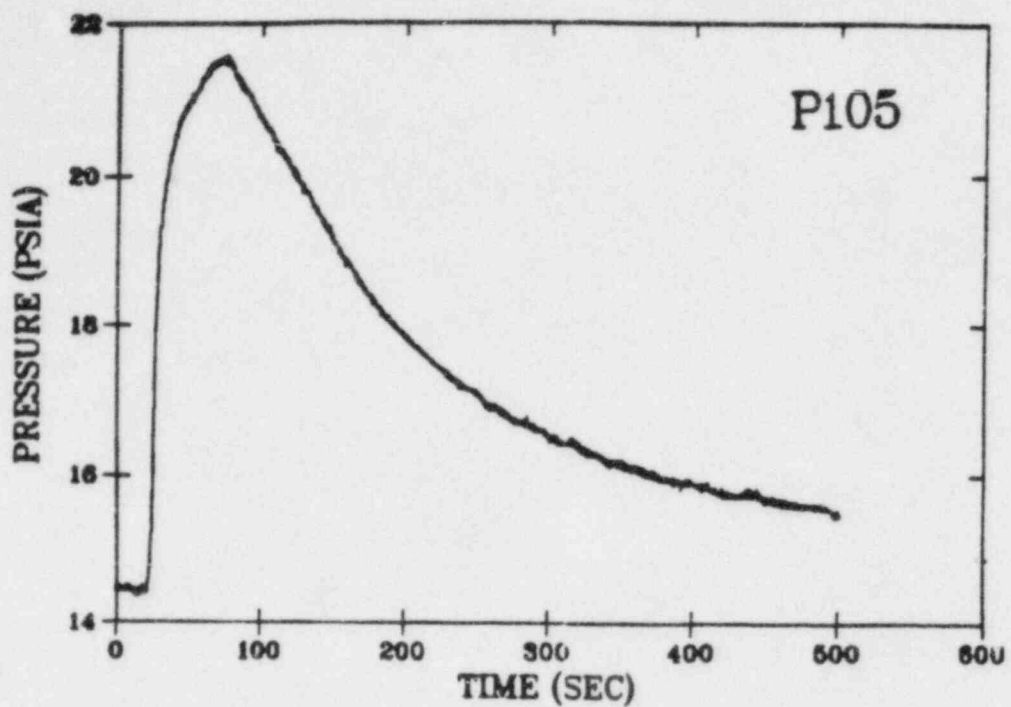


Figure 3.55. Pressure and Calorimeter Temperatures from August 4 Test (Nominally Test P1)



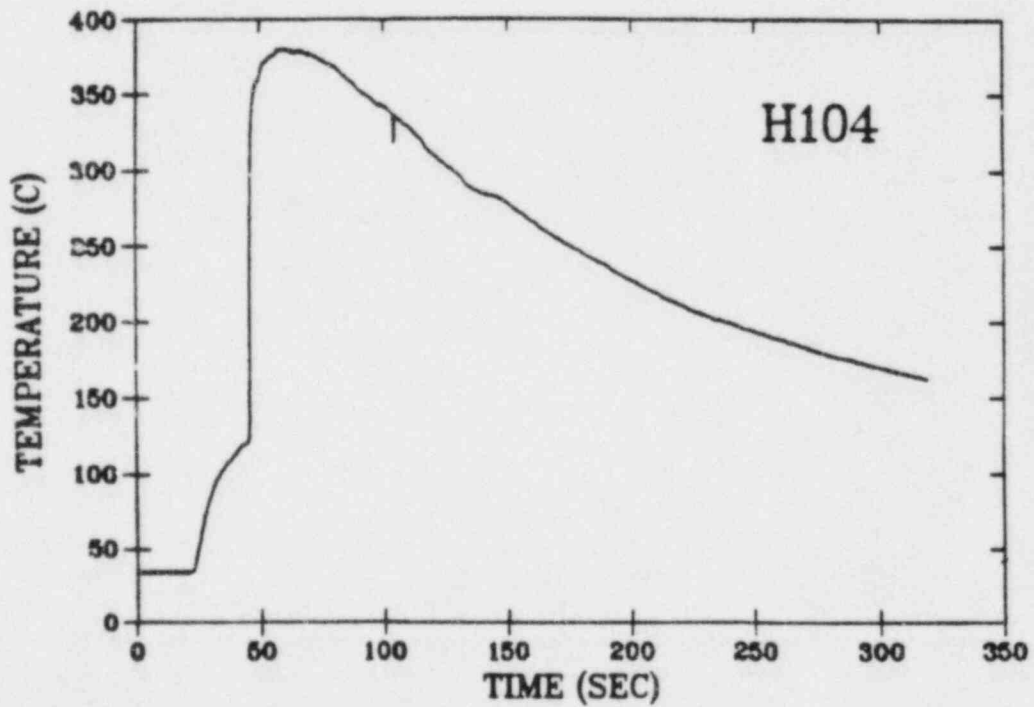
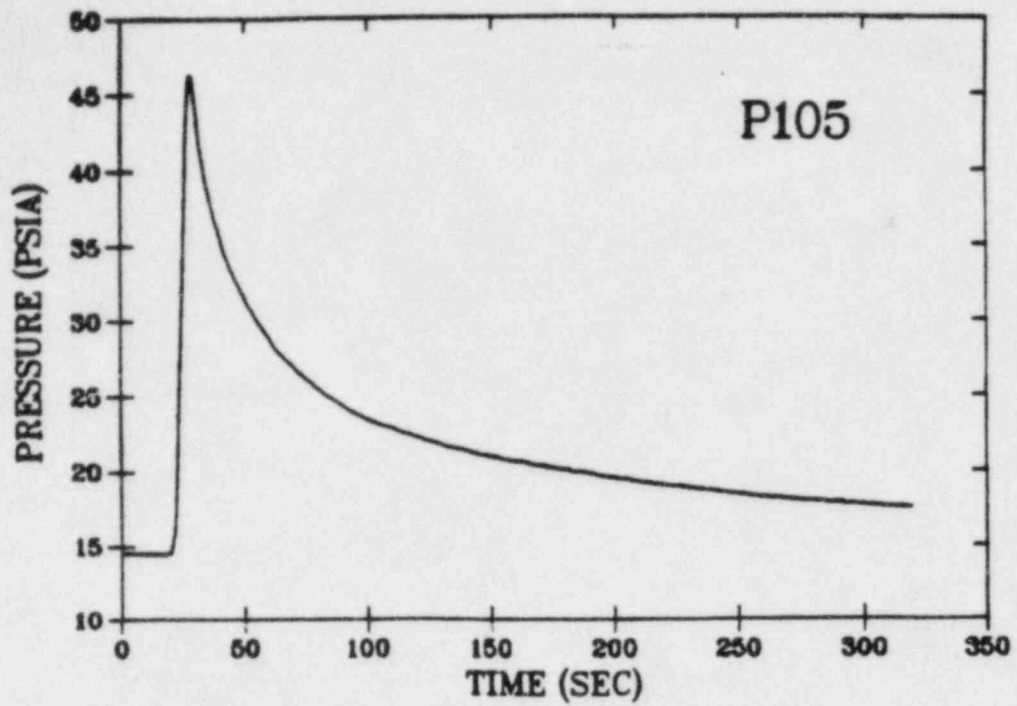


Figure 3.56. Pressure and Calorimeter Temperatures from August 9 Test (Nominally Test P4)

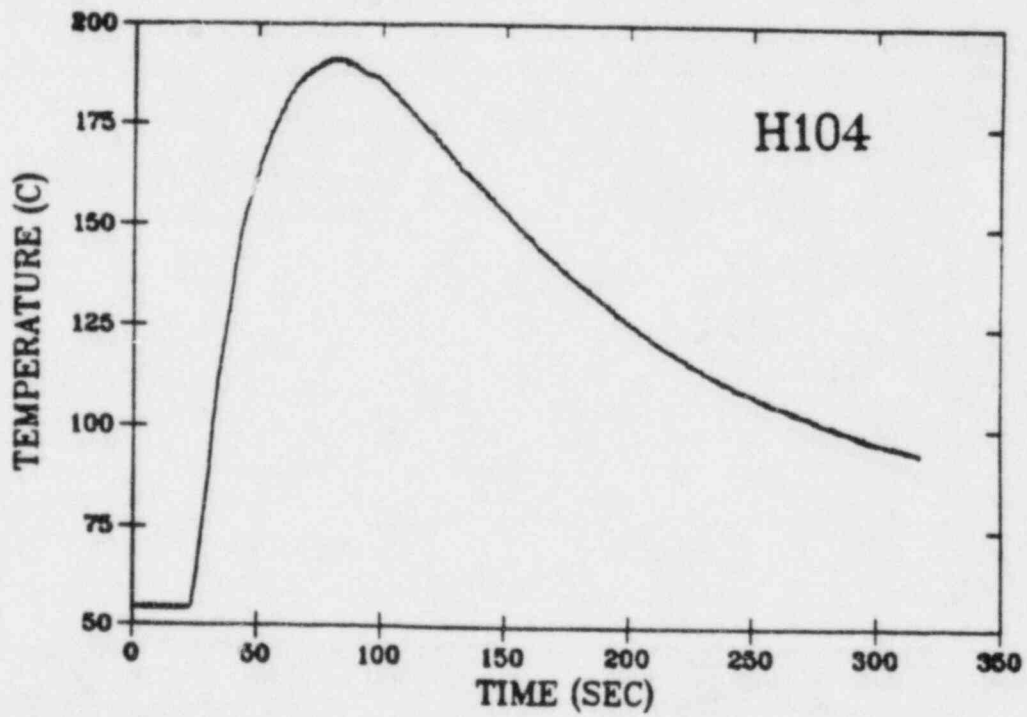
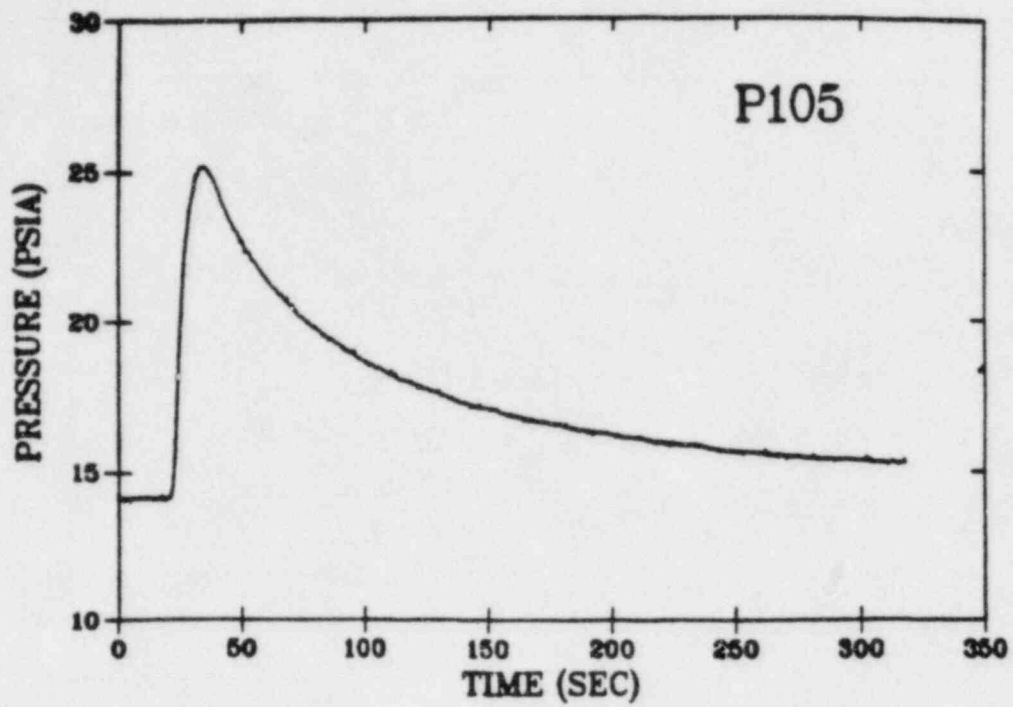


Figure 3.57. Pressure and Calorimeter Temperatures from August 10 Test (Nominally Test P3)

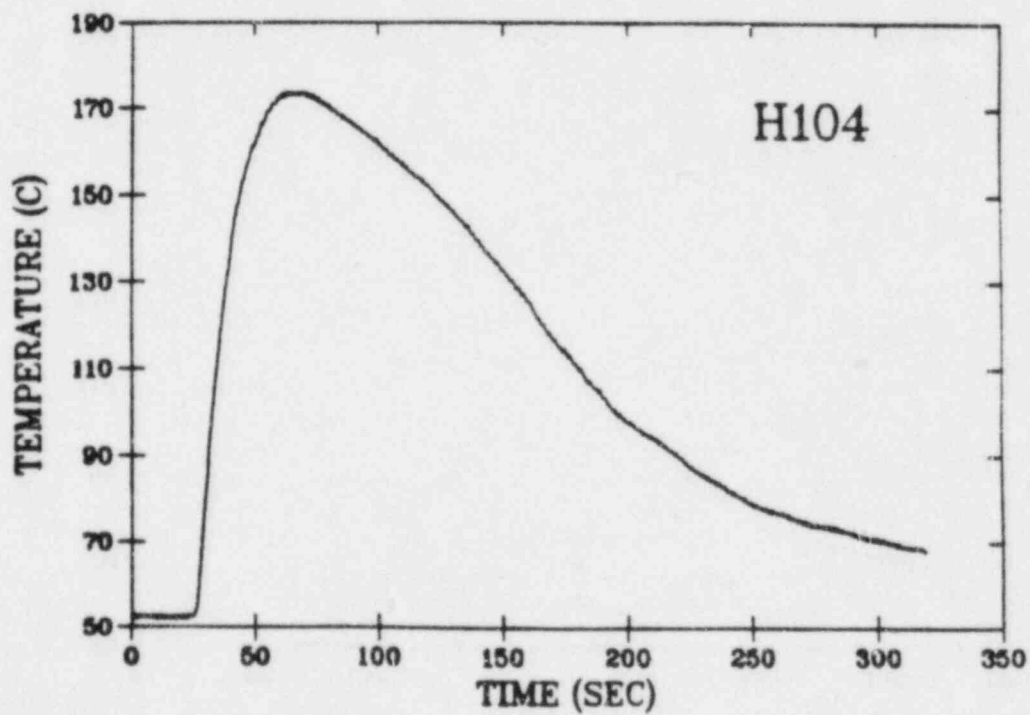
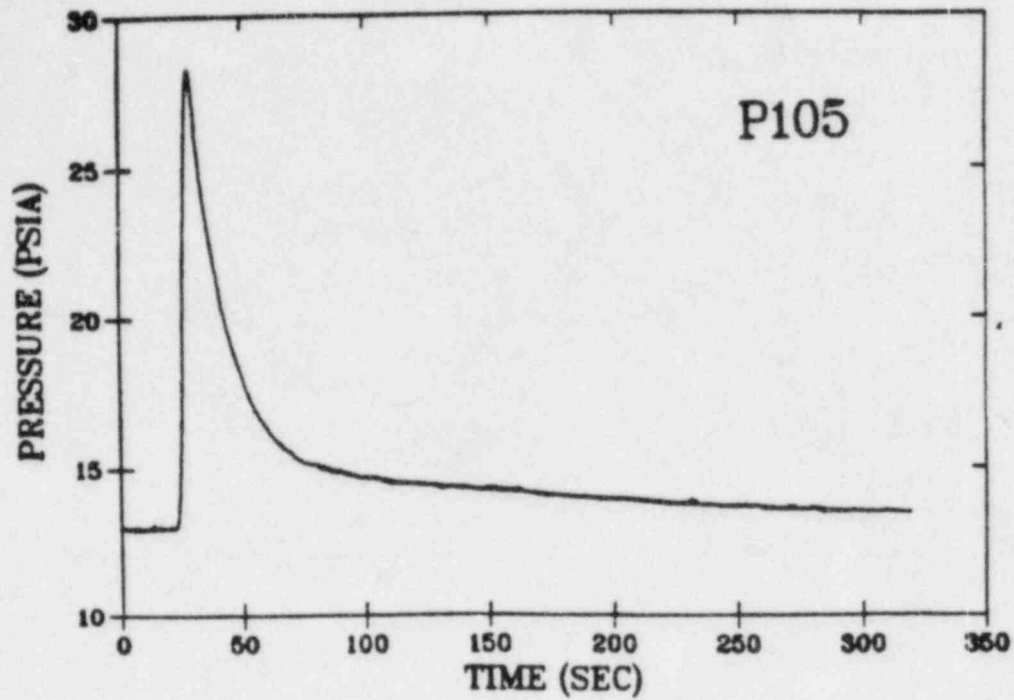


Figure 3.58. Pressure and Calorimeter Temperatures from August 12 Test (Nominally Test P2)

The total heat flux from the Gardon gauge H106 is plotted in Figures 3.59 and 3.60. The peak fluxes obtained on these gauges are compared in Table 3.7 to the peak fluxes obtained by differentiating the calorimeter signals. The fluxes were also integrated to obtain an energy deposition which is compared to the calorimeter results. The calorimeter signals have not been corrected for losses and the Gardon gauge signals have not been corrected for time lag.

Several problems arose with the Sandia instrumentation: We were unable to obtain consistent data from one pressure transducer and from any of the thin-film heat-flux gauges; pressure gauge P104 showed intermittent behavior on the first two tests and failed completely during the cooldown on test P4. We visited the site on August 12 and 16 and attempted to diagnose and repair our instruments. After disassembling the connections to P104, we discovered that the insulation on the wiring (which was inside a 3/8-in O.D. stainless steel tube) connecting the gauge to the inconel had melted! A quick test of the gauge revealed that it was not damaged, so we reinstalled the gauge with Teflon insulation over a new connecting cable. We added some additional felt metal protection to this gauge because the results of the first test indicated that there may have been some thermal effect.

The signal processing electronics for the thin-film gauge had some intermittent connections and was brought back to Sandia for repair. The problems have been identified and repaired and the processor was reinstalled at NTS August 22. These problems resulted in the loss of all total flux signals, but the radiative channel appears to have operated correctly. We are in the process of reducing the radiative data and comparing the results to the pressure gauge reduction.

The radiant slug calorimeter data were of poor quality on all tests except P4. Signal levels are much lower than we expected, but that may be the result of the very low temperature of the combustion products and the window cutoff effects. After the thin-film radiative data are reduced, we will be able to make a better diagnosis. The total slug calorimeter gave good results except for the peculiar signal observed on test P4. The temperature took a sudden increase at 46 s, which does not correlate with any other gauge.

Initial concentrations given in Table 3.7 are only preliminary, and we do not have the final burn completeness results. The preliminary burn completeness (fraction of initial hydrogen burned) information at this time is: P1, 40%; P2, 60%; P3, 33%; P4, 100%.

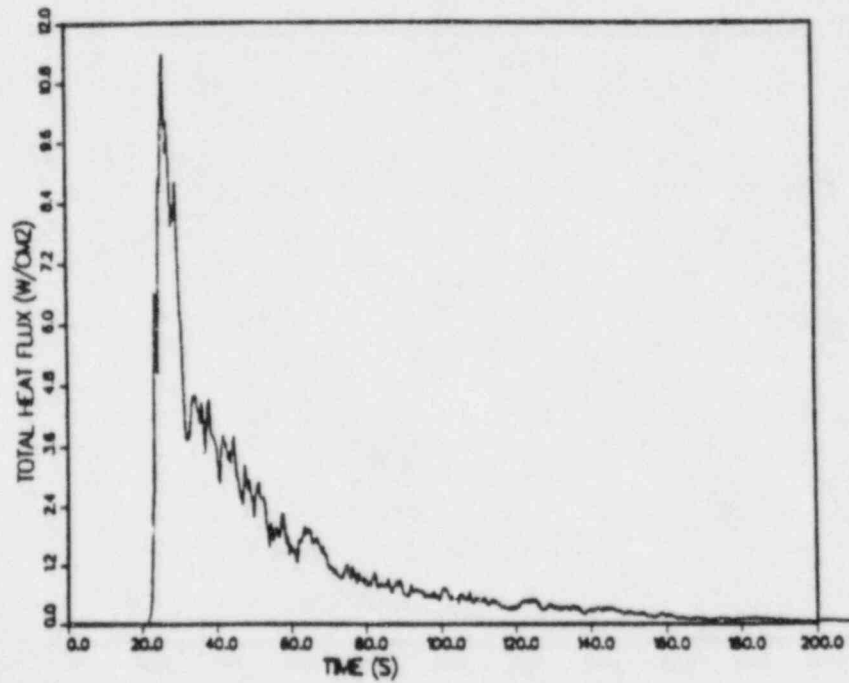
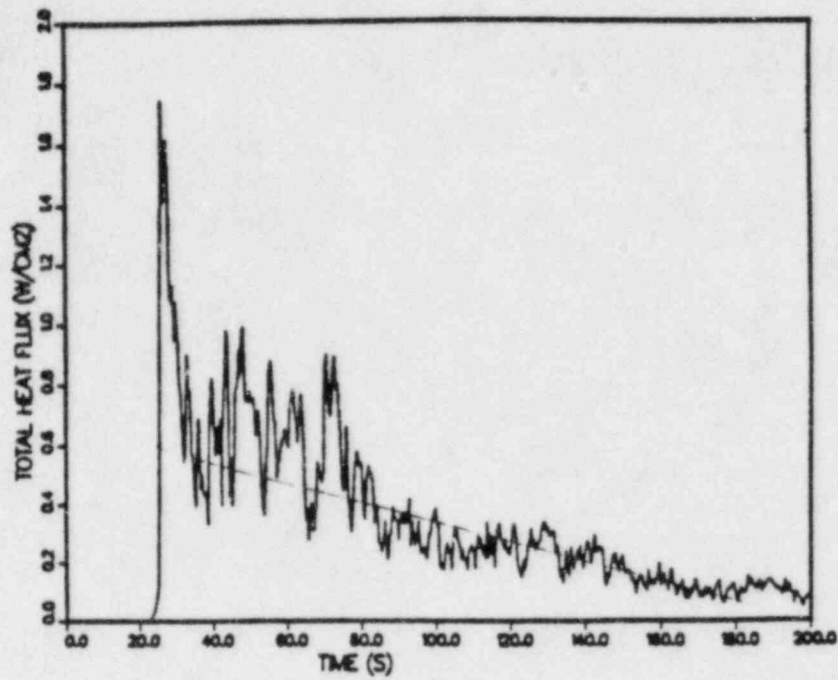


Figure 3.59. Total Heat Flux from the Gardon Gauge Calorimeter H106. Top figure, August 4 test (P1); bottom figure, August 9 test (P4).

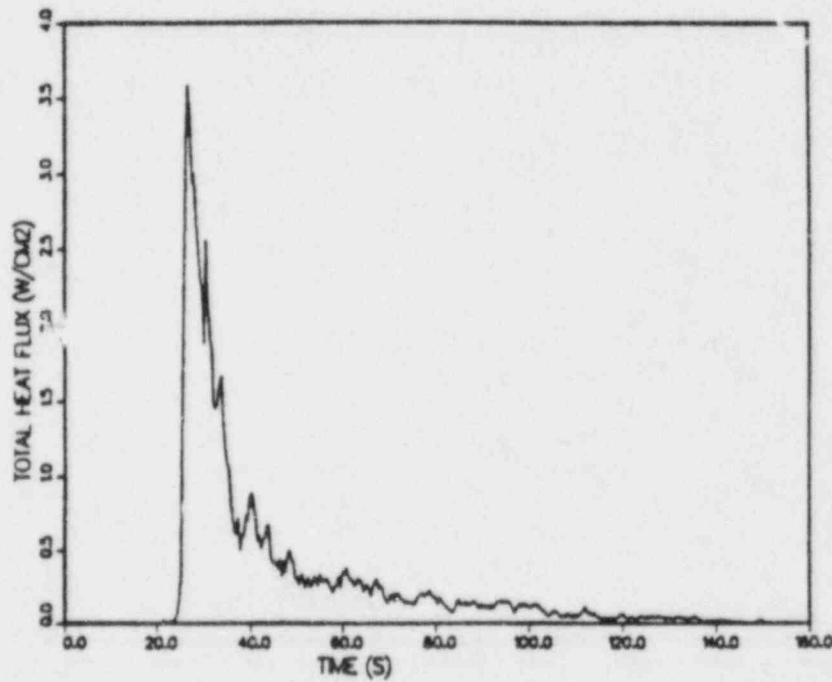
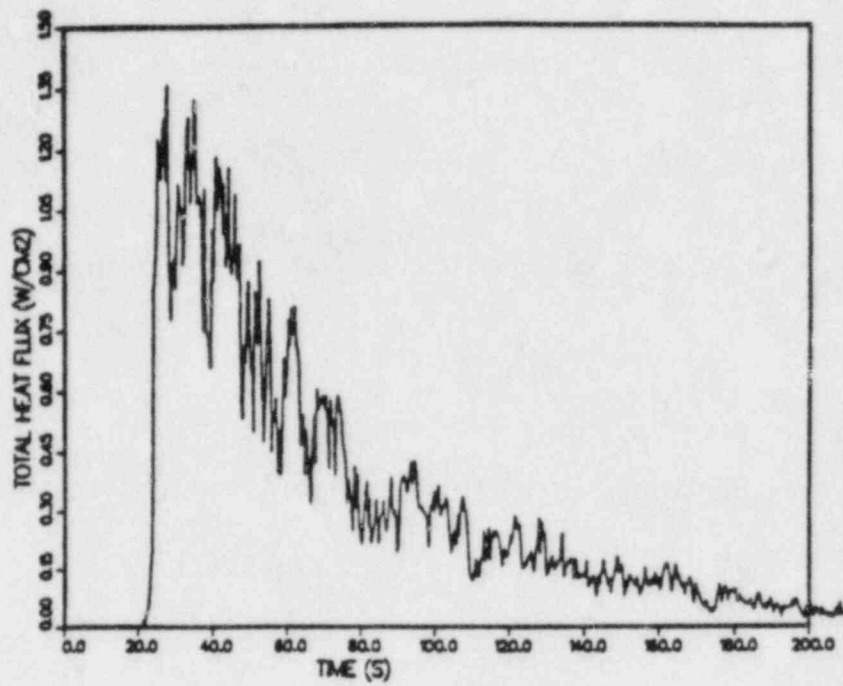


Figure 3.60. Total Heat Flux from the Gardon Gauge Calorimeter H106. Top figure, August 10 test (P3); bottom figure, August 12 test (P2).

### 3.3 References for Section 3

1. Safety Evaluation Report Related to the Operation of Sequoyah Nuclear Plant, Units 1 and 2, NUREG-0011 Supplement No. 6, U.S. Nuclear Regulatory Commission, Draft Copy, November 1982.
2. F. E. Haskin, V. L. Behr, and J. Jung, "Containment Management Study for Severe PWR Accidents," SAND82-2120C, presented at the Tenth Water Reactor Safety Research Information Meeting, Gaithersburg, Maryland, October 15, 1982.
3. John C. Cummings, et al., "Review of the Grand Gulf Hydrogen Igniter System," NUREG/CR-2530, SAND82-0218, Sandia National Laboratories, March 1983.
4. W. T. Ashurst and P. K. Barr, "Discrete Vortex Simulation of Flame Acceleration Due to Obstacle-Generated Flow," presented at the 1982 Fall Meeting of the Western States Section of the Combustion Institute, Paper WSS/CI 82-84; also Sandia National Laboratories Report SAND82-8724.
5. J. H. S. Lee, R. Knystautas, C. Chan, P. K. Barr, J. F. Grcar, and W. T. Ashurst, "Turbulent Flame Acceleration: Mechanisms and Computer Modeling," presented at the International Meeting on Light-Water Reactor Severe Accident Evaluation, Cambridge, MA, August 28 - September 1, 1983, Paper 9.8, sponsored by ANS and ENS; also Sandia National Laboratories Report SAND83-8655.
6. P. K. Barr, W. T. Ashurst, and J. F. Grcar, "Vortex Dynamics Modelling of Flame Acceleration," included in the bimonthly status reports for the Sandia Hydrogen Programs for April-May 1983.
7. C. K. Chan, J. H. S. Lee, P. Barr, and W. Ashurst, "Flame Acceleration in Multiple Chambers," to be presented at the 1983 Technical Meeting of the Eastern Section of the Combustion Institute (November 8-10, 1983), Paper 50.
8. P. K. Barr, W. T. Ashurst, and J. F. Grcar, "Vortex Dynamics Modelling of Flame Acceleration," included in the bimonthly status reports for the Sandia Hydrogen Programs for August-September 1983.
9. See, e.g., the bimonthly status reports for the Sandia Hydrogen programs for October-November 1981 and December 1981-January 1982.

10. D. D. S. Liu and R. MacFarlane, "Laminar Burning Velocities of Hydrogen-Air and Hydrogen-Air-Steam Flames," Comb. and Flame 49, 59 (1983).
11. See the semiannual report for the Sandia Hydrogen Programs for October 1982-March 1982.
12. See the bimonthly status reports for the Sandia Hydrogen Programs for April-May 1983.
13. K. D. Marx, A. E. Lutz, and H. A. Dwyer, "Computation of Flame-Water Droplet Interaction," Proceedings of the International Meeting on Light-Water Reactor Severe Accident Evaluation, Cambridge, MA, August 28-September 1, 1983, Paper TS-9.5. Also available as Sandia National Laboratories Report SAND83-8647, August 1983.
14. R. G. Zalosh and S. N. Bajpai, "Water Fog Inerting of Hydrogen-Air Mixtures," presented at the Second International Workshop on the Impact of Hydrogen on Water Reactor Safety, Albuquerque, NM, October 3-7, 1982.
15. D. D. S. Liu and R. MacFarlane, "Laminar Burning Velocities of Hydrogen-Air and Hydrogen-Air-Steam Flames," Comb. and Flame 49, 59 (1983).
16. G. Dixon-Lewis, "Kinetic Mechanism, Structure and Properties of Premixed Flames in Hydrogen-Oxygen Nitrogen Mixtures," Phil. Trans. Roy. Soc. London, A. Mathematical and Physical Sciences, 292, 45 (1979).
17. M. D. Smooke, J. A. Miller, and R. J. Kee, "Determination of Adiabatic Flame Speeds by Boundary Value Methods," Sandia National Laboratories Report SAND83-8650 (1983).
18. J. C. Mark, Memorandum for ACRS Members, "Notes on Hydrogen Burn with Igniters," December 4, 1980.
19. L. S. Darken and R. W. Gurry, 1946, "The System Iron-Oxygen. II. Equilibrium and Thermodynamics of Liquid Oxide and Other Phases," J. Amer. Soc. 68, 798-816.
20. A. L. Camp in M. Berman Light Water Reactor Research Program Semiannual Report, October 1981-March 1982, NUREG/CR-2841, SAND82-1572, Sandia National Laboratories, Albuquerque, NM, 1982.
21. L. S. Nelson in M. Berman, Light Water Reactor Safety Research Program Semiannual Report, October 1982-March 1983, Sandia National Laboratories, Albuquerque, NM, to be published.



22. L. S. Nelson in M. Berman, Light Water Reactor Safety Research Program Semiannual Report, April-September 1982, NUREG/CR-3407, SAND83-1576, Sandia National Laboratories, Albuquerque, NM, 1983.
23. W. H. Walton and W. C. Prewett, "The Production of Sprays and Mists of Uniform Drop Size by Means of Spinning Disc Type Sprayers," Proc. Phys. Soc. 62, 341-350 (1944).
24. L. M. Mills, TVA, to E. Adensam, USNRC, "Additional Testing Performed on Tayco Igniters, Sequoyah Nuclear Plant", Enclosure No. 1 Letter, dated January 31, 1983, Tennessee Valley Authority, January 1983.
25. R. G. Gido, Los Alamos National Laboratories, 1983, personal communication.
26. I. O. Moen, M. Donato, R. Knystautas, and J. H. S. Lee, "Flame Acceleration Due to Turbulence Produced by Obstacles," Comb. and Flame 39, p. 21 (1980).
27. B. H. Hjertager, K. Fuhre, S. J. Parker, and J. R. Bakke, "Flame Acceleration of Propane-Air in a Large-Scale Obstructed Tube," Proceedings to the 9th International Colloquium on Dynamic of Explosions and Reactive Systems, Poitiers, France (1983).
28. J. H. S. Lee, C. Chan, and R. Knystautas, "Hydrogen-Air Deflagration: Recent Results," Proceedings to 2nd International Workshop on the Impact of Hydrogen on Water Reactor Safety, Albuquerque, NM, 1982.
29. J. H. Lee, R. Knystautas, C. Guirao, W. Benedick, and J. Shepherd, "Hydrogen-Air Detonation," Proceedings to 2nd International Workshop on Water Reactor Safety, Albuquerque, NN, 1982.
30. I. O. Moen, M. Donato, R. Knystautas, and J. H. S. Lee, 1980, "Flame Acceleration Due to Turbulence Produced by Obstacles," Comb. and Flame 39, p. 21-32 (1980).
31. I. O. Moen, M. Donato, R. Knystautas, and J. H. S. Lee, 1981, "Turbulent Flame Propagation and Acceleration in the Presence of Obstacles," Progress in Astronautics and Aeronautics, 75, pp. 33-47.
32. C. Chan, I. O. Moen, and J. H. S. Lee, 1983, "Influence of Confinement on Flame Acceleration Due to Repeated Obstacles," Comb. and Flame 49, pp. 27-39.
33. J. H. S. Lee and I. O. Moen, 1980, "The Mechanism of Transition from Deflagration to Detonation in Vapor Cloud Explosions," Prog. Energy Combust. Sci. 6, pp. 359-389.

34. H. Lamb, 1945, Hydrodynamics.
35. T. Maxworthy, 1971, "The Structure and Stability of Vortex Rings," J. Fluid Mech. 51, pp. 15-32.
36. T. Maxworthy, 1974, "Turbulent Vortex Rings," J. Fluid Mech. 64, pp. 227-239.
37. T. Maxworthy, 1976, "Some Experimental Studies on Vortex Rings," J. Fluid Mech. 81, pp. 467-495.
38. P. J. Jaffman, 1981, "Dynamics of Vorticity," J. Fluid Mech. 106, pp. 49-58.
39. P. D. McCormack, K. Scheller, G. Mueller, and R. Tisher, 1972, "Flame Propagation in a Vortex Core," Comb. and Flame 19, pp. 297-303.
40. P. D. McCormack, 1972, "Combustible Vortex Rings," Proceeding of the Royal Irish Academy, 71, A6.
41. C. M. Guirao, R. Knystautas, J. H. S. Lee, W. Benedick, and M. Berman, 19th (International) Symposium on Combustion, The Combustion Institute, Pittsburgh, PA, pp. 583-590 (1982).
42. A. A. Vasiliev, T. P. Gavrilenko, and M. E. Topchian, "On the Chapman-Jouguet Surface in Multi-headed Gaseous Detonations," Astronautica Acta 17, pp. 499-502 (1972).
43. R. Knystautas, J. H. S. Lee, and C. M. Guirao, Comb. and Flame 48, pp. 63-83 (1982).
44. C. Bowick, "Detonations in Diverging Channels," McGill University (1982).
45. Y. K. Liu, J. H. Lee, and R. Knystautas, "Effect of Geometry on the Transmission of Detonation Through an Orifice," submitted to Combustion and Flame.
46. W. B. Benedick, R. Knystautas, and J. H. S. Lee, "Large-Scale Experiments on the Transmission of Fuel-Air Detonations from Two-Dimensional Channels," presented at the 9th International Colloquium on Dynamics of Explosions and Reactive Systems, Poitiers, France (1983).
47. A. A. Vasiliev, T. P. Gavrilenko, and M. E. Topchian, Astronautica Acta 17, No. 4-5, pp. 499-502 (1972).
48. D. H. Edwards, A. T. Jones, and D. E. Philipps, J. Phys. D: Appl. Phys. 9, pp. 1331-1342 (1976).
49. J. H. S. Lee, R. Knystautas, and N. Yoshikawa, Acta Astronautica 5, pp. 971-982 (1977).

50. R. Knystautas, J. H. Lee, I. Moen, and H. G. Wagner, 17th Symposium (International) on Combustion, The Combustion Institute, Pittsburgh, PA, pp. 1235-1245 (1978).
51. R. Knystautas and J. H. Lee, Comb. and Flame, 27, pp. 221-228 (1976).
52. R. Knystautas, J. H. Lee, and C. M. Guirao, Comb. and Flame 48, pp. 63-83 (1982).
53. J. H. Lee, R. Knystautas, C. Guirao, W. B. Benedick, and J. E. Shepherd, Second International Workshop on the Impact of Hydrogen on Water Reactor Safety, Albuquerque, NM (1982).
54. H. Matsui, and J. H. Lee, 17th Symposium (International) on Combustion, The Combustion Institute, Pittsburgh, PA, pp. 1269-1280 (1978).
55. V. V. Mitrofanov, and R. I. Soloukhin, Soviet Physics - Doklady 9, 12, p. 1055 (1965).
56. R. A. Strehlow, R. E. Maurer, and S. Rajan, AIAA Journal 7, No. 2, pp. 323-328 (1969).
57. R. A. Strehlow and C. D. Engel, AIAA Journal 7, 3, pp. 492-496 (1969).
58. E. E. Zukoski and T. Kubota, 1978, A Computer Model for the Fluid Dynamic Aspects of a Transient Fire in a Room, California Institute of Technology, Pasadena, CA.
59. E. E. Zukoski, T. Kubota, and B. Cetegen, "Entrainment in Fire Plumes," Fire Safety Journal 13, 107 (1980).
60. H. A. You and G. M. Faeth, "Ceiling Heat Transfer During Fire Plume and Fire Impingement," Fire and Materials 3, 140 (1970).
61. R. B. Bird, W. E. Stewart, and E. N. Lightfoot, "Transport Phenomena," Wiley, New York (1960).

Division of Technical Information  
and Document Control  
NRC Distribution Contractor  
U.S. Nuclear Regulatory Commission  
15700 Crabbs Branch Way  
Rockville, MD 20850  
275 copies for R3

U. S. Bureau of Mines  
Pittsburgh Research Center  
P. O. Box 18070  
Pittsburgh, PA 15236  
Attn: M. Hertzberg

U. S. Nuclear Regulatory Commission (6)  
Office of Nuclear Regulatory Research  
Washington, DC 20555  
Attn: G. A. Arlotto  
R. T. Curtis  
J. T. Larkins  
L. C. Shao  
K. G. Steyer  
P. Worthington

U. S. Nuclear Regulatory Commission (5)  
Office of Nuclear Regulatory Research  
Washington, DC 20555  
Attn: B. S. Burson  
M. Silberberg  
J. L. Telford  
T. J. Walker  
R. W. Wright

U. S. Nuclear Regulatory Commission (6)  
Office of Nuclear Reactor Regulation  
Washington, DC 20555  
Attn: J. K. Long  
J. F. Meyer  
R. Palla  
K. I. Parczewski  
G. Quittschreiber  
D. D. Yue

U. S. Nuclear Regulatory Commission (6)  
Office of Nuclear Reactor Regulation  
Washington, DC 20555  
Attn: V. Benaroya  
W. R. Butler  
G. W. Knighton  
T. M. Su  
Z. Rosztoczy  
C. G. Tinkler

U. S. Department of Energy  
Operational Safety Division  
Albuquerque Operations Office  
P.O. Box 5400  
Albuquerque, NM 87185  
Attn: J. R. Roeder, Director  
Dr. M. Peehs

Acurex Corporation  
485 Clyde Avenue  
Mountain View, CA 94042

Applied Sciences Association, Inc.  
P. O. Box 2687  
Palos Verdes Pen., CA 90274  
Attn: D. Swanson

Argonne National Laboratory  
9700 South Cass Avenue  
Argonne, IL 60439  
Attn: H. M. Chung

Astron  
2028 Old Middlefield Way  
Mountainview, CA 94043  
Attn: Ray Torok

Battelle Columbus Laboratory  
505 King Avenue  
Columbus, OH 43201  
Attn: P. Cybulskis (2)  
R. Denning

Bechtel Power Corporation  
P. O. Box 3965  
San Francisco, CA 94119  
Attn: R. Tosetti

Bechtel Power Corporation  
15740 Shady Grove Road  
Gaithersburg, MD 20877  
Attn: D. Ashton

Brookhaven National Laboratory  
Upton, NY 11973  
Attn: R. A. Bari (2)  
T. Pratt

Duke Power Co.  
P. O. Box 33189  
Charlotte, NC 28242  
Attn: F. G. Hudson (2)  
A. L. Sudduth

EG&G Idaho  
Willow Creek Building, W-3  
P. O. Box 1625  
Idaho Falls, ID 83415  
Attn: Server Sadik

Electric Power Research Institute  
3412 Hillview Avenue  
Palo Alto, CA 94303  
Attn: J. J. Haugh (3)  
K. A. Nilsson  
G. Thomas

Factory Mutual Research Corporation  
P. O. Box 688  
Norwood, MA 02062  
Attn: R. Zalosh

Fauske & Associates  
627 Executive Drive  
Willowbrook, IL 60521  
Attn: R. Henry

General Electric Co.  
175 Curtner Avenue  
Mail Code N 1C157  
San Jose, CA 95125  
Attn: K. W. Holtzclaw

General Physics Corporation  
1000 Century Plaza  
Columbia, MD 21044  
Attn: Chester Kupiec

Los Alamos National Laboratory  
P. O. Box 1663  
Los Alamos, NM 87545  
Attn: H. S. Cullingford (4)  
R. Gido  
G. Schott  
J. Travis

University of Michigan  
Department of Aerospace Engineering  
Ann Arbor, MI 47109  
Attn: Martin Sichel

Mississippi Power & Light  
P. O. Box 1640  
Jackson, MS 39205  
Attn: S. H. Hobbs

Northwestern University  
Chemical Engineering Department  
Evanston, IL 60201  
Attn: S. G. Bankoff

NUS Corporation  
4 Research Place  
Rockville, MD 20850  
Attn: R. Sherry

Offshore Power System (2)  
8000 Arlington Expressway  
Box 8000  
Jacksonville, FL 32211  
Attn: G. M. Fuls  
D. H. Walker

Power Authority State of NY  
10 Columbus Circle  
New York, NY 10019  
Attn: R. E. Deem (2)  
S. S. Iyer

Purdue University  
School of Nuclear Engineering  
West Lafayette, IN 47907  
Attn: T. G. Theofanous

Sandia National Laboratories  
Directorate 6400  
P. O. Box 5800  
Albuquerque, NM 87185  
Attn: R. Cochrell (20)

Sandia National Laboratories  
Organization 6427  
P. O. Box 5800  
Albuquerque, NM 87185  
Attn: G. Shaw (20)

Dr. Roger Strehlow  
505 South Pine Street  
Champaign, IL 61820

TVA  
400 Commerce  
W9C157-CD  
Knoxville, TN 37902  
Attn: Wang Lau

Thompson Associates  
639 Massachusetts Avenue  
Third Floor  
Cambridge, MA 02139  
Attn: Timothy Woolf

UCLA  
Nuclear Energy Laboratory  
405 Hilgard Avenue  
Los Angeles, CA 90024  
Attn: I. Catton

Westinghouse Corporation  
P. O. Box 355  
Pittsburgh, PA 15230  
Attn: N. Liparulo (3)  
J. Olhoeft  
V. Srinivas

Westinghouse Hanford Company  
P. O. Box 1970  
Richland, WA 99352  
Attn: G. R. Bloom (3)  
L. Muhlstein  
R. D. Peak

University of Wisconsin  
Nuclear Engineering Department  
1500 Johnson Drive  
Madison, WI 53706  
Attn: M. L. Corradini



Australian Atomic Energy Commission  
Private Mail Bag  
Sutherland, NSW 2232  
AUSTRALIA  
Attn: John W. Connolly

Director of Research, Science & Education  
CEC  
Rue De La Loi 200  
1049 Brussels  
BELGIUM  
Attn: B. Tolley

AEC, Ltd.  
Whiteshell Nuclear Research Establishment  
Pinawa, Manitoba, CANADA  
Attn: D. Liu (2)  
H. Tamm

McGill University  
315 Querbes  
Outremont, Quebec  
CANADA H2V 3W1  
Attn: John H. S. Lee (3)

CNEN NUCLIT  
Rome, ITALY  
Attn: A. Morici

Battelle Institut E. V.  
Am Roemerhof 35  
6000 Frankfurt am Main 90  
FEDERAL REPUBLIC OF GERMANY  
Attn: Dr. Werner Baukal

Gesellschaft fur Reakforsicherheit (GRS)  
Postfach 101650  
Glockengasse 2  
5000 Koeln 1  
FEDERAL REPUBLIC OF GERMANY  
Attn: Dr. M. V. Banaschik

Gesellschaft fur Reaktorsicherheit (GRS mbH)  
8046 Garching  
FEDERAL REPUBLIC OF GERMANY  
Attn: E. F. Hicken (2)  
H. L. Jahn

Institute fur Kernenergetik  
und Energiesysteme  
University of Stuttgart  
Stuttgart  
FEDERAL REPUBLIC OF GERMANY  
Attn: G. Froehlich (2)  
M. Buerger

Kernforschungszentrum Karlsruhe  
Postfach 3640  
75 Karlsruhe  
FEDERAL REPUBLIC OF GERMANY  
Attn: Dr. S. Hagen (3)  
Dr. J. P. Hosemann  
Dr. M. Reihmann

Kraftwerk Union  
Hammerbacherstrasse 12 & 14  
Postfach 3220  
D-8520 Erlangen 2  
FEDERAL REPUBLIC OF GERMANY  
Attn: Dr. K. Hassman (2)

Technische Universitaet Muenchen  
D-8046 Garching  
FEDERAL REPUBLIC OF GERMANY  
Attn: Dr. H. Karwat

Swedish State Power Board  
El-Och Vaermeteknik  
SWEDEN  
Attn: Eric Ahlstroem

AERE Harwell  
Didcot  
Oxfordshire OX11 0RA  
UNITED KINGDOM  
Attn: J. Gittus, AETB (2)  
J. R. Matthews, TPD

Berkeley Nuclear Laboratory  
Berkeley GL 139PB  
Gloucestershire  
UNITED KINGDOM  
Attn: J. E. Antill

British Nuclear Fuels, Ltd.  
Building 396  
Springfield Works  
Salwick, Preston  
Lancs  
UNITED KINGDOM  
Attn: W. G. Cunliffe

National Nuclear Corp. Ltd.  
Cambridge Road  
Whetstone, Leicester, LE83LE  
UNITED KINGDOM  
Attn: R. May

Simon Engineering Laboratory  
University of Manchester  
M139PL,  
UNITED KINGDOM  
Attn: Prof. W. B. Hall

UKAEA Safety & Reliability Directorate  
Wigshaw Lane, Culcheth  
Warrington WA34NE  
Cheshire  
UNITED KINGDOM  
Attn: J. G. Collier  
S. F. Hall  
A. J. Wickett

(3)

Sandia Distribution:  
1131 W. B. Benedick  
1131 J. Fisk  
1512 J. C. Cummings  
1513 S. N. Kempka  
1513 A. C. Ratzel  
2512 V. M. Loyola  
2513 J. E. Shepherd  
6400 A. W. Snyder  
6410 J. W. Hickman  
6411 V. L. Behr  
6411 S. E. Dingman  
6411 F. E. Haskin  
6412 A. L. Camp  
6420 J. V. Walker  
6421 J. B. Rivard  
6422 D. A. Powers  
6423 K. Muramatsu  
6425 W. J. Camp  
6425 W. Frid  
6425 K. Schoenefeld  
6425 S. Unwin  
6427 M. Berman (15)  
6427 K. P. Guay  
6427 J. T. Hitchcock  
6427 J. Kotas  
6427 M. S. Krein  
6427 B. W. Marshall, Jr.  
6427 L. S. Nelson  
6427 O. Seebold  
6427 M. P. Sherman  
6427 S. R. Tieszen  
6427 G. Valdez  
6427 M. J. Wester  
6427 C. C. Wong  
6440 D. A. Dahlgren  
6442 W. A. von Rieseemann  
6444 S. L. Thompson  
6445 E. H. Richards  
6449 K. D. Bergeron  
8424 M. A. Pound  
8513 W. J. McClean  
8523 P. M. Barr  
8523 K. D. Marx  
8523 B. R. Sanders  
3141 C. M. Ostrander (5)  
3151 W. L. Garner

**BIBLIOGRAPHIC DATA SHEET**

NUREG/CR-3784  
SAND84-0689

SEE INSTRUCTIONS ON THE REVERSE

2 TITLE AND SUBTITLE

LIGHT WATER REACTOR SAFETY RESEARCH PROGRAM  
SEMIANNUAL REPORT, APRIL 1983 - SEPT. 1983

3 LEAVE BLANK

4 DATE REPORT COMPLETED

MONTH

YEAR

August

1984

5 DATE REPORT ISSUED

MONTH

YEAR

August

1984

5 AUTHOR(S)

Marshall Berman

7 PERFORMING ORGANIZATION NAME AND MAILING ADDRESS (Include Zip Code)

Sandia National Laboratories  
Albuquerque, NM 87185

8 PROJECT TASK WORK UNIT NUMBER

9 FUND OR GRANT NUMBER

A1255, A1301, A1336

10 SPONSORING ORGANIZATION NAME AND MAILING ADDRESS (Include Zip Code)

Office of Nuclear Regulatory Research  
U.S. Nuclear Regulatory Commission  
Washington, DC 20555

11a TYPE OF REPORT

Semiannual

b PERIOD COVERED (Inclusive Dates)

April 1983 - Sept. 1983

12 SUPPLEMENTARY NOTES

13 ABSTRACT (200 words or less)

This report describes the investigations and analyses conducted at Sandia National Laboratories, Albuquerque, in support of the Light Water Reactor Safety Research Program from April 1983 through September 1983. The Molten Fuel/Concrete Interactions (MFCI) Study investigates the mechanism of concrete erosion by molten core materials, the nature and rate of generation of evolved gases, and the effects of fission-product release. The Core Melt/Coolant Interactions (CMCI) Study investigates the characteristics of explosive and nonexplosive interactions between molten core materials and concrete, and the probabilities and consequences of such interactions. In the Hydrogen Program, the HECTR code for modelling hydrogen deflagration is being developed, experiments (including those in the FITS facility) are being conducted, and the Grand Gulf Hydrogen Igniter System II is being reviewed. All activities are continuing.

14 DOCUMENT ANALYSIS - & KEYWORDS DESCRIPTIONS

15 IDENTIFIERS/OPEN ENDED TERMS

15 AVAILABILITY STATEMENT

Unlimited

16 SECURITY CLASSIFICATION

(This page)

Unclassified

(This report)

Unclassified

17 NUMBER OF PAGES

18 PRICE

120555078877 1 IANLR3  
US NRC  
ADM-DIV OF TIDC  
POLICY & PUB MGT BR-PDR NUREG  
W-501  
WASHINGTON DC 20555